Tetsuo Sasao and André B. Fletcher
Introduction to VLBI Systems
Chapter 2
Lecture Notes for KVN Students
Partly Based on Ajou University Lecture Notes
(to be further edited)
Version 1.
Created on December 05, 2004.
Revised on January 14, 2005.
Revised on March 18, 2005.
Revised on April 14, 2005.
Revised on July 27, 2006.
Revised on June 15, 2007.
Revised on March 5, 2008.
Revised on April 16, 2009.
Revised on September 27, 2009.

Radio Telescope Antennas

This chapter describes principles and characteristics of antennas as very important components of VLBI systems.

Contents

1 Antenna Overview

According to J.D. Kraus, the antenna is ‘a region between a guided wave and a free–space wave or vice versa’ and ‘the antenna interfaces electrons on conductors and photons in space’ (see Figure 1). In addition, he says that ‘the eye is another such device’ (J.D. Kraus, Electromagnetics, 3rd Edition, 1984).

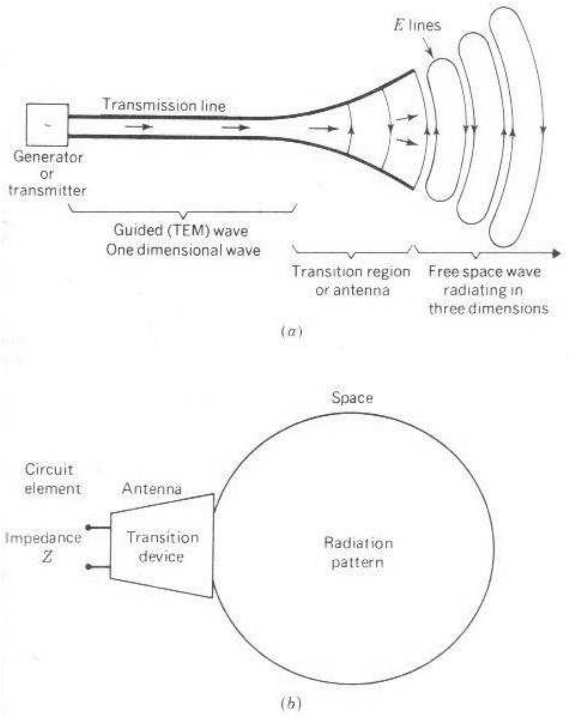

Figure 1: What is an antenna? (From Kraus, 1984).

1.1 Antennas for VLBI

Antennas are quite important components of VLBI (Very Long Baseline Interferometry), because

- They are the most expensive devices in VLBI.
  Usually antennas are more than an order of magnitude more expensive than receivers, data acquisition systems, frequency standards, and recorders.

- Data quality is sensitive to antennas.
  Characteristics of antennas, such as sensitivity, pointing, cross-polarization, gravitational and thermal deformation, and so on, directly affect quality of results of astrophysical and geodetic VLBI observations.

- It is difficult to repair or replace antennas.
  We have to stop observations for months, and pay very much money, to do so.

Therefore, we must have a good knowledge about antennas, and must do our best in designing and constructing antennas for making a good VLBI system.

1.2 Classifications of Radio Telescope Antennas

In the early history of radio astronomy, a variety of antennas, like dipole antennas or horn antennas, were used. However, the overwhelming majority of radio telescopes nowadays adopt the design of the paraboloidal (or, in exceptional cases, spherical) filled aperture antennas.

Existing radio telescope antennas may be classified into subgroups, according to several points of view.

1.2.1 Main Reflector Design

The rotationally symmetric paraboloidal shape is the most widely used in designs of main reflectors. The 100 m telescope at Effelsberg, Germany, is an example (see Figure 2).

The new Greenbank 100 m telescope (GBT), USA, adopts the offset paraboloidal design in order to achieve maximum efficiency in the reception of radio waves (see Figure 3).

In several huge radio telescopes in the world, partial paraboloidal surfaces are used in a cylindrical paraboloid design. The RATAN–600 telescope in Russia is an example (see Figure 4).

1.2.2 Mounting and Tracking Design

The most frequently used design for radio telescope mounting is the Alt–Azimuth design, which has a vertical azimuthal axis, and a horizontal altitude axis. The Alt–Azimuth mount (or ‘Az–El mount’ as frequently referred to by radio astronomers) is most symmetrical with respect to the direction

Figure 2: Effelsberg 100 m paraboloidal radio telescope, Germany.

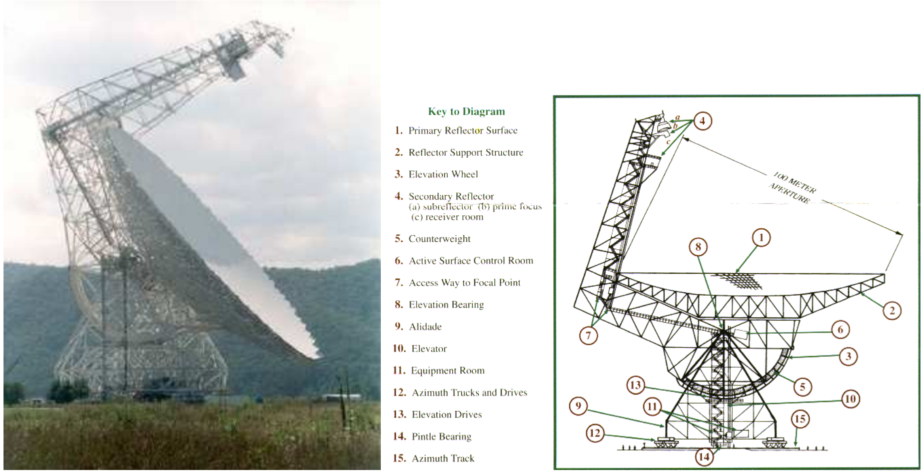

Figure 3: The giant offset paraboloid telescope GBT, USA.

Figure 4: The partial cylindrical paraboloid antenna RATAN–600, Russia.

of gravity, and hence is suited to the stable support of a large and heavy antenna structure. On the other hand, for tracking the diurnal motion of a radio source, real–time coordinate transformation from celestial equatorial (right ascention and declination) coordinates to horizontal (azimuth and elevation) coordinates, and simultaneous driving of the antenna around the two axes, are always required in this mount system. Moreover, it is in general difficult for an Alt–Azimuth telescope to track sources around the zenith direction. One of the 20 m antennas of the VERA (VLBI Exploration of Radio Astrometry) array at Iriki, Japan, is shown as an example of the Alt–Azimuth radio telescope (left panel in Figure 5).

The most popular mounting design for optical telescopes, except for recent huge ones, the Equatorial mount, has a polar axis parallel to the rotation axis of the Earth, and a declination axis. The Equatorial mount is suited for easy tracking of radio sources in any direction in the sky, and is used for relatively light–weight radio telescopes. The 25 m antennas in the Westerbork Synthesis Radio Telescope (WSRT, the Netherlands) are examples (right panel in Figure 5).

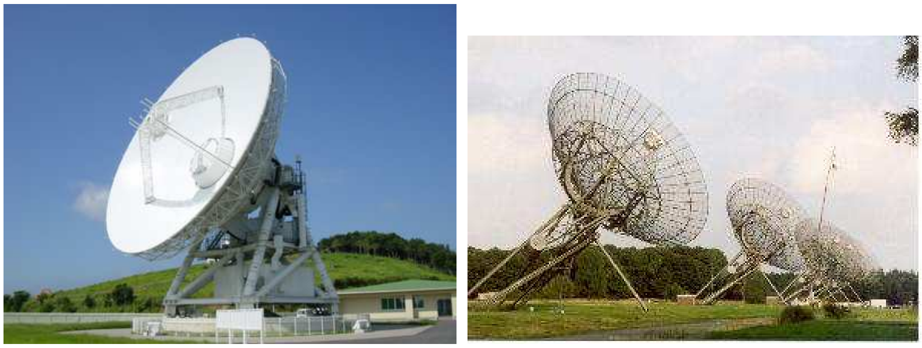

Figure 5: Alt–Azimuth mount antenna at the VERA Iriki station, Japan (Left), and Equatorial mount antennas in the WSRT, the Netherlands (Right).

In general, for orienting an antenna towards a desired sky position, we need an axis fixed with respect to the ground, which we call “fixed axis”, and another axis rotating around the fixed axis, which we call “moving axis”. In the Alt–Azimuth design, the fixed axis is the azimuthal axis, and the moving axis is the elevation axis. In the Equatorial design, the fixed axis is the polar axis, and the moving axis is the declination axis.

A little unusual XY mount design, with a horizontal fixed axis, is adopted in 26 m antenna at Hobart, University of Tasmania, Australia (Figure 6). This antenna was originally built by NASA for tracking space vehicles, and

Figure 6: XY mount antenna at Hobart, Australia.

was installed near Canberra. Later, the antenna was moved to Hobart, and now is intensively used for geodetic and astrophysical VLBI observations.

A very unique design consisting of a fixed spherical main reflector antenna is used in the giant 305 m radio telescope at Arecibo (Puerto Rico, USA). Instead of driving the main reflector, a cable suspended subreflector with special aberration correction optics is driven to track the radio source (see Figure 7).

Figure 7: A spherical fixed main reflector antenna at Arecibo, Puerto Rico, USA, 305 m diameter.

1.2.3 Wheel & Track and Yoke & Tower Alt–Azimuth Antennas

Figure 8 shows the 20 m VERA antenna (Left), and the 10 m antenna (Right), in NAO Mizusawa, Japan.

The entire structure of the 20 m antenna is supported by four wheels, which move on a circular rail fixed on the antenna foundation, in order to change the azimuthal orientation of the antenna. Such an antenna is called a "wheel & track" antenna.

Figure 8: Wheel & Track (left) and Yoke & Tower (Right) antennas.

In the 10 m antenna, an azimuth gear is attached to the top of the tower–like pedestal, and the antenna structure above the gear is rotated around the azimuth axis by the motor drives. Such an antenna is called "yoke & tower" antenna.

Generally, the yoke & tower design is suited to keep a fixed intersection point for the Azimuth and Elevation axes – this is an important reference point in geodetic VLBI. However, for mechanical reasons, the wheel & track design is more frequently used for large aperture antennas.

1.2.4 Stiffness

For some large aperture millimeter wave telescopes aimed mainly at spectroscopy and imaging of radio sources, a flexible structure is adopted to realize the so–called "homologous transformation", which is such that the deformed main reflector surface maintains a paraboloid shape, and forms a sharp focus, even when the telescope is tilted under the action of the Earth's

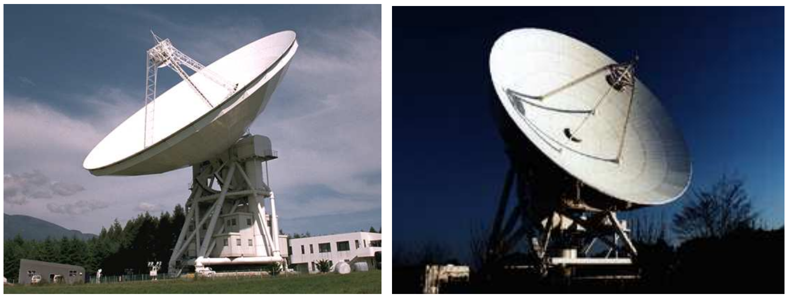

Figure 9: A flexible 45 m Millimeter–Wave Telescope at Nobeyama, Japan (left), and a "stiff" 32 m geodetic VLBI antenna at Tsukuba, Japan (Right).

gravity. The 45 m Millimeter–Wave Telescope at Nobeyama, Japan, is a successful example of such a design (see left panel in Figure 9).

On the other hand, radio telescope antennas for geodetic and astrometric VLBI observations are usually designed to be very stiff, to eliminate possible errors due to the deformation of the telescope. The 32 m geodetic VLBI antenna at Tsukuba, Japan, is an example of the "stiff" telescope (right panel in Figure 9).

1.2.5 Antenna Reference Point

Geodetic VLBI determines positions of reference points of antennas with typical accuracy of 1 cm or better. Therefore, it is very important to precisely define and maintain the reference points in the antennas.

In general, we can select any point in an antenna as a reference point, as far as the point is fixed with respect to the ground. There are certain preferable points, however, suitable to the geodetic analysis.

The best choice is the cross point of fixed and moving axes of the antenna, when the two axes intersect. In such a case, difference between a time t_r, when a wave front from an astronomical radio source crosses the reference point, and a time t_f, when a part of the same wave front, which is reflected by main– and subreflectors and then transmitted via a cable, reaches to a point where a time tag is added to the signal, is constant (i.e. $t_f - t_r =$ const) irrespective of a sky direction of the source, as far as time variations of antenna structure and receiver–transmission characteristics can be ignored or well calibrated. This is really comvenient for geodetic VLBI analysis since we can then assume that an observed delay between two stations A and B which is $\tau_{obs} = t_{f_B} - t_{f_A}$ is equal to a delay between arrival times of a same wave front at reference points of two antennas $\tau_{ref} = t_{r_B} - t_{r_A}$ plus a constant term (i.e. $\tau_{obs} = \tau_{ref}+$ const).

If the two axes do not intersect, we usually choose a point in the fixed axis closest to the moving axis and add a source–direction dependent correction term to the relation between τ_{obs} and τ_{ref}.

Figure 10: Alt–Azimuth mount 11 m antenna at Kashima, Japan (left), and Equatorial mount 43 m antenna at Green Bank, USA (Right). Locations of fixed and moving axes are schematically shown by straight lines.

In Alt–Azimuth mount antennas, the fixed azimuth axis and moving elevation axis are usually designed to intersect with each other. An example is 11 m antenna at Kashima, Japan (left panel in Figure 10). In Equatorial mount antennas, it is usually difficult to make the right–ascension and declination axes to intersect with each other. An example is 43 m antenna in Green Bank, USA (right panel in Figure 10).

Figure 11: 11 m antenna at Kashima, Japan, with the reference point directly visible from outside (Left), and 32 m antenna at Tsukuba, Japan, with the reference point invisible from outside (Middle). Also shown is a cat's eye used in ground geodetic measurements.

It is very important for geodetic VLBI to tie the antenna reference point with geodetic markers on the ground, in order, for example, to combine a national geodetic network with the VLBI–based international frame. For this purpose, we conduct ground geodetic measurement of the position of the reference point with respect to the geodetic markers, using special devices such as "cat's eye" (rightmost panel of Figure 11). It is very convenient in such measurements if the position of the reference point is directly "visible" from outside where we can place a cat's eye. Figure 11 shows examples of Alt–Azimuth antennas with visible and invisible reference points.

Figure 12: In 20 m geodetic VLBI antenna (Top, Left) at Wettzell, Germany, a compact receiver room is located in the back structure of the main reflector, and the Az–El cross point is covered by a cabin fixed on a rotating disk above the azimuth gear (Top, Middle). There is a firmly supported meausrement bench in the cabin (Bottom, Middle). Vertical displacement of the bench is accurately monitored with respect to the invar tube which is fixed to the ground and vertically extended along the Az–axis (Bottom, Left). The target on the bench (Right) is adjusted to the right cross–point of the two axes, and is measured from geodetic markers on the ground through a hatch of the cabin (Top, Midle).

A geodetic VLBI antenna with 20 m diameter in Wettzell Fundamental Station, Germany, is specially designed for precise measurements of the reference point (Figure 12).

1.2.6 Observing Frequency

The most significant factor in antenna design today is the maximum frequency of observation. Antennas are often called as "cm–wave–", "mm–wave–" or "submm-wave" antennas, according to their maximum observing frequency (or shortest observing wavelength). In order to convert wavelength λ to frequency ν, one can use a convenient approximate formula:

$$\nu \text{ (in GHz) } \simeq \frac{30}{\lambda \text{ (in cm)}} \, . \tag{1}$$

For cm–wave antennas, the requirements of surface and pointing accuracy are not very severe for present–day antenna manufacturing technology. It is therefore relatively easy to make large antennas in the cm–wave range. At the low–frequency end, the main reflectors of cm–wave antennas can be made of meshed wires. The 25.6 m antenna at Onsala, Sweden, is an example (Figure 13).

Figure 13: A cm–wave antenna at Onsala, Sweden, 25.6 m diameter.

For mm–wave antennas, the surface accuracy must be as small as 0.1 mm rms, and the pointing accuracy must be as good as 0.001 degree rms. The large aperture mm–wave antennas like the IRAM 30 m (Spain, EU; left panel in Figure 14), the Nobeyama 45 m (left panel in Figure 9), and the Effelsberg 100 m (Figure 2) are the result of state–of–the–art achievements of modern technology. Some of the mm–wave telescopes, including the TRAO 14 m telescope at Daejeon, Korea (see right panel in Figure 14), are covered by radomes to avoid the effects of strong wind and inhomogeneous solar heating.

The most stringent tolerances in antenna construction are required in the submm–wave range. As a result, all existing submm–wave antennas are relatively small (with diameters around 10 m or smaller), and some of them are located within domes, just like the big optical telescopes. Since the atmosphere is largely opaque in the submm–wave range at low altitude sites near sea level, but fairly transparent at dry high altitude sites, submm–wave telescopes are built on high moutains, with altitudes of 3000–5000 m above sea level (see Figures 15 and 16).

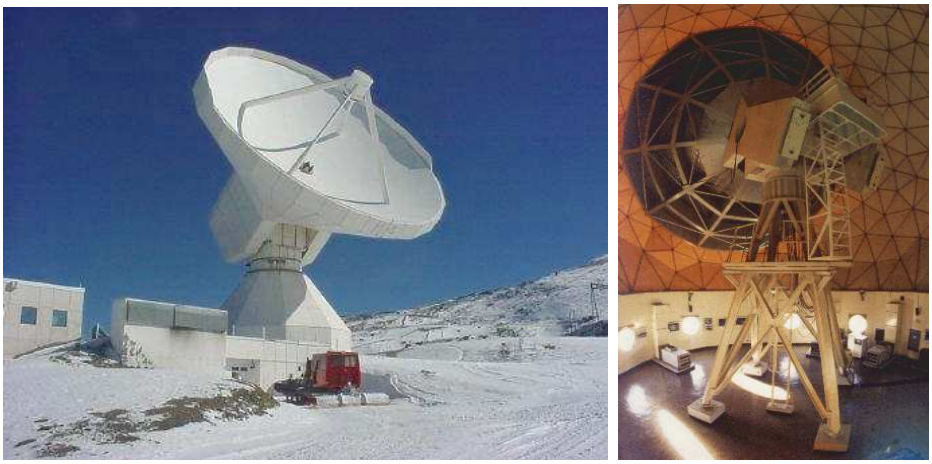

Figure 14: IRAM mm–wave telescope, Spain, 30 m diameter (Left), and radome–covered TRAO 14 m mm–wave telescope at Daejeon, Korea (Right).

Figure 15: The largest submm–wave antenna JCMT, UK, 15 m diameter, at Mauna Kea, Hawaii.

Figure 16: Main reflector (Left) and radome (Right) of the 1.2 m submm–wave telescope which worked for several years at the Top of Mount Fuji, Japan.

1.3 Basic Structure of a Paraboloidal Antenna

The basic components of the structure of an Alt–Azimuth paraboloidal antenna are shown in Figure 17. The paraboloidal structure is rotated around the fixed vertical Azimuth axis, and the horizontal Elevation axis, in order to point to any direction in the sky. Usually, the main reflector is composed of a number of panels made of aluminum or carbon fiber, etc, which are fixed to the back structure by adjustable supports. The feed horn is a kind of small antenna, and there is a so–called **waveguide to coaxial–cable (or coaxial to waveguide) converter** at the neck of the feed horn, where the electromagnetic field in space generates the voltage in circuits or vice versa. The waveguide to coaxial–cable converter is the only “real antenna” in strict sense of the second definition of the antenna by Kraus: ‘the antenna interfaces electrons on conductors and photons in space’. The huge structures such as the main reflectors and subreflectors, can be regarded as auxilliary reflecting devices.

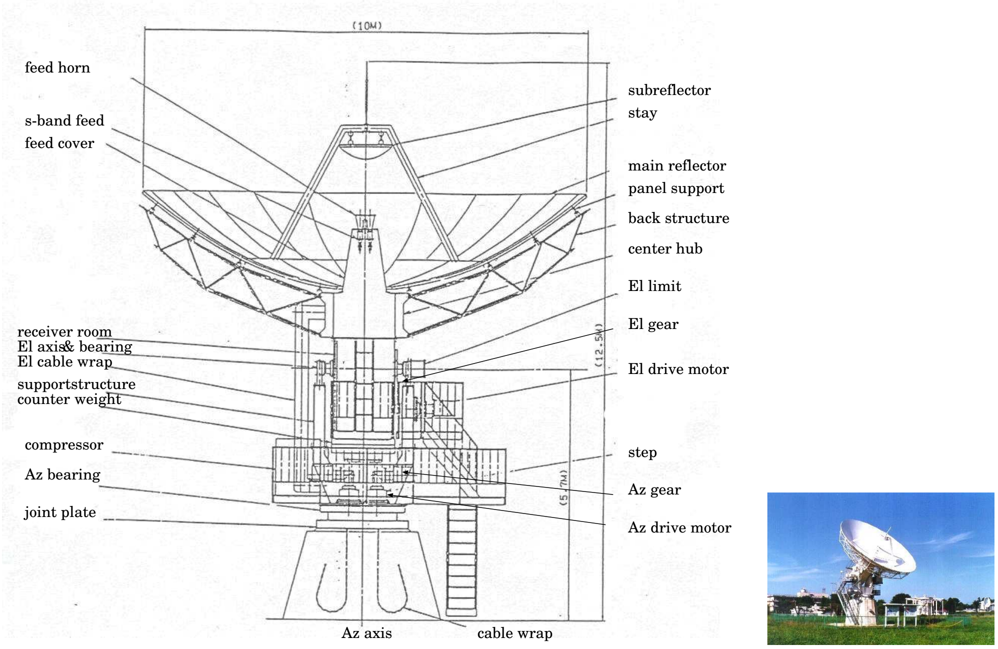

Figure 17: Structure of 10 m VLBI antenna at NAO Mizusawa, Japan.

1.4 Why Paraboloid?

Why are paraboloidal antennas the most frequently used for radio telescopes? This is because paraboloids collect plane radio waves coming from astronomical sources towards a focal point where we can place the waveguide to coaxial–cable converter, which transforms the energy of photons in free space to the energy of electrons in conductors in the most efficient way.

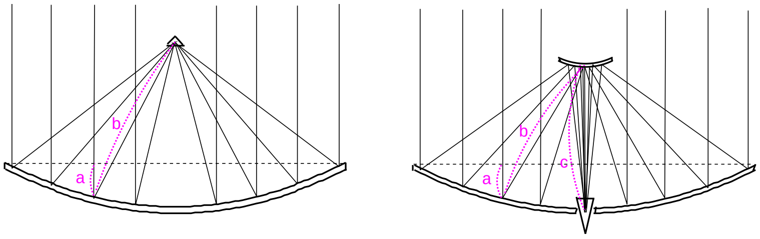

Figure 18: Primary (Left) and secondary (Right) foci of paraboloidal antennas.

In the secondary focus system shown in the right panel of Figure 18, a combination of a paraboloidal main reflector and a hyperboloidal subreflector produces the secondary focus near the main reflector, where the receivers can be conveniently placed. The path length of a ray from the aperture plane — shown by dotted horizontal lines in Figure 18 — to the focus is $a + b$ in the primary focus system, and $a+b+c$ in the secondary focus system; this length is kept constant for any ray coming parallel with the symmetry axis of the paraboloid. Therefore, the radio waves are collected and summed up with equal phases (i.e. in a “phase–coherent” way) at the foci of the paraboloidal antennas.

There are two possible designs for forming the secondary focus in paraboloidal antennas which use convex (Cassegrain) and concave (Gregorian) hyperboloidal mirrors, respectively, as subreflectors (Figure 19).

The Cassegrain design is widely adopted in radio telescopes, because it allows a relatively stable structure against gravitational deformation and wind pressure. On the other hand, the Gregorian design is better suited to the cases where both the primary and secondary foci are used for receiving different frequency bands. In fact, in the Gregorian design, the primary focus feed horn can simply be inserted in front of the subreflector when needed and then removed to allow the secondary focus to be formed.

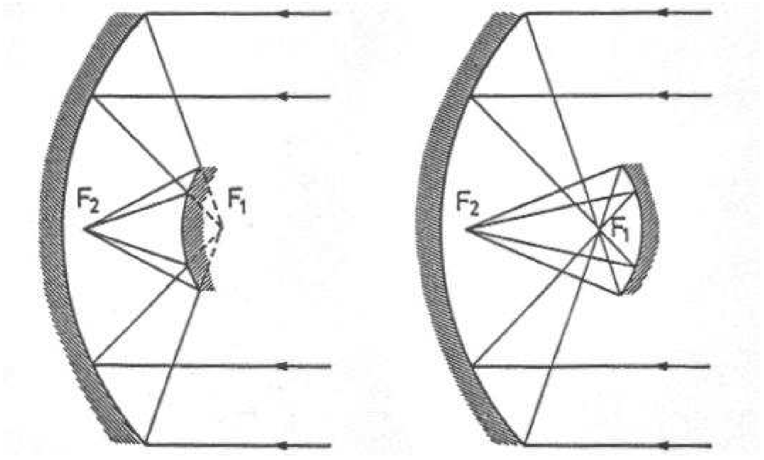

Figure 19: Cassegrain (Left) and Gregorian (Right) foci of paraboloidal antennas.

2 Antenna Beams

2.1 Some Elements of Vector Algebra

Many textbooks list formulae of vector algebra such as shown in Figure 20. It is not easy to memorize all these complicated formulae. Moreover, they may often contain typographic errors! Without knowledge of these formulae, however, it is difficult to understand electromagnetic theory of radiotelescope antennas.

Fortunately, it is not necessary at all to memorize all these formulae. Instead, we have to memorize just two symbols and one formula, only. They are the Kronecker symbol δ_{ij}, the Levi–Civita symbol ϵ_{ijk}, and a formula $\epsilon_{ijk}\epsilon_{ilm} = \delta_{jl}\delta_{km} - \delta_{jm}\delta_{kl}$. Here, repeated indecies i implies summation, as we will see below.

Let us consider a rectangular (Cartesian) coordinate system, with basis vectors $\boldsymbol{i}_1$, $\boldsymbol{i}_2$, and $\boldsymbol{i}_3$, in a three–dimensional Euclidean space (Figure 21).

In this coordinate system, we consider a radius vector $\boldsymbol{r}$ with elements (or components) x_1, x_2, and x_3 drawn from the origin of the coordinate system to a point with coordinates x_1, x_2, and x_3. We consider also a scalar field $\Phi(\boldsymbol{r})$ and a vector field $\boldsymbol{A}(\boldsymbol{r})$ with elements A_1, A_2, and A_3, as functions of $\boldsymbol{r}$.

Now let us introduce following notations and conventions.

1. **Kronecker's delta symbol** δ_{ij}

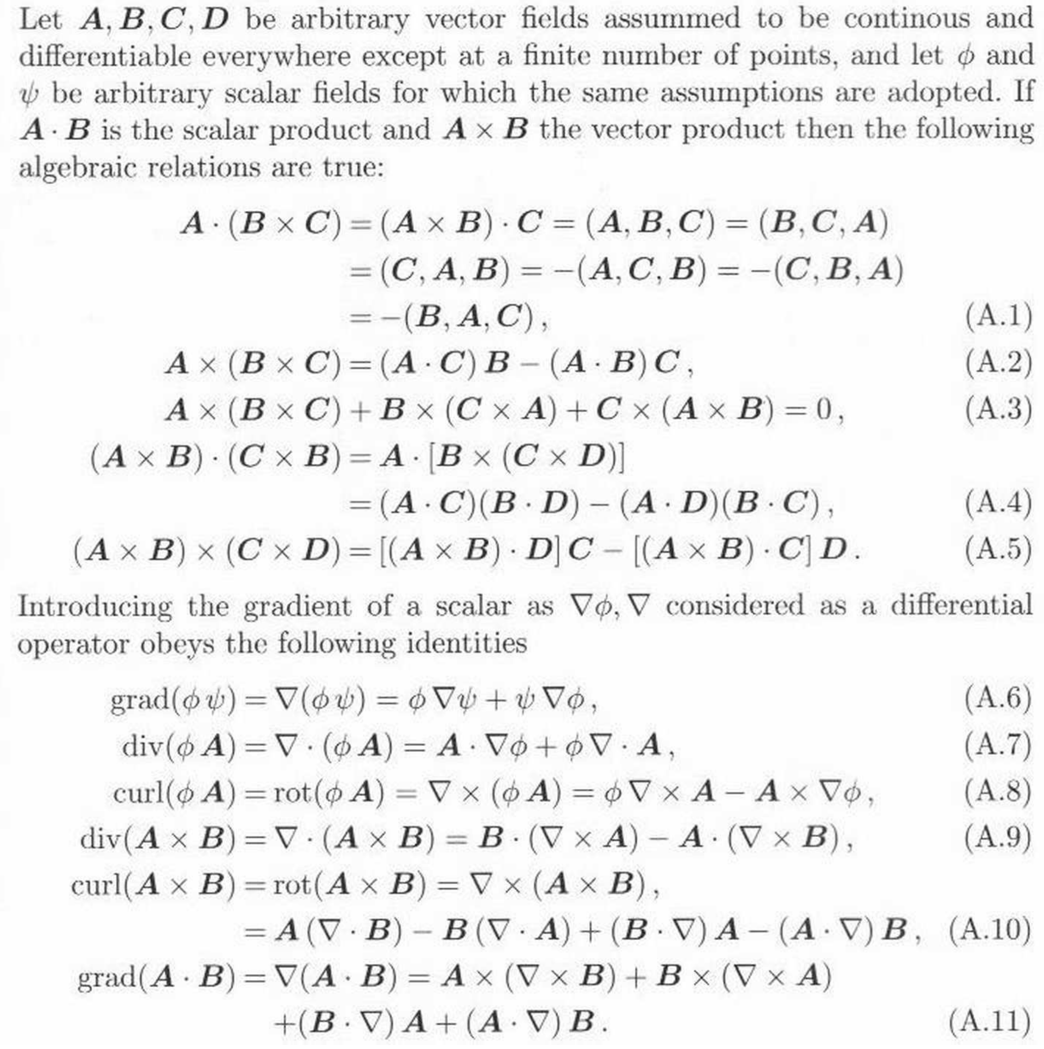

Let $\boldsymbol{A}, \boldsymbol{B}, \boldsymbol{C}, \boldsymbol{D}$ be arbitrary vector fields assummed to be continous and differentiable everywhere except at a finite number of points, and let ϕ and ψ be arbitrary scalar fields for which the same assumptions are adopted. If $\boldsymbol{A} \cdot \boldsymbol{B}$ is the scalar product and $\boldsymbol{A} \times \boldsymbol{B}$ the vector product then the following algebraic relations are true:

$$\begin{aligned}
\boldsymbol{A} \cdot (\boldsymbol{B} \times \boldsymbol{C}) &= (\boldsymbol{A} \times \boldsymbol{B}) \cdot \boldsymbol{C} = (\boldsymbol{A}, \boldsymbol{B}, \boldsymbol{C}) = (\boldsymbol{B}, \boldsymbol{C}, \boldsymbol{A}) \\
&= (\boldsymbol{C}, \boldsymbol{A}, \boldsymbol{B}) = -(\boldsymbol{A}, \boldsymbol{C}, \boldsymbol{B}) = -(\boldsymbol{C}, \boldsymbol{B}, \boldsymbol{A}) \\
&= -(\boldsymbol{B}, \boldsymbol{A}, \boldsymbol{C})\,, && \text{(A.1)} \\
\boldsymbol{A} \times (\boldsymbol{B} \times \boldsymbol{C}) &= (\boldsymbol{A} \cdot \boldsymbol{C})\, \boldsymbol{B} - (\boldsymbol{A} \cdot \boldsymbol{B})\, \boldsymbol{C}\,, && \text{(A.2)} \\
\boldsymbol{A} \times (\boldsymbol{B} \times \boldsymbol{C}) + \boldsymbol{B} \times (\boldsymbol{C} \times \boldsymbol{A}) + \boldsymbol{C} \times (\boldsymbol{A} \times \boldsymbol{B}) &= 0\,, && \text{(A.3)} \\
(\boldsymbol{A} \times \boldsymbol{B}) \cdot (\boldsymbol{C} \times \boldsymbol{B}) &= \boldsymbol{A} \cdot [\boldsymbol{B} \times (\boldsymbol{C} \times \boldsymbol{D})] \\
&= (\boldsymbol{A} \cdot \boldsymbol{C})(\boldsymbol{B} \cdot \boldsymbol{D}) - (\boldsymbol{A} \cdot \boldsymbol{D})(\boldsymbol{B} \cdot \boldsymbol{C})\,, && \text{(A.4)} \\
(\boldsymbol{A} \times \boldsymbol{B}) \times (\boldsymbol{C} \times \boldsymbol{D}) &= [(\boldsymbol{A} \times \boldsymbol{B}) \cdot \boldsymbol{D}]\, \boldsymbol{C} - [(\boldsymbol{A} \times \boldsymbol{B}) \cdot \boldsymbol{C}]\, \boldsymbol{D}\,. && \text{(A.5)}
\end{aligned}$$

Introducing the gradient of a scalar as $\nabla\phi, \nabla$ considered as a differential operator obeys the following identities

$$\begin{aligned}
\operatorname{grad}(\phi\,\psi) &= \nabla(\phi\,\psi) = \phi\,\nabla\psi + \psi\,\nabla\phi\,, && \text{(A.6)} \\
\operatorname{div}(\phi\,\boldsymbol{A}) &= \nabla \cdot (\phi\,\boldsymbol{A}) = \boldsymbol{A} \cdot \nabla\phi + \phi\,\nabla \cdot \boldsymbol{A}\,, && \text{(A.7)} \\
\operatorname{curl}(\phi\,\boldsymbol{A}) &= \operatorname{rot}(\phi\,\boldsymbol{A}) = \nabla \times (\phi\,\boldsymbol{A}) = \phi\,\nabla \times \boldsymbol{A} - \boldsymbol{A} \times \nabla\phi\,, && \text{(A.8)} \\
\operatorname{div}(\boldsymbol{A} \times \boldsymbol{B}) &= \nabla \cdot (\boldsymbol{A} \times \boldsymbol{B}) = \boldsymbol{B} \cdot (\nabla \times \boldsymbol{A}) - \boldsymbol{A} \cdot (\nabla \times \boldsymbol{B})\,, && \text{(A.9)} \\
\operatorname{curl}(\boldsymbol{A} \times \boldsymbol{B}) &= \operatorname{rot}(\boldsymbol{A} \times \boldsymbol{B}) = \nabla \times (\boldsymbol{A} \times \boldsymbol{B})\,, \\
&= \boldsymbol{A}\,(\nabla \cdot \boldsymbol{B}) - \boldsymbol{B}\,(\nabla \cdot \boldsymbol{A}) + (\boldsymbol{B} \cdot \nabla)\,\boldsymbol{A} - (\boldsymbol{A} \cdot \nabla)\,\boldsymbol{B}\,, && \text{(A.10)} \\
\operatorname{grad}(\boldsymbol{A} \cdot \boldsymbol{B}) &= \nabla(\boldsymbol{A} \cdot \boldsymbol{B}) = \boldsymbol{A} \times (\nabla \times \boldsymbol{B}) + \boldsymbol{B} \times (\nabla \times \boldsymbol{A}) \\
&\quad + (\boldsymbol{B} \cdot \nabla)\,\boldsymbol{A} + (\boldsymbol{A} \cdot \nabla)\,\boldsymbol{B}\,. && \text{(A.11)}
\end{aligned}$$

Figure 20: Typical formulae of vector algebra.

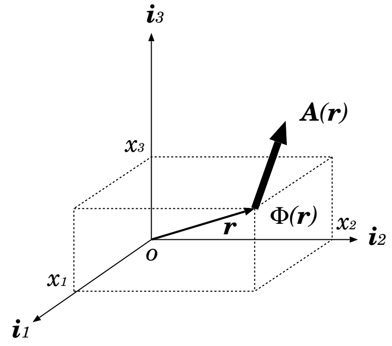

Figure 21: Rectangular coordinate system in a three–dimensional space.

δ_{ij} is 1 when the two indecies take the same value, and 0 when they are different.

$$\delta_{ij} = \begin{cases} 0 & \text{at } i \neq j \\ 1 & \text{at } i = j \end{cases} \qquad (\text{with } \; i,j = 1,2,3). \tag{2}$$

Therefore, $\delta_{11} = \delta_{22} = \delta_{33} = 1$, and $\delta_{12} = \delta_{13} = \cdots = \delta_{32} = 0$.

2. **Levi–Civita's anti–symmetric symbol ϵ_{ijk}**

   ϵ_{123} is defined to be 1, and sign is changed whenever adjacent indecies are substituted.

$$\begin{aligned} &\epsilon_{123} = 1 \\ &\epsilon_{213} = -\epsilon_{123} = -1, \\ &\epsilon_{312} = -\epsilon_{132} = \epsilon_{123} = 1, \\ &\epsilon_{321} = -\epsilon_{231} = \epsilon_{213} = -\epsilon_{123} = -1, \\ &\epsilon_{112} = -\epsilon_{112} = 0, \; \epsilon_{232} = -\epsilon_{232} = 0, \\ &\cdots . \end{aligned} \tag{3}$$

3. **Einstein's summation convention**

   Repeated indecies, ii say, imply summation over 11, 22 and

33. For example,

$$\begin{aligned} &A_iB_i \equiv \sum_{i=1}^{3} A_iB_i = A_1B_1 + A_2B_2 + A_3B_3, \\ &\text{and} \\ &C_{jj} \equiv \sum_{i=1}^{3} C_{ii} = C_{11} + C_{22} + C_{33}. \end{aligned} \tag{4}$$

4. **Nabla symbol of spatial derivative ∇**

   ∇ is a vector like differential operator with three 'elements'

   $$\frac{\partial}{\partial x_1}, \quad \frac{\partial}{\partial x_2}, \quad \text{and } \frac{\partial}{\partial x_3}, \tag{5}$$

   where $\frac{\partial}{\partial x_i}$ stands for a partial derivative with respect to x_i.

If we apply the above symbols and notations to vector fields $\boldsymbol{A}(\boldsymbol{r})$ and $\boldsymbol{B}(\boldsymbol{r})$, as well as to a scalar field $\Phi(\boldsymbol{r})$, we can express:

- a scalar (or inner) product $\boldsymbol{A} \cdot \boldsymbol{B}$ as

  $$\boldsymbol{A} \cdot \boldsymbol{B} = A_iB_i, \tag{6}$$

- i–th element of a vector (or outer) product $\boldsymbol{A} \times \boldsymbol{B}$ as

  $$(\boldsymbol{A} \times \boldsymbol{B})_i = \epsilon_{ijk}A_jB_k, \tag{7}$$

  in fact, $\epsilon_{1jk}A_jB_k = A_2B_3 - A_3B_2$, $\epsilon_{2jk}A_jB_k = A_3B_1 - A_1B_3$, and $\epsilon_{3jk}A_jB_k = A_1B_2 - A_2B_1$, in agreement with the definition of the vector product,

- i–th element of a gradient $grad\Phi$ as

  $$(grad\Phi)_i = (\nabla\Phi)_i = \frac{\partial}{\partial x_i}\Phi = \frac{\partial \Phi}{\partial x_i}, \tag{8}$$

- a divergence $div\boldsymbol{A}$ as

  $$div\boldsymbol{A} = \nabla \cdot \boldsymbol{A} = \frac{\partial}{\partial x_i}A_i = \frac{\partial A_i}{\partial x_i}, \tag{9}$$

  and

- i–th element of a rotation (or curl) $rot\boldsymbol{A}$ as

$$(rot\boldsymbol{A})_i = (\nabla \times \boldsymbol{A})_i = \epsilon_{ijk}\frac{\partial}{\partial x_j}A_k = \epsilon_{ijk}\frac{\partial A_k}{\partial x_j}. \tag{10}$$

A very useful relationship is known between the Levi–Civita's and Kronecker's symbols, which is described by the formula mentioned earlier:

$$\epsilon_{ijk}\epsilon_{ilm} = \delta_{jl}\delta_{km} - \delta_{jm}\delta_{kl}. \tag{11}$$

We can verify this formula by examining all possible combinations of indecies.

In view of Einstein's summation convention, equation (11) is equivalent to

$$\epsilon_{1jk}\epsilon_{1lm} + \epsilon_{2jk}\epsilon_{2lm} + \epsilon_{3jk}\epsilon_{3lm} = \delta_{jl}\delta_{km} - \delta_{jm}\delta_{kl}. \tag{12}$$

Since j, k, l and m may be 1, 2 or 3, equation (11) or (12) has, in general, $3^4 = 81$ components. However, symmetry conditions greately reduce number of components which we really have to individually consider.

First, let us consider what happens if we substitute indecies j and k, or l and m. Because of the antisymmetric property of Levi–Civita symbol, the LHS of equation (11) is antisymmetric (only sign is changed) with respect to such a substitution, and the RHS is also antisymmetric, since if we substitute j and k, for example, the RHS changes its sign as:

$$\delta_{kl}\delta_{jm} - \delta_{km}\delta_{jl} = -(\delta_{jl}\delta_{km} - \delta_{jm}\delta_{kl}).$$

This says that, if we prove equation (11) for jk or lm, then the equation is automatically proven for kj or ml. Moreover, if $j = k$ or $l = m$, the both sides must be equal to 0 (therefore, equal to each other), since for any number A, if $A = -A$, then $A = 0$. Consequently, among 9 components of jk and 9 components of lm, we have to individually consider only 3 and 3 components, which are '12', '13' and '23', for example (see equation (13)).

$$jk = \begin{pmatrix} 11 & \mathbf{12} & \mathbf{13} \\ 21 & 22 & \mathbf{23} \\ 31 & 32 & 33 \end{pmatrix}, \quad \text{and} \quad lm = \begin{pmatrix} 11 & \mathbf{12} & \mathbf{13} \\ 21 & 22 & \mathbf{23} \\ 31 & 32 & 33 \end{pmatrix}. \tag{13}$$

Hence, in total, $3 \times 3 = 9$ components were left to be individually considered.

Furthermore, it can be easily seen that if l or m in equation (11) is not equal to neither j nor k, then both sides must be equal to 0. In fact, if jk is '12', for example, equation (12) becomes

$$\epsilon_{312}\epsilon_{3lm} = \delta_{1l}\delta_{2m} - \delta_{1m}\delta_{2l}.$$

Both sides of this equation are equal to 0, if l or m is 3.

So, we have to consider individually, only three cases when both jk and lm = '12', both jk and lm = '13', and both jk and lm = '23'. They are

$$\begin{aligned}
&\text{for '12}', \quad LHS = \epsilon_{312}\epsilon_{312} = 1, && \text{and} \quad RHS = \delta_{11}\delta_{22} = 1,\\
&\text{for '13}', \quad LHS = \epsilon_{213}\epsilon_{213} = 1, && \text{and} \quad RHS = \delta_{11}\delta_{33} = 1,\\
&\text{for '23}', \quad LHS = \epsilon_{123}\epsilon_{123} = 1, && \text{and} \quad RHS = \delta_{22}\delta_{33} = 1.
\end{aligned}$$

Thus, we proved equation (11).

If we use the above symbols and equation (11), all the complicated formulae of vector algebra are derived in straight forward ways. For example,

$$\begin{aligned}
&[\boldsymbol{A} \times (\boldsymbol{B} \times \boldsymbol{C})]_i = \epsilon_{ijk} A_j \epsilon_{klm} B_l C_m\\
&= \epsilon_{kij}\epsilon_{klm} A_j B_l C_m = (\delta_{il}\delta_{jm} - \delta_{im}\delta_{jl}) A_j B_l C_m\\
&= A_j B_i C_j - A_j B_j C_i = B_i A_j C_j - C_i A_j B_j\\
&= [\boldsymbol{B}(\boldsymbol{A} \cdot \boldsymbol{C}) - \boldsymbol{C}(\boldsymbol{A} \cdot \boldsymbol{B})]_i,
\end{aligned}$$

and, therefore,

$$\boldsymbol{A} \times (\boldsymbol{B} \times \boldsymbol{C}) = \boldsymbol{B}(\boldsymbol{A} \cdot \boldsymbol{C}) - \boldsymbol{C}(\boldsymbol{A} \cdot \boldsymbol{B}). \tag{14}$$

We used here a property of Kronecker's symbol: $\delta_{ij} A_j = A_i$.

Also,

$$(\boldsymbol{A} \times \boldsymbol{B}) \cdot (\boldsymbol{C} \times \boldsymbol{D}) = \epsilon_{ijk}\epsilon_{ilm} A_j B_k C_l D_m = A_j B_k C_j D_k - A_j B_k C_k D_j,$$

and, hence

$$(\boldsymbol{A} \times \boldsymbol{B}) \cdot (\boldsymbol{C} \times \boldsymbol{D}) = (\boldsymbol{A} \cdot \boldsymbol{C})(\boldsymbol{B} \cdot \boldsymbol{D}) - (\boldsymbol{A} \cdot \boldsymbol{D})(\boldsymbol{B} \cdot \boldsymbol{C}). \tag{15}$$

Furthermore,

$$\begin{aligned}
&[\nabla \times (\nabla \times \boldsymbol{A})]_i = \epsilon_{ijk} \tfrac{\partial}{\partial x_j} \epsilon_{klm} \tfrac{\partial}{\partial x_l} A_m\\
&= (\delta_{il}\delta_{jm} - \delta_{im}\delta_{jl}) \tfrac{\partial}{\partial x_j} \tfrac{\partial}{\partial x_l} A_m = \tfrac{\partial}{\partial x_j} \tfrac{\partial}{\partial x_i} A_j - \tfrac{\partial}{\partial x_j} \tfrac{\partial}{\partial x_j} A_i\\
&= [\nabla(\nabla \cdot \boldsymbol{A}) - \nabla^2 \boldsymbol{A}]_i,
\end{aligned}$$

where

$$\nabla^2 \equiv \frac{\partial^2}{\partial x_1^2} + \frac{\partial^2}{\partial x_2^2} + \frac{\partial^2}{\partial x_1^3},$$

and, therefore,

$$\nabla \times (\nabla \times \boldsymbol{A}) = \nabla(\nabla \cdot \boldsymbol{A}) - \nabla^2 \boldsymbol{A}. \tag{16}$$

Other useful examples are:

$$\nabla \cdot (\boldsymbol{A} \times \boldsymbol{B}) = \frac{\partial}{\partial x_i}\epsilon_{ijk}(A_j B_k) = B_k \epsilon_{kij}\frac{\partial}{\partial x_i}A_j - A_j \epsilon_{jik}\frac{\partial}{\partial x_i}B_k, \quad \Rightarrow$$

$$\nabla \cdot (\boldsymbol{A} \times \boldsymbol{B}) = \boldsymbol{B} \cdot (\nabla \times \boldsymbol{A}) - \boldsymbol{A} \cdot (\nabla \times \boldsymbol{B}), \tag{17}$$

$$[\nabla \times (\nabla\Phi)]_i = \epsilon_{ijk}\frac{\partial}{\partial x_j}\frac{\partial}{\partial x_k}\Phi = \epsilon_{ikj}\frac{\partial}{\partial x_k}\frac{\partial}{\partial x_j}\Phi = -\epsilon_{ijk}\frac{\partial}{\partial x_j}\frac{\partial}{\partial x_k}\Phi = 0, \quad \Rightarrow$$

$$rot(grad\Phi) = \nabla \times (\nabla\Phi) = 0, \tag{18}$$

$$\nabla \cdot (\nabla \times \boldsymbol{A}) = \frac{\partial}{\partial x_i}\epsilon_{ijk}\frac{\partial}{\partial x_j}A_k = \epsilon_{ijk}\frac{\partial}{\partial x_i}\frac{\partial}{\partial x_j}A_k = 0, \quad \Rightarrow$$

$$div(rot\boldsymbol{A}) = \nabla \cdot (\nabla \times \boldsymbol{A}) = 0, \tag{19}$$

and,

$$\nabla \cdot (\Phi\boldsymbol{A}) = \frac{\partial}{\partial x_i}(\Phi A_i) = \frac{\partial \Phi}{\partial x_i}A_i + \Phi\frac{\partial A_i}{\partial x_i} = \nabla\Phi \cdot \boldsymbol{A} + \Phi\,\nabla \cdot \boldsymbol{A}, \quad \Rightarrow$$

$$div(\Phi\boldsymbol{A}) = grad\Phi \cdot \boldsymbol{A} + \Phi\, div\boldsymbol{A}. \tag{20}$$

2.2 Electromagnetic Waves in a Free Space

Prior to considering receptions and transmissions of radio waves (or, more generally speaking, electromagnetic waves) by antennas , we will briefly discuss general behaviors of the electromagnetic waves in a free space, based on the classical theory of electromagnetic fields.

2.2.1 Maxwell Equations

Let us consider following vector and scalar field quantities:

symbol	*name*	*unit in* SI *system*
$\boldsymbol{E}$	electric field intensity	V m^{-1}
$\boldsymbol{D}$	electric flux density	A s m^{-2}
$\boldsymbol{H}$	magnetic field intensity	A m^{-1}
$\boldsymbol{B}$	magnetic flux density	V s m^{-2}
$\boldsymbol{J}$	current density	A m^{-2}
ρ	charge density	A s m^{-3}
σ	specific conductivity	A V^{-1} m^{-1}
ϵ	permittivity	A s V^{-1} m^{-1}
μ	permeability	V s A^{-1} m^{-1}

Note that V A = W (watt) = J s^{-1}, V A^{-1} = Ω (ohm), and V s m^{-2} = T (tesla).

These quantities obey the basic equations of the electromagnetics, the Maxwell equations:

$$\nabla \times \boldsymbol{E} = -\frac{\partial \boldsymbol{B}}{\partial t}, \tag{21}$$

$$\nabla \times \boldsymbol{H} = \boldsymbol{J} + \frac{\partial \boldsymbol{D}}{\partial t}, \tag{22}$$

$$\nabla \cdot \boldsymbol{D} = \rho, \tag{23}$$

$$\nabla \cdot \boldsymbol{B} = 0, \tag{24}$$

$$\boldsymbol{J} = \sigma \boldsymbol{E}, \tag{25}$$

$$\boldsymbol{D} = \epsilon \boldsymbol{E}, \tag{26}$$

$$\boldsymbol{B} = \mu \boldsymbol{H}. \tag{27}$$

In the vacuum, coefficients in the last three equations, which are sometimes called as ‘equations of state’, take following values:

$$
\begin{aligned}
&\sigma_0 = 0, \\
&\epsilon_0 = 8.854 \times 10^{-12}\ \ \mathrm{A\ s\ V^{-1}\ m^{-1}}, \\
&\mu_0 = 1.257 \times 10^{-6}\ \ \mathrm{V\ s\ A^{-1}\ m^{-1}}, \\
&\text{which satisfy} \\
&\epsilon_0 \mu_0 = c_0^{-2},
\end{aligned}
\tag{28}
$$

where suffix 0 implies a vacuum value, and $c_0 = 2.998 \times 10^8$ m s^{-1} is the light velocity in the vacuum.

2.2.2 Equation of Continuity

From Maxwell equations (22) and (23), and a formula of vector algebra given in equation (19), we obtain

$$\frac{\partial \boldsymbol{\rho}}{\partial t} + \nabla \cdot \boldsymbol{J} = 0. \tag{29}$$

This equation implies that time variation of the electric charge, contained within a finite region, is eqaul to the electric current flowing into (or flowing out of) the region within a unit time. Therefore, this equation is called ‘equation of continuity of electric charge’ or ’equation of conservation of electric charge’.

2.2.3 Conservation of Energy and Poynting Vector

If we take scalar products of equations (21) and (22) with $-\boldsymbol{H}$ and $\boldsymbol{E}$, respectively, and sum them up, we obtain

$$
\begin{aligned}
\boldsymbol{E} \cdot \frac{\partial \boldsymbol{D}}{\partial t} + \boldsymbol{H} \cdot \frac{\partial \boldsymbol{B}}{\partial t} &= -\boldsymbol{E} \cdot \boldsymbol{J} + \boldsymbol{E} \cdot (\nabla \times \boldsymbol{H}) - \boldsymbol{H} \cdot (\nabla \times \boldsymbol{E}) \\
&= -\boldsymbol{E} \cdot \boldsymbol{J} - \nabla \cdot (\boldsymbol{E} \times \boldsymbol{H}),
\end{aligned}
\tag{30}
$$

where we used a formula of vector algebra given in equation (17).

Considering equations (25), (26), and (27), and assuming that permittivity ϵ and permeability μ are constant in time, we can express equation (30) in a form:

$$\frac{1}{2}\frac{\partial(\boldsymbol{E} \cdot \boldsymbol{D} + \boldsymbol{H} \cdot \boldsymbol{B})}{\partial t} + \nabla \cdot (\boldsymbol{E} \times \boldsymbol{H}) = -\sigma E^2. \tag{31}$$

Then, taking into account that

1. $u \equiv \frac{1}{2}(\boldsymbol{E} \cdot \boldsymbol{D} + \boldsymbol{H} \cdot \boldsymbol{B})$ is the energy density of the electromagnetic field [J m^{-3}],
2. $\boldsymbol{S} \equiv \boldsymbol{E} \times \boldsymbol{H}$ is the energy flux of the electromagnetic field, called 'Poynting vector' [W m^{-2}],
3. $-\sigma E^2$ is the Joule heat generated per unit time and unit volume due to the Ohmic dissipation [W m^{-3}],

we can interpret equation (31) as an equation of conservation of eletromagnetic energy (Figure 22):

$$\frac{\partial u}{\partial t} + \nabla \cdot \boldsymbol{S} = -\sigma E^2. \tag{32}$$

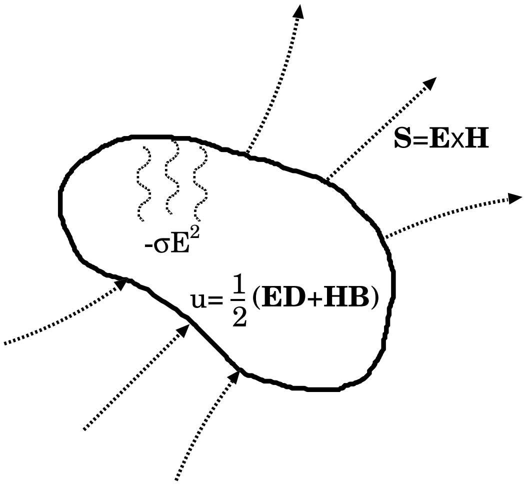

Figure 22: Energy conservation of electromagnetic energy.

Among the quantities characterizing radiation from an astronomical source, which were introduced in the previous chapter "Basic Knowledge of Radio Astronomy', the 'power flux density' (or 'energy/radiation flux density') $\mathcal{S}$:

$$\mathcal{S} = \int_{-\infty}^{\infty} \mathcal{S}_\nu \, d\nu, \tag{33}$$

where $\mathcal{S}_\nu$ is the spectral flux density, has the same unit [W m^{-2}] as the Poynting vector $\boldsymbol{S}$. According to a standard definition adopted by the IEEE

(Institute of Electrical and Electronics Engineers, Inc.) in 1977, the power flux density is equal to the time average of the Poynting vector of the electromagnetic wave. This is an important definition which interrelates the radio astronomy with the electromagnetics, as we will see later.

2.2.4 Wave Equations in a Stationary Homogeneous Neutral Medium

Let us consider a medium, where the specific conductivity σ, permittivity ϵ and permeability μ are real and constant both in time and space, and the charge density is zero ($\rho = 0$, i.e., the medium is electrically neutral).

In this case, the first four of the Maxwell equations (21) – (24) take simpler forms:

$$\begin{aligned} \nabla \times \boldsymbol{E} &= -\mu \frac{\partial \boldsymbol{H}}{\partial t}, \\ \nabla \times \boldsymbol{H} &= \sigma \boldsymbol{E} + \epsilon \frac{\partial \boldsymbol{E}}{\partial t}, \\ \nabla \cdot \boldsymbol{E} &= 0, \\ \nabla \cdot \boldsymbol{H} &= 0. \end{aligned}$$

Taking time derivatives of the first two equations, and using relations:

$$\begin{aligned} \nabla \times (\nabla \times \boldsymbol{E}) &= \nabla(\nabla \cdot \boldsymbol{E}) - \nabla^2 \boldsymbol{E} = -\nabla^2 \boldsymbol{E}, \\ \nabla \times (\nabla \times \boldsymbol{H}) &= \nabla(\nabla \cdot \boldsymbol{H}) - \nabla^2 \boldsymbol{H} = -\nabla^2 \boldsymbol{H}, \end{aligned}$$

which are derived from a formula of vector algebra in equation (16), and taking into account the last two of the above equations, we obtain

$$\begin{aligned} \epsilon\mu \frac{\partial^2 \boldsymbol{E}}{\partial t^2} + \sigma\mu \frac{\partial \boldsymbol{E}}{\partial t} - \nabla^2 \boldsymbol{E} &= 0, \\ \epsilon\mu \frac{\partial^2 \boldsymbol{H}}{\partial t^2} + \sigma\mu \frac{\partial \boldsymbol{H}}{\partial t} - \nabla^2 \boldsymbol{H} &= 0, \end{aligned}$$

which are equations of the electromagnetic wave in a dissipative medium. If we further assume a dissipationless medium, where $\sigma = 0$, and, therefore, $\boldsymbol{J} = 0$ (no current), the wave equations are described in a familiar form:

$$\begin{aligned} \frac{\partial^2 \boldsymbol{E}}{\partial t^2} - c^2 \nabla^2 \boldsymbol{E} &= 0, \\ \frac{\partial^2 \boldsymbol{H}}{\partial t^2} - c^2 \nabla^2 \boldsymbol{H} &= 0, \end{aligned} \tag{34}$$

where

$$c \equiv \frac{1}{\sqrt{\epsilon\mu}}, \tag{35}$$

is the velocity of the electromagnetic wave (or light), which is equal to $c_0 = 2.998 \times 10^8$ m s^{-1} in the vacuum.

2.2.5 Monochromatic Plane Waves

The simplest way to describe a solution of the wave equations (34) in the stationary, homogeneous, neutral ($\rho = 0$), and dissipationless ($\sigma = 0$) medium is to represent it as a superposition of monochromatic plane waves:

$$\begin{aligned} \boldsymbol{E} &= \boldsymbol{E}_{0r} \cos(\boldsymbol{k} \cdot \boldsymbol{r} - \omega t) - \boldsymbol{E}_{0i} \sin(\boldsymbol{k} \cdot \boldsymbol{r} - \omega t), \\ \boldsymbol{H} &= \boldsymbol{H}_{0r} \cos(\boldsymbol{k} \cdot \boldsymbol{r} - \omega t) - \boldsymbol{H}_{0i} \sin(\boldsymbol{k} \cdot \boldsymbol{r} - \omega t), \end{aligned} \tag{36}$$

where $\omega \equiv 2\pi\nu$ is an angular frequency of a particular monochromatic plane wave component (for simplicity, we will call the component as a 'plane wave'), $\boldsymbol{r}$ is a radius vector with components x_1, x_2, and x_3 at a certain point in the medium, $\boldsymbol{k}$ is a wave number vector of the plane wave, which satisfies

$$\omega^2 = c^2 k^2, \quad \text{with} \ \ k =\mid \boldsymbol{k} \mid, \tag{37}$$

while $\boldsymbol{E}_{0r}$, $\boldsymbol{E}_{0i}$, $\boldsymbol{H}_{0r}$, and $\boldsymbol{H}_{0i}$ are constant vector coefficients. For further convenience, we introduce complex vector coefficients:

$$\boldsymbol{E}_0 = \boldsymbol{E}_{0r} + i\boldsymbol{E}_{0i}, \quad \text{and} \ \ \boldsymbol{H}_0 = \boldsymbol{H}_{0r} + i\boldsymbol{H}_{0i}, \tag{38}$$

where i is the imaginary unit. Then, we can express equation (36) for a plane wave in an equivalent form:

$$\begin{aligned} \boldsymbol{E} &= \Re\,[\boldsymbol{E}_0 e^{i(\boldsymbol{k}\cdot\boldsymbol{r}-\omega t)}], \\ \boldsymbol{H} &= \Re\,[\boldsymbol{H}_0 e^{i(\boldsymbol{k}\cdot\boldsymbol{r}-\omega t)}], \end{aligned} \tag{39}$$

where $\Re$ implies a real part, using the well known Euler formulae:

$$e^{i\theta} = \cos\theta + i\sin\theta, \quad \text{and} \quad e^{-i\theta} = \cos\theta - i\sin\theta, \quad \text{for any } \theta.$$

Furthermore, we will omit this real part symbol $\Re$ in most of following discussions, since, as long as we perform linear operations, including differentiation and integration, to quantities described in the form as equation (39), there is no difference, if we take the real part before or after the linear operations. Therefore, we can perform all the calculations for complex quantities, and, only after we obtain final solutions, recall that actual physical quantities correspond to real parts of the complex ones. This will greatly simplify our mathematical manipulations. Thus, we will use a complex version of equation (39):

$$\begin{aligned} \boldsymbol{E} &= \boldsymbol{E}_0 e^{i(\boldsymbol{k}\cdot\boldsymbol{r}-\omega t)}, \\ \boldsymbol{H} &= \boldsymbol{H}_0 e^{i(\boldsymbol{k}\cdot\boldsymbol{r}-\omega t)}, \end{aligned} \tag{40}$$

where $\boldsymbol{E}$ and $\boldsymbol{H}$ are now regarded as complex quantities, remembering that actual electric and magnetic field intensities are $\Re\,\boldsymbol{E}$ and $\Re\,\boldsymbol{H}$, respectively, which we hereafter denote as

$$\boldsymbol{E}_r = \Re\boldsymbol{E}, \quad \text{and} \quad \boldsymbol{H}_r = \Re\boldsymbol{H}. \tag{41}$$

The reason, why the wave in equation (40) is called "plane wave", is evident from Figure 23. In fact, a surface of the constant phase ($\boldsymbol{k}\cdot\boldsymbol{r} - \omega t$ = const), or a "wave front" forms a flat plane, which is perpendicular to the wave number vector $\boldsymbol{k}$, and moves along $\boldsymbol{k}$ with the speed $\omega/k = c$ as time t increases.

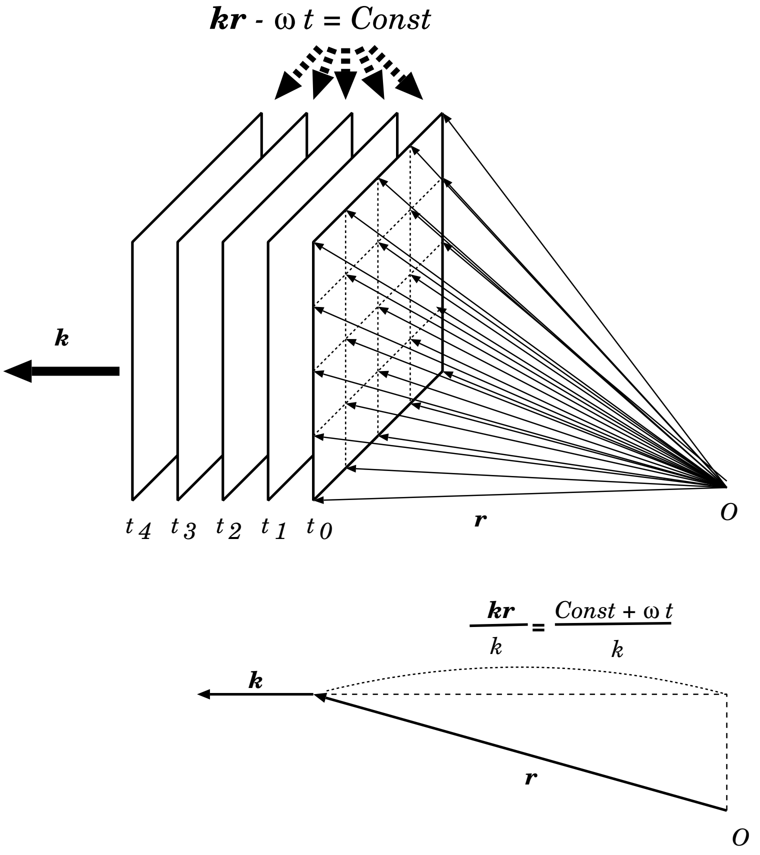

Figure 23: Wave front of a plane wave forms a flat plane moving towards $\boldsymbol{k}$ with the speed $\omega/k = c$.

Now we can easily verify that the plane waves as described in equation (40) really satisfy wave equations (34). In fact, if we take the electric field

$\boldsymbol{E}$ in equation (40), for example, we have

$$\frac{\partial^2 \boldsymbol{E}}{\partial t^2} = \boldsymbol{E}_0 \frac{\partial^2}{\partial t^2} e^{i(\boldsymbol{k}\cdot\boldsymbol{r}-\omega t)} = -\omega^2 \boldsymbol{E}_0 e^{i(\boldsymbol{k}\cdot\boldsymbol{r}-\omega t)} = -\omega^2 \boldsymbol{E}, \tag{42}$$

and also

$$\nabla^2 \boldsymbol{E} = \frac{\partial}{\partial x_i}\frac{\partial}{\partial x_i}\boldsymbol{E} = \boldsymbol{E}_0 \frac{\partial}{\partial x_i}\frac{\partial}{\partial x_i} e^{i(\boldsymbol{k}\cdot\boldsymbol{r}-\omega t)},$$

where

$$\begin{aligned} \frac{\partial}{\partial x_i} e^{i(\boldsymbol{k}\cdot\boldsymbol{r}-\omega t)} &= i\frac{\partial}{\partial x_i}(\boldsymbol{k}\cdot\boldsymbol{r}) e^{i(\boldsymbol{k}\cdot\boldsymbol{r}-\omega t)} = i\frac{\partial}{\partial x_i}(k_j x_j) e^{i(\boldsymbol{k}\cdot\boldsymbol{r}-\omega t)} \\ &= i k_j \frac{\partial x_j}{\partial x_i} e^{i(\boldsymbol{k}\cdot\boldsymbol{r}-\omega t)} = i k_j \delta_{ij} e^{i(\boldsymbol{k}\cdot\boldsymbol{r}-\omega t)} = i k_i e^{i(\boldsymbol{k}\cdot\boldsymbol{r}-\omega t)}, \end{aligned}$$

and, therefore,

$$\frac{\partial}{\partial x_i}\frac{\partial}{\partial x_i} e^{i(\boldsymbol{k}\cdot\boldsymbol{r}-\omega t)} = -k^2 e^{i(\boldsymbol{k}\cdot\boldsymbol{r}-\omega t)},$$

which yields

$$\nabla^2 \boldsymbol{E} = -k^2 \boldsymbol{E}_0 e^{i(\boldsymbol{k}\cdot\boldsymbol{r}-\omega t)} = -k^2 \boldsymbol{E}. \tag{43}$$

From equations (42) and (43), it is clear that the plane wave $\boldsymbol{E}$ satisfies the wave equation:

$$\frac{\partial^2 \boldsymbol{E}}{\partial t^2} - c^2 \nabla^2 \boldsymbol{E} = 0,$$

in view of the relation $\omega^2 = c^2 k^2$, given in equation (37), between the angular frequency ω and the wave number k. The same discussion holds for the magnetic field $\boldsymbol{H}$, too.

2.2.6 Electric and Magnetic Fields in a Plane Wave

Although any plane wave, with arbitrary constant $\boldsymbol{E}_0$ or $\boldsymbol{H}_0$ in equation (40), satisfies the wave equation (34), as we have just seen above, actual electric and magnetic fields in an electromagnetic wave must be mutually related to each other, and must exhibit certain characteristic properties.

These additional properties, which will be shown below, come from the fact that the electric $\boldsymbol{E}$ and magnetic $\boldsymbol{H}$ fields must satisfy, not only the wave equations (40), where they are completely separated, but also the original Maxwell equations, where they are related to each other.

1. **The waves are transversal.**
   In our homogeneous and neutral medium case, Maxwell equations (23) and (24) are reduced to

$$\begin{aligned} \nabla \cdot \boldsymbol{E} &= 0, \\ \nabla \cdot \boldsymbol{H} &= 0. \end{aligned}$$

Inserting the plane wave form of the electric field $\boldsymbol{E}$, given in equation (40), into the upper one of the above equations, we have

$$\nabla \cdot \boldsymbol{E} = E_{0i} \frac{\partial}{\partial x_i} e^{i(\boldsymbol{k} \cdot \boldsymbol{r} - \omega t)} = i k_i E_{0i} e^{i(\boldsymbol{k} \cdot \boldsymbol{r} - \omega t)} = i \boldsymbol{k} \cdot \boldsymbol{E}_0 e^{i(\boldsymbol{k} \cdot \boldsymbol{r} - \omega t)} = 0.$$

Since this relation holds for arbitrary $e^{i(\boldsymbol{k} \cdot \boldsymbol{r} - \omega t)}$, we have $\boldsymbol{k} \cdot \boldsymbol{E}_0 = 0$ and, therefore, $\boldsymbol{k} \cdot \boldsymbol{E} = 0$. The same argument holds for the magnetic field as well in the lower equation. Thus, we obtain

$$\begin{aligned} \boldsymbol{k} \cdot \boldsymbol{E} &= 0, \\ \boldsymbol{k} \cdot \boldsymbol{H} &= 0. \end{aligned} \tag{44}$$

Taking real parts of these complex equations, we easily see that the actual physical fields $\boldsymbol{E}_r$ and $\boldsymbol{H}_{\boldsymbol{r}}$, which are the real parts $\boldsymbol{E}_r = \Re \boldsymbol{E}$ and $\boldsymbol{H}_r = \Re \boldsymbol{H}$ as defined in equation (41), also satisfy

$$\begin{aligned} \boldsymbol{k} \cdot \boldsymbol{E}_r &= 0, \\ \boldsymbol{k} \cdot \boldsymbol{H}_r &= 0, \end{aligned} \tag{45}$$

which show that the vector fields are perpendicular to the direction $\boldsymbol{n}$ of the wave propagation:

$$\boldsymbol{n} \equiv \frac{\boldsymbol{k}}{k}. \tag{46}$$

This means that the plane electromagnetic waves are transversal.

2. **Orthogonality of electric and magnetic fields.**
   In our stationary, homogeneous, dissipationless ($\sigma = 0$, $\boldsymbol{J} = 0$), and neutral ($\rho = 0$) medium, Maxwell equations (21) and (22) are reduced to

   $$\begin{aligned} \nabla \times \boldsymbol{E} &= -\mu \frac{\partial \boldsymbol{H}}{\partial t}, \\ \nabla \times \boldsymbol{H} &= \epsilon \frac{\partial \boldsymbol{E}}{\partial t}. \end{aligned}$$

   Let us insert the plane wave forms of the electric ($\boldsymbol{E}$) and magnetic ($\boldsymbol{H}$) field intensities, given in equation (40), into the upper one of the above equations.

   Since

   $$(\nabla \times \boldsymbol{E})_i = \epsilon_{ijk} E_{0k} \frac{\partial}{\partial x_j} e^{i(\boldsymbol{k} \cdot \boldsymbol{r} - \omega t)} = i \, \epsilon_{ijk} k_j E_{0k} e^{i(\boldsymbol{k} \cdot \boldsymbol{r} - \omega t)},$$

   we obtain

   $$\nabla \times \boldsymbol{E} = i \, \boldsymbol{k} \times \boldsymbol{E}.$$

Also,

$$\frac{\partial \boldsymbol{H}}{\partial t} = \boldsymbol{H}_0 \frac{\partial}{\partial t} e^{i(\boldsymbol{k}\cdot\boldsymbol{r}-\omega t)} = -i\,\omega \boldsymbol{H}_0 e^{i(\boldsymbol{k}\cdot\boldsymbol{r}-\omega t)} = -i\,\omega \boldsymbol{H}.$$

Similar relations:

$$\nabla \times \boldsymbol{H} = i\,\boldsymbol{k} \times \boldsymbol{H}, \quad \text{and} \quad \frac{\partial \boldsymbol{E}}{\partial t} = -i\,\omega \boldsymbol{E},$$

hold for the lower equation. Therefore, we have

$$\begin{aligned} \boldsymbol{k} \times \boldsymbol{E} &= \mu\,\omega \boldsymbol{H}, \\ \boldsymbol{k} \times \boldsymbol{H} &= -\epsilon\,\omega \boldsymbol{E}. \end{aligned} \tag{47}$$

Taking real parts of these complex equations, we obtain the same relations:

$$\begin{aligned} \boldsymbol{k} \times \boldsymbol{E}_r &= \mu\,\omega \boldsymbol{H}_r, \\ \boldsymbol{k} \times \boldsymbol{H}_r &= -\epsilon\,\omega \boldsymbol{E}_r, \end{aligned} \tag{48}$$

for the actual physical field quantities $\boldsymbol{E}_r$ and $\boldsymbol{H}_r$ (equation (41)), as well.

Therefore, we have

$$\boldsymbol{E}_r \cdot \boldsymbol{H}_r = 0, \tag{49}$$

which means that the electric and magnetic fields are perpendicular (orthogonal) to each other (Figure 24).

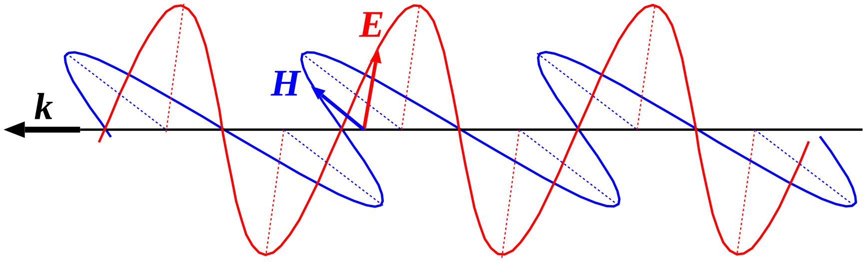

Figure 24: Electric and magnetic fields in a monochromatic plane wave are perpendicular to a direction of propagation, and to each other.

3. **Amplitudes of electric and magnetic fields. Intrinsic impedance.** From equations (45) and (48), and also from a formula of vector algebra given in equation (15), we have

$$\mid \boldsymbol{E}_r \mid^2 = \boldsymbol{E}_r \cdot \boldsymbol{E}_r = \frac{1}{\omega^2\epsilon^2}(\boldsymbol{k} \times \boldsymbol{H}_r)\cdot(\boldsymbol{k} \times \boldsymbol{H}_r) = \frac{1}{\omega^2\epsilon^2} k^2 \mid \boldsymbol{H}_r \mid^2,$$

and

$$\mid \boldsymbol{H}_r \mid^2 = \frac{1}{\omega^2 \mu^2} k^2 \mid \boldsymbol{E}_r \mid^2 .$$

Since we have

$$\frac{k^2}{\omega^2} = \frac{1}{c^2} = \epsilon\, \mu,$$

from equaions (37) and (35), the above two equations are equivalent, and express the same relation, describing the amplitude ratio of the electric and magnetic fields in a monochromatic plane wave:

$$\mid \boldsymbol{E}_r \mid = \sqrt{\frac{\mu}{\epsilon}} \mid \boldsymbol{H}_r \mid, \quad \text{or} \quad \mid \boldsymbol{H}_r \mid = \sqrt{\frac{\epsilon}{\mu}} \mid \boldsymbol{E}_r \mid . \tag{50}$$

The coefficient:

$$Z \equiv \sqrt{\frac{\mu}{\epsilon}}, \tag{51}$$

which is equal to

$$Z = \frac{\mid \boldsymbol{E}_r \mid}{\mid \boldsymbol{H}_r \mid},$$

is called 'intrinsic impedance' of the medium, and is measured by a unit: [V A^{-1} = Ω (Ohm)], which is the same with the unit of the resistance in an electrical circuit. The value of the intrinsic impedance in the vacuum is equal to

$$Z_0 = \sqrt{\frac{\mu_0}{\epsilon_0}} = 376.3 \ \ \Omega.$$

4. **Poynting vector.**
From equations (45) and (48), and also from equation (14) of vector algebra, the Poynting vetor $\boldsymbol{S}$ of the monochromatic plane wave is expressed as

$$\begin{aligned}\boldsymbol{S} &= \boldsymbol{E}_r \times \boldsymbol{H}_r = \frac{1}{\omega\, \mu} \boldsymbol{E}_r \times (\boldsymbol{k} \times \boldsymbol{E}_r) = \frac{k}{\omega\, \mu} \boldsymbol{n} \mid \boldsymbol{E}_r \mid^2 \\ &= \sqrt{\frac{\epsilon}{\mu}} \boldsymbol{n} \mid \boldsymbol{E}_r \mid^2 = \frac{1}{Z} \boldsymbol{n} \mid \boldsymbol{E}_r \mid^2,\end{aligned}$$

where

$$\boldsymbol{n} = \frac{\boldsymbol{k}}{k},$$

is the direction of the wave propagation as defined in equation (46), and, therefore,

$$\boldsymbol{S} = \frac{1}{Z} \boldsymbol{n} \mid \boldsymbol{E}_r \mid^2 = Z\, \boldsymbol{n} \mid \boldsymbol{H}_r \mid^2 . \tag{52}$$

2.3 Generation of Electromagnetic Waves

Now, let us consider generation of electromagnetic waves from a matter (from an antenna, in particular), where we must take into account existence of the electric current and the charge.

If we try to describe this new problem, still using the electric and magnetic field intensities $\boldsymbol{E}$ and $\boldsymbol{H}$ as basic quantities, as we did in the previous section for the free space case, equations involved get fairly complicated. A much more transparent treatment is achieved, when we use so–called electromagnetic potentials as basic quantities.

2.3.1 Electromagnetic Potentials

As we saw in equations (19) and (18), for any vector field $\boldsymbol{F}(\boldsymbol{r})$ and any scalar field $f(\boldsymbol{r})$, we have identity relations:

$$\nabla \cdot (\nabla \times \boldsymbol{F}) = 0,$$
$$\nabla \times (\nabla f) = 0.$$

It is known that following inverse relations generally hold (see, for example, "Classical Electricity and Magnetism, Second Edition" by Panofsky and Phillips, 1962):

> If a relation $\nabla \cdot \boldsymbol{Q}(\boldsymbol{r}) = 0$ holds everywhere for a vector field $\boldsymbol{Q}(\boldsymbol{r})$, then such a vector field can be always expressed as a rotation of a certain vector field $\boldsymbol{F}(\boldsymbol{r})$, i.e., $\boldsymbol{Q} = \nabla \times \boldsymbol{F}$.
>
> If another relation $\nabla \times \boldsymbol{R}(\boldsymbol{r}) = 0$ holds everywhere for a vector field $\boldsymbol{R}(\boldsymbol{r})$, then such a vector field can be always expressed as a gradient of a certain scalar field $f(\boldsymbol{r})$, i.e., $\boldsymbol{R} = \nabla f$.

From Maxwell equations (24) and (21), we know that relations:

$$\nabla \cdot \boldsymbol{B} = 0,$$
$$\nabla \times \boldsymbol{E} = -\frac{\partial \boldsymbol{B}}{\partial t},$$

hold everywhere.

Therefore, in view of the upper one of the above two equations, we can express the magnetic flux density $\boldsymbol{B}$ as

$$\boldsymbol{B} = \nabla \times \boldsymbol{A}, \tag{53}$$

through an appropriate vector field $\boldsymbol{A}(\boldsymbol{r}, t)$, which we call hereafter 'vector potential'.

Then, the lower one of the above two equations now becomes

$$\nabla \times (\boldsymbol{E} + \frac{\partial \boldsymbol{A}}{\partial t}) = 0.$$

Therefore, we can express the vector $\boldsymbol{E} + \partial \boldsymbol{A}/\partial t$ through an appropriate scalar field $\Phi(\boldsymbol{r}, t)$, which we call 'scalar potential', as

$$\boldsymbol{E} + \frac{\partial \boldsymbol{A}}{\partial t} = -\nabla \Phi,$$

and, hence, the electric field intensity $\boldsymbol{E}$ is expressed as

$$\boldsymbol{E} = -\nabla \Phi - \frac{\partial \boldsymbol{A}}{\partial t}. \tag{54}$$

The vector potential $\boldsymbol{A}(\boldsymbol{r}, t)$ and scalar potential $\Phi(\boldsymbol{r}, t)$, brought together, are called 'electromagnetic potentials'. They are regarded as auxiliary quantities, which are not directly measurable, but help to effectively express actual, physically measurable, quantities such as $\boldsymbol{E}$ and $\boldsymbol{B}$. Units of the electromagnetic potentials are

$$\begin{aligned} \boldsymbol{A}(\boldsymbol{r}, t) : &\quad \mathrm{V\ s\ m^{-1}}, \\ \Phi(\boldsymbol{r}, t) : &\quad \mathrm{V}, \end{aligned}$$

respectively.

2.3.2 Lorentz Gauge

Electromagnetic potentials $\boldsymbol{A}(\boldsymbol{r}, t)$ and $\Phi(\boldsymbol{r}, t)$, which satisfy equations (53) and (54), are not unique. In fact, it is easy to confirm that for an arbitrary scalar field $\Lambda(\boldsymbol{r}, t)$, a new set of potentials

$$\begin{aligned} \boldsymbol{A}' &= \boldsymbol{A} + \nabla \Lambda, \\ \Phi' &= \Phi - \frac{\partial \Lambda}{\partial t}, \end{aligned} \tag{55}$$

also satisfy equations (53) and (54), if $\boldsymbol{A}$ and Φ do.

It is a usual practice, in the wave generation problem, to introduce a constraint between $\boldsymbol{A}$ and Φ called 'Lorentz gauge':

$$\nabla \cdot \boldsymbol{A} + \epsilon\, \mu \frac{\partial \Phi}{\partial t} = 0, \tag{56}$$

using the above ambiguity, or, better to say, the freedom. The Lorentz gauge, as given in equation (56), allows us to formulate the generation of electromagnetic waves in a very smart way, as we will see below.

It is remarkable that any electromagnetic potentials $\boldsymbol{A}_n$ and Φ_n, which originally do not satisfy the Lorentz gauge:

$$\nabla \cdot \boldsymbol{A_n} + \epsilon \, \mu \, \frac{\partial \Phi_n}{\partial t} \neq 0,$$

can be converted to new ones $\boldsymbol{A}_y$ and Φ_y fulfilling the Lorentz gauge equation (56), by using a scalar field Λ in equation (55):

$$\boldsymbol{A}_y = \boldsymbol{A}_n + \nabla \Lambda, \ \text{ and } \ \Phi_y = \Phi_n - \frac{\partial \Lambda}{\partial t},$$

which satisfies an equation:

$$\epsilon \, \mu \, \frac{\partial^2 \Lambda}{\partial t^2} - \nabla^2 \Lambda = \nabla \cdot \boldsymbol{A_n} + \epsilon \, \mu \, \frac{\partial \Phi_n}{\partial t}.$$

Of course, the physically measurable fields, such as $\boldsymbol{E}$ and $\boldsymbol{B}$, are not affected by this conversion.

Therefore, we can always select electromagnetic potentials $\boldsymbol{A}$ and Φ, which correspond to real electromagnetic fields through equations (53) and (54), and, at the same time, satisfy the Lorentz gauge (equation (56)):

$$\begin{aligned} \boldsymbol{B} &= \nabla \times \boldsymbol{A}, \\ \boldsymbol{E} &= -\nabla \Phi - \frac{\partial \boldsymbol{A}}{\partial t}, \\ \nabla \cdot \boldsymbol{A} + \epsilon \, \mu \, \frac{\partial \Phi}{\partial t} &= 0. \end{aligned}$$

Hereafter, we will consider only such electromagnetic potentials.

2.3.3 Wave Equations with Source Terms

We will assume, for simplicity, a homogeneous and stationary medium with respect to the permittivity ϵ and the permeability μ, i.e., $\epsilon = \text{const}$ and $\mu = \text{const}$ both in time and space.

Inserting equations (53) and (54) into a Maxwell equation (22):

$$\nabla \times \boldsymbol{H} = \boldsymbol{J} + \epsilon \, \frac{\partial \boldsymbol{E}}{\partial t},$$

we have

$$\frac{1}{\mu} \nabla \times (\nabla \times \boldsymbol{A}) = \boldsymbol{J} - \epsilon \, (\frac{\partial^2 \boldsymbol{A}}{\partial t^2} + \nabla \frac{\partial \Phi}{\partial t}).$$

In view of equation (16), this equation is reduced to

$$\nabla(\nabla\cdot\boldsymbol{A})-\nabla^2\boldsymbol{A}=\mu\,\boldsymbol{J}-\epsilon\,\mu\,\frac{\partial^2\boldsymbol{A}}{\partial t^2}-\epsilon\,\mu\,\nabla\frac{\partial\Phi}{\partial t},$$

and, then,

$$\nabla^2\boldsymbol{A}-\epsilon\,\mu\,\frac{\partial^2\boldsymbol{A}}{\partial t^2}=-\mu\,\boldsymbol{J}+\nabla(\nabla\cdot\boldsymbol{A}+\epsilon\,\mu\,\frac{\partial\Phi}{\partial t})=-\mu\,\boldsymbol{J},$$

where we used equation (56) of the Lorentz gauge.

Also, another Maxwell equation (23):

$$\epsilon\,\nabla\cdot\boldsymbol{E}=\rho,$$

can be expressed as

$$-\epsilon\,\nabla\cdot(\nabla\Phi+\frac{\partial\boldsymbol{A}}{\partial t})=\rho,$$

through the electromagnetic potentials, and is reduced to

$$\nabla^2\Phi+\frac{\partial}{\partial t}(\nabla\cdot\boldsymbol{A})=-\frac{1}{\epsilon}\,\rho,$$

and, then

$$\nabla^2\Phi-\epsilon\,\mu\,\frac{\partial^2\Phi}{\partial t^2}=-\frac{1}{\epsilon}\,\rho,$$

where we again used equation (56) of the Lorentz gauge.

Introducing again the light velocity c ($c^2=1\,/\,\epsilon\,\mu$), we obtain equations

$$\nabla^2\boldsymbol{A}-\frac{1}{c^2}\,\frac{\partial^2\boldsymbol{A}}{\partial t^2}=-\mu\,\boldsymbol{J}, \tag{57}$$

$$\nabla^2\Phi-\frac{1}{c^2}\,\frac{\partial^2\Phi}{\partial t^2}=-\frac{1}{\epsilon}\,\rho, \tag{58}$$

which have the simple form of the wave equation. The only difference from the free space case in equation (34) is the existence of RHS terms, which are source terms of the wave equations. These equations describe the interaction of the electric current $\boldsymbol{J}$ and charge ρ within a source region with the electromagnetic waves $\boldsymbol{A}$ and Φ, i.e., the current and charge may generate the waves in a free space (transmission), or the waves in the free space may generate the current and charge in the source region (reception), as schematically shown in Figure 25.

Equations (57) and (58) are consistent with equation (56) of the Lorentz gauge, as we can easily verify using equation (29) of continuity (or conservation) of electric charge.

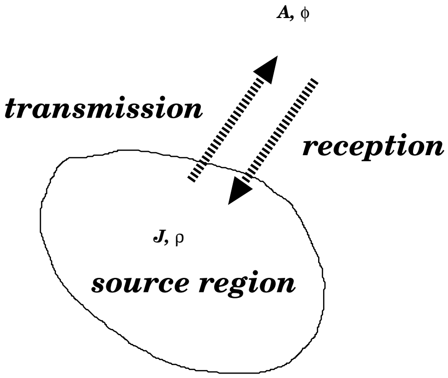

Figure 25: A schematic view of the interaction of the current and charge in a source region with the electromagnetic waves in a free space.

2.3.4 Solution of the Wave Equation with the Source Term

Let us consider solutions of equations (57) and (58). Since each component of vector equation (57) and scalar equation (58) have the same general form of

$$\nabla^2\Psi(\boldsymbol{r},t) - \frac{1}{c^2}\frac{\partial^2\Psi(\boldsymbol{r},t)}{\partial t^2} = -f(\boldsymbol{r},t), \tag{59}$$

where f and Ψ are functions of the time t and the space $\boldsymbol{r}$, we will confine ourselves to seeking a solution $\Psi(\boldsymbol{r},t)$ of equation (59) with a source term $-f(\boldsymbol{r},t)$. We assume that the source term takes some finite value only within a certain source region.

In order to express the RHS of equation (59) in an integral form, we use Dirac's delta function $\delta(\boldsymbol{r})$, which has following functional properties:

$$\begin{aligned} \delta(\boldsymbol{r}) &= 0, \text{ when } \boldsymbol{r} \neq 0, \\ \int\limits_V \delta(\boldsymbol{r}-\boldsymbol{r}')\,dV' &= 1, \\ \int\limits_V F(\boldsymbol{r}')\delta(\boldsymbol{r}-\boldsymbol{r}')\,dV' &= F(\boldsymbol{r}), \text{ for any function } F(\boldsymbol{r}), \end{aligned}$$

where $\boldsymbol{r}'$ is a variable radius vector with elements x_1', x_2', and x_3', $dV' = dx_1'dx_2'dx_3'$ is a volume element, and the integration is taken over some volume V containing a point $\boldsymbol{r}$. Now we can express the RHS of equation (59) as:

$$\nabla^2\Psi(\boldsymbol{r},t) - \frac{1}{c^2}\frac{\partial^2\Psi(\boldsymbol{r},t)}{\partial t^2} = -\int\limits_V f(\boldsymbol{r}',\,t)\delta(\boldsymbol{r}-\boldsymbol{r}')\,dV', \tag{60}$$

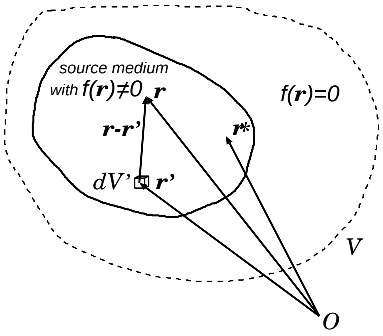

Figure 26: Geometry of the source medium region.

where the integration is taken over an appropriate volume V, containing the source region and a point $\boldsymbol{r}$ (see Figure 26).

Using this form, we will solve the equation in terms of the **Green function method**, which works in the following way.

- Consider the wave equation with a time-variable point source at the origin O with $\boldsymbol{r} = 0$:

$$\nabla^2\psi - \frac{1}{c^2}\frac{\partial^2\psi}{\partial t^2} = -f(\boldsymbol{r}_*,\, t)\delta(\boldsymbol{r}), \tag{61}$$

  where $\boldsymbol{r}^*$ denotes some particular point in the source region, and $-f(\boldsymbol{r}_*,\, t)$ is a function of time t.

- If $\psi(\boldsymbol{r}_*,\, \boldsymbol{r},\, t)$ is a solution of the above equation (which is the Green function), then, $\psi(\boldsymbol{r}_*, \boldsymbol{r} - \boldsymbol{r}',\, t)$ must be a solution of equation:

$$\nabla^2\psi - \frac{1}{c^2}\frac{\partial^2\psi}{\partial t^2} = -f(\boldsymbol{r}_*,\, t)\delta(\boldsymbol{r} - \boldsymbol{r}'),$$

  for any $\boldsymbol{r}'$.

- Therefore, $\psi(\boldsymbol{r}',\, \boldsymbol{r} - \boldsymbol{r}',\, t)$ must be a solution of equation:

$$\nabla^2\psi - \frac{1}{c^2}\frac{\partial^2\psi}{\partial t^2} = -f(\boldsymbol{r}',\, t)\delta(\boldsymbol{r} - \boldsymbol{r}'),$$

  in a special case when $\boldsymbol{r}_* = \boldsymbol{r}'$.

- Finally, in view of the principle of superposition of solutions in a linear equation, an integral of the function $\psi(\boldsymbol{r}',\, \boldsymbol{r} - \boldsymbol{r}',\, t)$ with respect to $\boldsymbol{r}'$:

$$\Psi(\boldsymbol{r}, t) = \int\limits_V \psi(\boldsymbol{r}',\, \boldsymbol{r} - \boldsymbol{r}',\, t)\, dV', \tag{62}$$

must be a solution of our wave equation (60):

$$\nabla^2\Psi(\boldsymbol{r},t) - \frac{1}{c^2}\frac{\partial^2\Psi(\boldsymbol{r},t)}{\partial t^2} = -\int\limits_V f(\boldsymbol{r}',\, t)\delta(\boldsymbol{r}-\boldsymbol{r}')\,dV'.$$

Thus, the solution $\psi(\boldsymbol{r}_*,\, \boldsymbol{r},\, t)$ of equation (61) is really a Green function, which enables us to obtain a solution of equation (60), or equivalently equation (59).

Now, we can express the solution $\psi(\boldsymbol{r}_*,\, \boldsymbol{r},\, t)$ (Green function) in a form:

$$\psi(\boldsymbol{r}_*, \boldsymbol{r}, t) = \frac{f(\boldsymbol{r}_*,\, t \mp \frac{r}{c})}{4\pi r}, \tag{63}$$

where r is the length of the radius vector $\boldsymbol{r}$, i.e. $r = \mid \boldsymbol{r} \mid = \sqrt{x_i x_i} = \sqrt{x_1^2 + x_2^2 + x_3^2}$. Let us veryfy this in the following way.

1. We use following general formulae.

   - For a radius vector $\boldsymbol{r}$,

$$\begin{aligned} \nabla r &= \frac{\boldsymbol{r}}{r}, \ \text{ and } \ \nabla\cdot\boldsymbol{r} = 3, \ \text{ since} \qquad (64)\\ (\nabla r)_i &= \frac{\partial r}{\partial x_i} = \frac{\partial}{\partial x_i}\sqrt{x_j x_j} = \frac{1}{2\sqrt{x_j x_j}}\frac{\partial}{\partial x_i}(x_k x_k) = \frac{x_i}{r},\\ \text{and} \quad \nabla\cdot\boldsymbol{r} &= \frac{\partial x_i}{\partial x_i} = \delta_{ii} = 3. \end{aligned}$$

   - For a function $R(r)$ of the radius r,

$$\begin{aligned} \nabla^2 R(r) &= \frac{d^2R(r)}{dr^2} + \frac{2}{r}\frac{dR(r)}{dr}, \ \text{ since} \qquad (65)\\ \nabla^2 R(r) &= \nabla\cdot\nabla R(r) = \nabla\cdot\left(\frac{dR}{dr}\nabla r\right) = \nabla\cdot\left(\frac{dR}{dr}\frac{\boldsymbol{r}}{r}\right)\\ &= \nabla\left(\frac{1}{r}\frac{dR}{dr}\right)\cdot\boldsymbol{r} + \left(\frac{1}{r}\frac{dR}{dr}\right)\nabla\cdot\boldsymbol{r}\\ &= r\frac{d}{dr}\left(\frac{1}{r}\frac{dR}{dr}\right) + 3\left(\frac{1}{r}\frac{dR}{dr}\right) = \frac{d^2R}{dr^2} + \frac{2}{r}\frac{dR}{dr}. \end{aligned}$$

   - For a particular function $1/r$, which is singular at the origin, we have

$$\nabla^2\left(\frac{1}{r}\right) = -4\pi\,\delta(\boldsymbol{r}), \tag{66}$$

as we know from the potential theory (electrostatic potential around a point charge, Newtonian gravitaional potential around a point mass, etc., ...). We can veryfy this equation by integrating both sides through an arbitrary volume V, covered by a surface $\mathcal{S}$ with a normal $\boldsymbol{n}$, and apply to the LHS Gauss's integration theorem:

$$\int_V \nabla \cdot \boldsymbol{A} \, dV = \oint_{\mathcal{S}} \boldsymbol{A} \cdot \boldsymbol{n} \, d\mathcal{S}, \tag{67}$$

where $\boldsymbol{A}$ is an arbitrary vector field, V is a closed volume, covered by a surface $\mathcal{S}$ with a normal vector $\boldsymbol{n}$.

In fact, the RHS gives

$$-4\pi \int_V \delta(\boldsymbol{r}) \, dV = \begin{cases} -4\pi & (\text{if } V \text{ contains the origin } \boldsymbol{r} = 0), \\ 0 & (\text{otherwise}), \end{cases}$$

and the LHS also yields

$$\int_V \nabla\cdot\nabla \left(\frac{1}{r}\right) \, dV = \oint_S \nabla \left(\frac{1}{r}\right) \cdot \boldsymbol{n} \, d\mathcal{S} = -\oint_S \frac{\boldsymbol{r}}{r^3} \cdot \boldsymbol{n} \, d\mathcal{S} = \begin{cases} -\oint d\Omega = -4\pi, \\ 0, \end{cases}$$

depending again if V contains the origin or not, where $d\Omega$ is a solid angle element.

2. Let us introduce a notation:

$$u \equiv t \mp \frac{r}{c}.$$

Then, the function ψ in equation (63) is now expressed as

$$\psi(\boldsymbol{r}_*, \, \boldsymbol{r}, \, t) = \frac{f(\boldsymbol{r}_*, \, u)}{4\pi r}.$$

Noting that

$$\frac{\partial f}{\partial t} = \frac{df}{du} \frac{\partial u}{\partial t}, \quad \frac{\partial f}{\partial r} = \frac{df}{du} \frac{\partial u}{\partial r}, \quad \text{with} \quad \frac{\partial u}{\partial t} = 1, \quad \text{and} \quad \frac{\partial u}{\partial r} = \mp \frac{1}{c},$$

we obtain

$$\frac{\partial^2 \psi}{\partial t^2} = \frac{1}{4\pi r} \frac{d^2 f}{du^2},$$

and, using equation (65),

$$\begin{aligned}\nabla^2\psi &= \frac{1}{4\pi r}\nabla^2 f + 2\nabla\left(\frac{1}{4\pi r}\right)\cdot\nabla f + f\,\nabla^2\left(\frac{1}{4\pi r}\right)\\ &= \frac{1}{4\pi r}\left(\frac{\partial^2 f}{\partial r^2} + \frac{2}{r}\frac{\partial f}{\partial r}\right) - \frac{2}{4\pi r^2}\frac{\partial f}{\partial r} - f\,\delta(\boldsymbol{r})\\ &= \frac{1}{4\pi r}\frac{1}{c^2}\frac{d^2 f}{du^2} - f\,\delta(\boldsymbol{r}).\end{aligned}$$

Therefore, the function $\psi(\boldsymbol{r}_*,\,\boldsymbol{r},\,t)$ in equation (63) really satisfies the wave equation (61) with a point source term at the origin:

$$\nabla^2\psi - \frac{1}{c^2}\frac{\partial^2\psi}{\partial t^2} = -f(\boldsymbol{r}_*, u)\,\delta(\boldsymbol{r}) = -f(\boldsymbol{r}_*,\,t\mp\frac{r}{c}\,)\,\delta(\boldsymbol{r}) = -f(\boldsymbol{r}_*,\,t)\,\delta(\boldsymbol{r}),$$

and, hence, can be used as a Green function for solving equation (59) in the form given in equation (62).

2.3.5 Retarded Potential

Now, from equations (62) and (63), a solution of the wave equation with the source term (59) is expressed as:

$$\Psi(\boldsymbol{r},t) = \frac{1}{4\pi}\int\limits_V \frac{f(\boldsymbol{r}',\,t\mp\frac{|\boldsymbol{r}-\boldsymbol{r}'|}{c})}{|\,\boldsymbol{r}-\boldsymbol{r}'\,|}\,dV'. \tag{68}$$

In actuality, there are two choices of solutions corresponding to '+' sign and '−' sign of the ∓ term in the numerator of the integrand. One solution with '−' sign is called 'retarded potential', and another with '+' sign is called 'advanced potential'.

Meanings of the retarded and advanced potentials can be better understood in the simplest case of the point source term at the origin ($\boldsymbol{r} = 0$), when the solution takes the same form as the one in equation (63):

$$\Psi(\boldsymbol{r},t) = \frac{g(t\,\mp\,\frac{r}{c})}{4\pi r},$$

where $g(t)$ is a function describing the time variation of the source term.

First we consider the retarded potential case with '−' sign. In this case, the function $g(t-\frac{r}{c})$ keeps a constant value as far as the argument $t-\frac{r}{c}$ is constant. This means that the retarded potential

$$\Psi(\boldsymbol{r},t) = \frac{g(t\,-\,\frac{r}{c})}{4\pi r},$$

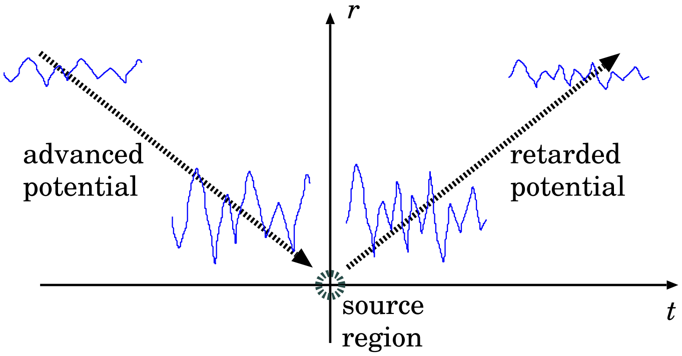

Figure 27: Pattern propagations in retarded and advanced potentials.

describes some pattern of time variation (for example, a sinusoidal oscillation), originated in the source region (a point in this case), **propagating outward** with velocity c, and decreasing its amplitude in proportion to $1/r$. The pattern at a distant point (with larger r) is **retarded** compared with the one at a near point (with smaller r). This shows a typical example of the transmission of the electromagnetic wave from the source region (Figure 27).

On the other hand, the advanced potential with '+' sign describes that some pattern of time variation **propagates inward**, and induces the same sort of time variation in the source region. The pattern at a distant point (with larger r) is **advanced** compared with the one at a near point (with smaller r). This obviously represents the reception of the electromagnetic wave, coming from outside, at the source region (Figure 27). However, this is not a 'typical' example of the wave reception, because the proportionality to $1/r$ implies that the incoming wave must be amplified as it approaches to the source region. This occurs, for example, in the converging wave reflected by a paraboloidal mirror of a radio telescope antenna, but in a limited space–time range.

We will consider, hereafter, the problem of the transmission of electromagnetic waves from a source region (or an antenna). Therefore, we will use the retarded potential only.

Coming back to the electromagnetics, we obtain retarded potential solutions for wave equations (57) and (58) with source terms as follows:

$$\boldsymbol{A}(\boldsymbol{r},\,t) = \frac{\mu}{4\pi}\int \frac{\boldsymbol{J}(\boldsymbol{r}',\,t-\frac{|\boldsymbol{r}-\boldsymbol{r}'|}{c})}{|\,\boldsymbol{r}-\boldsymbol{r}'\,|}\,dV', \tag{69}$$

$$\Phi(\boldsymbol{r},\,t) = \frac{1}{4\pi\epsilon}\int \frac{\rho(\boldsymbol{r}',\,t-\frac{|\boldsymbol{r}-\boldsymbol{r}'|}{c})}{|\,\boldsymbol{r}-\boldsymbol{r}'\,|}\,dV'. \tag{70}$$

Since the vector potential $\boldsymbol{A}$ and the scalar potential Φ derived here are not independent to each other, but related by Lorentz gauge in equation (56):

$$\nabla\boldsymbol{A} + \epsilon\mu\,\frac{\partial\Phi}{\partial t} = 0,$$

we will consider hereafter the vector potential $\boldsymbol{A}$ only.

2.3.6 Transmission of Radio Wave from a Harmonically Oscillating Source

Let us consider a case when the current density $\boldsymbol{J}(\boldsymbol{r},\,t)$ is harmonically (or, sinusoidally) oscillating everywhere in a source region with the same angular frequency $\omega = 2\pi\nu$:

$$\boldsymbol{J}(\boldsymbol{r},\,t) = \boldsymbol{J}(\boldsymbol{r})e^{-i\omega t}. \tag{71}$$

In this complex representation, we again use the convention, that the actual physical quantity is expressed by the real part of the complex quantity (in the above particular example, the actual current density is $\Re\left[\boldsymbol{J}(\boldsymbol{r})e^{-i\omega t}\right]$). The assumption of the same frequency throughout the source region, and the resultant separation of spatial and temporal variables, might seem a little artificial. But this must be valid for a frequency component in a Fourier expansion of the time variable current density.

The vector potential $\boldsymbol{A}(\boldsymbol{r},\,t)$, generated by such a current, is also expressed in a similar form:

$$\boldsymbol{A}(\boldsymbol{r},\,t) = \boldsymbol{A}(\boldsymbol{r})e^{-i\omega t}. \tag{72}$$

In fact, inserting equation (71) to the formula of the retarded potential in equation (69), we obtain

$$\boldsymbol{A}(\boldsymbol{r},\,t) = \frac{\mu}{4\pi}\int \frac{\boldsymbol{J}(\boldsymbol{r}',\,t-\frac{|\boldsymbol{r}-\boldsymbol{r}'|}{c})}{|\,\boldsymbol{r}-\boldsymbol{r}'\,|}\,dV' = \left[\frac{\mu}{4\pi}\int \boldsymbol{J}(\boldsymbol{r}')\frac{e^{ik|\boldsymbol{r}-\boldsymbol{r}'|}}{|\,\boldsymbol{r}-\boldsymbol{r}'\,|}\,dV'\right]e^{-i\omega t},$$

where $k \equiv \omega/c = 2\pi/\lambda$, with λ being the wavelength corresponding to the angular frequency ω. Therefore, we know that $\boldsymbol{A}(\boldsymbol{r},\,t)$ is really expressed in the form of equation (72), with

$$\boldsymbol{A}(\boldsymbol{r}) = \frac{\mu}{4\pi}\int \boldsymbol{J}(\boldsymbol{r}')\frac{e^{ik|\boldsymbol{r}-\boldsymbol{r}'|}}{|\,\boldsymbol{r}-\boldsymbol{r}'\,|}\,dV'. \tag{73}$$

Since harmonically oscillating current density $\boldsymbol{J}(\boldsymbol{r},\,t) = \boldsymbol{J}(\boldsymbol{r})\,e^{-i\omega t}$ generates oscillating vector potential $\boldsymbol{A}(\boldsymbol{r},\,t) = \boldsymbol{A}(\boldsymbol{r})\,e^{-i\omega t}$, it also generates oscillating electric and magnetic field intensities as well, according to equations:

$$\boldsymbol{B} = \nabla\times\boldsymbol{A}, \ \text{ and } \ \nabla\times\boldsymbol{H} = \boldsymbol{J} + \frac{\partial\boldsymbol{D}}{\partial t},$$

which are the definition of the vector potential and one of the Maxwell equations. In homogeneous medium outside of the source region, where we have no current ($\boldsymbol{J} = 0$) and $\epsilon,\ \mu = \text{const}$, the above equations are reduced to

$$\boldsymbol{H} = \frac{1}{\mu}\nabla\times\boldsymbol{A}, \tag{74}$$

and

$$-i\omega\epsilon\boldsymbol{E} = \nabla\times\boldsymbol{H}. \tag{75}$$

Therefore, the generated magnetic and electric fields are expressed as:

$$\boldsymbol{H}(\boldsymbol{r},\,t) = \boldsymbol{H}(\boldsymbol{r})e^{-i\omega t}, \quad \text{with} \quad \boldsymbol{H}(\boldsymbol{r}) = \frac{1}{\mu}\nabla\times\boldsymbol{A}(\boldsymbol{r}), \tag{76}$$

$$\boldsymbol{E}(\boldsymbol{r},\,t) = \boldsymbol{E}(\boldsymbol{r})e^{-i\omega t}, \quad \text{with} \quad \boldsymbol{E}(\boldsymbol{r}) = i\frac{c}{k}\,\nabla\times(\nabla\times\boldsymbol{A}(\boldsymbol{r})), \tag{77}$$

where we used the relations $c^2 = 1/\epsilon\mu$ and $\omega = kc$.

2.3.7 Electromagnetic Fields Far from the Source Region

Let us now calculate the electromagnetic fields generated by the harmonically oscillating current in the source region, taking into account the explicit expression for $\boldsymbol{A}(\boldsymbol{r})$, given in equation (73). For definiteness, we choose the origin of radius vectors $\boldsymbol{r}$ and $\boldsymbol{r}'$ within the source region. Note that $\boldsymbol{r}$ represents an arbitrary point in space, but $\boldsymbol{r}'$ is meaningful within the source region only, in equation (73).

i–th component of the rotation of $\boldsymbol{A}(\boldsymbol{r})$ in equation (76) is given by

$$(\nabla\times\boldsymbol{A}(\boldsymbol{r}))_i = \epsilon_{ijk}\frac{\partial}{\partial x_j}A_k(\boldsymbol{r}) = \frac{\mu}{4\pi}\epsilon_{ijk}\int J_k(\boldsymbol{r}')\frac{\partial}{\partial x_j}\frac{e^{ik|\boldsymbol{r}-\boldsymbol{r}'|}}{|\,\boldsymbol{r}-\boldsymbol{r}'\,|}\,dV'. \tag{78}$$

Since

$$\frac{\partial}{\partial x_i}\,|\,\boldsymbol{r}-\boldsymbol{r}'\,| = \frac{x_i - x_i'}{|\,\boldsymbol{r}-\boldsymbol{r}'\,|},$$

we have, in the integrand of equation (78),

$$\begin{aligned}\frac{\partial}{\partial x_j}\frac{e^{ik|\boldsymbol{r}-\boldsymbol{r}'|}}{\mid \boldsymbol{r}-\boldsymbol{r}' \mid} &= \frac{1}{\mid \boldsymbol{r}-\boldsymbol{r}' \mid}\frac{\partial}{\partial x_j}e^{ik|\boldsymbol{r}-\boldsymbol{r}'|} + e^{ik|\boldsymbol{r}-\boldsymbol{r}'|}\frac{\partial}{\partial x_j}\frac{1}{\mid \boldsymbol{r}-\boldsymbol{r}' \mid} \\ &= \frac{ik(x_j - x'_j)}{\mid \boldsymbol{r}-\boldsymbol{r}' \mid^2}e^{ik|\boldsymbol{r}-\boldsymbol{r}'|} - \frac{x_j - x'_j}{\mid \boldsymbol{r}-\boldsymbol{r}' \mid^3}e^{ik|\boldsymbol{r}-\boldsymbol{r}'|}. \end{aligned} \tag{79}$$

Let us assume that we observe the electromagnetic field at a point, which is far from the source region. If we assume that the distance of the point from the source region is much larger than the wavelength:

$$\mid \boldsymbol{r}-\boldsymbol{r}' \mid \gg \lambda, \tag{80}$$

(see Figure 28) and, hence,

$$\frac{1}{k \mid \boldsymbol{r}-\boldsymbol{r}' \mid} \ll 1,$$

then we can neglect the second term in the RHS of equation (79), compared with the first term, so that

$$\frac{\partial}{\partial x_j}\frac{e^{ik|\boldsymbol{r}-\boldsymbol{r}'|}}{\mid \boldsymbol{r}-\boldsymbol{r}' \mid} = \frac{ik(x_j - x'_j)}{\mid \boldsymbol{r}-\boldsymbol{r}' \mid^2}\, e^{ik|\boldsymbol{r}-\boldsymbol{r}'|}.$$

If we, furthermore, assume that the distance of the observation point from the source region is much larger than the size of the source region (see Figure 28), we have,

$$\mid \boldsymbol{r} \mid \gg \mid \boldsymbol{r}' \mid, \tag{81}$$

and, therefore, we can finally approximate equation (79) with

$$\frac{\partial}{\partial x_j}\frac{e^{ik|\boldsymbol{r}-\boldsymbol{r}'|}}{\mid \boldsymbol{r}-\boldsymbol{r}' \mid} = \frac{ikx_j}{r^2}\, e^{ik|\boldsymbol{r}-\boldsymbol{r}'|},$$

where $r = \mid \boldsymbol{r} \mid$, as before. Inserting this approximate formula into equation (78), and introducing a unit vector

$$\boldsymbol{n} = \frac{\boldsymbol{r}}{r}, \tag{82}$$

we obtain

$$\nabla \times \boldsymbol{A}(\boldsymbol{r}) = \frac{ik\mu}{4\pi}\frac{\boldsymbol{r}}{r^2} \times \int \boldsymbol{J}(\boldsymbol{r}')\, e^{ik|\boldsymbol{r}-\boldsymbol{r}'|}\, dV' = \frac{ik\mu}{4\pi r}\boldsymbol{n} \times \int \boldsymbol{J}(\boldsymbol{r}')\, e^{ik|\boldsymbol{r}-\boldsymbol{r}'|}\, dV'. \tag{83}$$

The same sort of discussions, under the same approximations of equations (80) and (81), lead to

$$\nabla \times (\nabla \times \boldsymbol{A}(\boldsymbol{r})) = -\frac{k^2\mu}{4\pi r}\,\boldsymbol{n} \times (\boldsymbol{n} \times \int \boldsymbol{J}(\boldsymbol{r'})\, e^{ik|\boldsymbol{r}-\boldsymbol{r'}|}\, dV'). \tag{84}$$

Therefore, in view of equations (73), (76) and (77), we have approximate formulae for the vector potential, magnetic field and electric field:

$$\boldsymbol{A}(\boldsymbol{r}) = \frac{\mu}{4\pi r}\int \boldsymbol{J}(\boldsymbol{r'})\, e^{ik|\boldsymbol{r}-\boldsymbol{r'}|}\, dV', \tag{85}$$

$$\boldsymbol{H}(\boldsymbol{r}) = \frac{1}{\mu}\nabla \times \boldsymbol{A}(\boldsymbol{r}) = \frac{ik}{4\pi r}\,\boldsymbol{n} \times \int \boldsymbol{J}(\boldsymbol{r'})\, e^{ik|\boldsymbol{r}-\boldsymbol{r'}|}\, dV', \tag{86}$$

$$\boldsymbol{E}(\boldsymbol{r}) = \frac{c}{k}\nabla \times (\nabla \times \boldsymbol{A}(\boldsymbol{r})) = -\frac{iZk}{4\pi r}\,\boldsymbol{n} \times (\boldsymbol{n} \times \int \boldsymbol{J}(\boldsymbol{r'})\, e^{ik|\boldsymbol{r}-\boldsymbol{r'}|}\, dV'), \tag{87}$$

where $Z = \sqrt{\mu/\epsilon}$ is the intrinsic impedance, as defined in equation (51), and we used relation $c = 1/\sqrt{\epsilon\mu}$, as given in equation (35).

2.3.8 Far Field Solution and Fraunhofer Region

It is worth to note that we did not approximate $\mid \boldsymbol{r} - \boldsymbol{r'} \mid$ by r in the arguments of exponential functions in equations (85), (86) and (87), even though we assumed that $\mid \boldsymbol{r} \mid \gg \mid \boldsymbol{r'} \mid$. Such approximation is not valid, in general, in an argument (or phase) of any sinusoidal function, since only remainder of the argument divided by 2π is meaningful in such a function (for example, $\cos(983517826^\circ + 132^\circ) = \cos(983517826^\circ \times (1 + 1.34212107 \times 10^{-7}))$ is not close to $\cos(983517826^\circ)$ at all).

However, if we find an 'absolutely' small term in the argument, which is much smaller than 1 radian, say, we can safely neglect such a term, and this may allow us to derive a useful approximate formula.

Let a characteristic size of our source region (aperture diameter of an antenna, for example) be D, distance to the observation point from the origin in the source region be r, and the wavelength be $\lambda = 2\pi/k$. We can generally expand the argument in the exponential term $k \mid \boldsymbol{r} - \boldsymbol{r'} \mid$ into a Taylor series:

$$k \mid \boldsymbol{r} - \boldsymbol{r'} \mid = k\sqrt{r^2 - 2\boldsymbol{r}\cdot\boldsymbol{r'} + r'^2} \cong kr\,(1 - \frac{\boldsymbol{r}\cdot\boldsymbol{r'}}{r^2} + \frac{1}{2}\frac{r'^2}{r^2} + \cdots). \tag{88}$$

If a condition, which is called "Fraunhofer condition",

$$\frac{2D^2}{\lambda} \ll r, \tag{89}$$

is satisfied among r, D and λ (see Figure 28), the third term in the expansion

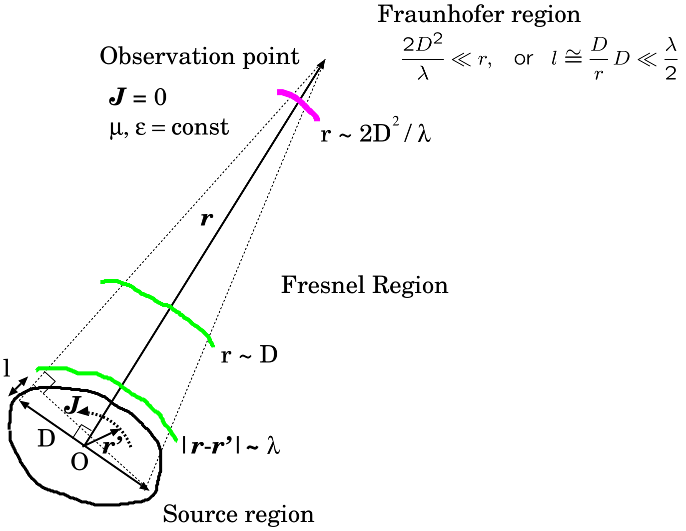

Figure 28: Fraunhofer condition.

of equation (88) fulfills

$$\frac{1}{2}\,k\,\frac{r'^2}{r} \sim \frac{\pi}{\lambda}\frac{D^2}{r} \ll \frac{\pi}{2} \approx 1.57 \;\; \text{radian.}$$

Therefore, we can neglect the third and higher order terms in the expansion of equation (88), in the argument of the exponential function, and obtain

$$e^{ik|\boldsymbol{r}-\boldsymbol{r}'|} \cong e^{ikr - ik\boldsymbol{n}\cdot\boldsymbol{r}'}, \tag{90}$$

where $\boldsymbol{n} = \boldsymbol{r}/r$, as before. Note that, on the contrary, the second term has the order of magnitude of

$$k\boldsymbol{n}\cdot\boldsymbol{r}' \sim \frac{2\pi D}{\lambda},$$

and cannot be neglected at all, in general, in the argument of the exponential (or, sinusoidal) function.

In this approximation, equation (85) for the vector potential, in particular, is expressed as

$$\boldsymbol{A}(\boldsymbol{r}) = \frac{\mu}{4\pi}\,\frac{e^{ikr}}{r}\int \boldsymbol{J}(\boldsymbol{r}')\,e^{-ik\boldsymbol{n}\cdot\boldsymbol{r}'}\,dV'.$$

Now the integral term is a function of the direction $\boldsymbol{n}$ only, and does not depend on the distance r to the observation point.

The region where $r > 2D^2/\lambda$ is called **"Fraunhofer region"** or **"far field"**, and the region where $r < 2D^2/\lambda$ is called **"Fresnel region"** or **"near field"**.

In the Fraunhofer region, we can approximate the exponential term as shown in equation (90). Therefore, introducing a vector $\boldsymbol{T}(\boldsymbol{n})$, characterizing a directional pattern of the radiation in the far field,

$$\boldsymbol{T}(\boldsymbol{n}) = \int \boldsymbol{J}(\boldsymbol{r}')e^{-ik\boldsymbol{n}\cdot\boldsymbol{r}'}\,dV', \tag{91}$$

and taking into account the temporal variation of the electromagnetic fields, we obtain, from equations (72), (76), (77), (85), (86), (87) and (90), so–called far field solutions:

$$\boldsymbol{A}(\boldsymbol{r},\,t) = \frac{\mu}{4\pi}\frac{e^{i(kr-\omega t)}}{r}\,\boldsymbol{T}(\boldsymbol{n}), \tag{92}$$

$$\boldsymbol{H}(\boldsymbol{r},\,t) = i\,\frac{1}{2\lambda}\frac{e^{i(kr-\omega t)}}{r}\,\boldsymbol{n}\times\boldsymbol{T}(\boldsymbol{n}), \tag{93}$$

$$\boldsymbol{E}(\boldsymbol{r},\,t) = -i\,\frac{Z}{2\lambda}\frac{e^{i(kr-\omega t)}}{r}\,\boldsymbol{n}\times[\boldsymbol{n}\times\boldsymbol{T}(\boldsymbol{n})]. \tag{94}$$

These equations describe harmonically oscillating and spherically expanding directional patterns $\boldsymbol{T}(\boldsymbol{n})$, $\boldsymbol{n}\times\boldsymbol{T}(\boldsymbol{n})$, and $\boldsymbol{n}\times[\boldsymbol{n}\times\boldsymbol{T}(\boldsymbol{n})]$, i.e. the **spherical waves**.

It is clear from equations (93) and (94), that we have

$$\boldsymbol{n}\cdot\boldsymbol{H} = 0,\quad \boldsymbol{n}\cdot\boldsymbol{E} = 0,\quad\text{and}\quad \boldsymbol{H}\cdot\boldsymbol{E} = 0, \tag{95}$$

which imply that the magnetic $\boldsymbol{H}$ and electronic $\boldsymbol{E}$ waves are transversal and mutually orthogonal. It is also clear from the same equations that

$$\boldsymbol{E} = -Z\,\boldsymbol{n}\times\boldsymbol{H},\quad\text{and}\quad \boldsymbol{H} = \frac{1}{Z}\,\boldsymbol{n}\times\boldsymbol{E}. \tag{96}$$

Taking real parts of these complex equations, we see that the same relations hold for actual electromagnetic fields, which are real parts of the complex expressions: $\boldsymbol{H}_r = \Re\,\boldsymbol{H}$ and $\boldsymbol{E}_r = \Re\,\boldsymbol{E}$, i.e.

$$\boldsymbol{E}_r = -Z\,\boldsymbol{n}\times\boldsymbol{H}_r,\quad\text{and}\quad \boldsymbol{H}_r = \frac{1}{Z}\,\boldsymbol{n}\times\boldsymbol{E}_r.$$

Therefore, the Poynting vector $\boldsymbol{S}$ for the spherical wave is expressed as:

$$\boldsymbol{S} = \boldsymbol{E}_r\times\boldsymbol{H}_r = Z\,\boldsymbol{n}\mid\boldsymbol{H}_r\mid^2 = \frac{1}{Z}\,\boldsymbol{n}\mid\boldsymbol{E}_r\mid^2. \tag{97}$$

This equation means that the Poynting vector of the spherical wave is directed towards $\boldsymbol{n} = \boldsymbol{r}/r$, which is nothing but the direction of propagation of the wave, and the amplitude ratio of the electric and magnetic fields is

$$\frac{|\ \boldsymbol{E}_r\ |}{|\ \boldsymbol{H}_r\ |} = Z, \tag{98}$$

i.e. equal to the intrinsic impedance of the medium $Z = \sqrt{\mu/\epsilon}$. These properties are the same with those in the plane wave case, which we discussed earlier. Of course, the spherical waves locally approach to the plane waves when $r \to \infty$.

2.3.9 Hertz Dipole

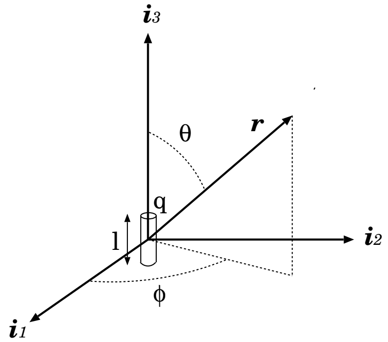

Figure 29: Hertz dipole.

We are now in position to derive some results on transmission of the electromagnetic waves from simple antennas, using the far field solutions in equations (92), (93) and (94). First, we will consider an idealized antenna, composed of an infinitesimal electric dipole called "Hertz dipole", which was discussed by Heinrich Hertz in 1888.

Let us consider an infinitesimally small cylinder with infinitesimal cross section q and infinitesimal length l, which is located at the origin of a rectangular coordinate system and directed towards 3–rd axis (Figure 29).

Let us assume a homogeneous electric current I, which is flowing within the cylinder and harmonically oscillating in time proportionally to $e^{-i\omega t}$.

In this case, the vector $\boldsymbol{T}(\boldsymbol{n})$ characterizing the radiation pattern in the far field in equation (91) takes a particularly simple form. In fact, if we assume that $l \ll \lambda$, where λ is the wavelength, we have

$$k\boldsymbol{n}\cdot\boldsymbol{r}' \sim \frac{2\pi}{\lambda} l \ll 1, \quad \text{and, therefore,} \quad e^{-ik\boldsymbol{n}\cdot\boldsymbol{r}'} \cong 1,$$

in equation (91), and, consequently,

$$\boldsymbol{T}(\boldsymbol{n}) = \int \boldsymbol{J}\, dV' = \boldsymbol{J}\, l\, q = I\, l\, \boldsymbol{i}_3, \tag{99}$$

where $\boldsymbol{i}_3$ is the unit vector along the 3–rd axis. Applying equation (99) to equations (92), (93) and (94), we obtain non–zero components of the far field solutions of the transmitted wave:

$$A_3(\boldsymbol{r},\, t) = \frac{\mu\, I\, l}{4\pi}\, \frac{e^{i(kr-\omega t)}}{r}, \tag{100}$$

$$H_\phi(\boldsymbol{r},\, t) = -i\, \frac{I\, l}{2\lambda}\, \frac{e^{i(kr-\omega t)}}{r}\, \sin\theta, \tag{101}$$

$$E_\theta(\boldsymbol{r},\, t) = -i\, \frac{Z\, I\, l}{2\lambda}\, \frac{e^{i(kr-\omega t)}}{r}\, \sin\theta, \tag{102}$$

where θ and ϕ are angular variables shown in Figure 29. Or, for actual physical quantities $\boldsymbol{A}_r$, $\boldsymbol{H}_r$ and $\boldsymbol{E}_r$, which are real parts of the respective complex quantities, we have the non-zero components in the far field:

$$A_{r3}(\boldsymbol{r},\, t) = \Re A_3(\boldsymbol{r},\, t) = \frac{\mu\, I\, l}{4\pi}\, \frac{\cos(kr-\omega t)}{r}, \tag{103}$$

$$H_{r\phi}(\boldsymbol{r},\, t) = \Re H_\phi(\boldsymbol{r},\, t) = \frac{I\, l}{2\lambda}\, \frac{\sin(kr-\omega t)}{r}\, \sin\theta, \tag{104}$$

$$E_{r\theta}(\boldsymbol{r},\, t) = \Re E_\theta(\boldsymbol{r},\, t) = \frac{Z\, I\, l}{2\lambda}\, \frac{\sin(kr-\omega t)}{r}\, \sin\theta. \tag{105}$$

The $\sin\theta$ dependence of the magnetic and electric field intensities shows effectiveness of transmission of the electromagnetic wave to a certain direction θ, ϕ, which is generally called **"field pattern"**, in the far field. Since the above equations do not have any dependence on ϕ, the field pattern of Hertz dipole is axisymmetric, and has a torus–like shape shown in Figure 30.

Now we consider power flux density $\mathcal{S}$ of the radio wave generated from the Hertz dipole. For this purpose, following the definition of the IEEE (1977), we calculate time average $\overline{\boldsymbol{S}}$ of Poynting vector $\boldsymbol{S}$, which is given by $\boldsymbol{S} = \boldsymbol{E}_r \times \boldsymbol{H}_r = E_{r_\theta}\, H_{r_\phi}\, \boldsymbol{n}$ in this case. Taking absolute value, we have

$$\mathcal{S} = \mid \overline{\boldsymbol{S}} \mid = \overline{E_{r\theta} H_{r\phi}} = Z \left(\frac{Il}{2\lambda}\right)^2 \frac{\sin^2\theta}{r^2}\, \overline{\sin^2(kr-\omega t)} = \frac{Z}{2} \left(\frac{Il}{2\lambda}\right)^2 \frac{\sin^2\theta}{r^2}, \tag{106}$$

since, in general,

$$\overline{\sin^2(kr-\omega t)} = \frac{1}{2}.$$

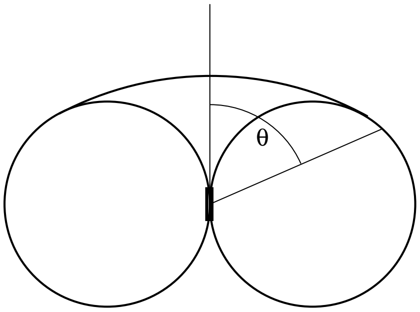

Figure 30: Field pattern of Hertz dipole.

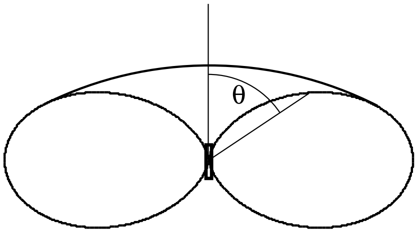

Figure 31: Power pattern of Hertz dipole.

The $\sin^2\theta$ dependence shows effectiveness of transmission of the power of the electromagnetic wave to a certain direction, which is called the **"power pattern"** (Figure 31).

Figure 32 shows time variation of the electromagnetic field in the near field of the oscillating Hertz dipole, which can be calculated using exact equations (73), (76) and (77).
This figure is copied from a webpage
http://didaktik.physik.uni-wuerzburg.de/~pkrahmer/home/dipol.html.
One can see an animation movie of the transmission of the electromagnetic wave from the Hertz dipole in this webpage.

2.3.10 Linear Dipole Antenna of Finite Length

The Hertz dipole was still an idealized antenna. We now consider a realistic antenna, a linear dipole of finite length, with an oscillating current fed from its center (Figure 33).

Let us assume that a linear dipole of length L is directed towards $\boldsymbol{i}_3$ axis and its center is located at the origin. Let us also assume that the spatial distribution of the harmonically oscillating electric current ($\propto \exp(-i\omega t)$) is

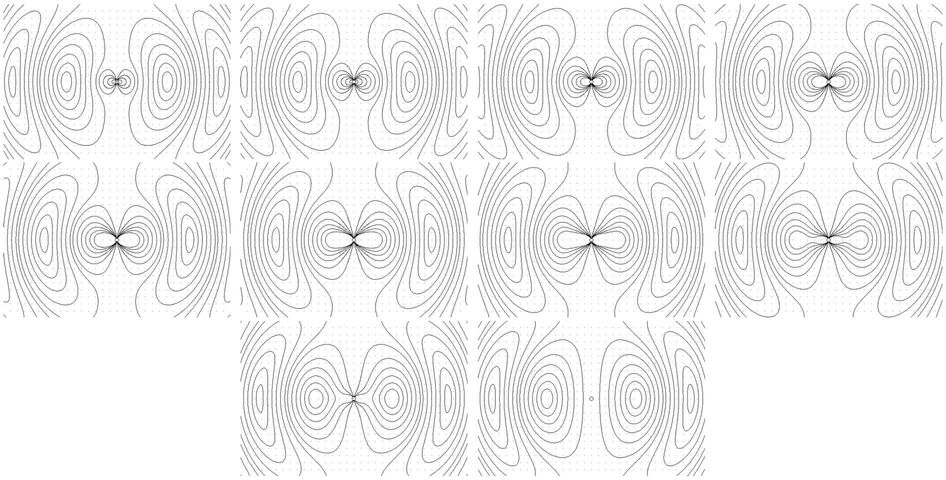

Figure 32: Time variation of the electromagnetic field close to the Hertz dipole (from http://didaktik.physik.uni-wuerzburg.de/~pkrahmer/home/dipol.html).

given by an empirical formula:

$$I(z) = I_0 \sin\left[k\left(\frac{L}{2} - \mid z \mid\right)\right], \tag{107}$$

where z is distance from the origin along $\boldsymbol{i}_3$ axis, and $k = 2\pi/\lambda$.

Then, in the far field, we have

$$\begin{aligned}\boldsymbol{T}(\boldsymbol{n}) &= \int \boldsymbol{J}(\boldsymbol{r}')e^{-ik\boldsymbol{n}\cdot\boldsymbol{r}'}\,dV' = \boldsymbol{i}_3\int_{-L/2}^{L/2} I(z)e^{-ikz\cos\theta}\,dz \\ &= I_0\,\boldsymbol{i}_3\int_{-L/2}^{L/2}\sin\left[k\left(\frac{L}{2} - \mid z \mid\right)\right]e^{-ikz\cos\theta}\,dz \\ &= 2\,I_0\,\boldsymbol{i}_3\int_0^{L/2}\sin\left(\frac{kL}{2} - kz\right)\cos(kz\cos\theta)\,dz \\ &= \frac{2\,I_0}{k\sin^2\theta}\,\boldsymbol{i}_3\left[\cos\left(\frac{kL}{2}\cos\theta\right) - \cos\left(\frac{kL}{2}\right)\right],\end{aligned} \tag{108}$$

where θ is an angle of the direction of propagation $\boldsymbol{n}$ from the $\boldsymbol{i}_3$ axis. Therefore, equation (94) gives a non–zero component of the far field solution of the electric field:

$$E_\theta(\boldsymbol{r},\,t) = -i\,\frac{ZI_0}{2\pi}\,\frac{e^{i(kr-\omega t)}}{r}\,\frac{\cos\left(\frac{kL}{2}\cos\theta\right) - \cos\left(\frac{kL}{2}\right)}{\sin\theta}. \tag{109}$$

This result shows that the field pattern of the linear dipole antenna is different with different ratio L/λ between the dipole length and wavelength. Figure

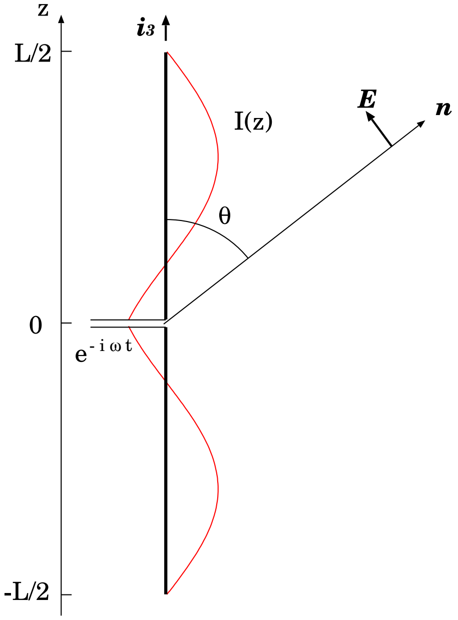

Figure 33: A linear dipole of finite length.

34 shows field patterns of linear dipole antennas with different L/λ ratios in the far field region, calculated on the basis of equation (109).

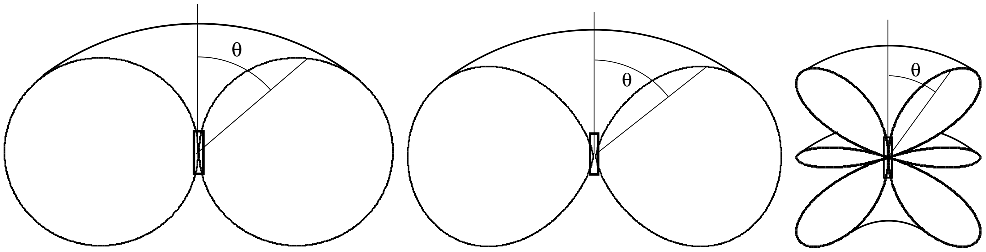

Figure 34: Field patterns of linear dipole antennas with lengths $L = 0.5\lambda$ (Left), $L = 1.0\lambda$ (Middle), and $L = 1.5\lambda$ (Right) in the far field region.

Thus, we succeeded to transmit the electromagnetic wave from a realistic antenna!

Fifure 35 shows time variation of the near field around the linear dipole (from Kraus, Electromagnetics, Third Edition, Mc Graw-Hill, 1984).

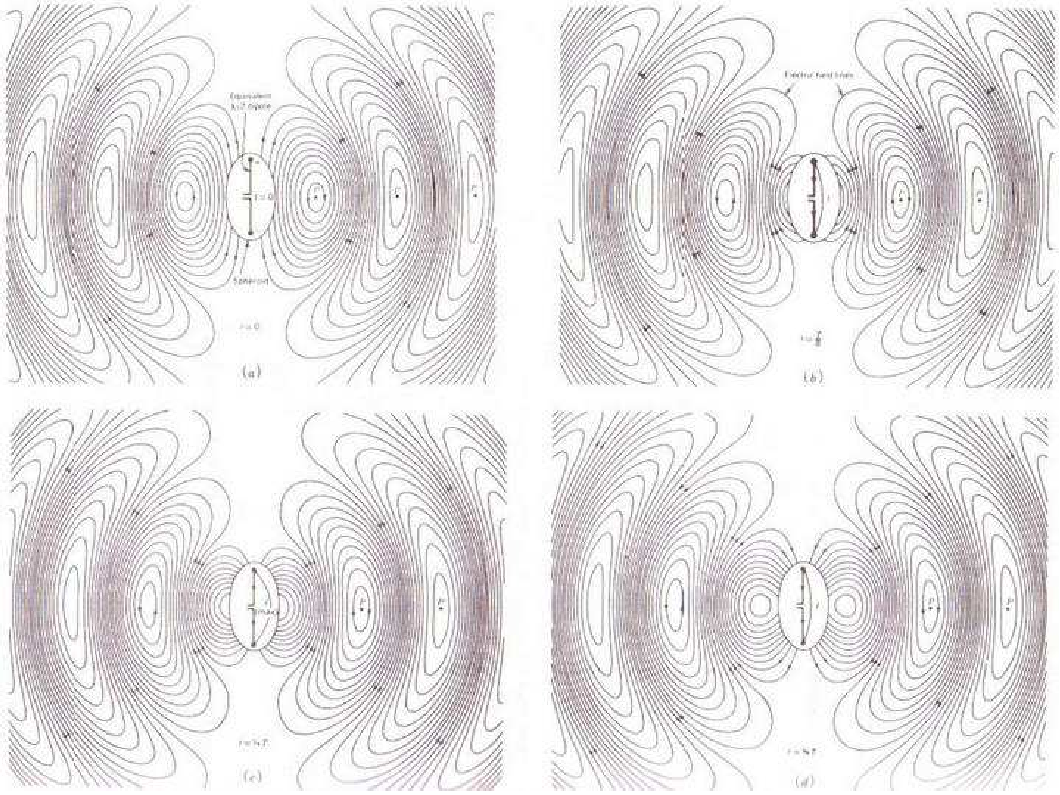

Figure 35: Time variation of the electric field lines in the near field region of a $L = \lambda/2$ linear dipole antenna (from Kraus, 1984).

2.4 Transmitting and Receiving Antennas

2.4.1 The Reciprocity Theorem

We derived field patterns of the simplest dipole antennas as dependences of transmitted electromagnetic fields on different directions, which characterize transmission efficiencies towards those directions. It is well known that the same antennas can be used both for transmission and reception of the electromagnetic waves. For receptions, we also call "field patterns" or "voltage reception patterns" the efficiencies of the reception from an emitter at different directions. Then, how the transmission and reception field patterns of the same antenna are related to each other? In order to answer to this question, we will consider Rayleigh's Reciprocity Theorem (1894) as applied to the electromagetics.

The reciprocity theorem states the followings.

> Let the electromagnetic fields, generated by two source currents $\boldsymbol{J}_1$ and $\boldsymbol{J}_2$, be $\boldsymbol{E}_1$, $\boldsymbol{H}_1$ and $\boldsymbol{E}_2$, $\boldsymbol{H}_2$, respectively. If the source currents exist within two finite spatial regions V_1 and V_2 only (Figure 36), and if a volume V includes both the two regions, then we have
>
> $$\int_V (\boldsymbol{E}_1 \cdot \boldsymbol{J}_2 - \boldsymbol{E}_2 \cdot \boldsymbol{J}_1)\, dV = 0. \tag{110}$$

Let us prove this theorem in a case of homogeneous medium (ϵ, $\mu =$ const), and harmonically oscillating currents ($\propto \exp(-i\omega t)$). In this case, from Maxwell equations (21) and (22), we have:

$$\nabla \times \boldsymbol{H}_1 = \boldsymbol{J}_1 - i\omega\epsilon \boldsymbol{E}_1, \qquad \nabla \times \boldsymbol{H}_2 = \boldsymbol{J}_2 - i\omega\epsilon \boldsymbol{E}_2, \tag{111}$$

$$\nabla \times \boldsymbol{E}_1 = i\omega\mu \boldsymbol{H}_1, \qquad \nabla \times \boldsymbol{E}_2 = i\omega\mu \boldsymbol{H}_2. \tag{112}$$

Using a formula of vector algebra in equation (17):

$$\nabla \cdot (\boldsymbol{A} \times \boldsymbol{B}) = \boldsymbol{B} \cdot (\nabla \times \boldsymbol{A}) - \boldsymbol{A} \cdot (\nabla \times \boldsymbol{B}),$$

and equations (111) and (112), we have

$$\begin{aligned}
\nabla \cdot (\boldsymbol{E}_1 \times \boldsymbol{H}_2) &= \boldsymbol{H}_2 \cdot (\nabla \times \boldsymbol{E}_1) - \boldsymbol{E}_1 \cdot (\nabla \times \boldsymbol{H}_2) \\
&= i\omega\mu \boldsymbol{H}_1 \cdot \boldsymbol{H}_2 - \boldsymbol{E}_1 \cdot \boldsymbol{J}_2 + i\omega\epsilon \boldsymbol{E}_1 \cdot \boldsymbol{E}_2, \\
\nabla \cdot (\boldsymbol{E}_2 \times \boldsymbol{H}_1) &= \boldsymbol{H}_1 \cdot (\nabla \times \boldsymbol{E}_2) - \boldsymbol{E}_2 \cdot (\nabla \times \boldsymbol{H}_1) \\
&= i\omega\mu \boldsymbol{H}_1 \cdot \boldsymbol{H}_2 - \boldsymbol{E}_2 \cdot \boldsymbol{J}_1 + i\omega\epsilon \boldsymbol{E}_1 \cdot \boldsymbol{E}_2.
\end{aligned}$$

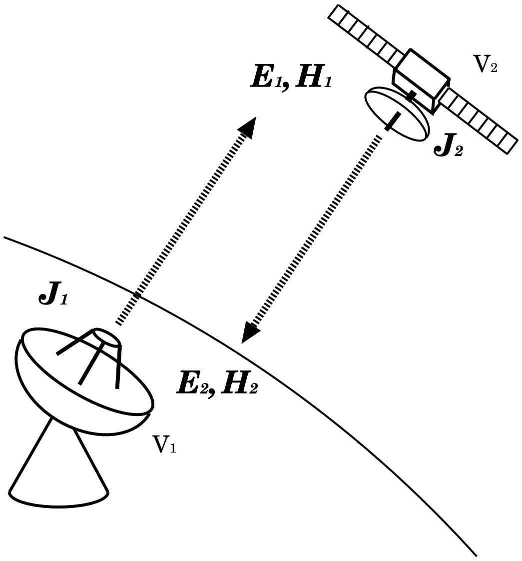

Figure 36: Electromagnetic fields generated by two source currents confined within two finite spatial regions.

Taking difference of the above equations, we obtain

$$\nabla \cdot (\boldsymbol{E}_1 \times \boldsymbol{H}_2 - \boldsymbol{E}_2 \times \boldsymbol{H}_1) = \boldsymbol{E}_2 \cdot \boldsymbol{J}_1 - \boldsymbol{E}_1 \cdot \boldsymbol{J}_2.$$

Then, integrating the both sides of the above equation through the volume V, which includes source regions of both $\boldsymbol{J}_1$ and $\boldsymbol{J}_2$, and applying Gauss's integration theorem in equation (67) to the LHS, we have

$$\oint (\boldsymbol{E}_1 \times \boldsymbol{H}_2 - \boldsymbol{E}_2 \times \boldsymbol{H}_1) \cdot \boldsymbol{n}_n d\mathcal{S} = \int\limits_V (\boldsymbol{E}_2 \cdot \boldsymbol{J}_1 - \boldsymbol{E}_1 \cdot \boldsymbol{J}_2)\, dV, \tag{113}$$

where $\boldsymbol{n}_n d\mathcal{S}$ is a vector of the surface element on the volume V with a unit normal vector $\boldsymbol{n}_n$.

Let us denote radius vectors from centers of the two source current regions to a point on the surface (point A, say) of the volume V as $\boldsymbol{r}_1$ and $\boldsymbol{r}_2$, and let us also denote a radius vector from the origin O, at the Middle point of the two current regions, to the point A as $\boldsymbol{r}$, as shown in Figure 37.

If we adopt a sufficiently big volume V, so that its surface is in far field regions from the two current regions, the electromagnetic fields are approximated by the spherical waves, which satisfy

$$\boldsymbol{E}_1 = -Z\,\boldsymbol{n}_1 \times \boldsymbol{H}_1, \qquad \boldsymbol{E}_2 = -Z\,\boldsymbol{n}_2 \times \boldsymbol{H}_2, \tag{114}$$

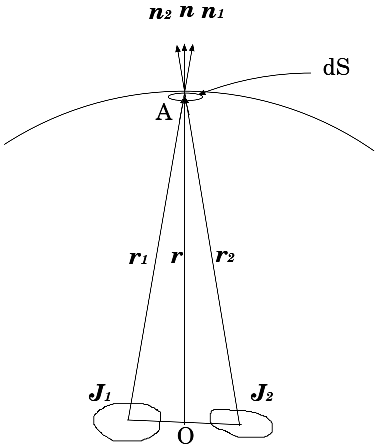

Figure 37: Geometry of the source current regions and radius vectors to a point on the surface of the volume V.

where $\boldsymbol{n}_1 = \boldsymbol{r}_1/r_1$ and $\boldsymbol{n}_2 = \boldsymbol{r}_2/r_2$.

Let us further assume, for simplicity, that the surface is a sphere with the center at the origin O. In that case, the unit normal vector $\boldsymbol{n}_n$ to the surface element at the point A is $\boldsymbol{n}_n = \boldsymbol{n} = \boldsymbol{r}/r$. Then, the surface integral in the LHS of equation (113) becomes

$$\begin{aligned}
&\oint (\boldsymbol{E}_1 \times \boldsymbol{H}_2 - \boldsymbol{E}_2 \times \boldsymbol{H}_1) \cdot \boldsymbol{n}_n \, d\mathcal{S} \\
&\quad = - Z \oint [(\boldsymbol{n}_1 \times \boldsymbol{H}_1) \times \boldsymbol{H}_2 - (\boldsymbol{n}_2 \times \boldsymbol{H}_2) \times \boldsymbol{H}_1] \cdot \boldsymbol{n} \, d\mathcal{S} \\
&\quad = - Z \oint [(\boldsymbol{n} \cdot \boldsymbol{H}_1)(\boldsymbol{n}_1 \cdot \boldsymbol{H}_2) - (\boldsymbol{n} \cdot \boldsymbol{H}_2)(\boldsymbol{n}_2 \cdot \boldsymbol{H}_1) \\
&\qquad - \boldsymbol{n} \cdot (\boldsymbol{n}_1 - \boldsymbol{n}_2)(\boldsymbol{H}_1 \cdot \boldsymbol{H}_2)] \, d\mathcal{S} \\
&\quad = - Z \oint [(\boldsymbol{n} \cdot \boldsymbol{H}_1)(\boldsymbol{n}_1 - \boldsymbol{n}) \cdot \boldsymbol{H}_2 - (\boldsymbol{n} \cdot \boldsymbol{H}_2)(\boldsymbol{n}_2 - \boldsymbol{n}) \cdot \boldsymbol{H}_1 \\
&\qquad - \boldsymbol{n} \cdot (\boldsymbol{n}_1 - \boldsymbol{n}_2)(\boldsymbol{H}_1 \cdot \boldsymbol{H}_2)] \, d\mathcal{S}, \qquad (115)
\end{aligned}$$

where we used a formula of vector algebra

$$\boldsymbol{A} \times (\boldsymbol{B} \times \boldsymbol{C}) = \boldsymbol{B}(\boldsymbol{A} \cdot \boldsymbol{C}) - \boldsymbol{C}(\boldsymbol{A} \cdot \boldsymbol{B}),$$

given in equation (14).

Now, if we tend the radius r of the sphere to the infinity ($r \to \infty$), then

$$
\begin{aligned}
&d\mathcal{S} \propto r^2, && \text{since } d\mathcal{S} = r^2 \sin\theta \, d\theta \, d\phi,\\
&\mid \boldsymbol{H}_1 \mid \mid \boldsymbol{H}_2 \mid \propto r^{-2}, && \text{because they are spherical waves,}\\
&\boldsymbol{n}_1 \to \boldsymbol{n},\ \boldsymbol{n}_2 \to \boldsymbol{n}, && \text{hence } \boldsymbol{n}_1 - \boldsymbol{n} \to 0,\ \boldsymbol{n}_2 - \boldsymbol{n} \to 0,\ \boldsymbol{n}_1 - \boldsymbol{n}_2 \to 0.
\end{aligned}
$$

Consequently, the LHS of equation (115), and therefore LHS of equation (113), too, tends to zero, when $r \to \infty$.

Thus, for a sufficiently large spherical volume V, equation (113) gives us

$$\int\limits_V (\boldsymbol{E}_2 \cdot \boldsymbol{J}_1 - \boldsymbol{E}_1 \cdot \boldsymbol{J}_2) dV = 0. \tag{116}$$

But, since we assume that the currents $\boldsymbol{J}_1 = 0$ and $\boldsymbol{J}_2 = 0$ outside of the finite regions V_1 and V_2, respectively, equation (116) must hold for an arbitrary volume V, including V_1 and V_2. Thus, we proved the reciprocity theorem.

Equation (116) can be expressed also in a form:

$$\int\limits_{V_1} \boldsymbol{E}_2 \cdot \boldsymbol{J}_1 \, dV = \int\limits_{V_2} \boldsymbol{E}_1 \cdot \boldsymbol{J}_2 \, dV. \tag{117}$$

2.4.2 Equivalence of Field Patterns in Transmission and Reception

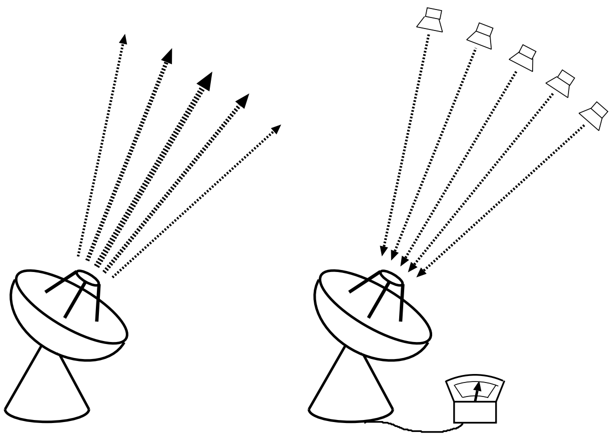

Figure 38: Transmission (Left) and reception (Right) field patterns of an antenna.

Suppose an antenna, which is transmitting the radio wave towards the sky. The **transmission field pattern** is defined as the direction dependence of the amplitude of the electromagnetic field transmitted from the antenna (see left panel of Figure 38). Now suppose the same antenna is receiving radio wave from a hypothetical distant emitter of unit strength located in an arbitrary direction of the sky. The **reception field pattern**, or **voltage reception pattern**, is defined as dependence of the amplitude of the received electromagnetic field, or the resultant voltage in a receiver system, on the direction of the emitter (see right panel of Figure 38).

The reciprocity theorem shows us that the transmission field pattern and the reception field pattern of the same antenna are identical.

In order to prove this statement, let us again consider that a current $\boldsymbol{J}_1$ in an antenna 1 generates an electric field $\boldsymbol{E}_1$ around another antenna 2, while a current $\boldsymbol{J}_2$ in the antenna 2 generates an electric field $\boldsymbol{E}_2$ around the antenna 1 (see Figure 36).

Let us assume, for simplicity, that the antennas are small dipoles with length l and cross–section q (Figure 39). This is not necessarily a very unrealistic assumption, since co–axial to waveguide converters in feedhorns of existing antennas are often composed of simple dipoles. Then, we can adopt in equation (117),

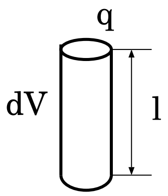

Figure 39: A small dipole with length l and cross-section q.

volume element : $dV = ql$

current : $I =\mid \boldsymbol{J} \mid q$

voltage : $U = El.$

And, therefore, equation (117) can now be expressed as:

$$U_2\, I_1 = U_1\, I_2. \tag{118}$$

Let us now consider that antenna 1 is fixed at some position and antenna 2 moves from position A to position B, and then to position C (Figure 40). Let us denote voltages, generated by the current I_1 in antenna 1 at positions

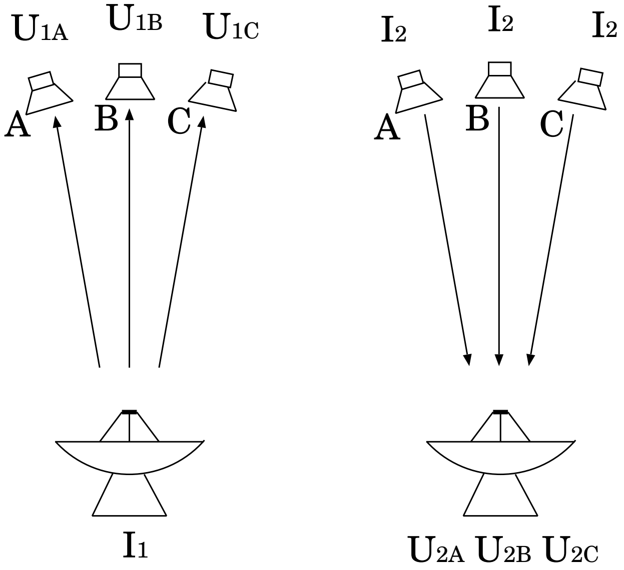

Figure 40: Current and voltage at fixed antenna 1 and moving antenna 2.

A, B, and C of antenna 2, as U_{1A}, U_{1B}, and U_{1C}. We also denote voltages at antenna 1, generated by the current I_2 of antenna 2 at positions A, B, and C, as U_{2A}, U_{2B}, and U_{2C}. From the reciprocity theorem, as described in equation (118), we have

$$\begin{aligned} U_{2A}\, I_1 &= U_{1A}\, I_2, \\ U_{2B}\, I_1 &= U_{1B}\, I_2, \\ U_{2C}\, I_1 &= U_{1C}\, I_2. \end{aligned} \tag{119}$$

Therefore, U_1 is always proportional to U_2, irrespective of the direction of antenna 2 viewed from antenna 1. Since U_1 expresses the transmission field pattern, while U_2 expresses the reception field pattern, of antenna 1, the proportionality $U_1 \propto U_2$ proves the equivalence of the transmission and reception field patterns of an antenna.

2.5 Transmission from Aperture Plane

2.5.1 Aperture Antennas

If a transmission antenna has a plane, through which the electromagnetic wave flows out towards the external space, we call such a plane “aperture plane”, and we call an antenna having an aperture plane “aperture antenna”.

As an example, let us consider a transmitting horn antenna, such as shown in Figure 41. Primary wave source (the oscillating current in the co–axial to waveguide converter) is located in the waveguide tube, and generates the electromagnetic fields in the horn. Then, the electromagnetic fields flow out of the horn towards the external space, through a plane A. This is the aperture plane, and the horn antenna is an aperture antenna. Parabololdal antennas are also typical aperture antennas (Figure 42).

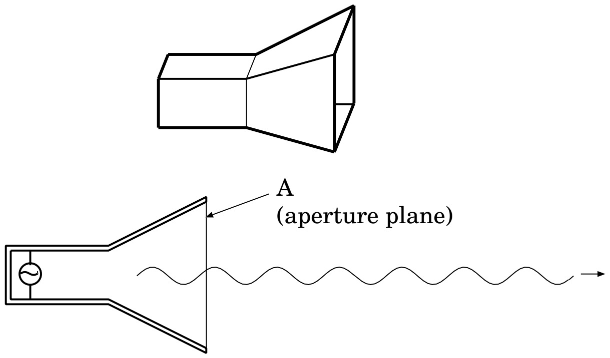

Figure 41: A horn antenna and an aperture plane.

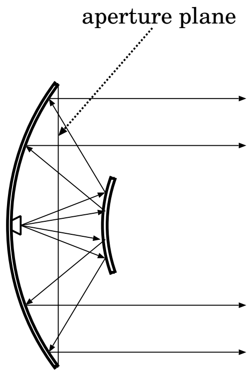

Figure 42: A paraboloidal antenna and an aperture plane.

On the other hand, the linear dipole antenna such as shown in Figure 33 is not an aperture antenna.

In order to consider the field transmission pattern of an aperture antenna, it is convenient to regard, as if the electromagnetic waves are generated by some fictitious wave source located on the aperture plane (Figure 43). Such a “secondary wave source” can be uniquely related to the electromagnetic

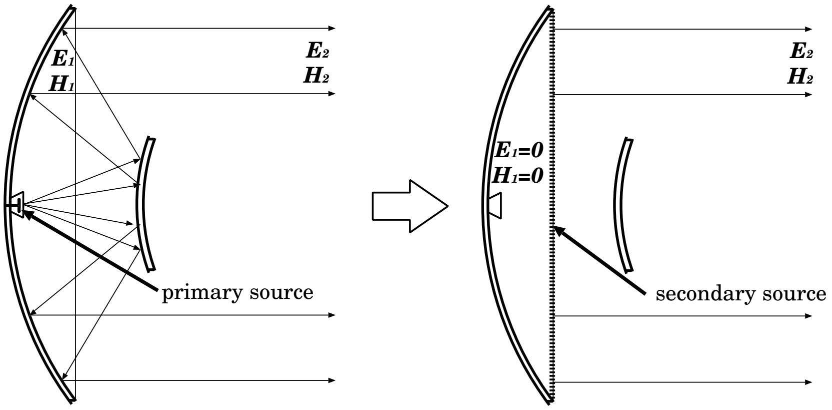

Figure 43: Electromagnetic wave, transmitted from an aperture antenna (Left), can be represented as a wave generated by an appropriately chosen secondary wave source on the aperture plane (Right).

field generated by the primary wave source, the actual oscillating current within the feed horn, and can exactly reproduce the actual field transmission pattern, as we will see below. The secondary source on an aperture plane can be interpreted in terms of Huygens and Fresnel's principle, which states "each point on a primary wavefront can be considered to be a new source of a secondary wave".

2.5.2 Boundary Conditions on the Aperture Plane "Magnetic Current" and "Magnetic Charge"

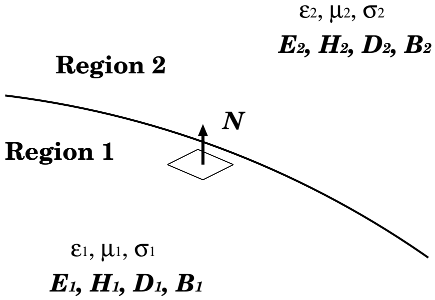

Figure 44: Regions with different electromagnetic properties.

If physical properties of a medium are discontinuous at some boundary surface, we solve physical equations on the both sides of the boundary, and then connect the solutions, using a set of boundary conditions. The boundary conditions for electromagnetic fields $\boldsymbol{E}_1$, $\boldsymbol{H}_1$, $\boldsymbol{D}_1$, $\boldsymbol{B}_1$ and $\boldsymbol{E}_2$, $\boldsymbol{H}_2$, $\boldsymbol{D}_2$, $\boldsymbol{B}_2$ in two regions with different ϵ_1, μ_1, σ_1 and ϵ_2, μ_2, σ_2, where ϵ, μ, and σ are permittivity, permeability, and specific conductivity, correspondingly, are well known: at a boundary surface, which separates the two regions, with a unit normal vector $\boldsymbol{N}$ (Figure 44), we have

$$\boldsymbol{N} \times (\boldsymbol{H}_2 - \boldsymbol{H}_1) = \boldsymbol{K}, \tag{120}$$

$$\boldsymbol{N} \times (\boldsymbol{E}_2 - \boldsymbol{E}_1) = 0, \tag{121}$$

$$\boldsymbol{N} \cdot (\boldsymbol{D}_2 - \boldsymbol{D}_1) = \Sigma, \tag{122}$$

$$\boldsymbol{N} \cdot (\boldsymbol{B}_2 - \boldsymbol{B}_1) = 0, \tag{123}$$

where $\boldsymbol{K}$ [A m^{-1}] is the surface density of electric current (or "surface electric current"), and Σ [A s m^{-2}] is the surface density of electric charge (or "surface electric charge").

However, having these usual boundary conditions alone is not sufficient to fulfil the requirements for the secondary source on the aperture plane, as shown in Figure 43, where $\boldsymbol{E}_1 = 0$ and $\boldsymbol{H}_1 = 0$ in the inner side of the aperture plane, while $\boldsymbol{E}_2 \neq 0$ and $\boldsymbol{H}_2 \neq 0$ in the outer side of the aperture plane.

In order to overcome this difficulty, we introduce virtual quantities called "**magnetic current density**" $\boldsymbol{J}_m$, with unit [V m^{-2}], and "**magnetic charge density**" ρ_m, with unit [V s m^{-3}], following Adachi (S. Adachi, Electromagnetic Wave Engineering, 1985). They are supposed to be related with the electromagnetic field quantities through "extended" Maxwell equations:

$$\nabla \times \boldsymbol{E} = -\boldsymbol{J}_m - \frac{\partial \boldsymbol{B}}{\partial t}, \tag{124}$$

$$\nabla \cdot \boldsymbol{B} = \rho_m, \tag{125}$$

and to fulfil following boundary conditions:

$$\boldsymbol{N} \times (\boldsymbol{H}_2 - \boldsymbol{H}_1) = 0, \tag{126}$$

$$\boldsymbol{N} \times (\boldsymbol{E}_2 - \boldsymbol{E}_1) = -\boldsymbol{K}_m, \tag{127}$$

$$\boldsymbol{N} \cdot (\boldsymbol{D}_2 - \boldsymbol{D}_1) = 0, \tag{128}$$

$$\boldsymbol{N} \cdot (\boldsymbol{B}_2 - \boldsymbol{B}_1) = \Sigma_m, \tag{129}$$

where $\boldsymbol{K}_m$ [V m^{-1}] is the surface density of magnetic current (or "surface magnetic current"), and Σ_m [V s m^{-2}] is the surface density of magnetic charge (or "surface magnetic charge").

Note that an equation of continuity:

$$\frac{\partial \rho_m}{\partial t} + \nabla \cdot \boldsymbol{J}_m = 0, \tag{130}$$

holds in view of equations (124) and (125).

Before discussing the boundary conditions at the aperture plane, let us first consider a closed surface surrounding a primary wave source (Figure 45). If we assume that the medium is continuous across the surface, the electromagnetic fields must be also continuous, i.e. conditions $\boldsymbol{E}_1 = \boldsymbol{E}_2$, $\boldsymbol{H}_1 = \boldsymbol{H}_2$, $\boldsymbol{D}_1 = \boldsymbol{D}_2$ and $\boldsymbol{B}_1 = \boldsymbol{B}_2$ must hold on the surface.

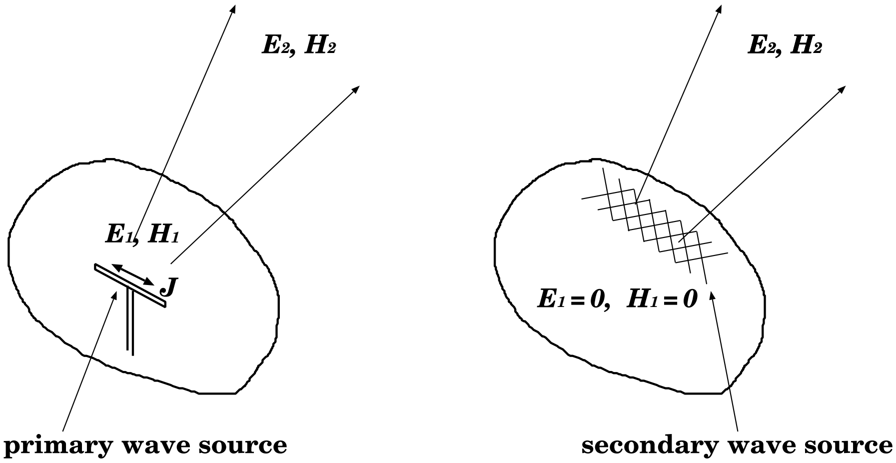

Figure 45: A closed surface surrounding a primary wave source (Left), which can be regarded as a secondary wave source with suitable surface currents and surface charges (Right).

Now, suppose we place surface electric current $\boldsymbol{K}$, surface magnetic current $\boldsymbol{K}_m$, surface electric charge Σ and surface magnetic charge Σ_m on the surface, which satisfy

$$\boldsymbol{K} = \boldsymbol{N} \times \boldsymbol{H}_1, \tag{131}$$

$$\boldsymbol{K}_m = -\boldsymbol{N} \times \boldsymbol{E}_1, \tag{132}$$

$$\Sigma = \boldsymbol{N} \cdot \boldsymbol{D}_1, \tag{133}$$

$$\Sigma_m = \boldsymbol{N} \cdot \boldsymbol{B}_1, \tag{134}$$

where $\boldsymbol{N}$ is a unit normal vector, perpendicular to the surface. And then, we remove the primary wave source, and set the electromagnetic fields inside of the closed surface to zero, i.e. $\boldsymbol{E}_1 = 0$, $\boldsymbol{H}_1 = 0$, $\boldsymbol{D}_1 = 0$ and $\boldsymbol{B}_1 = 0$. Of course, the electromagnetic fields become discontinous at the surface, in this case.

Let us compare boundary conditions at the surface in two cases, one with the real continuous fields, and another with the fictitious discontinuous fields, together with the surface currents and the surface charges on the boundary. They are

$$\begin{array}{ll}
\textit{Continuous fields case} & \textit{Discontinuous fields case} \\
\boldsymbol{N} \times \boldsymbol{H}_2 = \boldsymbol{N} \times \boldsymbol{H}_1, & \boldsymbol{N} \times \boldsymbol{H}_2 = \boldsymbol{K}, \\
\boldsymbol{N} \times \boldsymbol{E}_2 = \boldsymbol{N} \times \boldsymbol{E}_1, & \boldsymbol{N} \times \boldsymbol{E}_2 = -\boldsymbol{K}_m, \\
\boldsymbol{N} \cdot \boldsymbol{D}_2 = \boldsymbol{N} \cdot \boldsymbol{D}_1, & \boldsymbol{N} \cdot \boldsymbol{D}_2 = \Sigma, \\
\boldsymbol{N} \cdot \boldsymbol{B}_2 = \boldsymbol{N} \cdot \boldsymbol{B}_1, & \boldsymbol{N} \cdot \boldsymbol{B}_2 = \Sigma_m.
\end{array} \tag{135}$$

As long as we consider these relations as boundary conditions at the closed surface for external solutions of the electromagnetic fields, the left side conditions and the right side conditions are just equivalent to each other, in view of eauations from (131) to (134). Therefore, the external fields must be identical for these two sets of boundary conditions. This implies that we can calculate the external fields, provided that the appropriate surface currents and surface charges, including both electric and magnetic, are given on the closed boundary surface.

The same statement must be valid for the aperture plane, if the aperture plane is the only part of a closed surface surrounding the primary wave source through which the electromagnetic fields flow out.

Of course, we do not observe any magnetic current and magnetic charge in the real world, at least at present. It is interesting to note that equations (124) and (125) would really hold, if hypothetical magnetic monopoles exist. Although search for magnetic monopoles is one of the most exciting Topics in the modern physics, no firm detection of monopoles has been reported in the present level of technology (see, for example, an interesting article on this matter by B. Schwarzschild in *Physics Today*, July, 2006). In the present discussion, we use the magnetic current and the magnetic charge as auxiliary concepts, which help us to fulfil the requirements at the aperture plane, but leave no trace in our final results, as we will see later.

2.5.3 Wave Equations with Magnetic Current and Magnetic Charge

How can we calculate external electromagnetic fields when the surface currents and the surface charges are given at a surface?

In order to answer to this question, we will first consider the wave generations from the electric current & charge system, which we have seen before, and from the magnetic current & charge system, which are new for us, in parallel.

Electric Current & Charge System *Magnetic Current & Charge System*

Maxwell equations

$$
\begin{aligned}
\nabla \times \boldsymbol{E} &= -\frac{\partial \boldsymbol{B}}{\partial t}, &\qquad \nabla \times \boldsymbol{E} &= -\boldsymbol{J}_m - \frac{\partial \boldsymbol{B}}{\partial t}\\
\nabla \times \boldsymbol{H} &= \boldsymbol{J} + \frac{\partial \boldsymbol{D}}{\partial t}, &\qquad \nabla \times \boldsymbol{H} &= \frac{\partial \boldsymbol{D}}{\partial t},\\
\nabla \cdot \boldsymbol{D} &= \rho, &\qquad \nabla \cdot \boldsymbol{D} &= 0,\\
\nabla \cdot \boldsymbol{B} &= 0, &\qquad \nabla \cdot \boldsymbol{B} &= \rho_m.
\end{aligned}
$$

Equation of continuity

$$
\frac{\partial \rho}{\partial t} + \nabla \cdot \boldsymbol{J} = 0, \qquad \frac{\partial \rho_m}{\partial t} + \nabla \cdot \boldsymbol{J}_m = 0.
$$

Electromagnetic potentials

$$
\begin{aligned}
\boldsymbol{B} &= \nabla \times \boldsymbol{A}, &\qquad \boldsymbol{D} &= -\nabla \times \boldsymbol{A}_m,\\
\boldsymbol{E} &= -\nabla \Phi - \frac{\partial \boldsymbol{A}}{\partial t}, &\qquad \boldsymbol{H} &= -\nabla \Phi_m - \frac{\partial \boldsymbol{A}_m}{\partial t}.
\end{aligned}
$$

Lorentz gauge

$$
\nabla \cdot \boldsymbol{A} + \epsilon\, \mu \frac{\partial \Phi}{\partial t} = 0, \qquad \nabla \cdot \boldsymbol{A}_m + \epsilon\, \mu \frac{\partial \Phi_m}{\partial t} = 0.
$$

Wave equations with source terms

$$
\begin{aligned}
\nabla^2 \boldsymbol{A} - \frac{1}{c^2}\frac{\partial^2 \boldsymbol{A}}{\partial t^2} &= -\mu\, \boldsymbol{J}, &\qquad \nabla^2 \boldsymbol{A}_m - \frac{1}{c^2}\frac{\partial^2 \boldsymbol{A}_m}{\partial t^2} &= -\epsilon\, \boldsymbol{J}_m,\\
\nabla^2 \Phi - \frac{1}{c^2}\frac{\partial^2 \Phi}{\partial t^2} &= -\frac{1}{\epsilon}\, \rho, &\qquad \nabla^2 \Phi_m - \frac{1}{c^2}\frac{\partial^2 \Phi_m}{\partial t^2} &= -\frac{1}{\mu}\, \rho.
\end{aligned}
$$

Retarded potentials with harmonically oscillating sources

$$
\begin{aligned}
\boldsymbol{A}(\boldsymbol{r},\, t) &= \boldsymbol{A}(\boldsymbol{r}) e^{-i\omega t}, &\qquad \boldsymbol{A}_m(\boldsymbol{r},\, t) &= \boldsymbol{A}_m(\boldsymbol{r}) e^{-i\omega t},\\
\boldsymbol{E}(\boldsymbol{r},\, t) &= \boldsymbol{E}(\boldsymbol{r}) e^{-i\omega t}, &\qquad \boldsymbol{H}(\boldsymbol{r},\, t) &= \boldsymbol{H}(\boldsymbol{r}) e^{-i\omega t}.
\end{aligned}
$$

($\boldsymbol{J} = 0$, $\boldsymbol{J}_m = 0$, $\rho = 0$, and $\rho_m = 0$, outside of the source region)

$$\boldsymbol{A}(\boldsymbol{r}) = \frac{\mu}{4\pi}\int \boldsymbol{J}(\boldsymbol{r}')\frac{e^{ik|\boldsymbol{r}-\boldsymbol{r}'|}}{|\,\boldsymbol{r}-\boldsymbol{r}'\,|}\,dV', \quad \boldsymbol{A}_m(\boldsymbol{r}) = \frac{\epsilon}{4\pi}\int \boldsymbol{J}_m(\boldsymbol{r}')\frac{e^{ik|\boldsymbol{r}-\boldsymbol{r}'|}}{|\,\boldsymbol{r}-\boldsymbol{r}'\,|}\,dV',$$

$$\boldsymbol{H}(\boldsymbol{r}) = \frac{1}{\mu}\nabla\times\boldsymbol{A}(\boldsymbol{r}), \qquad \boldsymbol{E}(\boldsymbol{r}) = -\frac{1}{\epsilon}\nabla\times\boldsymbol{A}_m(\boldsymbol{r}),$$

$$\boldsymbol{E}(\boldsymbol{r}) = i\frac{c}{k}\,\nabla\times(\nabla\times\boldsymbol{A}(\boldsymbol{r})), \qquad \boldsymbol{H}(\boldsymbol{r}) = i\frac{c}{k}\,\nabla\times(\nabla\times\boldsymbol{A}_m(\boldsymbol{r})).$$

Far field solutions in Fraunhofer region

$$\boldsymbol{T}(\boldsymbol{n}) = \int \boldsymbol{J}(\boldsymbol{r}')e^{-ik\boldsymbol{n}\cdot\boldsymbol{r}'}\,dV', \qquad \boldsymbol{T}_m(\boldsymbol{n}) = \int \boldsymbol{J}_m(\boldsymbol{r}')e^{-ik\boldsymbol{n}\cdot\boldsymbol{r}'}\,dV',$$

$$\boldsymbol{A}(\boldsymbol{r}) = \frac{\mu}{4\pi}\,\frac{e^{ikr}}{r}\,\boldsymbol{T}(\boldsymbol{n}), \qquad \boldsymbol{A}_m(\boldsymbol{r}) = \frac{\mu}{4\pi}\,\frac{e^{ikr}}{r}\,\boldsymbol{T}_m(\boldsymbol{n}),$$

$$\boldsymbol{H}(\boldsymbol{r}) = i\,\frac{1}{2\lambda}\,\frac{e^{ikr}}{r}\,\boldsymbol{n}\times\boldsymbol{T}(\boldsymbol{n}), \qquad \boldsymbol{E}(\boldsymbol{r}) = -i\,\frac{1}{2\lambda}\frac{e^{ikr}}{r}\,\boldsymbol{n}\times\boldsymbol{T}_m(\boldsymbol{n}),$$

$$\boldsymbol{E}(\boldsymbol{r}) = -i\,\frac{Z}{2\lambda}\frac{e^{ikr}}{r}\,\boldsymbol{n}\times[\boldsymbol{n}\times\boldsymbol{T}(\boldsymbol{n})], \quad \boldsymbol{H}(\boldsymbol{r}) = -i\,\frac{1}{2\lambda Z}\,\frac{e^{ikr}}{r}\,\boldsymbol{n}\times[\boldsymbol{n}\times\boldsymbol{T}_m(\boldsymbol{n})].$$

Since the vector and scalar potentials are related to each other by Lorentz gauge relations, we considered here wave generations for vector potentials $\boldsymbol{A}(\boldsymbol{r},\,t)$ and $\boldsymbol{A}_m(\boldsymbol{r},\,t)$ only, as we did before.

In a case when both the electric current and the magnetic current co–exist, the electromagnetic fields are expressed by the superposition of two sets of solutions shown above. In the far field region, for example, we have

$$\boldsymbol{H}(\boldsymbol{r}) = i\,\frac{1}{2\lambda}\frac{e^{ikr}}{r}\left\{\boldsymbol{n}\times\boldsymbol{T}(\boldsymbol{n}) - \frac{1}{Z}\,\boldsymbol{n}\times[\boldsymbol{n}\times\boldsymbol{T}_m(\boldsymbol{n})]\right\}, \tag{136}$$

$$\boldsymbol{E}(\boldsymbol{r}) = -i\,\frac{Z}{2\lambda}\frac{e^{ikr}}{r}\left\{\boldsymbol{n}\times[\boldsymbol{n}\times\boldsymbol{T}(\boldsymbol{n})] + \frac{1}{Z}\,\boldsymbol{n}\times\boldsymbol{T}_m(\boldsymbol{n})\right\}. \tag{137}$$

For these spherical waves in the far field region, we again obtain:

$$\boldsymbol{n}\cdot\boldsymbol{H} = 0, \quad \text{and} \quad \boldsymbol{n}\cdot\boldsymbol{E} = 0, \quad \text{(transversal wave)},$$

and

$$\boldsymbol{E} = -Z\,\boldsymbol{n}\times\boldsymbol{H}, \quad \text{and} \quad \boldsymbol{H} = \frac{1}{Z}\,\boldsymbol{n}\times\boldsymbol{E}, \quad (\boldsymbol{E},\,\boldsymbol{H}\ \text{orthogonal}).$$

2.5.4 Radio Wave Transmission from a Surface

Now, how to describe the generation of electromagnetic waves from the surface electronic current $\boldsymbol{K}$ and the surface magnetic current $\boldsymbol{K}_m$ on a surface of the secondary wave source?

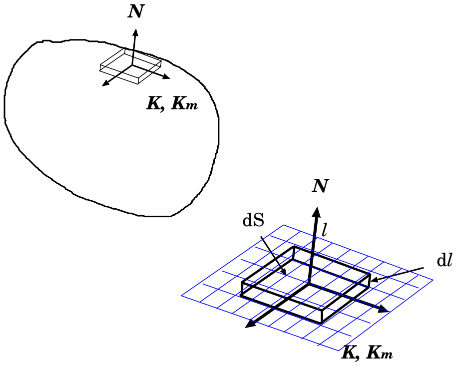

Figure 46: A volume density of a surface density.

For this purpose, let us consider "a volume density of a surface density" on a boundary surface. Let a unit normal vector, perpendicular to the boundary sourface, be $\boldsymbol{N}$. Let us consider a local rectangular coordinate system at a certain point on the surface, which are composed of an axis parallel to $\boldsymbol{N}$ and other two axes in a plane tangential to the boundary surface. If we denote the length along $\boldsymbol{N}$ direction as l, and an infinitesimal surface area element on the boundary as $d\mathcal{S}$, then we can express an infinitesimal volume element at the boundary as

$$dV = dl\, d\mathcal{S}.$$

Then, we can express the "volume densities" $\boldsymbol{J}$ and $\boldsymbol{J}_m$ of the surface densities $\boldsymbol{K}$ and $\boldsymbol{K}_m$ as

$$\begin{aligned} \boldsymbol{J} &= \boldsymbol{K}\,\delta(l - l_0), \\ \boldsymbol{J}_m &= \boldsymbol{K}_m\,\delta(l - l_0), \end{aligned} \tag{138}$$

where $l = l_0$ corresponds to the boundary surface, and $\delta(x)$ is the delta function. Indeed, if we integrate the volume densities through a small volume $\Delta V = \Delta l\, \Delta\mathcal{S}$, containing a part of the boundary surface $l = l_0$, we have

$$\begin{aligned} \int\limits_{\Delta V} \boldsymbol{J}\, dV &= \int\limits_{\Delta V} \boldsymbol{K}\delta(l - l_0)\, dl\, d\mathcal{S} = \int\limits_{\Delta\mathcal{S}} \boldsymbol{K}\, d\mathcal{S}, \\ \int\limits_{\Delta V} \boldsymbol{J}_m\, dV &= \int\limits_{\Delta V} \boldsymbol{K}_m\delta(l - l_0)\, dl\, d\mathcal{S} = \int\limits_{\Delta\mathcal{S}} \boldsymbol{K}_m\, d\mathcal{S}, \end{aligned} \tag{139}$$

as expected.

Therefore, using equations (138) at every small element of the boundary surface, we can express the retarded vector potentials generated by the currents localized at the boundary as

$$\boldsymbol{A}(\boldsymbol{r},\,t) = \frac{\mu}{4\pi}\,e^{-i\omega t}\int \boldsymbol{J}(\boldsymbol{r}')\,\frac{e^{ik|\boldsymbol{r}-\boldsymbol{r}'|}}{|\,\boldsymbol{r}-\boldsymbol{r}'\,|}\,dV' = \frac{\mu}{4\pi}\,e^{-i\omega t}\oint \boldsymbol{K}(\boldsymbol{r}')\,\frac{e^{ik|\boldsymbol{r}-\boldsymbol{r}'|}}{|\,\boldsymbol{r}-\boldsymbol{r}'\,|}\,d\mathcal{S}',$$

$$\boldsymbol{A}_m(\boldsymbol{r},\,t) = \frac{\mu}{4\pi}\,e^{-i\omega t}\int \boldsymbol{J}_m(\boldsymbol{r}')\,\frac{e^{ik|\boldsymbol{r}-\boldsymbol{r}'|}}{|\,\boldsymbol{r}-\boldsymbol{r}'\,|}\,dV' = \frac{\mu}{4\pi}\,e^{-i\omega t}\oint \boldsymbol{K}_m(\boldsymbol{r}')\,\frac{e^{ik|\boldsymbol{r}-\boldsymbol{r}'|}}{|\,\boldsymbol{r}-\boldsymbol{r}'\,|}\,d\mathcal{S}', \tag{140}$$

where surface integrals are taken over the whole boundary surface.

For the far field solutions, we have

$$\boldsymbol{T}(\boldsymbol{n}) = \oint \boldsymbol{K}(\boldsymbol{r}')e^{-ik\boldsymbol{n}\cdot\boldsymbol{r}'}\,d\mathcal{S}',$$

$$\boldsymbol{T}_m(\boldsymbol{n}) = \oint \boldsymbol{K}_m(\boldsymbol{r}')e^{-ik\boldsymbol{n}\cdot\boldsymbol{r}'}\,d\mathcal{S}', \tag{141}$$

$$\boldsymbol{A}(\boldsymbol{r},\,t) = \frac{\mu}{4\pi}\,\frac{e^{i(kr-\omega t)}}{r}\,\boldsymbol{T}(\boldsymbol{n}),$$

$$\boldsymbol{A}_m(\boldsymbol{r},\,t) = \frac{\mu}{4\pi}\,\frac{e^{i(kr-\omega t)}}{r}\,\boldsymbol{T}_m(\boldsymbol{n}), \tag{142}$$

and

$$\boldsymbol{H}(\boldsymbol{r},\,t) = i\,\frac{1}{2\lambda}\frac{e^{i(kr-\omega t)}}{r}\left\{\boldsymbol{n}\times\boldsymbol{T}(\boldsymbol{n}) - \frac{1}{Z}\,\boldsymbol{n}\times[\boldsymbol{n}\times\boldsymbol{T}_m(\boldsymbol{n})]\right\},$$

$$\boldsymbol{E}(\boldsymbol{r},\,t) = -i\,\frac{Z}{2\lambda}\frac{e^{i(kr-\omega t)}}{r}\left\{\boldsymbol{n}\times[\boldsymbol{n}\times\boldsymbol{T}(\boldsymbol{n})] + \frac{1}{Z}\,\boldsymbol{n}\times\boldsymbol{T}_m(\boldsymbol{n})\right\}, \tag{143}$$

where $\boldsymbol{n}$ is a unit vector along the direction of the propagation of the spherical wave, as before.

Comparing these equations with equations (136) and (137), we see that their forms are the same, and only difference is in the replacement of the volume integrals in the expressions of $\boldsymbol{T}(\boldsymbol{n})$ and $\boldsymbol{T}_m(\boldsymbol{n})$ by the surface integralas in equations (141).

Remembering here that the surface electric current and the surface magnetic current must equal to

$$\boldsymbol{K} = \boldsymbol{N}\times\boldsymbol{H}_1,$$

$$\boldsymbol{K}_m = -\boldsymbol{N}\times\boldsymbol{E}_1,$$

on the boundary surface with a unit normal vector $\boldsymbol{N}$, in view of equations (131) and (132), we can rewrite $\boldsymbol{T}(\boldsymbol{n})$ and $\boldsymbol{T}_m(\boldsymbol{n})$ in equations (141) as

$$\boldsymbol{T}(\boldsymbol{n}) = \oint \boldsymbol{K}(\boldsymbol{r}')e^{-ik\boldsymbol{n}\cdot\boldsymbol{r}'}\,d\mathcal{S}' = \oint \boldsymbol{N}\times\boldsymbol{H}_1(\boldsymbol{r}')e^{-ik\boldsymbol{n}\cdot\boldsymbol{r}'}\,d\mathcal{S}',$$

$$\boldsymbol{T}_m(\boldsymbol{n}) = \oint \boldsymbol{K}_m(\boldsymbol{r}')e^{-ik\boldsymbol{n}\cdot\boldsymbol{r}'}\,d\mathcal{S}' = -\oint \boldsymbol{N}\times\boldsymbol{E}_1(\boldsymbol{r}')e^{-ik\boldsymbol{n}\cdot\boldsymbol{r}'}\,d\mathcal{S}'. \tag{144}$$

Now we have no longer the fictitiuous magnetic current in the right hand side of equation (144), and the external electromagnetic fields in equations (143) are completely determined by the electromagnetic fields on the boundary surface. This is a clear expression of Huygens and Fresnel's principle that the wave front becomes the wave source.

2.5.5 Radio Wave Transmission from an Aperture Antenna

Let us consider an aperture antenna, with an aperture plane much larger in size than the wavelength. It is then possible to control the primary wave source in such a way that harmonically oscillating electromagnetic fields on the aperture plane, $\boldsymbol{H}_a$ and $\boldsymbol{E}_a$, satisfy conditions:

$$\begin{aligned}
&\boldsymbol{N}\cdot\boldsymbol{H}_a = 0, \quad \boldsymbol{N}\cdot\boldsymbol{E}_a = 0, \quad \text{(parallel to the aperture plane)},\\
&\text{and}\\
&\boldsymbol{H}_a = \frac{1}{Z}\boldsymbol{N}\times\boldsymbol{E}_a, \quad \text{(mutually orthogonal)}, \qquad (145)
\end{aligned}$$

where $\boldsymbol{N}$ is the unit normal vector, perpendicular to the aperture plane (Figure 47). This corresponds to the case when the electromagnetic fields on the aperture plane are close to plane waves propagating towards the direction perpendicular to the aperture plane.

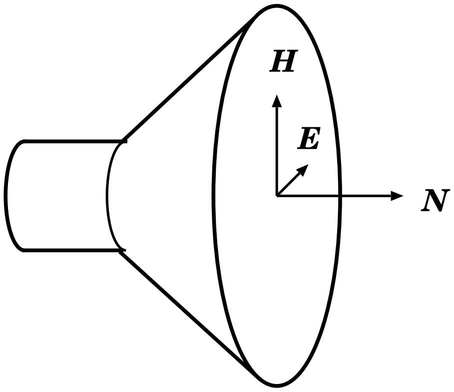

Figure 47: Electromagnetic field on an aperture plane.

We now apply these relations to calculate directional pattern vectors $\boldsymbol{T}(\boldsymbol{n})$ and $\boldsymbol{T}_m(\boldsymbol{n})$ in equations (144). Generally speaking, the surface integrals in equations (144) must be taken over a closed surface, surrounding the primary wave source. However, as we saw earlier, the closed surface can be replaced by the aperture plane $\mathcal{A}$, if the aperture plane is the only part of a closed surface through which the electromagnetic fields flow out. This condition is usually fulfilled in aperture antennas with aperture sizes much larger than the wavelengths (Figure 48).

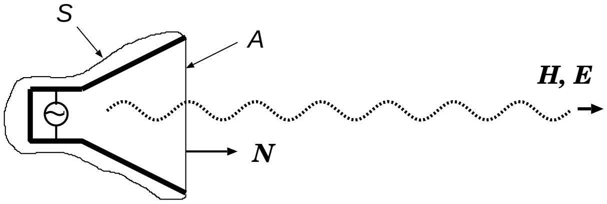

Figure 48: In an aperture antenna with aperture size much larger than the wavelength, most of the generated electromagnetic fields flow out through the aperture plane $\mathcal{A}$. In this respect, the contribution of other portion $\mathcal{S}$ of the closed surface, surrounding the antenna, is negligibly small compared with that of the aperture plane $\mathcal{A}$.

Therefore, we can rewrite equations (144) as

$$\begin{aligned} \boldsymbol{T}(\boldsymbol{n}) &= \int_{\mathcal{A}} \boldsymbol{N} \times \boldsymbol{H}_a \, e^{-ik\boldsymbol{n}\cdot\boldsymbol{r}'} \, d\mathcal{S}' = \frac{1}{Z} \int_{\mathcal{A}} \boldsymbol{N} \times (\boldsymbol{N} \times \boldsymbol{E}_a) \, e^{-ik\boldsymbol{n}\cdot\boldsymbol{r}'} \, d\mathcal{S}', \\ \boldsymbol{T}_m(\boldsymbol{n}) &= -\int_{\mathcal{A}} \boldsymbol{N} \times \boldsymbol{E}_a \, e^{-ik\boldsymbol{n}\cdot\boldsymbol{r}'} \, d\mathcal{S}', \end{aligned} \tag{146}$$

where, in the upper equation, we used an assumed property of the electromagnetic fields on the aperture plane, given in equations (145).

Now, we obtain the far field solution of the electric field $\boldsymbol{E}(\boldsymbol{r},\, t)$, transmitted from an aperture antenna, by inserting equations (146) into one of the equations (143) and using one of the conditions on the aperture plane, given in equations (145):

$$\boldsymbol{E}(\boldsymbol{r},\, t) = -i\,\frac{1}{2\lambda}\frac{e^{i(kr-\omega t)}}{r} \int_{\mathcal{A}} \boldsymbol{n} \times \{\boldsymbol{n} \times [\boldsymbol{N} \times (\boldsymbol{N} \times \boldsymbol{E}_a)] - \boldsymbol{N} \times \boldsymbol{E}_a\} \, e^{-ik\boldsymbol{n}\cdot\boldsymbol{r}'} \, d\mathcal{S}'. \tag{147}$$

For large aperture antennas, the electric field in the far field region has finite strength only when the direction $\boldsymbol{n}$ is close enough to the direction $\boldsymbol{N}$ perpendicular to the aperture plane. Therefore, we approximately take $\boldsymbol{n} = \boldsymbol{N}$ everywhere, except for in the argument of the exponential function. Then, using a formula of the vector algebra in equation (14), we obtain an equation:

$$\boldsymbol{E}(\boldsymbol{r},\, t) = -i\,\frac{1}{\lambda}\frac{e^{i(kr-\omega t)}}{r} \int_{\mathcal{A}} \boldsymbol{E}_a(\boldsymbol{r}') \, e^{-ik\boldsymbol{n}\cdot\boldsymbol{r}'} \, d\mathcal{S}', \tag{148}$$

which describes a relationship between electric fields on an aperture plane and in a spherical wave in the far field region.

2.5.6 Aperture Illumination and Field Pattern of an Aperture Antenna

In equation (148), the directional characteristics of the aperture antenna are solely determined by the integral:

$$\int_{\mathcal{A}} \boldsymbol{E}_a(\boldsymbol{r}')\, e^{-ik\boldsymbol{n}\cdot\boldsymbol{r}'}\, d\mathcal{S}'.$$

Regarding the distribution of the electric field $\boldsymbol{E}_a(\boldsymbol{r}')$ on the aperture plane,

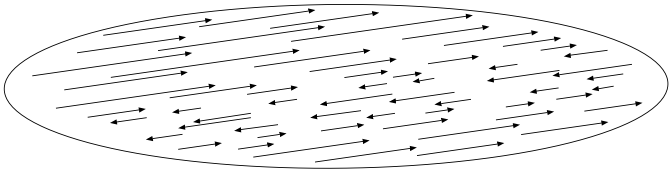

Figure 49: Harmonically oscillating electric field on the aperture plane, keeping a common field direction.

we assume that the electric field is parallel, and keep a constant direction, everywhere (Figure 49). This corresponds to a case of the linearly polarized oscillation. If the actual field distribution is a superposition of different polarization components, for example, a circularly polarized oscillation, which can be decomposed into two linearly polarized oscillations along two mutually perpendicular directions, this discussion is valid for a linear polarization component along a certain direction.

Let us express, in this case, the electric field on the aperture plane as

$$\boldsymbol{E}_a(\boldsymbol{r}') = \boldsymbol{E}_0\, g(\boldsymbol{r}'), \tag{149}$$

where $\boldsymbol{E}_0$ is a constant real vector, and $g(\boldsymbol{r}')$ is a complex (in general) function of the position on the aperture plane. The function $g(\boldsymbol{r}')$ is called **"aperture illumination"**. This shows how the primary wave source (for example, a feed horn), like a flashlight, "illuminates" the aperture plane. Using the aperture illumination, we can rewrite equation (148) in a form:

$$\boldsymbol{E}(\boldsymbol{r},\, t) = -i\, \boldsymbol{E}_0\, \lambda\, \frac{e^{i(kr-\omega t)}}{r}\, f(\boldsymbol{n}),$$

where

$$f(\boldsymbol{n}) = \int_{\mathcal{A}} g(\boldsymbol{r}')\, e^{-ik\boldsymbol{n}\cdot\boldsymbol{r}'}\, \frac{d\mathcal{S}'}{\lambda^2}. \tag{150}$$

The non–dimensional function $f(\boldsymbol{n})$ is the field pattern of the aperture antenna in the far field region, which shows the directional characteristics of the generated electric field.

Taking into account that $k = 2\pi/\lambda$, and formally extending the area of the integration to an infinite plane, by just assuming that $g(\boldsymbol{r}') = 0$ outside of the aperture plane $\mathcal{A}$, we obtain, from equation (150),

$$f(\boldsymbol{n}) = \int g(\boldsymbol{r}')\, e^{-i2\pi \boldsymbol{n}\cdot\frac{\boldsymbol{r}'}{\lambda}}\, \frac{d\mathcal{S}'}{\lambda^2}. \tag{151}$$

This equation shows that the aperture illumination $g(\boldsymbol{r}')$ and the field pattern in the far field region $f(\boldsymbol{n})$ of the aperture antenna form **a two dimensional spatial Fourier transform pair**.

2.5.7 Power Pattern of an Aperture Antenna

We can now derive the power pattern of an aperture antenna by calculating time–averaged Poynting vector, as we did for the Hertz dipole.

We saw in equation (97) that the Poynting vector $\boldsymbol{S}$ of the spherical wave is described as

$$\boldsymbol{S} = \boldsymbol{E}_r \times \boldsymbol{H}_r = \frac{1}{Z}\, \boldsymbol{n} \mid \boldsymbol{E}_r \mid^2,$$

where $\boldsymbol{E}_r$ is the real part of the complex form of the electric field, which represents the real physical quantity. Introducing the amplitude $\mid f(\boldsymbol{n}) \mid$ and the phase ϕ of the complex field pattern $f(\boldsymbol{n})$, we have

$$f(\boldsymbol{n}) = \mid f(\boldsymbol{n}) \mid\, e^{i\phi}. \tag{152}$$

Then, from equation (150), we obtain

$$\boldsymbol{E}_r = \Re \boldsymbol{E}(\boldsymbol{r},\, t) = \boldsymbol{E}_0\, \lambda\, \frac{\mid f(\boldsymbol{n}) \mid}{r}\, \sin(kr - \omega t + \phi). \tag{153}$$

Since the time–averaged squared sine function always gives

$$\overline{\sin^2(kr - \omega t + \phi)} = \frac{1}{2},$$

where $\overline{(\ )}$ denotes time averaging, we have

$$\overline{\mid \boldsymbol{S} \mid} = \frac{1}{2Z} \mid \boldsymbol{E}_0 \mid^2 \frac{\lambda^2}{r^2} \mid f(\boldsymbol{n}) \mid^2. \tag{154}$$

The non–dimensional term $\mid f(\boldsymbol{n}) \mid^2$ in equation (154) characterizes directional pattern of the transmitted power, and can be regarded as power pattern $P(\boldsymbol{n})$ in the far field region of an aperture antenna, though sometimes

$\overline{| \boldsymbol{S} |}$ itself is called power pattern. In practice, "**normalized power pattern**" $P_n(\boldsymbol{n})$, which is obtained by dividing the power pattern by its maximum value, is used more frequently than the power pattern. Thus, the normalized power pattern in the far field region of an aperture antenna is given by a formula:

$$P_n(\boldsymbol{n}) = \frac{P(\boldsymbol{n})}{P_{max}} = \frac{|\, f(\boldsymbol{n})\, |^2}{|\, f_{max}\, |^2}, \tag{155}$$

which is not affected by the difference of the two definitions of the power pattern, mentioned above.

2.5.8 Main Lobe, Sidelobes, HPBW and BWFN

A typical normalized power pattern of an aperture antenna is illustrated in Figure 50. Left panel shows a rectangular plot, with horizontal axis showing angle from the "aperture axis" in radian. The aperture axis is an axis perpendicular to the aperture plane, which is usually parallel to the "beam axis", i.e., the direction of the maximum power pattern. Right panel shows a polar plot, which gives more realistic view of the pattern shape.

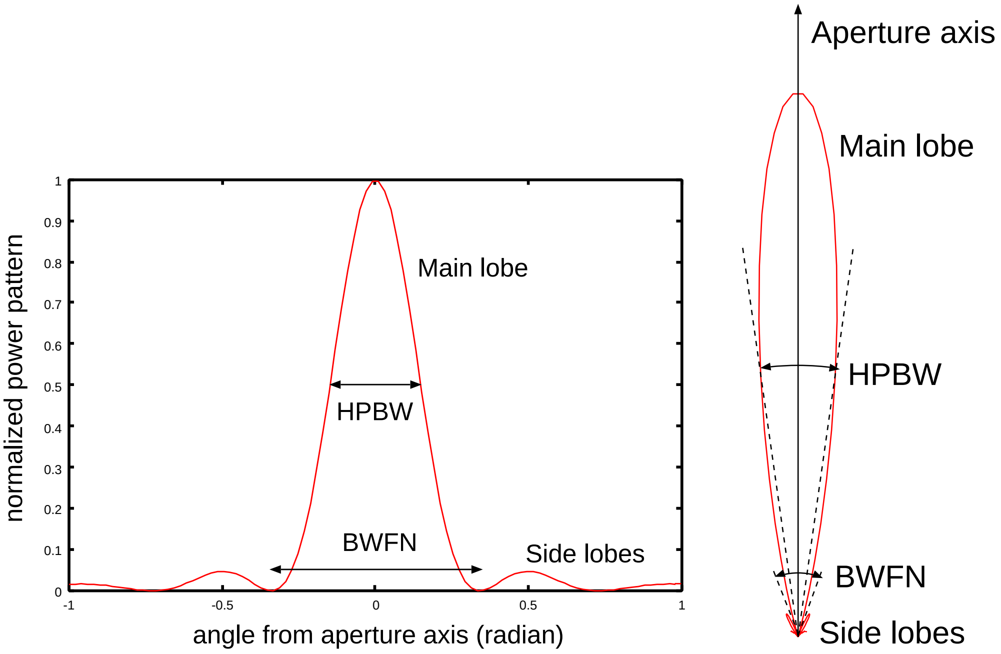

Figure 50: A normalized power pattern of an aperture antenna in a rectangular plot (Left) and in a polar plot (Right).

In both panels, a large **main lobe** (or **main beam**) is prominent. There are small **sidelobes** in both sides of the main lobe.

Two quantities are frequently used as measures of the width of the main lobe, which is an important characteristic of an aperture antenna. One is **"full half power beam width", or HPBW**, which stands for the twice of the angle of a direction, where the power pattern takes a half of the maximum value, from the aperture axis. Another is **"full beam width between first nulles", or BWFN**, which stands for the twice of the angle of a direction, where the power pattern drops to zero between the main lobe and the first sidelobe, from the aperture axis (Figure 50).

2.5.9 Uniformly Illuminated Rectangular Aperture Antenna

Let us consider, as one of the simplest examples of aperture antennas, a rectangular aperture antenna with an aperture plane located in xy–plane, which is uniformely illuminated as:

$$g(x,y) = \begin{cases} g & \text{for } \mid x \mid \leq \frac{L_x}{2}, \ \text{ and } \ \mid y \mid \leq \frac{L_y}{2}, \\ 0 & \text{otherwise,} \end{cases} \tag{156}$$

where g is a real constant (see Figure 51).

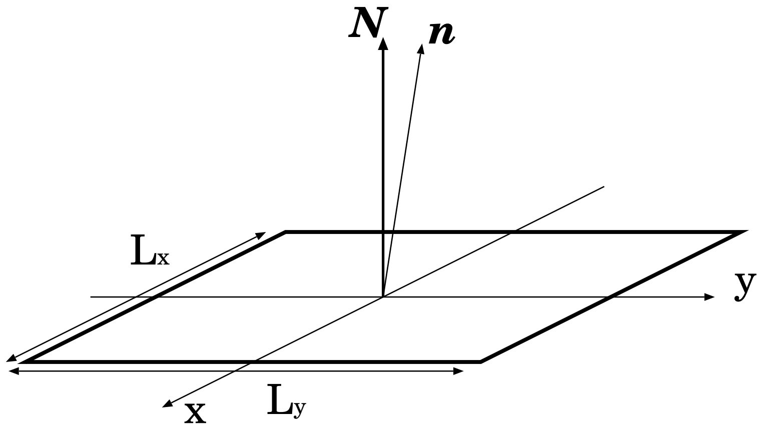

Figure 51: A rectangular aperture antenna.

From equation (151), the field pattern in the far field region $f(\boldsymbol{n})$, in a direction of a unit vector $\boldsymbol{n}$, with components n_x and n_y in the xy–plane, is expressed in this case as

$$f(\boldsymbol{n}) = \iint g(x,y)e^{-i2\pi(n_x x+n_y y)/\lambda}\frac{dx}{\lambda}\frac{dy}{\lambda} = g\int_{-\frac{L_y}{2}}^{\frac{L_y}{2}}\int_{-\frac{L_x}{2}}^{\frac{L_x}{2}} e^{-i2\pi(n_x x+n_y y)/\lambda}\frac{dx}{\lambda}\frac{dy}{\lambda}$$
$$= g\,\frac{\sin(\pi n_x L_x/\lambda)}{\pi n_x}\frac{\sin(\pi n_y L_y/\lambda)}{\pi n_y}. \tag{157}$$

Since this function takes the maximum value $(L_x/\lambda)(L_y/\lambda)$ when $\boldsymbol{n} = \boldsymbol{N}$ (or $n_x = 0,\ n_y = 0$), where $\boldsymbol{N}$ is the unit vector normal to the aperture plane, the normalized power pattern as given in equation (155), is

$$P_n(\boldsymbol{n}) = \frac{\mid f(\boldsymbol{n})\mid^2}{\mid f_{max}\mid^2} = \left[\frac{\sin(\pi n_x L_x/\lambda)}{\pi n_x L_x/\lambda}\frac{\sin(\pi n_y L_y/\lambda)}{\pi n_y L_y/\lambda}\right]^2. \tag{158}$$

Full beam width between first nulls and full half power beam width of such an antenna are

$$\mathrm{BWFN} = 2\,(\frac{\lambda}{L_x}\ \text{ and }\ \frac{\lambda}{L_y})\ \ (\mathrm{rad})\ = 114.^\circ 6\,(\frac{\lambda}{L_x}\ \text{ and }\ \frac{\lambda}{L_y}),$$

and

$$\mathrm{HPBW} = 0.88\,(\frac{\lambda}{L_x}\ \text{ and }\ \frac{\lambda}{L_y})\ \ (\mathrm{rad})\ = 50.^\circ 4\,(\frac{\lambda}{L_x}\ \text{ and }\ \frac{\lambda}{L_y}), \tag{159}$$

respectively.

2.5.10 Circular Aperture Antenna

Now let us consider a circular aperture antenna with diameter D, as shown in Figure 52. Let us assume an axisymmetric illumination around the aperture axis, which is directed towards a unit vector $\boldsymbol{N}$, perpendicular to the aperture plane, and let us choose a coordinate system, in which a directional unit vector $\boldsymbol{n}$ and a radius vector $\boldsymbol{r}'$ within the aperture plane are given as

$$\boldsymbol{n} \cong (-u,\ 0,\ 1), \tag{160}$$

and

$$\boldsymbol{r}' = (\lambda\rho\cos\phi,\ \lambda\rho\sin\phi,\ 0), \tag{161}$$

where λ is the wavelength, and ρ and ϕ are radial and azimuthal variables.

If we denote the axisymmetric aperture illumination as

$$g(\boldsymbol{r}') = g(\rho), \tag{162}$$

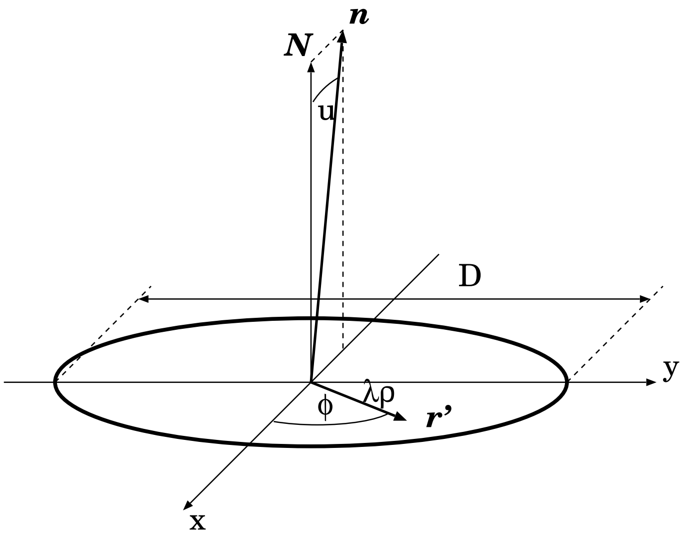

Figure 52: A circular aperture antenna.

then, according to equation (151), the field pattern at the direction $\boldsymbol{n}$ is described in a form:

$$f(u) = \int_0^{2\pi} \int_0^{\infty} g(\rho)\, e^{i2\pi u\rho\cos\phi} \rho d\rho d\phi. \tag{163}$$

Since Bessel function of zeroth order $J_0(z)$ is defined as

$$J_0(z) = \frac{1}{2\pi} \int_0^{2\pi} e^{iz\cos\phi} d\phi, \tag{164}$$

the field pattern is given by

$$f(u) = 2\pi \int_0^{\infty} g(\rho) J_0(2\pi u\rho) \rho d\rho. \tag{165}$$

Therefore, according to equation (155), the normalized power pattern is

$$P_n(u) = \left[\frac{\int_0^{\infty} g(\rho) J_0(2\pi u\rho) \rho d\rho}{\int_0^{\infty} g(\rho) \rho d\rho} \right]^2. \tag{166}$$

We consider the simplest case of uniform illumination:

$$g(\rho) = \begin{cases} g & \text{for } \rho \le \frac{D}{2\lambda}, \\ 0 & \text{otherwise,} \end{cases} \tag{167}$$

where g is a real constant. Then the normalized power pattern in equation (166) is reduced to

$$P_n(u) = \left[\frac{\int\limits_0^{D/2\lambda} J_0(2\pi u\rho)\rho d\rho}{\int\limits_0^{D/2\lambda} \rho d\rho} \right]^2 = \left[\frac{2\lambda^2}{\pi^2 u^2 D^2} \int\limits_0^{\pi u D/\lambda} J_0(z) z dz \right]^2 . \tag{168}$$

From a recurrence formula of Bessel function of m–th order:

$$\frac{d}{dz}\{z^m J_m(z)\} = z^m J_{m-1}(z), \tag{169}$$

we have

$$x^m J_m(x) = \int\limits_0^x z^m J_{m-1}(z) dz,$$

and hence, in a particular case of $m = 1$,

$$\int\limits_0^x J_0(z) z dz = x J_1(x).$$

Inserting this formula into equation (168), we obtain the normalized power pattern of the uniformly illuminated circular aperture antenna in the far field region:

$$P_n(u) = \left[\frac{2\lambda}{\pi u D} J_1\left(\frac{\pi u D}{\lambda}\right) \right]^2 . \tag{170}$$

Figures 53 and 54 show normalized power patterns (left pannel) and field amplitude pattern $\mid f(u) \mid / \mid f_{max} \mid$ (right panel) of a uniformly illuminated circular aperture antenna in rectangular and polar plots. In the rectangular plots (Figure 53), the horizontal axes show offset angle from the aperture axis normalized by λ/D.

Figure 55 shows three–dimensional rectangular and polar plots of the normalized power pattern and the field amplitude pattern of the uniformly illuminated circular aperture antenna.

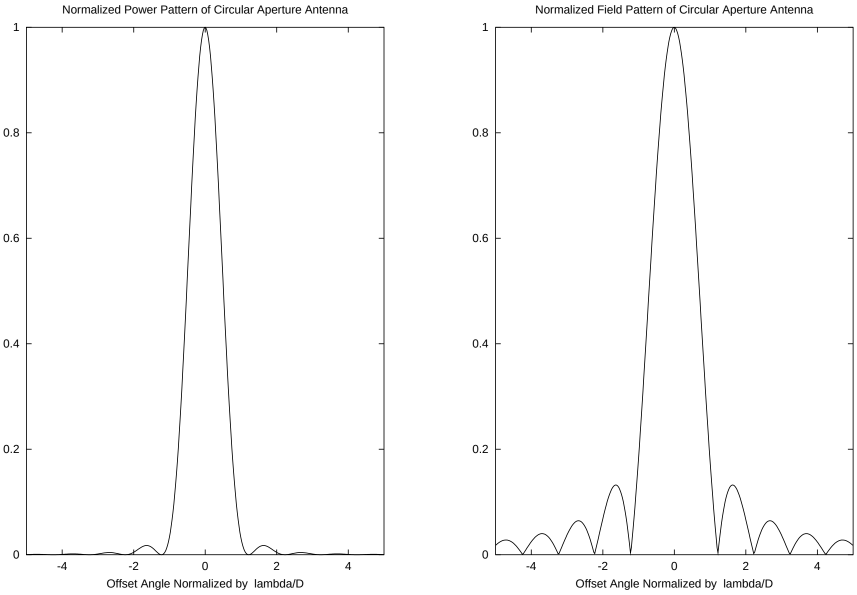

Figure 53: Rectangular plots of normalized power pattern (Left) and field amplitude pattern (Right) of a uniformly illuminated circular aperture antenna. Horizontal axes show offset angle from the aperture axis normalized by λ/D.

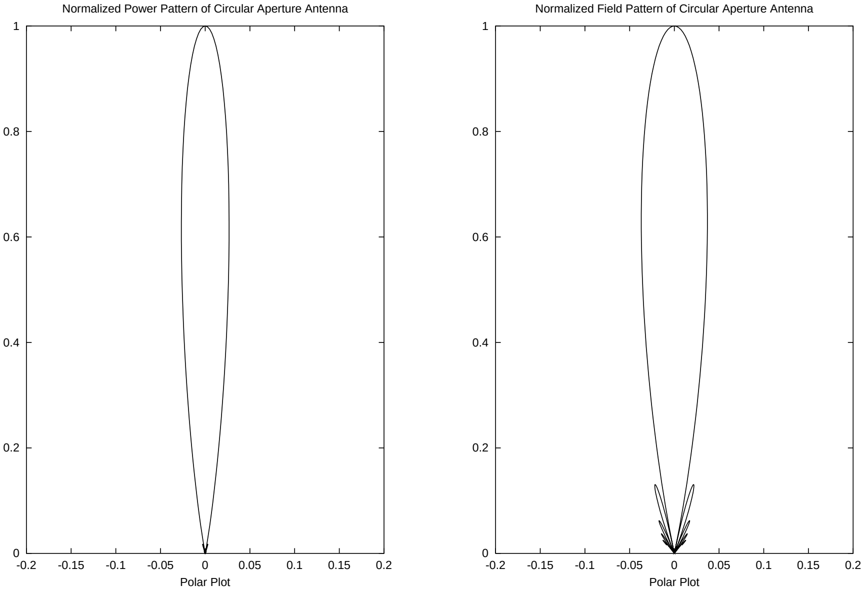

Figure 54: Polar plots of normalized power pattern (Left) and field amplitude pattern (Right) of a uniformly illuminated circular aperture antenna.

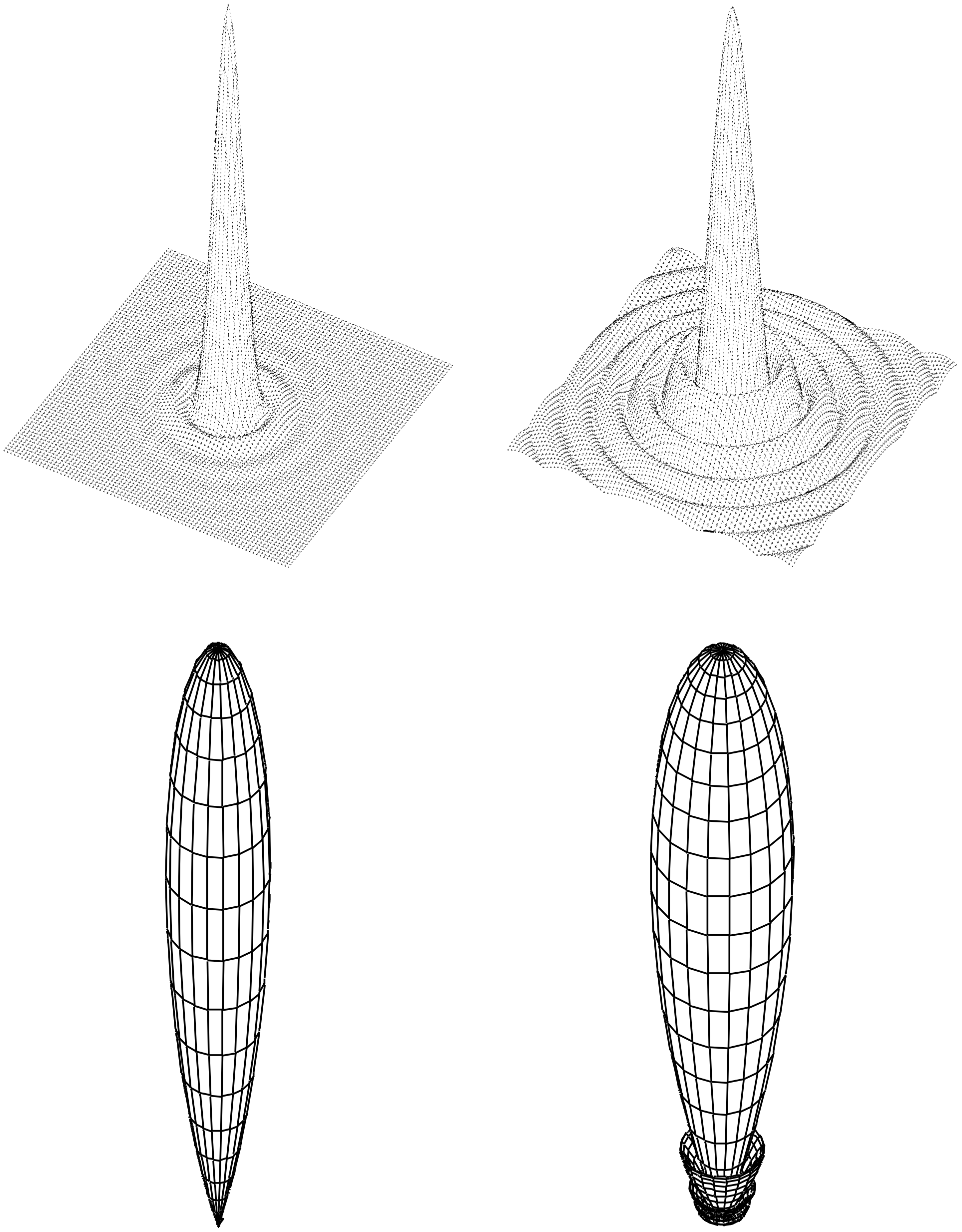

Figure 55: Three–dimensional rectangular (Top) and polar (Bottom) plots of the normalized power pattern (Left) and the field amplitude pattern (Right) of a uniformly illuminated circular aperture antenna. Sidelobes are hardly seen in the polar plot of the normalized power pattern.

From numerical values of Bessel function $J_1(x)$, we obtain full beam width between first nulls and full half power beam width of the uniformly illuminated circular aperture antenna as

$$\mathrm{BWFN} = 2.44\,\frac{\lambda}{D}\,(\mathrm{rad}) \;=\; 140^\circ\,\frac{\lambda}{D},$$

and

$$\mathrm{HPBW} = 1.02\,\frac{\lambda}{D}\,(\mathrm{rad}) \;=\; 58.^\circ 4\,\frac{\lambda}{D}, \tag{171}$$

respectively.

2.6 Beam Patters of Aperture Antennas

So far, we have discussed and derived field and power patterns of aperture antennas in the transmission mode. Because of the equivalence of field patterns in transmission and reception, which we saw earlier, the field transmission pattern must be the same with the field reception pattern. In the reception case, the field pattern is often called 'voltage reception pattern', as describing the magnitude of the received voltage as a function of the antenna direction.

Since the transmitted power is proportional to the square of the electric field, and the received power is proportional to the square of the received voltage, the power reception pattern must also be equivalent to the power transmission pattern.

The antenna beam pattern is a general concept, which means either the power pattern or the field (or voltage–reception) pattern, depending on the context.

2.6.1 Antenna–Fixed Coordinate System

For further convenience, let us introduce an 'antenna–fixed coordinate system' for a paraboloidal antenna.

As the origin of the coordinate system, we choose the center of the paraboloid surface of the main reflector. Then, let us take the aperture axis, or the symmetry axis of the paraboloid, as the polar axis z, and choose the x and y axes towards directions perpendicular and parallel to the elevation axis, as shown in Figure 56. Finally, let us denote a given direction in the sky by an angle from the polar axis θ, and an azimuthal angle ϕ measured from the x–axis towards the y–axis.

Then, the field pattern and power pattern can be described as functions of these angles, such as $f(\theta, \phi)$, and $P(\theta, \phi)$. For example, we can define the power pattern in the reception case as the power $P(\theta, \phi)$ received by an

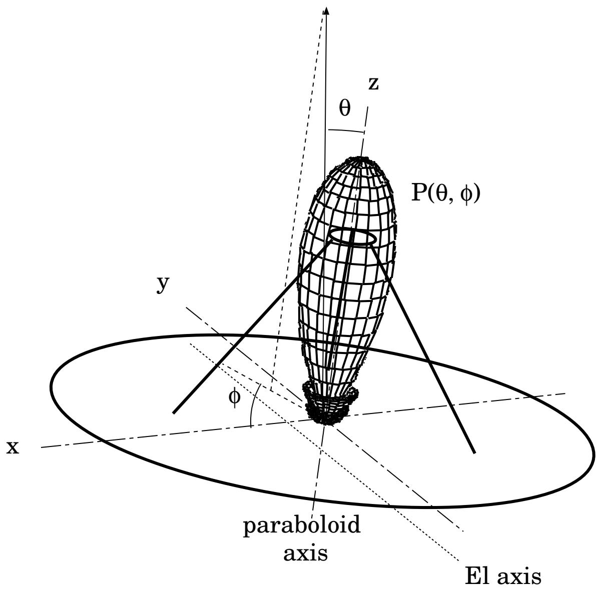

Figure 56: Antenna–fixed coordinate system.

antenna from a point–like source of unit flux density at direction θ and ϕ. Similarly to the transmission case, the normalized power pattern is given by

$$P_n(\theta,\phi) = \frac{P(\theta,\phi)}{P_{max}} = \frac{\mid f(\theta,\phi) \mid^2}{\mid f_{max} \mid^2}. \tag{172}$$

2.6.2 A Useful Formula: HPBW $\approx \lambda/D$

From the two simple examples of the aperture antennas, which we saw earlier, it is evident that HPBW $\cong \lambda/D$ (see equations (159) and (171)). This is generally valid for a wide variety of aperture antennas with realistic aperture illuminations. Therefore, the ratio λ/D is often used as a measure of the beam width, or the angular resolution, of radio telescope antennas (table 1).

Of course, it is not an easy task to direct a huge radio telescope with 45 m diameter, say, towards an astronomical object with an accuracy much better than 0.0025 degree!

2.6.3 Distance to Fraunhofer Region

As we saw earlier, the antenna beam pattern is a function of distance from the antenna in the Fresnel region, or in the near field, as schematically shown

diameter D	wavelength λ	frequency ν	λ/D
6 m	37.5 mm	8 GHz	0.°36
10 m	7.0 mm	43 GHz	0.°04
21 m	2.3 mm	129 GHz	0.°0063
45 m	2.0 mm	150 GHz	0.°0025

Table 1: Beam widths ($\lambda/D \approx$ HPBW) of antennas with different aperture diameters, observing at different frequencies.

in Figure 57 (Adachi, Electromagnetic Wave Engineering, 1985).

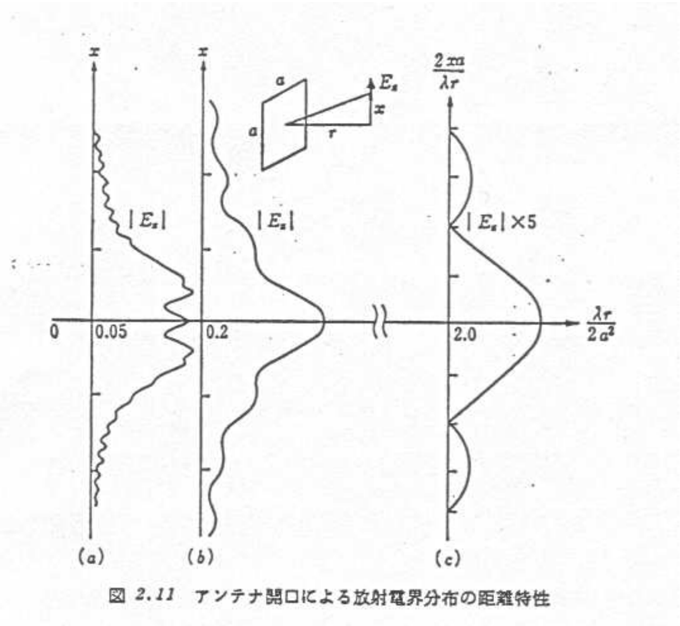

Figure 57: Variation of the electric field amplitude pattern with distance from the antenna (Adachi, Electromagnetic Wave Engineering, 1985).

However, in the Fraunhofer region, or in the far field, the beam pattern becomes almost independent of the distance, as illustraited by the rightmost curve of Figure 57.

For a paraboloidal antenna, we can use the aperture diameter as the characteristic size of the wave source region in the Fraunhofer condition given in (89). Therefore, the ‘distance to the Fraunhofer region’ r_F for a paraboloidal

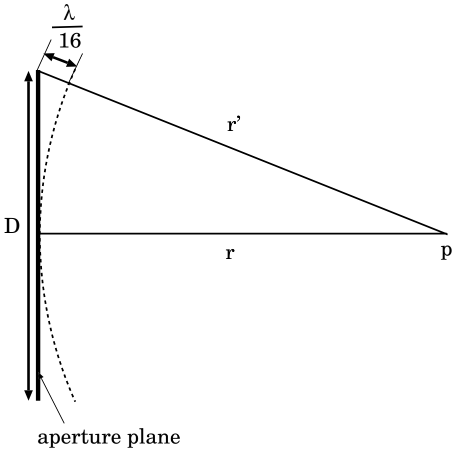

Figure 58: Distance to the Fraunhofer region as a condition for the plane wave approximation of the received wave.

antenna, with the aperture diameter D, receiving or transmitting a radio wave with wavelength λ, is given by

$$r_F \equiv \frac{2D^2}{\lambda}. \tag{173}$$

The Fraunhofer condition $r \gg r_F$ can be graphically illustrated as the condition where the difference between the distance from a distant point p to the edge of the aperture r', and that to the center of the aperture r, must be much smaller than $\lambda/16$ (Figure 58). This could be interpretted as a condition, that a spherical wave coming from the distant point can be practically approximated as a plane wave.

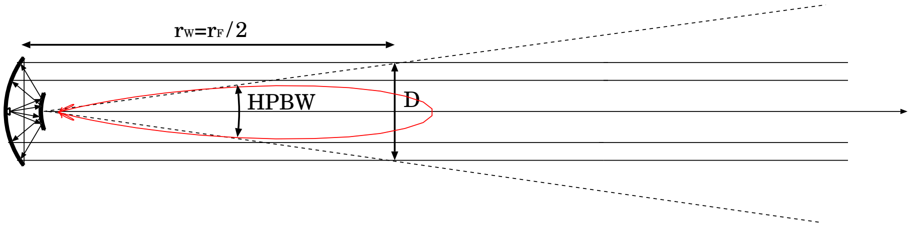

Figure 59: Distance to the Fraunhofer region as a condition for predominance of the far–field beam in the transmitted wave.

Also, r_F is equal to the twice of the distance r_w to a point, where the width of the far–field beam, measured at HPBW, becomes equal to the width

D	λ	$r_F = 2D^2/\lambda$
6 m	3.8 cm (8 GHz)	1.9 km
10 m	7 mm (43 GHz)	28.6 km
21 m	2.3 mm (129 GHz)	383 km
45 m	2 mm (150 GHz)	2025 km
2300 km	7 mm (43 GHz)	1.51×10^{12} km
VLBI		= 0.16 light year

Table 2: Distances to the Fraunhofer region.

of a circular cylinder with the diameter of the aperture D, i.e.,

$$\frac{\lambda}{D} r_w = D, \quad \text{and , hence,} \quad r_w = \frac{D^2}{\lambda} = \frac{r_F}{2},$$

(Figure 59). This could be interpreted as a condition that most of the transmitted power is confined within the far–field beam.

Table 2 shows typical examples of the distances to the Fraunhofer region. Can we measure the far–field patterns of our antennas on the ground?

2.7 Illumination Taper (or Gradation)

We can modify antenna beams by changing the electric field distribution on the aperture plane (the illumination pattern). Therefore, in order to realize

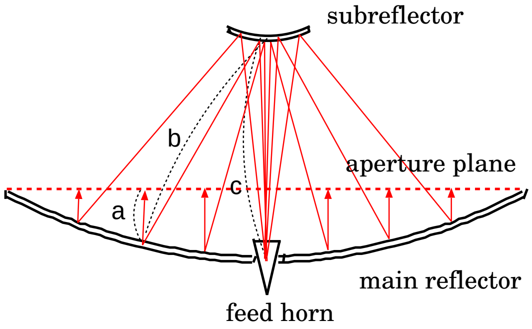

Figure 60: Aperture illumination.

a desired beam pattern, we can design a feed horn, so that the horn suitably 'illuminates' the aperture plane (Figure 60).

Generally speaking, it is desirable to have a beam pattern which would exhibit as narrow as possible main lobe and as low as possible sidelobe level. However, these two requirements are somewhat in conflict, as illustrated below.

Figure 62 shows field patterns in the far–field region normalized by their peak values for circular aperture antennas with simple aperture illumination patterns. The field patterns are derived by equation (165) which is based on the simple two–dimensional spatial Fourier transform relationship between the illumination patterns and the field patterns.

We can see in the figure that the main lobe is narrowest when the aperture illumination is uniform. However, the sidelobe level is rather high in the uniform illumination case. On the other hand, if we apply a Gaussian illumination, we get fairly low sidelobe level, but the main lobe becomes broader.

The non–uniform illumination, which is stronger in the central part of the aperture, and weaker in the outer parts, is called 'tapered' or 'gradated' illumination.

For radio telescopes, which receive very weak signals from astronomical radio sources, the thermal radiation of the ground (with temperature of $T \simeq 300$ K!) picked up by the sidelobes may seriously degrade the signal–to–noise (S/N) ratio. Likewise, the ground thermal radiation received from the outside of the main reflector edge (which is called 'spillover' in the transmission sense) is also quite harmful (Figure 61).

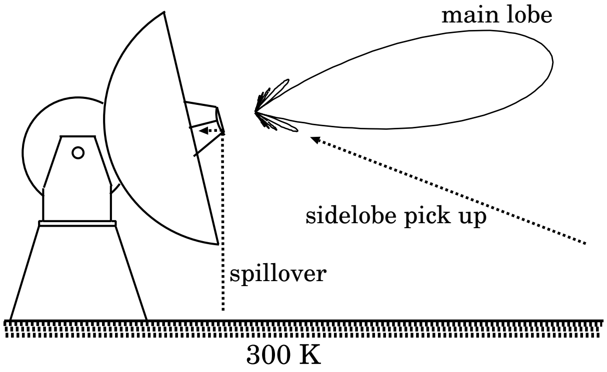

Figure 61: Why is strong tapering required for radio telescopes?

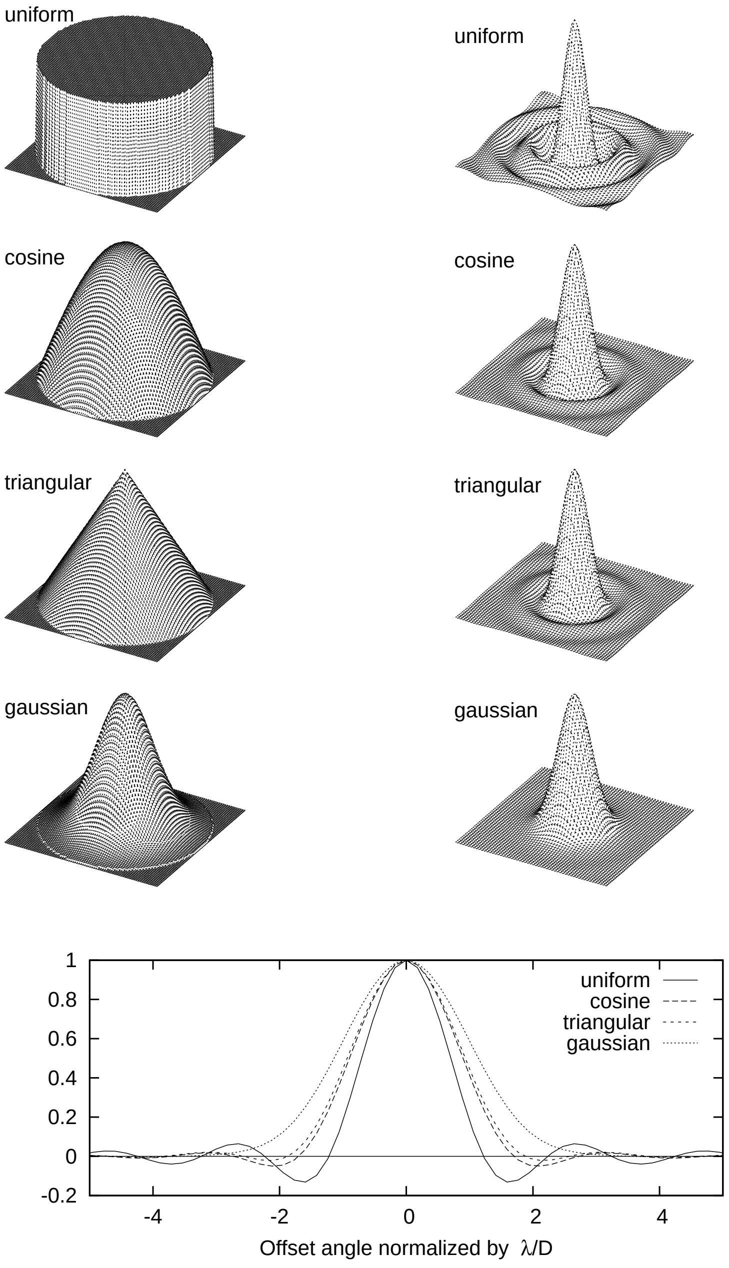

Figure 62: Aperture illumination patterns (Top, Left), corresponding normalized field patterns (Top, Right), and comparison of the normalized field patterns (Bottom).

Therefore, rather strong tapering is required for radio telescopes, although this of course means that we have to sacrifice some portion of their aperture areas as 'ineffective' areas.

2.8 Spectral Flux Density Received by an Antenna Beam

We defined earlier that the spectral flux density $\mathcal{S}_\nu$ is a portion of the radiation energy from an astronomical source incoming through a cross section of unit area, per unit frequency bandwidth, and per unit time. The spectral flux density was described, through the monochromatic intensity $I_\nu(\theta, \phi)$, by an integral over the source solid angle Ω:

$$\mathcal{S}_\nu = \iint\limits_{\Omega} I_\nu(\theta, \phi) \cos\theta \sin\theta \; d\theta \; d\phi,$$

where the $\cos\theta$ term arose due to a geometrical effect corresponding to the projection of a unit area onto the plane perpendicular to an incoming ray (left panel of Figure 63).

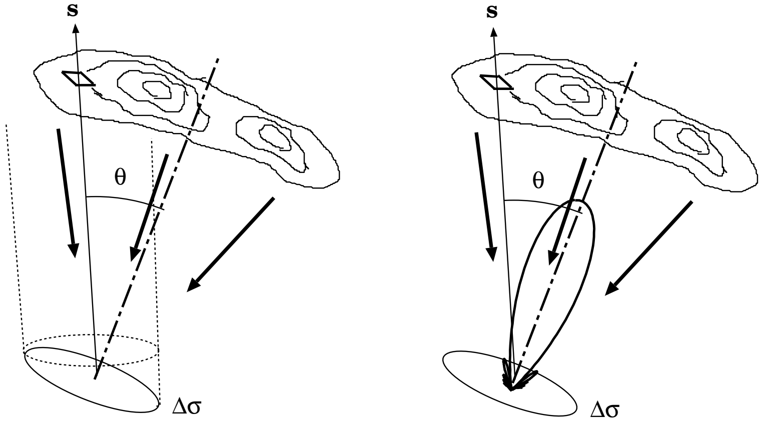

Figure 63: Flux density as received by a unit area in space (Left), and the effective flux density as received by a unit area on the aperture plane of a directional antenna (Right).

On the other hand, an antenna with a normalized power pattern $P_n(\theta, \phi)$ receives the radiation from the radio source in proportion to $P_n(\theta, \phi)$, which reflects not only the geometrical effect but also the electromagnetic effect. Therefore, the portion of the radiation energy received by a unit area on the antenna aperture plane, per unit frequency bandwidth, and per unit time, is described by

$$\mathcal{S}_\nu = \iint\limits_{\Omega} P_n(\theta, \phi)\, I_\nu(\theta, \phi) \sin\theta \; d\theta \; d\phi, \tag{174}$$

where θ and ϕ are the angular variables in the antenna–fixed coordinate system (right panel of Figure 63). We call this 'intensity collected by the antenna beam' $\mathcal{S}_\nu$ in equation (174) the 'effective flux density'. The effective flux density is equal to the usual total flux density when the angular size of the source is much smaller than the antenna beam width, and when the beam is exactly directed towards the source. Otherwise, the effective flux is smaller than the total flux. Henceforth, we use the word 'flux density' in the sense of the effective flux density, as far as radio wave reception with radio telescope antennas is concerned.

3 Antenna Characteristics

The performance of a radio wave antenna is characterized by a number of important parameters which usually figure in specifications of the antenna. The major peerformance parameters include

- Aperture diameter,
- Frequency Range,
- Surface accuracy,
- Pointing accuracy,
- Antenna reference point,
- Antenna gain,
- Range of motion and slewing speed,
- Survival loads.

Examples of antenna specifications are shown in tables 3 and 4.

We will introduce major performance characteristics of antennas, and discuss meanings of numbers in the specifications. We will also discuss ways to estimate important charactersitics such as aperture efficiency, antenna gain, and maximum observable frequency, on the basis of the specifications.

Optics	Cassegrain focus, central feed type	
	Primary diameter	21 m
	Primary focal length	7 m
	Secondary diameter	2 m
	Secondary focal length	37 cm
Mechanical operation	Fast switching up to 2.5° separation	
	Azimuth range	±270°
	Elevation range	0° – 91°
	Az max. slew speed	3°/s
	El max. slew speed	3°/s
	Az max. acceleration	$\geq 1^\circ/\mathrm{s}^2$
	El max. acceleration	$\geq 1^\circ/\mathrm{s}^2$
Surface accuracy	Appropriate for reception at 150 GHz	
	Panels	65 μm rms
	Total	150 μm rms (10 m/s wind)
Pointing performance	Appropriate for reception at 150 GHz	
	Pointing accuracy	0.001° rms (10 m/s wind)
	Az natural freq.	2.5 Hz
	El natural freq.	2.5 Hz
	Subref. spar nat. freq.	5 Hz
	Az El axes offset	3 mm
	Az El orthogonality	0.01°
Operational loads	Temperature	-20°C – 40°C
	Wind	10 m/s
Survival Loads	Wind	90 m/s
	Seismic acceleration	0.2 G horiz., 0.1 G vert.

Table 3: An example of specifications for an astrophysical VLBI antenna.

Aperture diameter	22 m
Frequency bands	2 GHz (S), 8 GHz (X), 22 GHz (K), 43 GHz (Q)
Polarization	RHCP or LHCP selectable for all 4 bands
Surface accuracy	$\leq$ 0.3 mm RMS (Panel $\leq$ 0.2 mm RMS)
Gain	S: 51.0 dB, X: 63.0 dB, K: 71.7 dB, Q: 77.7 dB
Subreflector	Accuracy $\leq$ 0.1 mm RMS, motorized hexapod
Pointing accuracy	$\leq 0.0022^\circ$ RMS (wind $\leq$ 10 m s^{-1})
Reference point	Measurable from outside, invar tube along Az–axis
Az–axis verticality	$\leq 0.0025^\circ$
Az, El–axes orthogonality	$\leq 0.0025^\circ$
Az, El–axes offset	$\leq$ 1.5 mm
Range of motion	$\pm\ 270^\circ$ in Az, $0^\circ \sim 90^\circ$ in El
Slew speed	max 5° s^{-1} in Az, max 5° s^{-1} in El
Operational wind load	15 m s^{-1}
Survival wind load	70 m s^{-1}
Foundation	Mat foundation + concrete piles

Table 4: An example of specifications for a geodetic VLBI antenna.

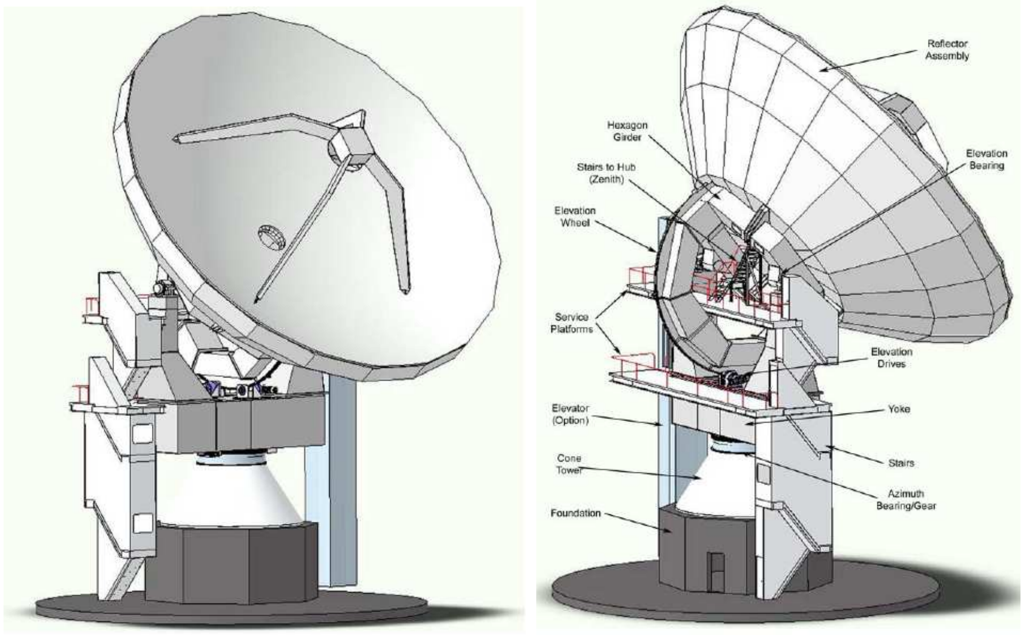

Figure 64: Design drawings of a 21 m antenna.

3.1 Directive Gain $G(\theta, \phi)$

The **"directive gain"** $G(\theta, \phi)$ of an antenna is defined in terms of the power pattern $P(\theta, \phi)$, in the antenna–fixed coordinate system with the angular variables θ and ϕ, as

$$G(\theta, \phi) = \frac{P(\theta, \phi)}{P} = \frac{4\pi P(\theta, \phi)}{\oint P(\theta, \phi) d\Omega}, \tag{175}$$

where

$$P \equiv \frac{1}{4\pi} \oint P(\theta, \phi) d\Omega,$$

is the mean value of the power pattern averaged over all directions.

Why is this quantity called directive "gain"? In the transmission case, the directive gain is a quantity describing how well your antenna can emit radio wave of a given total power towards the direction θ and ϕ, compared with an idealized "isotropic antenna" which would emit the same power of the radio wave isotropically. In the reception case, if you observe a point radio source at θ and ϕ, you would receive $G(\theta, \phi)$ times stronger power with your directional antenna than what you would receive with an idealized isotropic antenna. In both cases, you 'gain' stronger signal with the directional antenna, compared with the idealized isotropic antenna (Figure 65).

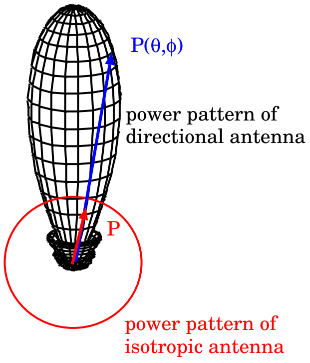

Figure 65: Directive gain: "gain" of a directional antenna compared with an idealized isotropic antenna.

3.2 Beam Solid Angle Ω_A

The **"beam solid angle"** Ω_A is another measure of the angular extent of the antenna beam, along with the HPBW and BWFN, defined by an equation:

$$\Omega_A = \oint P_n(\theta,\phi)d\Omega = \frac{\oint P(\theta,\phi)d\Omega}{P_{max}} = \frac{4\pi P}{P_{max}} \,, \tag{176}$$

where $P_n(\theta,\phi)$ is the normalized power pattern as defined in equation (155):

$$P_n(\theta,\phi) = \frac{P(\theta,\phi)}{P_{max}} \,.$$

If we display the antenna power pattern in a rectangular plot, where the x– and y– coordinates are angles in two perpendicular directions in the aperture plane, and if we approximate the solid angle by an area in this xy– plane, the beam solid angle is equal to the cross–sectional area of a cylinder which has a height of P_{max}, and the same "volume" as the power pattern in this rectangular coordinate system (Figure 66).

3.3 Main Beam Solid Angle Ω_M

The **"main beam solid angle"** is defined in a similar way to the beam solid angle, but now the integration covers the main lobe only:

$$\Omega_M = \int_{main\ \ lobe} P_n(\theta,\phi)d\Omega. \tag{177}$$

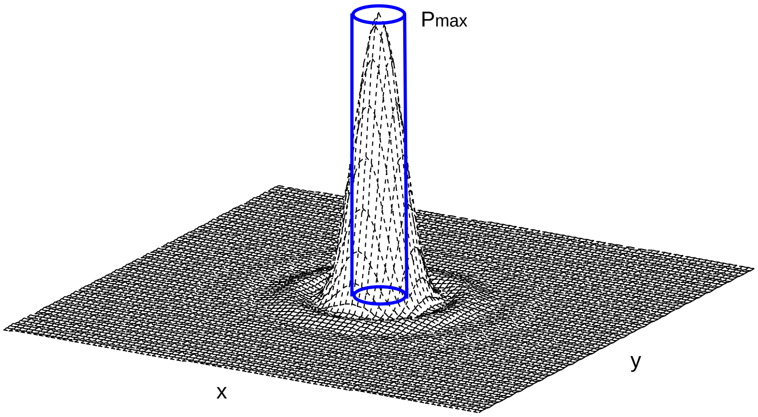

Figure 66: Beam solid angle as the cross-sectional area of a cylinder with a height of P_{max}, and the same volume as the antenna power pattern in this rectangular plot of the beam.

In the rectangular plot we saw above, the main beam solid angle is equal to the cross–sectional area of a cylinder which has the height of P_{max}, and the same volume as the main lobe of the power pattern.

3.4 Main Beam Efficiency η_M

The **"main beam efficiency"** (or simply the beam efficiency) is the ratio of the main beam solid angle to the beam solid angle:

$$\eta_M = \frac{\Omega_M}{\Omega_A}. \tag{178}$$

η_M is close to 1 if the antenna has a sharp main lobe, and sufficiently low sidelobe levels.

3.5 Directivity, Maximum Directive Gain, or "Gain" $\mathcal{D}$

The **"directivity"** is the maximum value of the directive gain, which is usually obtained in the direction of the symmetry axis:

$$\mathcal{D} = G_{max} = \frac{P_{max}}{P} = \frac{4\pi}{\Omega_A}. \tag{179}$$

The directivity describes how much a directional antenna "gains" at the beam center, as compared with the idealized isotropic antenna. This is an important antenna parameter which is also called the **“antenna gain”**, or simply **“gain”** (not to be confused with the “directive gain” $G(\theta, \phi)$).

The antenna gain is usually expressed in decibels (dB):

$$\mathcal{D} \text{ (in dB or dBi) } = 10 \ \log_{10}(\frac{P_{max}}{P}), \tag{180}$$

where log_{10} is the common (i.e. base 10) logarithm, and “**dBi**” here is the same as **dB** but stresses that the comparison is made with the *isotropic* case.

3.6 Antenna Polarization

3.6.1 Some Notes on Polarization of Electromagnetic Wave

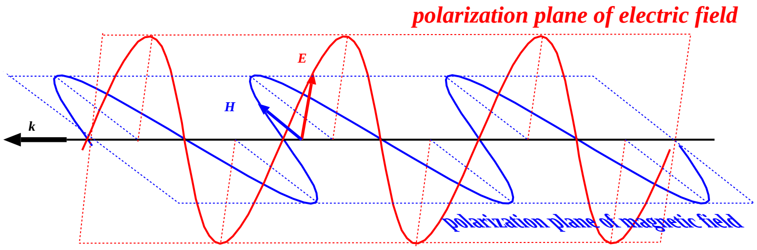

Figure 67: An electromagnetic wave as a polarized wave.

Since an electromagnetic wave is a transverse wave, as we saw in the discussions of the plane and spherical waves, the electric or magnetic field vector in the wave oscillates along a certain direction within a plane which is perpendicular to the direction of the propagation, and moves with the wave (Figure 67). Such a wave is said to be “polarized”.

There are two degrees of freedom in the oscillation within the plane. Therefore, any wave with a certain direction of polarization can be expressed as a linear combination of two independent polarization components. Such independent components could be two linearly polarized components in mutually orthogonal directions (horizontal and vertical, say) or two circularly polarized components with mutually opposite rotational senses (RHCP: Right Hand Circular Polarization, and LHCP: Left Hand Circular Polarization), as shown in Figure 68.

3.6.2 Polarization Characteristics of Antennas

Any antenna (or, better to say, any waveguide to coaxial–cable converter) can receive or transmit only one independent component of the polariza-

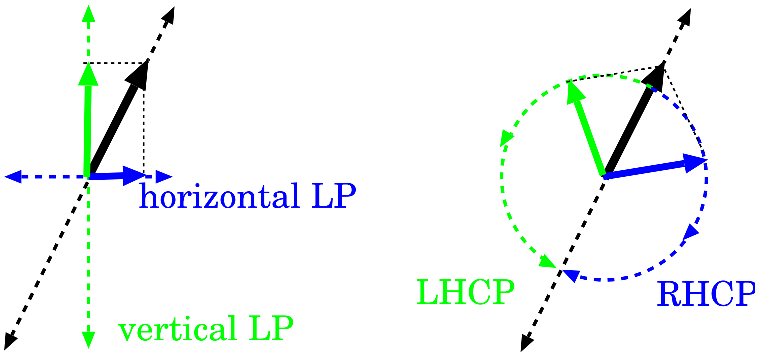

Figure 68: Representation of a polarized wave as a linear combination of two independent linear (Left), or circular (Right), polarization components.

tion. This can be generally understood in the following way. Although the electromagnetic wave in free space has two degrees of freedom in the polarization, the oscillation of the voltage or the current in a circuit is essentially one–dimensional. Therefore, we have to lose one degree of freedom, anyway.

For example, if the waveguide to coaxial–cable converter consists of a simple dipole, it receives or transmits only one linear polarization component, with the direction of oscillation parallel to the dipole (Figure 69). If the converter is a helix, on the other hand, it receives or transmits only one circular polarization component. In general, an antenna is designed to receive or transmit a certain polarization component. Therefore, an antenna could be designed, for example, for linear horizontal polarization, or for RHCP, etc.

Figure 69: X–band and K–band waveguide to coaxial-cable converters (Left). We see a "monopole on a conductor" inside of a X–band waveguide to coaxial-cable converter (Right), which is equivalent to a dipole.

Of course, the antenna polarization can be relatively easily changed by adjusting the waveguide to coaxial–cable converter or using special optical devices. Moreover, one can install two or more waveguide to coaxial–cable converters, and following receiving systems, in a common main–reflector and sub–reflector system in order to simultaneously receive or transmit the two polarization components by "a single antenna" (which, in actuality, contains two antennas in the strict sense of the second definition by Kraus).

The specification of the antenna polarization performance is usually given as **"polarization isolation"**. This shows how well an antenna can receive one polarization component, to which the antenna is designed, without being contaminated by another component (often called as "cross-polarization leakage"), which may arise due to some inperfection in the antenna optics.

3.6.3 Antenna Polarization and VLBI

In a majority of radio sources, two independent polarization components are only very weakly correlated ("unpolarized sources"). Therefore, it is quite important for VLBI observations that participating antennas observe radio sources in the same polarization mode, except in the cases when the weak correlation between different polarization components itself is the target of study ("polarization observation"). Wrong setting of polarization has been one of major sources of failures in VLBI observations.

It is not easy to use linear polarization antennas for VLBI observations, because the directions of the linear polarization fixed to antennas usually correspond to different sky directions, and the difference varies in time as the Earth rotates, for antennas located at different points on the Earth surface. Therefore, the VLBI antennas in the world are mostly designed to receive circular polarization components. In geodetic VLBI, RHCP has been conventionally used.

3.7 Effective Aperture A_e

Let us consider that the randomly polarized (or 'unpolarized") radio wave is incident to a radio telescope antenna. The word "unpolarized" here means that all kinds of waves with different polarization directions are randomly mixed up so that in average no net predominant polarization component is left. Radio waves from most of the astronomical sources are known to be practically unpolarized in this sense.

If an antenna receives a certain amount of power per unit frequency bandwidth W_ν by observing a randomly polarized radio source with the effective flux density $\mathcal{S}_\nu$, the **"effective aperture"** A_e of the antenna is defined by

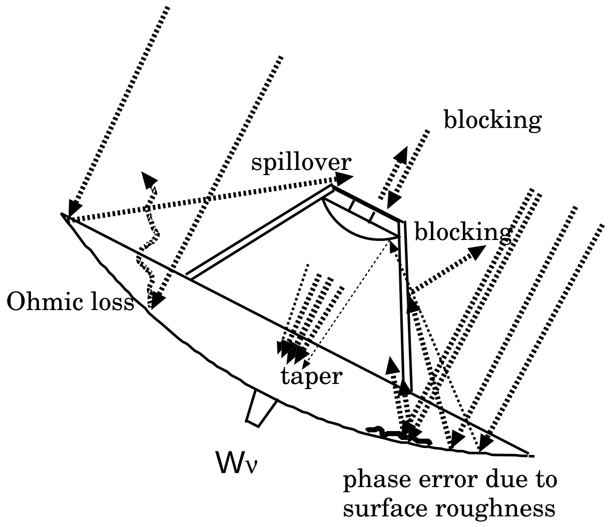

Figure 70: Factors reducing the effective aperture.

an equation:

$$W_\nu = \frac{1}{2} A_e \mathcal{S}_\nu, \tag{181}$$

where a factor 1/2 implies that the antenna is able to receive only a half of the power alloted to one independent component of the polarization.

The actually received power in equation (181) is smaller than the incident power W_ν^i:

$$W_\nu^i = \frac{1}{2} A_g \mathcal{S}_\nu,$$

where A_g is the geometrical aperture which is equal to $\pi D^2/4$ for a circular aperture with diameter D, for reasons illustrated in Figure 70. Therefore, the effective aperture is always smaller than the geometrical aperture:

$$A_e < A_g.$$

3.8 Aperture Efficiency η_A

The ratio of the effective aperture A_e to the geometrical aperture A_g is called **"aperture efficiency"** and is usually denoted by η_A.

$$\eta_A = \frac{A_e}{A_g}. \tag{182}$$

The aperture efficiency η_A is always smaller than 1 mainly due to

- the strong illumination taper (or gradation),

- the phase error due to the roughness of the antenna surface,
- the blocking by the subreflector and the stays,
- the spillover from the subreflector,
- the Ohmic dissipation on the surface,

as schematically illustrated in Figure 70.

3.9 Nyquist Theorem on Noise Power

In further discussions, we will often use an important theorem on the power of the noise derived by Nyquist (1928).

Suppose that we have an electric circuit with a resistor of resistance R which is in thermodynamical equilibrium with the environment of temperature T (Figure 71).

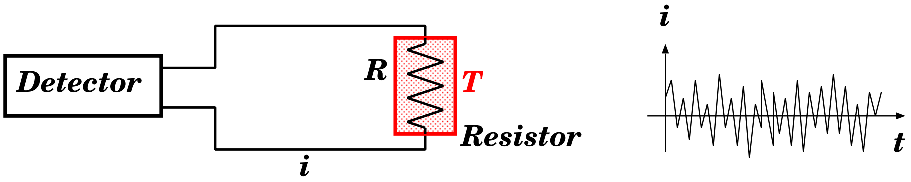

Figure 71: Power generated by a resistor which is in thermodynamical equilibrium with the environment of temperature T.

Then, we have electric current i in the circuit due to the thermal noise. Average of such noise current is usually zero: $\langle i \rangle = 0$. But average of square of the noise current is not, in general, zero: $\langle i^2 \rangle \neq 0$. So, we have some power due to the thermal noise.

According to the Nyquist Theorem (H. Nyquist, 1928, *Phys. Rev.*, **32**, 110–113), the average noise power W_ν per unit frequency bandwidth is given by

$$W_\nu = kT, \tag{183}$$

where k is Boltzmann constant ($k = 1.381 \times 10^{-23}$ J K^{-1}), in the classical limit $h\nu \ll kT$.

We will briefly see how the theorem is derived following discussions by Nyquist (1928).

Let us consider two conductors each of resistance R connected by a long non–dissipative transmission line which has characteristic impedance R and satisfies non–reflection condition at either end of the line (Figure 72). Let length of the transmission line be l and propagation velocity be v. Let the system be in the thermodynamical equilibrium with temperature T.

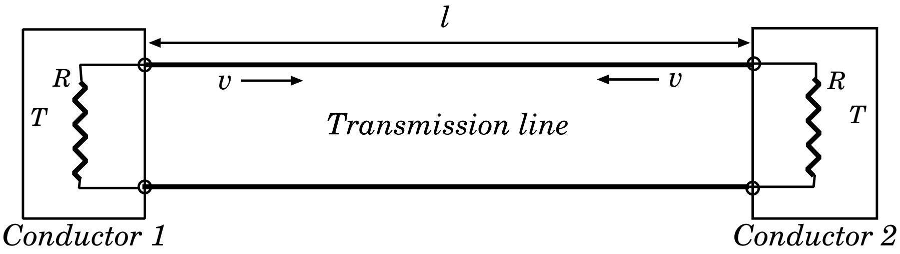

Figure 72: Two conductors each of resistance R and in temperature T connected by a dissipationless non–reflecting transmission line.

1. There are two trains of energy, one goes from left to right through the transmission line corresponding to the power generated in conductor 1 and absorbed in conductor 2, and another in the reverse direction. Under the thermodynamical equilibrium, the power flowing from conductor 1 to conductor 2 must be exactly equal to the power flowing from conductor 2 to conductor 1 at any frequency bandwidth (otherwise the second law of thermodynamics is violated).

2. Suppose that we isolate the transmission line from the conductors by applying short circuits at the two ends. Then complete reflection is set up at the ends and traveling waves in opposite directions are converted to standing waves (normal mode oscillations with fixed ends). Thus, the energy of the noise current is trapped in the transmission line.

3. Eigen frequencies of the normal modes are

$$\nu_1 = \frac{v}{2l}, \ \nu_2 = \frac{v}{l}, \ \nu_3 = \frac{3v}{2l}, \ \nu_4 = \frac{2v}{l}, \ \cdots,$$

   corresponding to the fundamental tone and overtones (Figure 73). Therefore, the number of normal modes contained in a frequency bandwidth from ν to $\nu + \Delta\nu$ is $(2l/v)\Delta\nu$.

4. In the classical limit ($h\nu \ll kT$), average energy per one normal mode oscillation is equal to kT in the thermodynamical equilibrium. One–half of this energy is magnetic and one–half is electric. (This is analogous to the string oscillation case, where average kinetic energy per one degree of freedom under the thermodynamical equilibrium is equal to $kT/2$ according to the law of equipartition of energy, while kinetic energy is equal to potential energy in the oscillation, and hence average total energy per one normal mode oscillation, is kT).

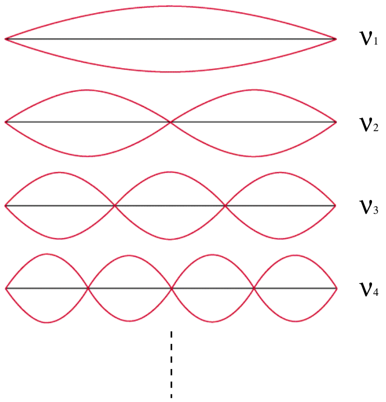

Figure 73: Fundamental tone and overtones of normal mode oscillations of a string with eigenfrequencies $\nu_1 = \frac{v}{2l}$, $\nu_2 = \frac{v}{l}$, $\nu_3 = \frac{3v}{2l}$, $\nu_4 = \frac{2v}{l}$, $\cdots$.

5. Therefore, the total energy contained in the frequency bandwidth from ν to $\nu + \Delta\nu$ is equal to $(2l/v)\,kT\,\Delta\nu$.

6. This amount of energy should have been transferred from the two conductors to the transmission line during the time of transit $\Delta t = (l/v)$ when the line was connected to the conductors. Consequently, the noise power per unit bandwidth generated by one conductor W_ν should be

$$W_\nu = \frac{1}{2}\,\frac{1}{\Delta t}\,\frac{1}{\Delta\nu}\,\frac{2l}{v}\,kT\,\Delta\nu = kT,$$

   as given in equation (183).

In the energy region where the condition of the classical limit $(h\nu \ll kT)$ does not hold, the simple law of equipartition of the total energy kT per one normal mode oscillation is no longer valid. For such a case, Nyquist (1928) gives a more general equation on power of the noise:

$$W_\nu = \frac{h\nu}{e^{\frac{h\nu}{kT}} - 1}.$$

3.10 Effective Aperture and Beam Solid Angle

The effective aperture A_e and the beam solid angle Ω_A are related with each other through the wavelength λ by a simple equation:

$$A_e \Omega_A = \lambda^2. \tag{184}$$

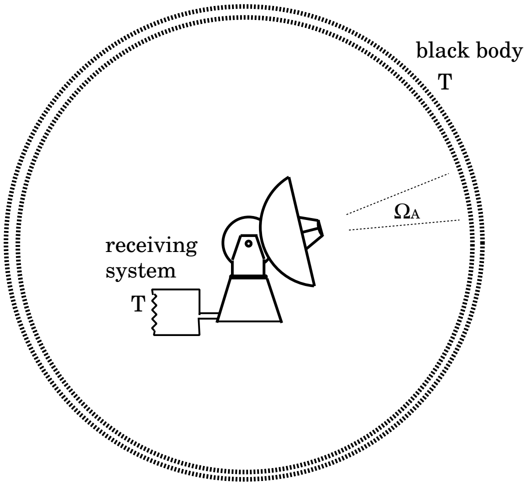

Figure 74: An antenna in a blackbody cavity.

Let us prove the relation assuming a simple case of the thermodynamical equilibrium. Consider a system consisting of an antenna and a surrounding blackbody, and assume that the system is in a complete thermodynamical equilibrium with temperature T (Figure 74).

Since the intensity I_ν of the blackbody radiation in the Reileigh–Jeans approximation:

$$I_\nu = \frac{2\nu^2}{c^2} kT = \frac{2kT}{\lambda^2}, \tag{185}$$

is essentially isotropic in this case ($I_\nu = \text{const}$ for any direction), the effective flux density incoming to the antenna can be expressed as

$$\mathcal{S}_\nu = \oint P_n(\theta, \phi)\, I_\nu \, d\Omega = I_\nu \, \Omega_A = \frac{2kT}{\lambda^2}\, \Omega_A. \tag{186}$$

Therefore, the power per unit frequency bandwidth W_ν received by the antenna is

$$W_\nu = \frac{1}{2} A_e \mathcal{S}_\nu = A_e \frac{kT}{\lambda^2} \Omega_A. \tag{187}$$

On the other hand, the power L_ν transmitted by the antenna per unit frequency bandwidth due to the noise in the antenna receiving system, which is in thermodynamical equilibrium with the temperature T, is equal to

$$L_\nu = kT,$$

according to the Nyquist theorem given by equation (183) (H. Nyquist, 1928). Now, the received power must equal the transmitted power in the detailed balance of the thermodynamical equilibrium. Therefore,

$$L_\nu = W_\nu \quad \longrightarrow \quad \frac{A_e \Omega_A}{\lambda^2} = 1 \quad \longrightarrow \quad A_e \Omega_A = \lambda^2. \tag{188}$$

Although we derived equation (184) in the thermodynamical equilibrium case, the resultant equation does not contain any thermodynamical quantity. Therefore, the equation must generally hold in other cases as well.

3.11 Directivity $\mathcal{D}$ and Aperture Efficiency η_A

As we saw earlier, the directivity (or gain) $\mathcal{D}$ is related to the beam solid angle Ω_A by equation (179):

$$\mathcal{D} = \frac{4\pi}{\Omega_A}.$$

Now using equation (184), we can transform the above equation to

$$\mathcal{D} = 4\pi \frac{A_e}{\lambda^2} = 4\pi \eta_A \frac{A_g}{\lambda^2}, \tag{189}$$

where A_g and λ are the geometrical aperture and the wave length, respectively.

For a circular aperture antenna with diameter D, we have

$$\mathcal{D} = \eta_A \left(\frac{\pi D}{\lambda} \right)^2. \tag{190}$$

If the aperture efficiency η_A is kept nearly constant, we could obtain higher gain with larger diameter and higher frequency. In actuality, however, it becomes increasingly difficult to realize the high aperture efficiency as we go to the higher frequency and/or to the larger diameter.

In performance descriptions of antennas, the gain of an idealized antenna with 100 % aperture efficiency:

$$\left(\frac{\pi D}{\lambda} \right)^2, \tag{191}$$

is often described as “100 % gain”, and usually given in dB. The 100 % gain can be directly calculated from the aperture diameter D and the observing wavelength λ. Therefore, if we can estimate the aperture efficiency η_A, we can easily get a value for the gain $\mathcal{D}$, as we will examine later.

3.12 Illumination Taper and Aperture Efficiency

Rather strong illumination taper is required in radio telescope antennas to avoid undesired ground pickups due to the sidelobes or the spillover from the main reflector as we saw in Section 2.7. The strong taper lowers the sidelobe level. At the same time, however, it increases the beam width as we saw in Figure 62. The increase of the beam width and therefore of the beam solid angle Ω_A decreases the effective aperture A_e as required from equation (184):

$$A_e = \frac{\lambda^2}{\Omega_A}.$$

In general, the illumination taper improves the main beam efficiency η_M but deteriorates the aperture efficiency η_A. The illumination taper is often the largest factor reducing the aperture efficiency of radio telescope antennas to the level of 50 – 60 %.

3.13 Surface Roughness and Aperture Efficiency

The surface roughness is another important factor which determines the aperture efficiency of radio telescope antennas.

Suppose that a real main reflector deviates from an ideal paraboloid due to the roughness of its surface. Then, the rays, which originally formed a wave front of equal phase in a plane wave, and were reflected at different points on the main reflector, reach at the focus with different path lengths, and, therefore, with different phases, due to the surface roughness. Thus, the rays reached at the focus are summed up with different phases. Therefore, the maximum power pattern P_{max} at the center of the main lobe becomes somewhat lower than the one in the ideal paraboloid case with perfectly smooth surface. On the other hand, the averaged power pattern P must not change by the surface roughness, since the total power must be conserved.

Therefore, the directivity $\mathcal{D} = P_{max}/P$, and the effective aperture $A_e = \mathcal{D}\lambda^2/(4\pi)$, are reduced, compared with the ideal case. Because of the same reason, the reduced power in the main lobe must be balanced by an increased power in the sidelobes.

Thus, the surface roughness deteriorates both the aperture efficiency η_A and the main beam efficiency η_M.

Let us calculate how the aperture efficiency is reduced due to the surface roughness of the main reflector, again in the transmission mode. For simplicity, we 'stretch' the actual paraboloid surface and treat it as a plane, parallel to the aperture plane, and regard that the rays are coming from a direction, perpendicular to the 'main–reflector plane', as shown in Figure 75.

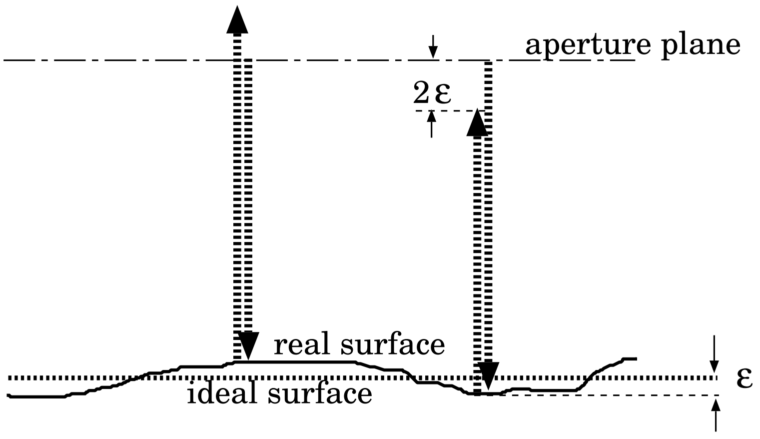

Figure 75: Phase error due to the surface roughness.

This implies that a subreflector, and a primary feed, must be also stretched to a 'plane'. If we adopt such a simplified scheme, all rays transmitted from a primary feed reaches at the aperture plane with the same path length, and, therefore, with equal phase, if the 'main reflector plane' is ideally smooth, just as in the aperture plane of an ideally smooth paraboloid. Such an approximation is permissible in the present discussion, focused only on the effect of the randomly distributed surface roughness in the beam center direction.

Suppose that a ray is reflected at a point of the main reflector surface, at a distance ϵ apart from the ideally smooth surface, as shown in Figure 75. In this case, the path length of the ray differs from the one in the ideal case by 2ϵ, when it reaches at a point $\boldsymbol{r}'$ of the aperture plane. Therefore, we have a phase error of

$$\delta(\boldsymbol{r}') = 2k\epsilon = \frac{4\pi\epsilon}{\lambda}, \tag{192}$$

in the electric field $\boldsymbol{E}_a(\boldsymbol{r}')$ on the aperture plane, where k and λ are the wave number and wavelength, respectively, as before.

Let us assume that the phase error $\delta(\boldsymbol{r}')$ is randomly distributed over the aperture plane with the Gaussian probability density:

$$\mathfrak{f}(\delta) = \frac{1}{\sqrt{2\pi}\,\sigma} e^{-\frac{\delta^2}{2\sigma^2}}, \tag{193}$$

where $\sigma^2 = \langle \delta^2 \rangle$ is the dispersion of δ, with $\langle \ \rangle$ here denoting an ensemble average.

Now, the aperture illumination, taking into account the phase error, is expressed as

$$g(\boldsymbol{r}') = g_0(\boldsymbol{r}') e^{i\delta(\boldsymbol{r}')}, \tag{194}$$

where $g_0(\boldsymbol{r}')$ is an ideal aperture illumination, which would be realized with the perfectly smooth main reflector surface. $g_0(\boldsymbol{r}')$ is a real quantity, since we assume the oscillating electric field with the equal phase throughout the aperture plane, in the idealized case.

Then, the field pattern $f(\boldsymbol{n})$ around the beam center direction in the far–field region is expressed according to equation (150) as

$$f(\boldsymbol{n}) = \int\limits_{\mathcal{A}} g_0(\boldsymbol{r}') e^{-i[2\pi \boldsymbol{n}\cdot\frac{\boldsymbol{r}'}{\lambda} - \delta(\boldsymbol{r}')]} \frac{d\mathcal{S}'}{\lambda^2}. \tag{195}$$

Now, we approximately replace the overall contribution of the phase error δ from the whole aperture plane, by an ensemble average $\langle e^{i\delta}\rangle$. Then, we have

$$\langle f(\boldsymbol{n})\rangle = \int\limits_{\mathcal{A}} g_0(\boldsymbol{r}') e^{-i2\pi \boldsymbol{n}\cdot\frac{\boldsymbol{r}'}{\lambda}} \langle e^{i\delta}\rangle \frac{d\mathcal{S}'}{\lambda^2}, \tag{196}$$

where $\langle e^{i\delta}\rangle$ can be described, by using the Gaussian probability density in equation (193),

$$\begin{aligned}\langle e^{i\delta}\rangle &= \int\limits_{-\infty}^{\infty} \mathfrak{f}(\delta) e^{i\delta} d\delta = \frac{1}{\sqrt{2\pi}\,\sigma} \int\limits_{-\infty}^{\infty} e^{i\delta - \frac{\delta^2}{2\sigma^2}} d\delta = e^{-\frac{\sigma^2}{2}} \\ &= e^{-\frac{\langle\delta^2\rangle}{2}} = e^{-\frac{1}{2}\left(\frac{4\pi\sqrt{\langle\epsilon^2\rangle}}{\lambda}\right)^2}, \end{aligned} \tag{197}$$

where we used a well known integration formula:

$$\int\limits_{-\infty}^{\infty} e^{iax - x^2} dx = \sqrt{\pi} e^{-\frac{a^2}{4}}, \tag{198}$$

and equation (192). Thus, we obtain

$$\langle f(\boldsymbol{n})\rangle = f_0(\boldsymbol{n}) e^{-\frac{1}{2}\left(\frac{4\pi\sqrt{\langle\epsilon^2\rangle}}{\lambda}\right)^2}, \tag{199}$$

where

$$f_0(\boldsymbol{n}) = \int\limits_{\mathcal{A}} g_0(\boldsymbol{r}') e^{-i2\pi \boldsymbol{n}\cdot\frac{\boldsymbol{r}'}{\lambda}} \frac{d\mathcal{S}'}{\lambda^2}, \tag{200}$$

is the ideal field pattern with the perfectly smoooth main reflector in the far field region.

Since the power pattern $P(\theta, \phi)$ in the far field region is proportional to $\mid f(\boldsymbol{n}) \mid^2$, we have

$$P(\theta, \phi) = P_0(\theta, \phi) e^{-\left(\frac{4\pi\sqrt{\langle\epsilon^2\rangle}}{\lambda}\right)^2}, \tag{201}$$

around the beam center direction, where $P_0(\theta, \phi)$ is the ideal power pattern with the perfectly smooth main refletor. Hence, we have

$$P_{max} = P_{0\,max} e^{-\left(\frac{4\pi\sqrt{\langle\epsilon^2\rangle}}{\lambda}\right)^2}. \tag{202}$$

Therefore, using equations (179), (189), and (182), we obtain following expressions of the directivity, the effective aperture and the aperture efficiency as functions of the root mean square surface roughness $\sqrt{\langle\epsilon^2\rangle}$:

$$\mathcal{D} = \mathcal{D}_0 e^{-\left(\frac{4\pi\sqrt{\langle\epsilon^2\rangle}}{\lambda}\right)^2}, \tag{203}$$

$$A_e = A_{e0} e^{-\left(\frac{4\pi\sqrt{\langle\epsilon^2\rangle}}{\lambda}\right)^2}, \tag{204}$$

$$\eta_A = \eta_{A0} e^{-\left(\frac{4\pi\sqrt{\langle\epsilon^2\rangle}}{\lambda}\right)^2}, \tag{205}$$

where the symbols with suffix 0, $\mathcal{D}_0 = P_{0\,max}/P$, $A_{e0} = \mathcal{D}_0\lambda^2/(4\pi)$, and $\eta_{A0} = A_{e0}/A_g$, represent the values for the idealized case when the main reflector surface is perfectly smooth. For a particular case of the circular aperture, the directivity or the gain is expressed in a form:

$$\mathcal{D} = \eta_{A0} \left(\frac{\pi D}{\lambda}\right)^2 e^{-\left(\frac{4\pi\sqrt{\langle\epsilon^2\rangle}}{\lambda}\right)^2}. \tag{206}$$

We derived the above relations for the transmission case. But the results are readily applicable to the reception case as well, in view of the equivalence of the antenna beam patterns in transmission and reception.

The gain curves as functions of wavelength are shown for some existing radio telescopes in Figure 76.

3.14 Surface Accuracy and Lower Limit of the Observing Wavelength

A normalized gain curve as a function of $x = \sqrt{\langle\epsilon^2\rangle}/\lambda$:

$$x^2 \, e^{-(4\pi x)^2}$$

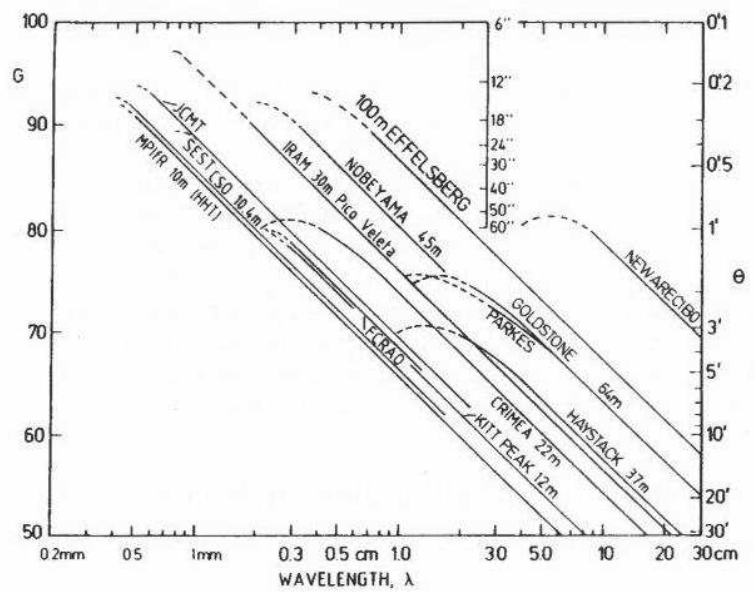

Figure 76: Gain in dB and HPBW of some existing radio telescope antennas as functions of wavelength (from Rohlfs and Wilson, 2000, Tools of Radio Astronomy, 3rd edition, Springer).

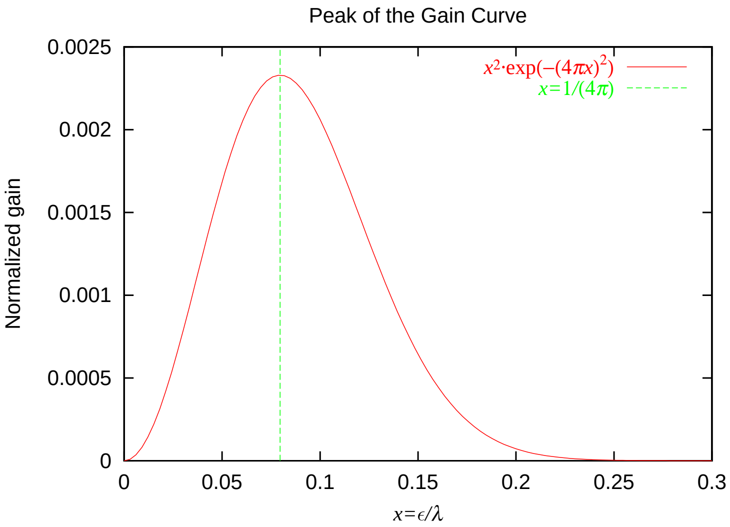

Figure 77: Normalized gain curve and its peak position.

is shown in Figure 77 in the linear scale (in this figure, the rms surface roughness $\sqrt{\langle\epsilon^2\rangle}$ is denoted as ϵ for simplicity). It is evident from the figure that the maximum gain is obtained at the wavelength:

$$\lambda_{peak} = 4\pi\sqrt{\langle\epsilon^2\rangle}$$

or at the frequency:

$$\nu_{peak} = \frac{c}{4\pi\sqrt{\langle\epsilon^2\rangle}},$$

depending on the rms surface roughness, or otherwise called **"surface accuracy"**, $\sqrt{\langle\epsilon^2\rangle}$.

It may appear from the above discussion that we can use an antenna with the surface accuracy $\sqrt{\langle\epsilon^2\rangle}$ at short wavelength down to around $4\pi\sqrt{\langle\epsilon^2\rangle} \simeq 12.6\sqrt{\langle\epsilon^2\rangle}$. But here we must be a little cautious.

What we actually receive from a radio source is the power:

$$W_\nu = \frac{1}{2}A_e\mathcal{S}_\nu = \frac{1}{2}\eta_A A_g\mathcal{S}_\nu$$

(see equation (181)), and equation (189) shows that

$$\mathcal{D} = 4\pi\frac{A_e}{\lambda^2}, \ \text{ and hence, } \ A_e = \frac{\mathcal{D}\lambda^2}{4\pi}. \tag{207}$$

Therefore, the received power is

$$W_\nu = \frac{1}{8\pi}\mathcal{D}\lambda^2\mathcal{S}_\nu. \tag{208}$$

Consequently, the wavelength dependence of the power is uniquely determined, i.e. without further dependence on the wavelength, by the wavelength dependence of the gain:

$$\mathcal{D} = 4\pi\eta_A\frac{A_g}{\lambda^2},$$

(see equation (189)), only when the flux density $\mathcal{S}_\nu$ is proportional to λ^{-2}, just like in the case of a thermal blackbody radiation source. Indeed such a source with temperature T and solid angle Ω_s has the flux density in the Rayleigh–Jeans region:

$$\mathcal{S}_\nu = \frac{2\nu^2}{c^2}kT\Omega_s = \frac{2kT}{\lambda^2}\Omega_s.$$

Therefore, the wavelength dependence of the gain, as shown in Figure 76, is really a good measure of the antenna sensitivity, when we observe thermal radio sources with the spectral index, which we defined as $\mathcal{S}_\nu \propto \nu^{-\alpha} \propto \lambda^\alpha$, of $\alpha = -2$.

For non–thermal radio sources, such as Synchrotron radiation sources, however, the spectral index α is not equal to -2, but usually positive. Therefore, the wavelength dependence of the received power W_ν is no longer uniquely determined by the gain $\mathcal{D}$ only.

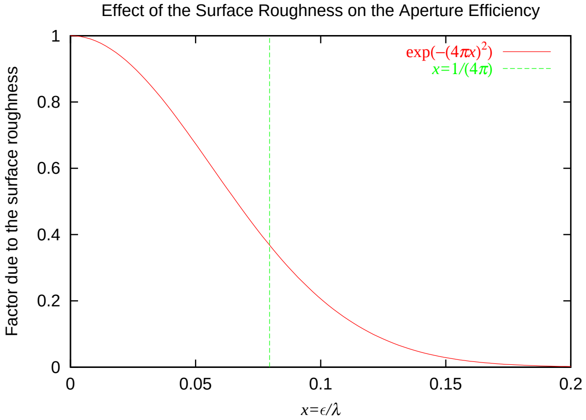

Figure 78: Dependence of the aperture efficiency on the ratio of the surface accuracy ϵ to the wavelength λ.

Consequently, it is more appropriate to use the wavelength dependence of the aperture efficiency η_A shown in equation (205) as a measure of the sensitivity of an antenna with a given diameter and a given surface accuracy as illustrated in Figure 78 (here again the surface accuracy $\sqrt{\langle\epsilon^2\rangle}$ is simply denoted as ϵ). As we see from the figure, the aperture efficiency is reduced by a factor of around 0.37 when the wavelength $\lambda \simeq 4\pi\sqrt{\langle\epsilon^2\rangle}$. Although we could still use an antenna with aperture efficiency $\leq 37\%$, and we actually do in some cases, it is usually accepted as a reasonable lower limit of the observing wavelength 20 times of the surface accuracy:

$$\lambda_{min} \simeq 20\sqrt{\langle\epsilon^2\rangle}, \tag{209}$$

where the reduction factor is around 70 %. This means that the surface accuracy specificatin of 150 μm rms, shown in table 3, is good enough for an observing wavelength as short as 3 mm (or, as high as 100 GHz in frequency).

The surface accuracy specification is often the most decisive factor in the cost estimation of an antenna, since tolerances in manufacturing of various parts of the antenna, including supporting structures and materials for main reflector panels, are largely determined by the required surface accuracy.

Items		Frequency in GHz				Remarks
		2.2	8.2	22.2	43.1	
Illumination taper		-2.39	-0.92	-1.30	-1.46	
Blocking	Subref.	-0.16	-0.16	-0.16	-0.16	
	Stay	-0.35	-0.35	-0.35	-0.35	
spillover	Main ref.	-0.27	-0.07	-0.01	-0.01	
	Subref.	-0.97	-0.51	-0.18	-0.09	
Surface accuracy	Main ref.	-0.01	-0.13	-0.94	-3.54	0.5mm rms
	Subref.	neg.	-0.02	-0.15	-0.57	0.2mm rms
	Setting	neg.	-0.04	-0.18	-0.66	Subref–feed
Horn cover loss		-0.07	-0.06	-0.11	-0.24	
Aperture efficiency	in dB	-4.24	-2.26	-3.38	-7.08	
	in %	37.6%	59.4%	45.9%	19.6%	
100 % gain in dB		47.2	58.6	67.3	73.1	
Gain in dB		43.0	56.4	63.9	66.0	
Feed & VSWR loss		-2.0	(TBD)	(TBD)	(TBD)	
Total gain in dB		41.0	(56.4)	(63.9)	(66.0)	
Total efficiency in %		23.8%	(59.4%)	(45.9%)	(19.6%)	
Nominal gain in dB		40.7	56.1	63.6	65.7	at horn neck

Table 5: An example of the gain calculation for a 10 m diameter antenna. Numerical values are given in dB, unless otherwise stated. TBD stands for “to be determined”.

Therefore, the surface accuracy is carefully specified under certain environmental conditions, such as, ‘at night time, under wind speed less than 10 m/s, and at elevation 45 degrees’. For high frequency radio telescopes, astronomers make regular efforts to improve the surface accuracy by precisely adjusting surface panels.

An example of the gain calculation, taking into account the surface accuracy, as well as illumination taper, blocking, and spillover effects, is given in table 5. One can easily confirm values of 100 % gain by equation (191), and values of surface accuracy effects for main reflector and subreflector by equation (205) (though we derived equation (205) for a main reflector, the same discussion is applicable for a subreflector as well).

3.15 Pointing Accuracy

The main lobe axis of a radio telescope antenna may not be exactly oriented towards a required direction due to the mechanical inaccuracy and the deformations due to the gravity and the wind pressure. The angular offset ϵ_θ between the actual and required directions is called “pointing error” or “tracking error” (Figure 79). The rms value of the pointing error is often called as **“pointing accuracy”** which we denote here as σ_θ

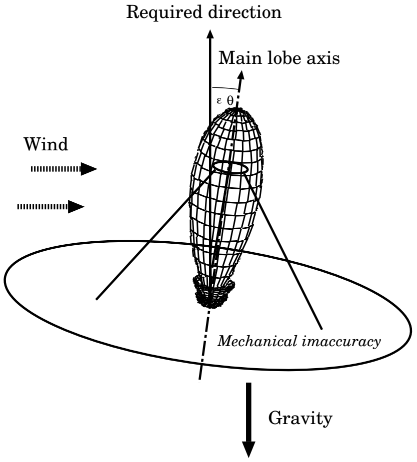

Figure 79: Pointing error.

$$\sigma_\theta = \sqrt{< \epsilon_\theta^2 >}. \tag{210}$$

Let us consider the loss of the received power from a radio source due to the pointing error. For simplicity, we assume a Gaussian power pattern $P(\theta)$

with the peak power P_0 and the HPBW Θ:

$$P(\theta) = P_0 e^{-ln2\left(\frac{2\theta}{\Theta}\right)^2} \tag{211}$$

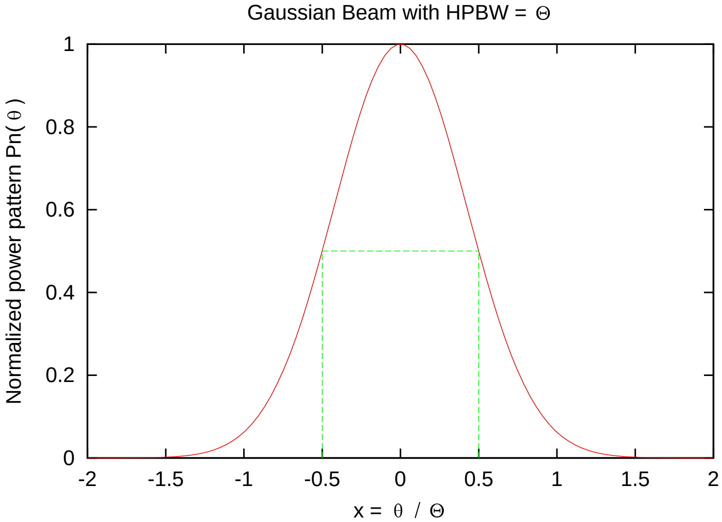

Figure 80: Gaussian beam.

If we assume that the main lobe axis is offset from the required direction in average by σ_θ, the received power from the radio source at the required direction is reduced in average by a factor of

$$\frac{P(\sigma_\theta)}{P_0} = e^{-4ln2\left(\frac{\sigma_\theta}{\Theta}\right)^2} = e^{-2.7726\left(\frac{\sigma_\theta}{\Theta}\right)^2}. \tag{212}$$

Figure 81 shows the power loss calculated by equation (212) as a function of the pointing accuracy σ_θ (which is denoted as σ in Figure 81 for simplicity).

It is evident from the figure that the pointing accuracy must be

$$\sigma_\theta \leq \frac{1}{10}\Theta \tag{213}$$

to keep the power loss smaller than several %. Table 6 shows the pointing accuracy requirement given in equation (213) for some typical cases of antenna diameter D and observing wavelength λ on the basis of the approximate formula $\Theta \simeq \lambda/D$.

Needless to say, a state–of–the–art technology of mechanical construction, good enough materials, and a sophisticated control system are needed, and

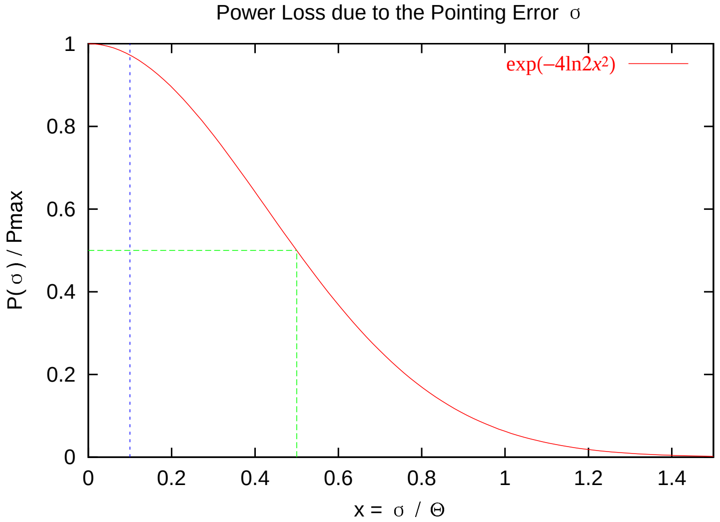

Figure 81: Power loss due to the pointing error.

D	10 m	20 m	22 m	21 m	45 m
ν_{max}	43 GHz	43 GHz	43 GHz	150GHz	200 GHz
λ_{min}	7 mm	7 mm	7 mm	2 mm	1.5 mm
HPBW $\cong \lambda/D$	0.°04	0.°02	0.°018	0.°0055	0.°0019
Required point. acc.	0.°004 (14”)	0.°002 (7.”2)	0.°0018 (6.”6)	0.°00055 (2.”0)	0.°00019 (0.”7)

Table 6: Requirements to the pointing accuracy.

hence a big money is required, to precisely keep the orientaion of a huge radio telescope antenna, with the accuracy of 0.001 degree or higher, under variable wind and heat conditions. The pointing accuracy is another cost–affecting factor, along with the surface accuracy.

To save the money, we sometimes take into account widening of the main beam due to the illumination taper in antenna specifications.

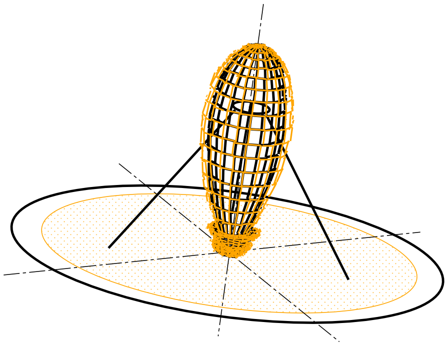

Figure 82: Widening of the main beam due to the illumination taper allows us to slightly ease the pointing accuracy requirement.

Rather strong illumination taper is necessary for avoiding pickup of the ground thermal noise radiation. The illumination taper widens the main beam. So we can take the effective aperture due only to the illumination taper, instead of the geometric aperture, in our calculation of the HPBW to ease the pointing requirement (Figure 82). Note, on the other hand, that degrading effects other than the illumination taper (surface roughness, blocking, etc) increase the sidelobe level, but not the main–beam width.

For example, let us consider an antenna of diameter $D = 22$ m with aperture efficiency due to the illumination taper $\eta_{Ait} = 75$ % at the highest frequency 43 GHz. Then, we have 'effective diameter' $D_e = D \times \sqrt{\eta_{Ait}} \cong 19$ m. Therefore, the effective HPBW becomes $0.^\circ 021$, and the required pointing accuracy becomes $0.^\circ 0021$, instead of $0.^\circ 0018$ shown in Table 6. This may have a sensible effect in cost estimation.

3.16 Design of the Feed System

While technological requirements to the surface and pointing accuracies are quite severe at high frequencies, major technological difficulties in designing the feed system occur at low frequencies.

In order to efficiently receive or transmit radio signal with a Cassegrain paraboloidal antenna, beam of the feed horn shoud not be too wide compared with the subreflector, since otherwise we would suffer from a significant spillover of the signal beyond the edge of the subreflector. Thus, if we denote the observing wavelength as λ, the diameter of the subreflector as D_S, the diameter of the feed horn as D_F, and the distance between the feed horn and the subreflector as L (Figure 83), we have to require that the beam width of the feed horn is smaller than D_S/L. The beam width is roughly given by λ/D_F in the far–field. However the far–field approximation is definitely inadequate in this case, since the subreflector is located in the near field (Fresnel region) of the feed horn, and therefore the beam is significantly broader than the far–field one. Usually, a stringent condition:

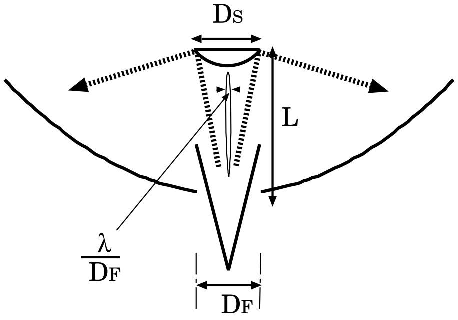

Figure 83: Diameters of the feed horn D_F and the subreflector D_S and their mutual distance L.

$$10\frac{\lambda}{D_F} < \frac{D_S}{L}, \tag{214}$$

is considered to be optimal.

Suppose that we use a paraboloidal antenna at several observing wavelengths. Let the longest wavelength and corresponding feed diameter be λ_{max} and $D_{F\,max}$, respectively. In order not to make either of the feed horn or the subreflector too large, it is natural to select that $D_S \simeq D_{F\,max}$. Thus the equation (214) is reduced to

$$\frac{D_{F\,max}^2}{\lambda_{max} L} \geq 10. \tag{215}$$

If we strictly adopt this condition, and assume $L = 10$ m for definiteness, we get following table of feed horn sizes for several cases of the longest wavelength. At observing frequencies as low as 1.4 GHz or 2 GHz, the optimum

λ_{max}	$D_{F\ max}$
3 mm (100 GHz)	0.55 m
7 mm (43 GHz)	0.84 m
1.4 cm (22 GHz)	1.2 m
3.8 cm (8 GHz)	2.0 m
15 cm (2 GHz)	3.9 m
21 cm (1.4 GHz)	4.6 m

Table 7: Maximum observing wavelengths vs. diameters of the feed horns.

sizes of the feed horns are quite large. An example is shown in Figure 84.

Sometimes, it is impractical to place big feed horns in receiver cabins. Therefore, we are often forced to design smaller feed horns by adopting larger subreflectors, though this would cause larger blocking. Moreover, it is a common practice to somewhat release the condition in equation (214) itself, partially sacrificing aperture efficiency at lower frequencies.

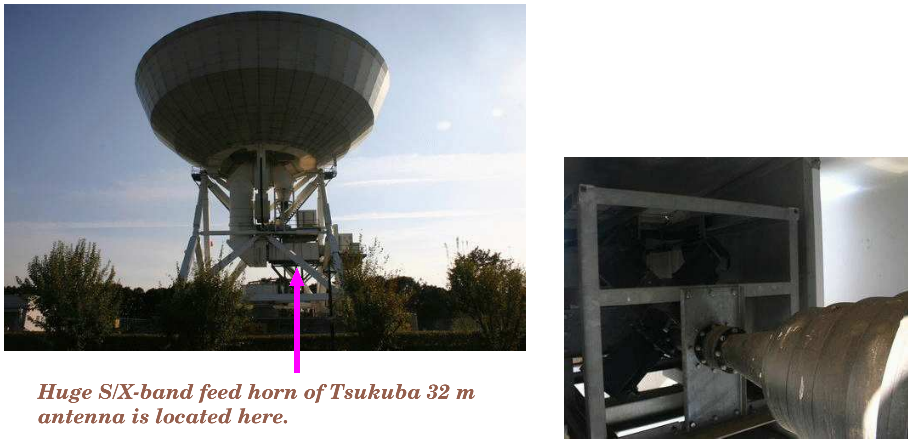

Huge S/X-band feed horn of Tsukuba 32 m antenna is located here.

Figure 84: 2 and 8 GHz feed horn of Tsukuba 32 m antenna.

An alternative way to receive the low frequency radio waves without too much increasing the feed–horn and subreflector sizes is to use the primary focus (Figure 85). In the primary focus case, a feed horn must ‘illuminate’ the whole area of a large main reflector. Therefore, a wide beam, and therefore a small diameter of the feed horn, is rather preferable.

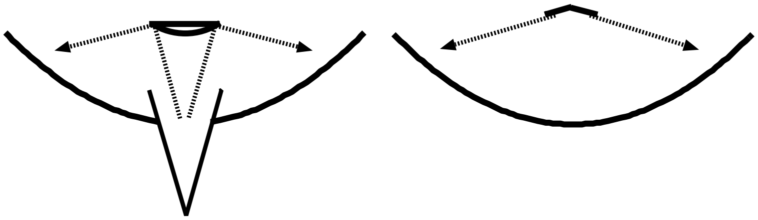

Figure 85: A large feed horn and subreflector system (Left) or a primary feed system (Right) is needed for low frequency observations.

The large feed horns and subreflectors, or the feed and receiver blocks on the primary focus, required for the low frequency observations, are nuisances for high frequency observations, since they may cause serious difficulties for achieving high aperture efficiency and pointing accuracy necessary at high frequencies. Nevertheless, it is a natural desire of radio astronomers to observe at as many frequency bands as possible, for example, from the 1.4 GHz line of the neutral hydrogen to the 115 GHz CO line, say, with a single radio telescope. Hence some sophisticated solutions are required (see examples in Figures 86, 87, and 88).

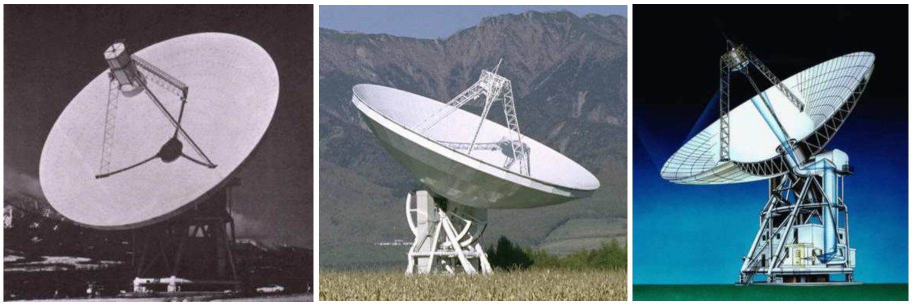

Figure 86: Initial Gregorian design of Nobeyama 45 m telescope, Japan (Left), adopted for receiving 1.4 GHz wave at primary focus, was later replaced by currently used Cassegrain design for better high–frequency performance (Middle). But still, a powerful wave–beam–guide feed system and a big receiver room (Right) allow to receive wide range of frequency bands from 20 GHz to 230 GHz.

A very unique design of feed system is adopted in radiotelescope antennas of KVN (Korean VLBI Network), Korea, for simultaneous reception of 4 observing bands at 22 GHz, 43 GHz, 86 GHz, and 129 GHz. Figure 89 shows a preliminary design drawing of the multi–frequency–channel receiving system consisting of frequency selective surfaces and metal mirrors suitably arranged to allow simultaneous feeding of the 4 frequency bands.

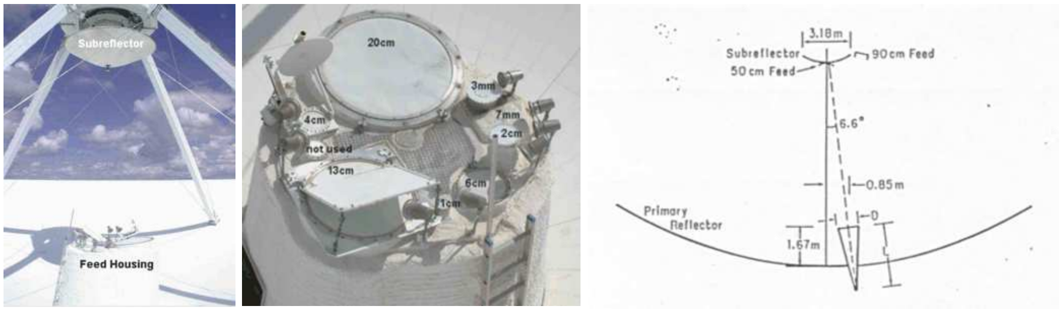

Figure 87: The tilted subreflector (Left) and feed horns arranged on a circle (Middle) in 25 m radio telescope of VLBA (Very Large Baseline Array), USA. Observing frequency bands from 1.4 GHz to 86 GHz can be easily changed by rotating the tilted subreflector around the symmetry axis of the main reflector as illustrated in a design drawing (Right).

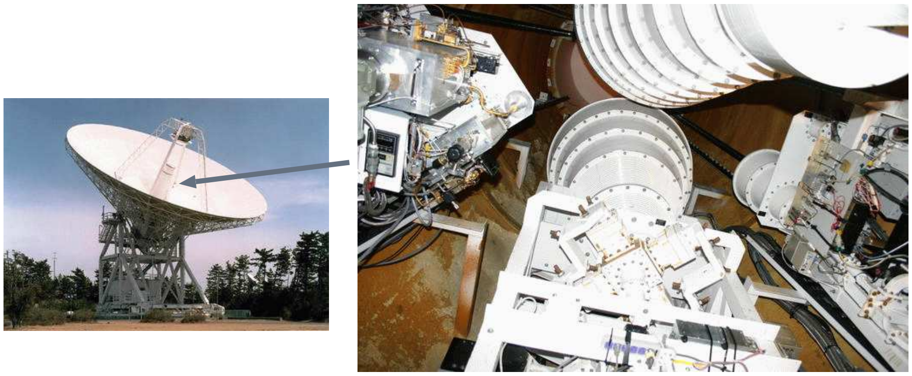

Figure 88: Feed horns and receivers of 34 m VLBI antenna (Left) at Kashima, Japan, for various frequency bands are uplifted to the focus one by one, along rails inside the "Feed Cone" (Right).

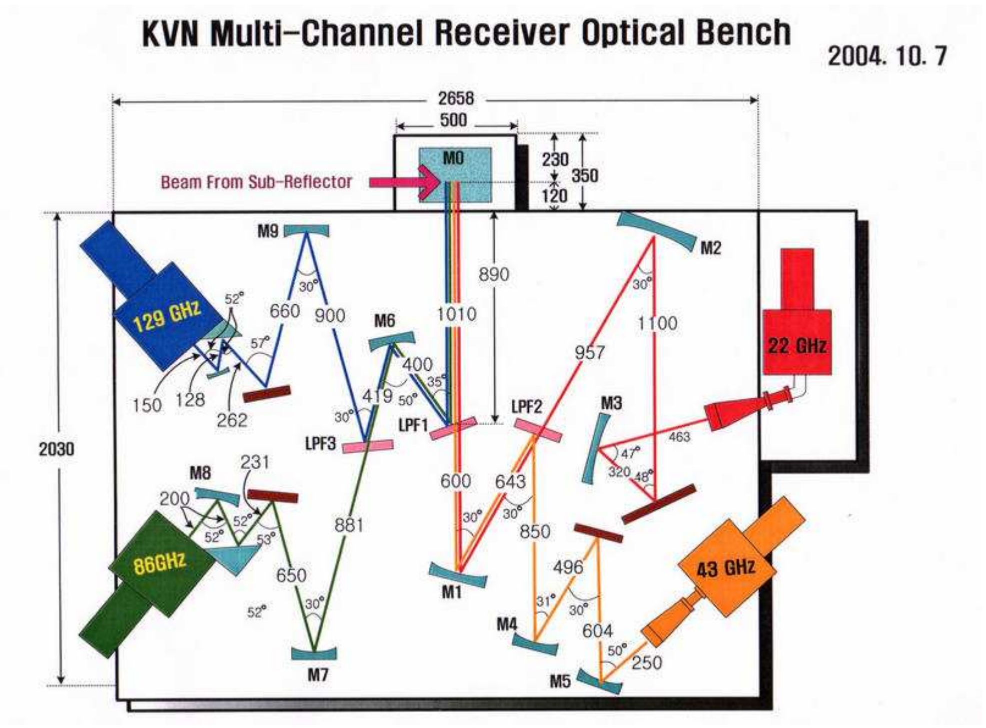

Figure 89: A preliminary design of the multi–frequency–channel quasi–optics receiving system of KVN (Korean VLBI Network), Korea.

3.17 Visible Reference Point

As we saw earlier, it is desirable to make an antenna reference point (usually the cross point of Az and El axes) visible from outside, in order to tie the point to geodetic markers on the ground. This should be specially specified, when necessary, since otherwise antenna designers may place a receiver cabin, a wave–beam–guide system or something else around the cross point.

Figure 90: In order to make the reference point visible from outside, one usually has to place whole feed and receiver system in a small cabin in the back structure of the main reflector (Left). For that purpose, we need compact feed systems. Examples of compact feeds, 1.4 GHz/2.3 GHz feed horn used in Australian Telescope, and helical array S/X feed used in VERA, are shown in right two panels.

To keep the cross point in an empty space, we have to place the receiver cabin somewhere else, most likely in a narrow space within the back structure under the vertex of the main reflector (left panel of Figure 90). For that purpose, we have to design compact feed horns and receivers settable in the narrow cabin (middle and right panels of Figure 90).

3.18 Alignment Errors and Offset of Axes

For both Alt–Azimuthal and Equatorial mount antennas, it is desirable that two axes (Az– and El–axes, or Right Ascension– and Declination–axes) exactly intersect at a point, and are mutually orthogonal. But after mechanical construction of antennas, the two axes usually show some finite offsets and alignment errors (Figure 91). Tolerances to these quantities are often specified to be less than a few mm and 0.01°, respectively.

Even though such requirements are satisfied, they may be still large enough to affect observational performances. The axes alignment erros may affect antenna pointings. The axes offset may require a correction in the high–precisioon geodetic VLBI analyses of an antenna position, since the offset no longer permits us to select the reference point on an exact cross point of the fixed and moving axes. Therefore, we must estimate and calibrate the axes alignment errors, based on antenna pointing measurements. Also, we

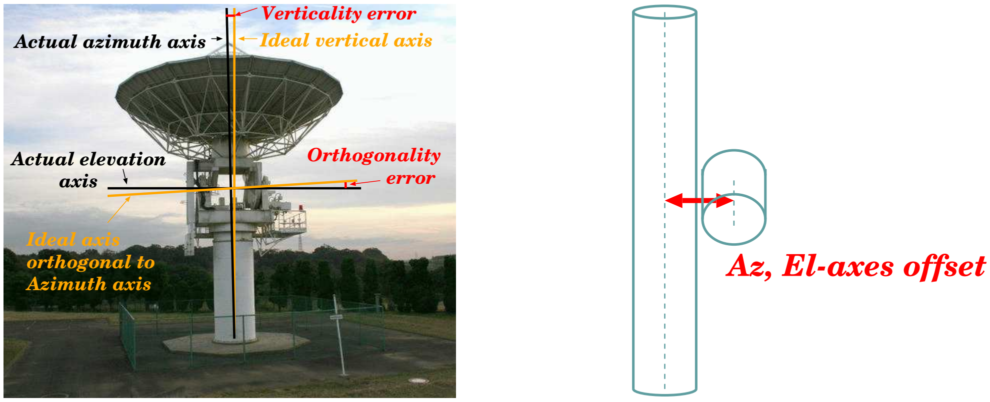

Figure 91: Images of Az axis verticality error, Az, El axes orthogonality error (Left), and Az, El axes offset (Right) in case of an Alt–Azimuth mount antenna.

have to estimate and calibrate the axes offset, based on local measurements and/or geodetic VLBI measurements themselves.

3.19 Range of Motion

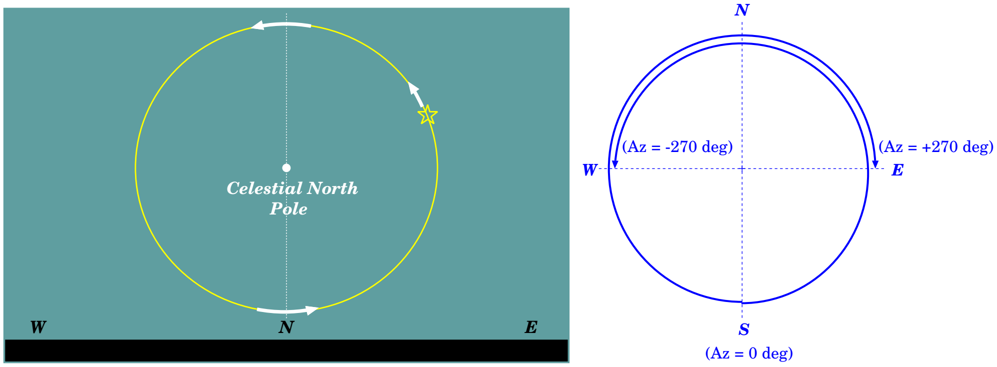

Figure 92: Diurnal motion of a circumpolar radio source (Left) and required range of azimuth motion (Right) for an Alt–Azimuth antenna.

For an Alt–Azimuth mount antenna, the range of azimuth and elevation angles must cover at least from $-180°$ to $+180°$ and from $0° \sim 5°$ to $90°$, respectively, in order to be able to point toward any direction in the sky. However, we have to also take into account that a radio source may cross the meridian line during an observation, from east to west, or west to east, in case of circumpolar sources, depending on their locations with respect to the celestial pole. In order to smoothly track such diurnal motions of radio sources, the azimuth motion range is usually chosen from −270° to +270° with 0° selected at South (the same range corresponds to −90° – +450° in the conventional azimuth angle measured eastward from North).

3.20 Slewing Speed

For VLBI antennas, especially for geodetic VLBI antennas, high slewing speeds both in azimuth and elevation are preferable, since the high slewing speeds allow us to effectively observe many sources on different points of sky within a limited telescope time, without losing much time for antenna repointing from one source to another. Generally, slew speeds larger than 2°/sec in both axes are desirable.

An IVS (International VLBI Service for Geodesy and Astrometry) Working Group Report "VLBI2010: Current and Future Requirements for Geodetic VLBI Systems" (2005) proposes slewing speeds of 5°/sec or higher in both axes for future geodetic VLBI antennas. The high slew rate is necessary mainly for estimating and removing atmospheric and clock–offset effects, which are the largest error sources in current geodetic VLBI.

In recent VLBI observations, a technique called "fast switching" is often used. In this technique, orientation of a telescope is switched between two closely spaced radio sources (typically, separated by less than a few degrees) within a period of time as short as 20 to 60 seconds, for compensating irregular atmospheric refraction effects (so called "phase–referencing"). For the fast switching, not only the slewing speeds, but also their accelerations must be sufficiently high, to realize the short switching cycle. For example, 3°/sec slewing speeds and $3°/\mathrm{sec}^2$ accelerations in both axes are recommended to achieve 20 second switching cycle for sources separated by 2 to 3 degrees.

3.21 Operational and Survival Loads

Operational and survival loads specify environmental conditions (temperature, wind speed, seismic acceleration, etc.) under which antennas can be used for observations, and can survive in a stable stow position (usually El = 90° and Az = 90° for an Az–El mount antenna) at rest, respectively. These loads must be determined depending on actual conditions of observing sites.

Usually, for mid–latitude stations with moderate wind, operational air temperature condition from ~ -20 to $\sim +40$ °C is appropriate.

As an example, we can distinguish following ranges of wind velocity v, though values listed are highly dependent on climatic conditions of observing sites, especially whether they are in strong typhoon (cyclon, or hurricane) areas or not.

- Accuracy guaranteed range: (for example, $0 \text{ ms}^{-1} \leq v \leq 10 \text{ ms}^{-1}$).
  Suarface and pointing accuracies are guaranteed.
- Operational range: (for example, $0 \text{ ms}^{-1} \leq v \leq 15 \text{ ms}^{-1}$).
  We can conduct observations, though desired surface and pointing accuracies may not be met at high frequencies.
- Operable range: (for example, $15 \text{ ms}^{-1} < v \leq 30 \text{ ms}^{-1}$).
  We must stop observations and move the antenna to "stow position".
- Survival range: (for example, $30 \text{ ms}^{-1} < v \leq 70 \text{ ms}^{-1}$).
  We must fix the antenna at the stow position with "stow pin".
- Out of range: (for example, $70 \text{ ms}^{-1} < v$).
  In the worst case, the antenna could be destroyed.

For a strong typhoon area, the survival wind load limit should be 90 ms^{-1} or higher.

4 Antenna Temperature and Single Dish Imaging

4.1 What Is the Antenna Temperature T_A?

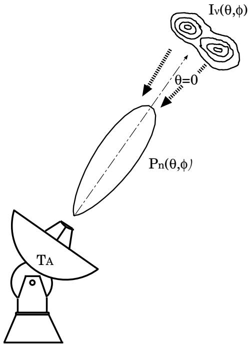

Figure 93: Antenna temperature.

"Antenna temperature", usually denoted as T_A, is an important, but again a little confusing, quantity often used in radio astronomy, as well as in VLBI geodesy. Actually, this is a quantity describing power W_ν per unit frequency bandwidth, centered at ν, received by an antenna. The power is regarded as a "noise power added to a detector", and converted to the "temperature of the noise" T_A according to the Nyquist theorem: $W_\nu = kT_A$. This is the antenna temperature.

Therefore, the amtenna temperature is a "temperature of a radio source as sensed by an antenna", and has nothing common with the temperature of the antenna body, measurable by a thermometer.

If we denote the effective aperture of the antenna as A_e and the effective flux density of the source as $\mathcal{S}_\nu$, then W_ν is $W_\nu = \frac{1}{2} A_e \mathcal{S}_\nu$, in view of equation (181). Therefore, the antenna temperature is given by

$$T_A = \frac{1}{2k} A_e S_\nu. \tag{216}$$

Then, denoting the normalized power pattern of the antenna as $P_n(\theta, \phi)$ and the source intensity distribution as $I_\nu(\theta, \phi)$ in the antenna–fixed coordinate system, we can transform the above equation to

$$W_\nu = \frac{1}{2} A_e \mathcal{S}_\nu = \frac{1}{2} A_e \iint\limits_{\Omega} P_n(\theta, \phi)\, I_\nu(\theta, \phi) \sin\theta \, d\theta \, d\phi,$$

in view of equation (174). We can formally extend the above range of the integration to the whole sky, since $P_n(\theta, \phi) \simeq 0$ outside the narrow beam anyway. Thus, using the solid angle element $d\Omega = \sin\theta d\theta d\phi$, we express the antenna temperature in equation (216) as

$$T_A = \frac{1}{2k} A_e \oint P_n(\theta, \phi)\, I_\nu(\theta, \phi)\, d\Omega, \tag{217}$$

(see Figure 93).

Taking into account equation (184) which relates the effective aperture A_e, the beam solid angle Ω_A and the wavelength λ

$$A_e \Omega_A = \lambda^2,$$

and the relation

$$\Omega_A = \oint P_n(\theta, \phi) d\Omega,$$

we can further transform equation (217) into

$$T_A = \frac{\lambda^2}{2k} \frac{\oint P_n(\theta, \phi)\, I_\nu(\theta, \phi)\, d\Omega}{\oint P_n(\theta, \phi) d\Omega}. \tag{218}$$

If we express the intensity I_ν through the brightness temperature T_B:

$$I_\nu = \frac{2k}{\lambda^2} T_B,$$

we obtain

$$T_A = \frac{\oint P_n(\theta,\phi)\, T_B(\theta,\phi)\, d\Omega}{\oint P_n(\theta,\phi) d\Omega}. \tag{219}$$

Therefore, the antenna temperature is the brightness temperature averaged over the antenna beam with the weighting function $P_n(\theta,\phi)$, which is the normalized power pattern.

4.2 Imaging with the Single Dish Radio Telescope

From the above discussions, we can interpret that the single dish radio telescope is a "huge power meter" measuring the weighted mean brightness temperature at a certain direction of the sky with the antenna power pattern as the weight. The single dish radio telescope can draw the image of the radio source by scanning from point to point meshed on the sky measuring the distribution of the brightness (intensity) averaged over the beam. It is thus naturally understood that the angular resolution of the image obtained by

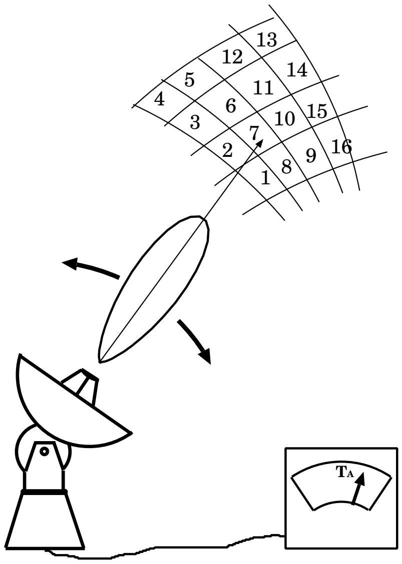

Figure 94: Scanning observation for radio source imaging with a single dish radio telescope.

the single dish radio telescope is determined by the beam size $\sim \lambda/D$, where λ is an observing wavelength and D is an antenna diameter (see Figure 94).

Let us examine three simplest cases of the source brightness distribution.

1. Point source $I_\nu(\boldsymbol{s}) = \mathcal{S}_\nu \delta(\boldsymbol{s} - \boldsymbol{s}_0)$, where $\mathcal{S}_\nu$ is the source flux density, while $\boldsymbol{s}$ and $\boldsymbol{s}_0$ are unit vectors, and $\boldsymbol{s}_0$ is parallel to the beam axis. In this case we have

   $$T_A = \frac{1}{2k} A_e \oint P_n(\boldsymbol{s})\, \mathcal{S}_\nu\, \delta(\boldsymbol{s} - \boldsymbol{s}_0)\, d\Omega = \frac{1}{2k} A_e\, \mathcal{S}_\nu. \tag{220}$$

   We can measure the effective aperture A_e or the aperture efficiency η_A by observing a point source of known flux density on the basis of this equation.

2. Source of finite extent which slightly exceeds the main lobe:

   $$T_A = T_B \frac{\int\limits_{main\ lobe} P_n(\theta, \phi) d\Omega}{\oint P_n(\theta, \phi) d\Omega} = \frac{\Omega_M}{\Omega_A} T_B = \eta_M T_B. \tag{221}$$

   We can measure the main beam efficiency η_M by observing this kind of source with known brightness temperature (for example, a planet) on the basis of the above equation.

   Correct account of the main beam efficiency η_M is essential for proper recovery of the sky distribution of T_B of the radio source in the single dish imaging. In most of VLBI observations, on the other hand, η_M is not important since source sizes of VLBI objects are usually much smaller than the main lobe size.

3. Widely extended homogeneous source:

   $$T_A = T_B. \tag{222}$$

   For example, we always receive the antenna temperature of 2.7 K from the cosmic microwave backgroud radiation.

Usually, the antenna temperature added by an astronomical radio source is very low, typically ranging from milli–Kelvins to Kelvins depending on the source and the telescope. For example, if we receive a relatively strong radio source with the effective flux density of 1 Jy ($= 10^{-26}$ W m^{-2} Hz^{-1}) using an 20 m diameter antenna with the aperture efficiency of 60 %, the antenna temperature is only about

$$T_A = \frac{1}{2k} A_e \mathcal{S}_\nu = \frac{1}{8k} \eta_A \pi D^2 \mathcal{S}_\nu \simeq 0.068 \text{ K}.$$

This is of course much lower than the physical temperature of an antenna body which is always ≃ 300 K.

Q : Why can't a radio telescope give us an image of the radio source just by a single observation like any optical telescope does?
A : Unlike the photo plate or CCD plate, a radio telescope is usually equipped with only one detecting element, the receiver. So what you can sense is whether the received power is strong or weak in the beam direction. If you have many receivers on the focal plane, then you will get the two–dimensional image at once. Now so–called multi–beam receiving systems are intensively developed at many radio astronomical observatories of the world for that purpose.

5 Receiving Systems

The very weak high frequency radio signal from an astronomical radio source collected by the main reflector is amplified and frequency converted by the receiving system and sent to the signal processing unit as the tractable signal of low frequency and with enough strength (Figure 95).

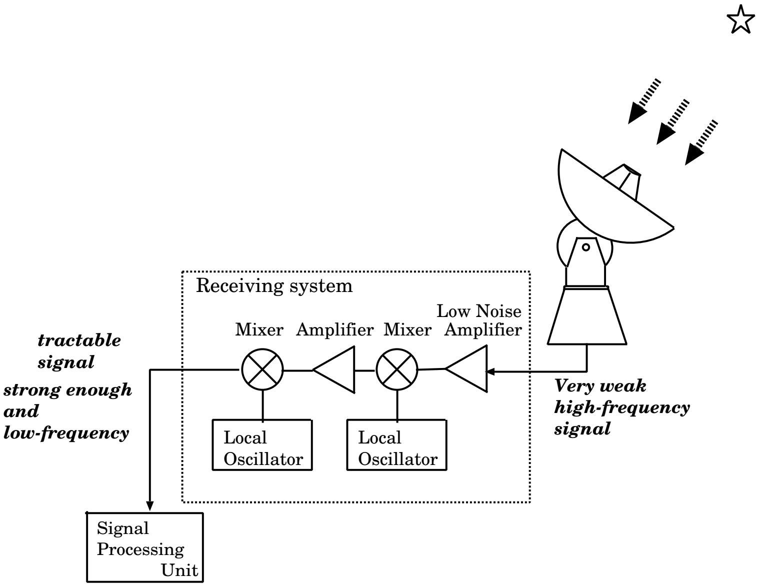

Figure 95: A schematic view of a radio telescope receiving system.

On the other hand, the receiving system inevitably adds some noise to the received signal, which may make it difficult to extract scientifically useful information with sufficiently high signal–to–noise ratio. Also, it is difficult to keep the ultra–high amplification ratio of the receiving system very stable in time. The gain variation effect must be well removed from the observed data for any measurement of the received power from a radio source.

So, the topics here will cover the system noise temperature, signal–to–noise ratio, frequency conversion and removal of the gain–variation effect.

5.1 System Noise Temperature

5.1.1 The "Input Equivalent Noise"

The word "system noise" means the "input–equivalent" of the sum of all noises generated in the receiving system (in the amplifiers, attenuators, connectors, ...), as well as in the ground pickups due to the sidelobes and the spillovers, and also in the thermal radiation of the atmosphere.

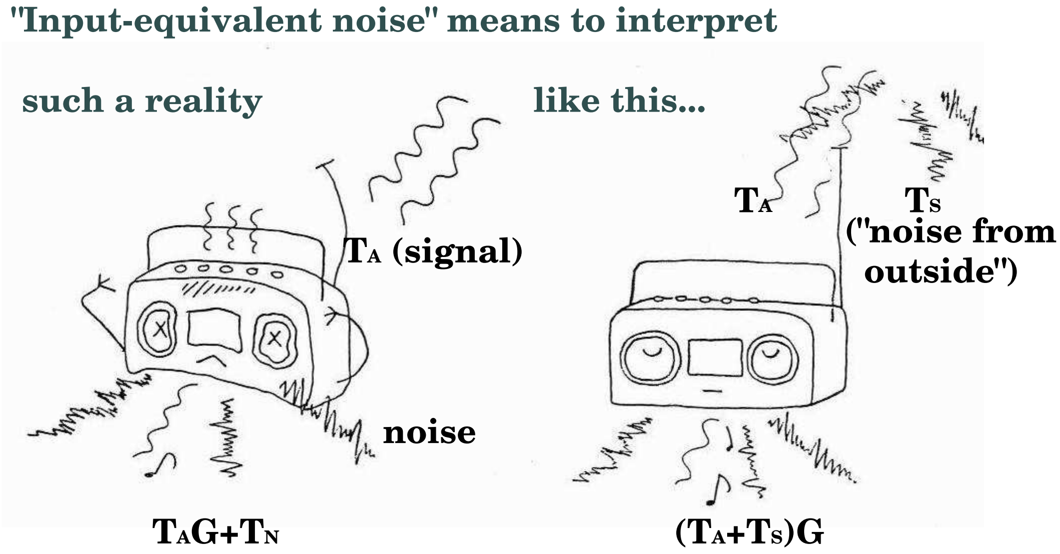

Figure 96: What is the "input equivalent noise"?

The "input equivalent" implies here to treat something occuring within and/or outside the system as if all come from the outside of the system as schematically illustrated in Figure 96.

If our system has a total gain G and if the noise power per unit frequency bandwidth at the output of our system is $W_{N\nu}$, then the power $W_{S\nu}$ of the input–equivalent system noise is

$$W_{S\nu} = \frac{W_{N\nu}}{G}.$$

The “system noise temperature” T_S is a temperature representing the power $W_{S\nu}$ of the system noise in terms of the Nyquist theorem $W_{S\nu} = kT_S$, i.e.,

$$T_S = \frac{W_{S\nu}}{k} = \frac{W_{N\nu}}{kG}.$$

5.1.2 Signal Attenuation and Thermal Noise

Let us consider how the thermal noise emerges within the receiving system using a model based on the radiative transfer equation, since it is likely that the absorption and emission of the radio wave occur in a similar way both in the wave guide systems of the receivers and in the interstellar clouds.

Let us apply the radiative transfer equation:

$$\frac{dI_\nu}{dl} = -\kappa_\nu I_\nu + \epsilon_\nu \, , \tag{223}$$

to some “lossy piece” of our receiving system with temperature T (Figure 97). For simplicity, we ignore the amplification for a while and consider the effect of the attenuation only. In equation (223), I_ν again stands for the intensity of the radio wave, l is the length along the optical path, and κ_ν and ϵ_ν are the opacity (or absorption coefficient) and the emissivity, respectively.

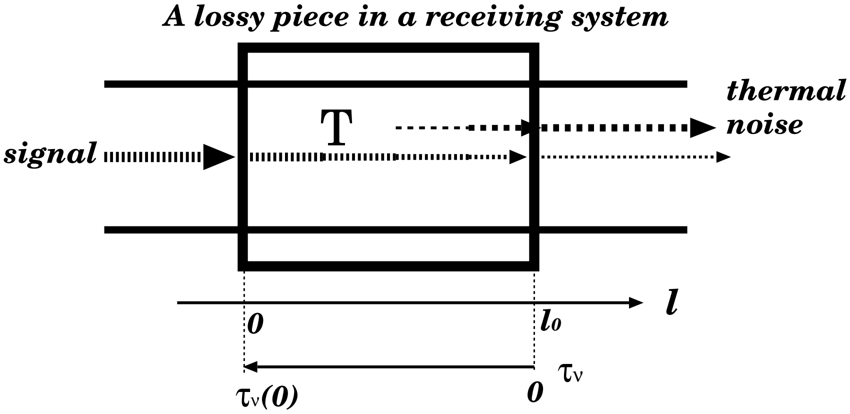

Figure 97: Signal attenuation and thermal noise emission in a lossy piece of the receiving system.

Since it is likely that every element of the lossy piece, for example attenuator, wave guide tube, connector, etc., is nearly in the thermodynamical eqilibrium with each other, giving rise to the Boltzmann distribution among energy levels, we assume the LTE (Local Thermodynamic Equilibrium) in the lossy piece. This means that Kirchhoff's law

$$\frac{\epsilon_\nu}{\kappa_\nu} = \mathcal{B}_\nu(T),$$

holds as a good approximation, although the radiation is not in the thermodynamic equilibrium with the elements of the lossy piece

$$I_\nu \neq \mathcal{B}_\nu(T),$$

where

$$\mathcal{B}_\nu(T) = \frac{2h\nu^3}{c^2}\frac{1}{e^{\frac{h\nu}{kT}}-1} \simeq \frac{2\nu^2}{c^2}kT \ \ (\text{when} \ \ h\nu \ll kT),$$

is the Planck function for the intensity of the blackbody radiation in the environmental temperature T of the lossy piece, which we approximate by the Rayleigh–Jeans function in our radio frequency range with $h\nu \ll kT$. Using the Kirchhoff's law and introducing the optical depth τ_ν

$$d\tau_\nu = -\kappa_\nu dl,$$

we can reduce equation (223) into

$$\frac{dI_\nu}{d\tau_\nu} = I_\nu - \mathcal{B}_\nu(T).$$

If we express the intensity I_ν through some "temperature" T_B as

$$I_\nu = \frac{2\nu^2}{c^2}kT_B$$

which is an equivalent of the brightness temperature in the interstellar–medium case, the equation (223) is further reduced to

$$\frac{dT_B}{d\tau_\nu} = T_B - T. \tag{224}$$

In the isothermal environment (T = const), a solution of equation (224) within the lossy piece, where $0 \leq l \leq l_0$ and $\tau_\nu(0) \geq \tau_\nu \geq 0$ as shown in Figure 97, is

$$T_B(l) = T_B(0)e^{\tau_\nu - \tau_\nu(0)} + T(1 - e^{\tau_\nu - \tau_\nu(0)}), \tag{225}$$

where $T_B(0)$ now can be interpreted as representing the power of the incoming signal at the input (left–most edge in Figure 97) of the lossy piece. In particular, a solution at the output (right–most edge in Figure 97) is

$$T_B(l) = T_B(0)e^{-\tau_\nu(0)} + T(1 - e^{-\tau_\nu(0)}). \tag{226}$$

The first term in the RHS of equation (226) corresponds to the power of the input signal attenuated by a factor of $e^{-\tau_\nu(0)}$ in the lossy piece, while the second term shows the power of the newly added thermal noise.

Note that, if $\tau_\nu(0) = 0$, the second term of the RHS of equation (226) is zero, so no thermal noise is added. Thus our general discussion, based on a simple model, leads to an important conclusion that **every receiver element adds thermal noise as far as it attenuates the input signal**.

Let us denote $\varepsilon = e^{-\tau_\nu(0)}$ and call it "transmission efficiency". $\varepsilon = 1$ means perfect lossless transmission, and $\varepsilon = 0$ means complete attenuation or zero efficiency.

The thermal noise T_N added in the system in temperature T with a transmission efficiency ε is $T_N = T(1-\varepsilon)$ according to equation (226). Therefore, the input–equivalent system noise temperature T_S of such a system is by definition

$$T_S = \frac{T_N}{\varepsilon} = \frac{T(1-\varepsilon)}{\varepsilon}. \tag{227}$$

In order to get a low–noise device, one must achieve a high transmission efficiency ε and/or cool the whole system in order to lower the environmental temperature T. This is the reason why modern highly sensitive radio telescope receivers are usually cooled to a very low temperature close to ~ 15 K or lower using cryogenic systems.

Q: Sometimes we see in advertisements of receivers for satellite broadcasting phrases like "65 K low noise amplifier in the room temperature". Isn't such a statement against the principles of the thermodynamics?
A: "65 K" here implies the system noise temperature which is the input–equivalent temperature of the noise added in the system. Since well made systems could transmit signals with high efficiency ($\varepsilon \simeq 1$) even in the room temperature $T \simeq 290K$, there is no violation of the thermodynamics.

Q: If we slightly misalign a wave guide tube, the system noise temperature of our receiving system could be as high as several thousand Kelvin. But why the purely passive element like wave guide tube can increase the temperature to such a high value?
A: You could increase the input–equivalent noise temperature to an arbitrarily high value if you only degrade the transmission efficiency. In fact, if $\varepsilon = 0$, then $T_N = T$, but $T_S = \infty$!

5.1.3 System Noise Temperature of the Multistage Receiving System

Receiving systems of the radio telescopes are usually composed of serially connected several amplifiers, frequency converters, and other related devices. Such a multistage design is required because it is extremely difficult to realize by a single amplifier the ultra–high amplification of the very weak signal of an astronomical radio source to the level of the tractable signal. In addition, it is also difficult to convert the high frequency signal to the low frequency signal by just one frequency converter.

For example, the power received from a source of the effective flux density $\mathcal{S}_\nu = 1$ Jy by an antenna with the diameter D =30 m, the aperture efficiency η_A =0.6 and the frequency bandwidth B = 200 MHz is

$$\begin{aligned} W &= \frac{1}{2} A_e \mathcal{S}_\nu B = \frac{1}{8} \eta_A \pi D^2 \mathcal{S}_\nu B \\ &= \frac{1}{8} \times 0.6 \times 3.145 \times 30^2 \times 1 \times 10^{-26} \times 200 \times 10^6 = 4.2 \times 10^{-16} \text{ W}. \end{aligned}$$

Even if we apply 100 dB (i.e., 10^{10} times) amplification to this signal, we obtain 4.2 μW only!

Therefore, a receiving system is usually implemented as a series of linear devices each having a gain G_i and a system noise temperature T_{Si}. A passive device like a transmission cable can be regarded as having a gain (= transmission efficiency ε) smaller than 1. For a device which both amplifies the signal and generates the noise, we can conceptually regard that a passive attenuator first reduces the signal power by a factor of ε_i and adds the thermal noise $T(1-\varepsilon_i)$, and then a lossless amplifier increases both the signal and the noise by a factor of G_i/ε_i, so that the total gain and the system noise temperature are described as G_i and $T_{Si} = T(1-\varepsilon_i)/\varepsilon_i$, respectively.

We do not include to this linear multistage receiving system the square law detectors or correlators because they are essentially non–linear devices.

Because of the linearity, the total gain G of an n–element multistage receiving system is expressed as

$$G = \prod_{i=1}^{n} G_i.$$

If we describe the gain in dB ($\tilde{G} = 10 \log_{10} G$, and $\tilde{G}_i = 10 \log_{10} G_i$), then we have

$$\tilde{G} = \sum_{i=1}^{n} \tilde{G}_i.$$

Now let us describe the output power P_i of i-th device in the n–element multistage receiving system through its gain G_i, system noise power kT_{Si}, and input P_{i-1}, which is the output power of (i–1)–th device, as

$$P_i = (P_{i-1} + kT_{Si})G_i, \tag{228}$$

(see Figure 98).

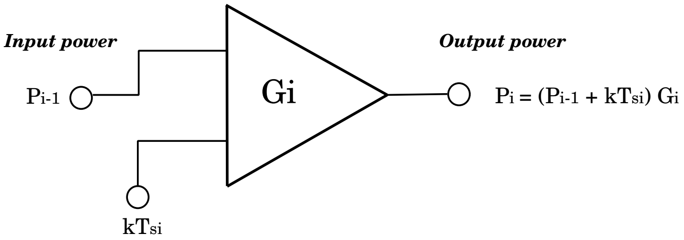

Figure 98: Input and output of a linear device with gain G_i and system noise temperature T_{Si}.

Then if we denote the input power to the first device as $P_0 = kT_A$, where T_A is the antenna temperature due to an astronomical source, the output power of n–th device is expressed as

$$\begin{aligned} P_n &= \{\cdots\{[(P_0 + kT_{S1})G_1 + kT_{S2}]G_2 + kT_{S3}\}G_3 + \cdots + kT_{Sn}\}G_n \\ &= kT_A \prod_{i=1}^{n} G_i + kT_{S1} \prod_{i=1}^{n} G_i + kT_{S2} \prod_{i=2}^{n} G_i + kT_{S3} \prod_{i=3}^{n} G_i \\ &\quad + \cdots + kT_{Sn}G_n, \end{aligned} \tag{229}$$

(Figure 99).

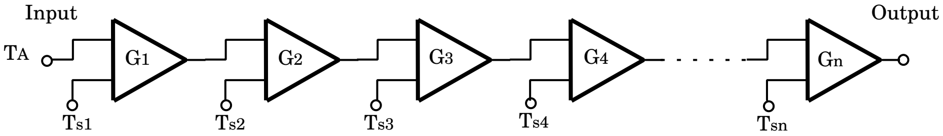

Figure 99: Multistage receiving system.

Denoting the total gain of the system as $G = \prod_{i=1}^{n} G_i$ and equating P_n in equation (229) to the sum of the input power and the sytem noise power multiplied by the total gain

$$P_n = k(T_A + T_S)G, \tag{230}$$

we obtain an expression for the total system noise temperature:

$$T_S = T_{S1} + \frac{T_{S2}}{G_1} + \frac{T_{S3}}{G_1 G_2} + \cdots + \frac{T_{Sn}}{G_1 G_2 \cdots G_{n-1}}. \qquad (231)$$

Since usually $G_i \gg 1$, the system noise temperature of a device in a later stage does not contribute much to the total system noise temperature T_S. On the other hand, the system noise temperature of the first stage device directly contributes to T_S and practically determines the system noise performance of the whole system. Therefore, **it is important to make the first stage device (mostly amplifiers) as low–noise as possible**. For this purpose, the first stage device is often cooled down to $\sim$ 15 Kelvin or lower. First stage amplifiers are frequently called “low noise amplifiers (LNA)”.

What we showed above can be summarized as replacing the actual multistage receiving system shown in the upper panel of Figure 100 by a simple total system shown in the lower panel.

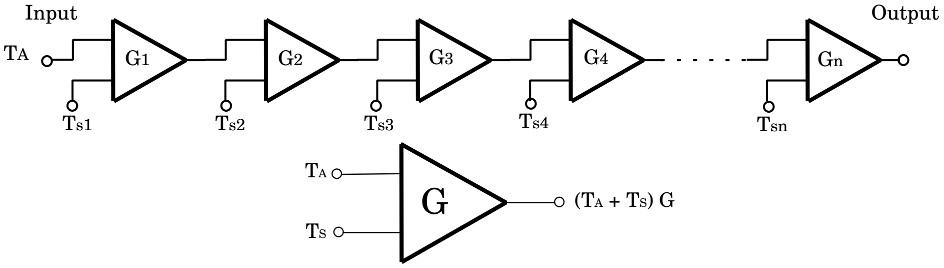

Figure 100: Total gain and total system temperature of the multistage receiving system.

The total system noise temperature T_S figuring in the output of the whole system as shown in equation (230) or in the lower panel of Figure 100 is relatively easily measured and provides the ratio T_A/T_S which is important in the signal–to–noise ratio considerations.

5.1.4 Receiver Noise Temperature T_{RX}

The system noise temperature of the receiving system only (i.e., not including other effects like atmospheric effects or ground pickups) is often called as “receiver noise temperature” and is denoted by T_{RX}.

Historically, a variety of low noise devices were used for the first stage which practically determines T_{RX}. Some examples of receiver noise temperatures of various devices in 1980s are shown in Figure 101 as functions of observing frequency.

Nowadays, low noise amplifiers (LNA's) made of HEMT (High Electron Mobility Transistor) are mostly used in a wide frequency range lower than 100 GHz, because HEMT amplifiers are stable, easy to handle and capable of receiving sufficiently wide bandwidth. HEMT amplifiers for 22 GHz or higher frequency are usually cooled by He–gas cryogenic system (Figure 103). At 8 and 2 GHz which are used in the current geodetic VLBI observations, He–cooling is rarely applied since the HEMT amplifiers are good enough at these frequency ranges even in the room temperature or in the electronically cooled system to provide T_{RX} as low as several tens of Kelvins.

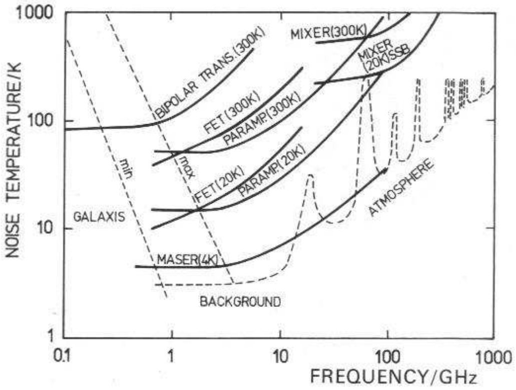

Figure 101: Receiver noise temperatures T_{RX} vs frequency diagram given in the 1st edition of 'Tools of Radio Astronomy' by K. Rohlfs (1986).

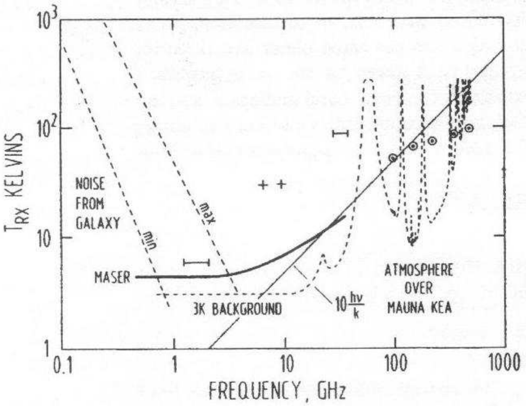

Figure 102: Receiver noise temperatures T_{RX} (bars and crosses: HEMT, circled dots: SIS mixers) vs frequency diagram given in the 3rd edition of 'Tools of Radio Astronomy' by K. Rohlfs and T.L. Wilson (2000).

At frequency higher than 100 GHz, He–cooled SIS (superconductor–insulator–superconductor) mixers instead of the amplifiers are usually used as the first stage device, since it is still difficult to make reliable low noise amplifiers for the high frequency range (Figure 104).

Figure 102 shows performance of the HEMT amplifiers and SIS mixers in 2000s. Note that many devices shown in Figure 101, including old FET and Parametric amplifiers, are no longer shown in Figure 102, because they are mostly replaced by HEMT amplifiers.

Figure 103: He–cooled 22 GHz and 43 GHz HEMT amplifiers placed in common cryogenic dewers and mounted on VERA dual–beam receiving system.

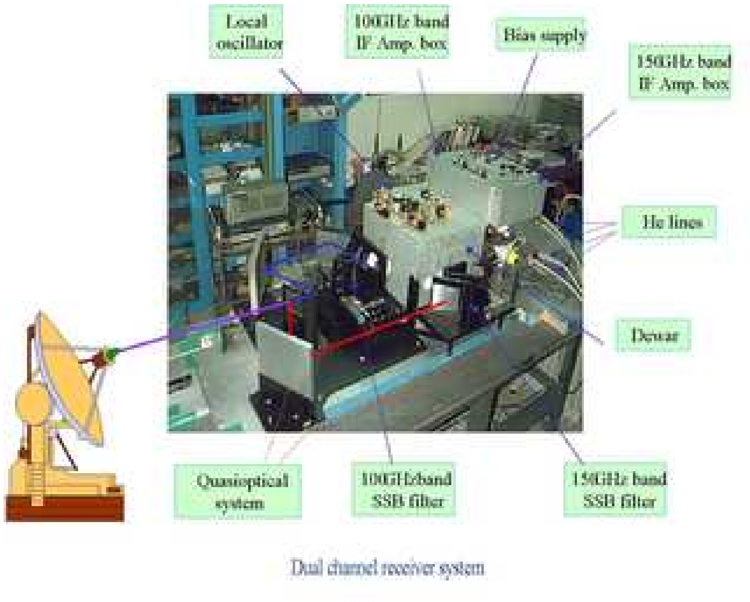

Figure 104: He–cooled SIS–mixer in the 100 GHz and 150 GHz dual channel receiver system of Taedok Radio Astronomy Observatory, Korea.

Recently, the "monothlic microwave integrated circuit (MMIC)" technology is replacing all separate components of an HEMT amplifier with a single chip, which can be mass produced, realizing inexpensive LNAs with great reproducibility and reliability. Figure 105 shows an example of the MMIC HEMT amplifier chip developed for VERA (VLBI Exploration of Radio Astronomy), Japan.

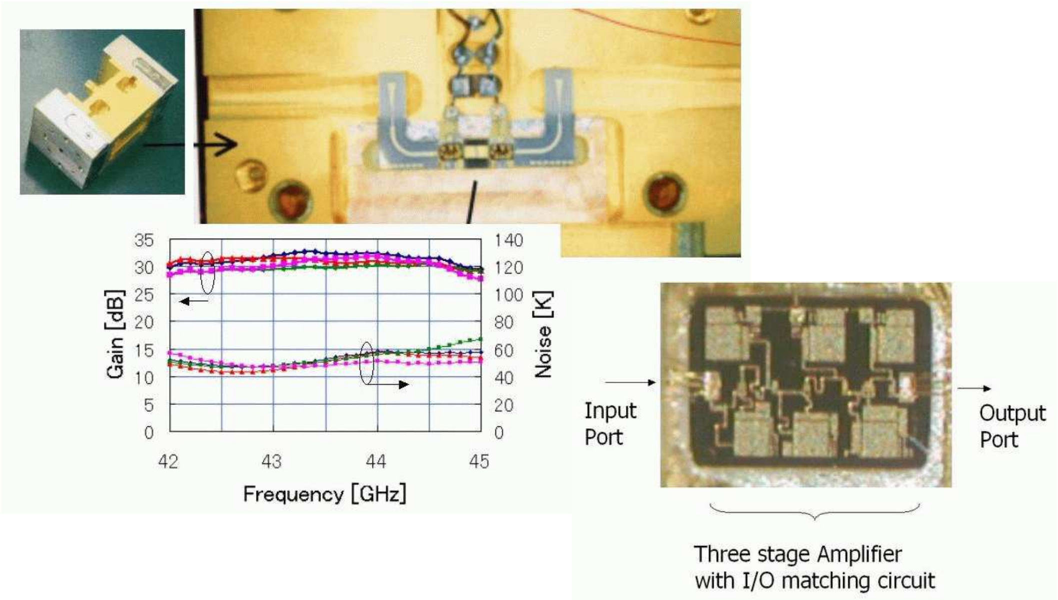

Figure 105: An MMIC HEMT amplifier chip developed for LNAs of VERA receivers. Lower left panel shows measured gain and receiver noise temperature of the chip.

5.1.5 Antenna Noise Temperature T_{ant} and Atmospheric Contribution to the System Noise Temperature

Besides the thermal noise generated within the receiving system, we have other contributions to the system noise as shematically illustrated in Figure 106.

The thermal radiation from the ground, which is picked up by sidelobes or spillovers from the main reflector edge, and all other noises which could be picked up or generated by the antenna structure, can be regarded as forming some "antenna related" noise power. We call a temperature which is calculated from the power using the Nyquist theorem the "antenna noise temperature" and denote as T_{ant}. Since the antenna noise temperature T_{ant} comes from outside of the antenna receiving system, it can be treated just

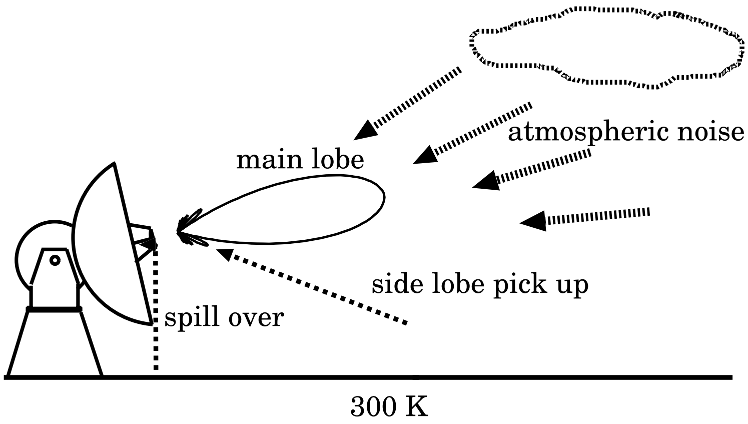

Figure 106: Atmospheric and ground pickup contributions to the system noise temperature.

as an input noise to the first stage of the receiving system. This means that T_{ant} can be simply added to T_{S1} in the RHS of equation (231). Of course, the antenna noise temperature must strongly depend on the elevation of the antenna beam since the ground pickup must be stronger at lower elevations.

The noise temperature T_{Nair} due to the thermal radiation of the atmosphere of temperature T_{atm} also contributes to the system noise temperature. The noise generation and signal attenuation in the atmosphere are described by the radiative transfer theory, which we discussed in Chapter 1 and used in subsection 5.1.2 for modeling the noise generation in a lossy piece of the receiving system.

Specifically, the radiative transfer equation under the assumption of the local thermodynamic equilibrium is given by equation (224):

$$\frac{dT_B}{d\tau_\nu} = T_B - T_{atm},$$

where T_B is the brightness temperature and τ_ν is the optical depth at an observing frequency ν. If we assume the isothermal atmosphere (i.e. $T_{atm} =$ const, which is not a very bad approximation in lower layers of the atmosphere where the signal attenuation is significant), solution of the above equation at the bottom of the atmosphere is given by equation (226):

$$T_B = T_B^\star e^{-\tau_{atm}} + T_{atm}(1 - e^{-\tau_{atm}}),$$

where $T_B^\star$ is the brightness temperature of a radio source outside of the atmosphere and τ_{atm} is the total optical depth at frequency ν due to the whole atmosphere. Note that first and second terms in the RHS of this equation represent contributions from the extra–atmospheric radio source and the atmospheric thermal noise, respectively.

Now we calculate the "temperature sensed by an antenna" directed towards a radio source as a weighted average of T_B over the antenna beam using equation (219):

$$\frac{\oint P_n(\theta,\phi)\, T_B(\theta,\phi)\, d\Omega}{\oint P_n(\theta,\phi) d\Omega} = \frac{\oint P_n(\theta,\phi)\, T_B^{\star}(\theta,\phi)\, d\Omega}{\oint P_n(\theta,\phi) d\Omega}\, e^{-\tau_{atm}} + T_{atm}(1 - e^{-\tau_{atm}}),$$

where θ and ϕ are angular coordinates in the antenna–fixed coordinate system as before, $P_n(\theta,\phi)$ is the normalized power pattern, and τ_{atm} here is the total otical depth along the direction of the antenna beam. When we derived the above equation, we assumed that T_{atm} and τ_{atm} are almost constant within the narrow solid angle of the antenna beam. The first term in the RHS is the antenna temperature due to the attenuated signal from the extra–atmospheric radio source:

$$T_A = \frac{\oint P_n(\theta,\phi)\, T_B^{\star}(\theta,\phi)\, d\Omega}{\oint P_n(\theta,\phi) d\Omega}\, e^{-\tau_{atm}},$$

and the second term is the thermal noise generated in the atmosphere:

$$T_{Nair} = T_{atm}(1 - e^{-\tau_{atm}}). \tag{232}$$

Note that τ_{atm} and therefore T_{Nair} vary significantly with elevation of the antenna beam.

Since both T_A and T_{Nair} are inputs of the antenna from outside, the atmospheric noise temperature T_{Nair} is just added to T_{S1} in the RHS of equation (231) when we calculate the total system noise temperature.

Therefore, the total system noise temperature T_S, including the receiver noise, the antenna noise and the atmospheric noise effects, is given by

$$T_S = T_{RX} + T_{ant} + T_{atm}(1 - e^{-\tau_{atm}}). \tag{233}$$

Equation (233) is usually given as a general expression of the system noise temperature.

However, when a radio telescope is covered by a radome or a feed–cone cover (see Figure 88 as an example) which slightly emits thermal noise radiation, or is exposed to a strong human made radio frequency interference (RFI), one should take into acount contributions of these additional noise sources to the system noise temperature.

When we consider the contribution of the radome or feed–cone cover to the system noise temperature, in particular, we have to distinguish reflection loss and absorption loss due to the cover. Reflection on the cover material and supporting frames blocks a part of incident rays and therefore reduces signal power to be received, but does not generate noise radiation. On the other hand, absorption induces both signal attenuation and noise generation. Consequently, only the absorption loss contributes to the system noise.

If we denote the absorption loss of the radome or feed–cone cover as $1 - e^{-\tau_{mem}}$, where τ_{mem} is the optical depth of the cover membrane at the observing frequency, and if we assume that temperature of the membrane is just equal to the air temperature T_{atm}, then both signal and atmospheric noise are attenuated by $e^{-\tau_{mem}}$ and, at the same time, new thermal noise $T_{atm}(1 - e^{-\tau_{mem}})$ is generated in the membrane. Therefore, we have

$$T_A = \frac{\oint P_n(\theta, \phi)\, T_B^{\star}(\theta, \phi)\, d\Omega}{\oint P_n(\theta, \phi) d\Omega}\, e^{-(\tau_{atm}+\tau_{mem})},$$

and

$$T_S = T_{RX} + T'_{ant} + T_{atm}[1 - e^{-(\tau_{atm}+\tau_{mem})}],$$

for the antenna temperature T_A and the system noise temperature T_S when the radome or feed–cone cover effect is significant. Here we denoted the antenna noise temperature as T'_{ant} taking into account that a part of the ground pickup radiation must be attenuated by the cover membrane.

5.2 Frequency Conversion

If a radio signal is band limited, that means it has non–zero spectral power within a certain frequency range with a finite bandwidth only, we can shift the central frequency of such a signal (usually to the lower side) without losing any spectral information (Figure 107). This is the principle of the frequency conversion, which can be generally interpreted as a result of the shift theorem of Fourier transformation.

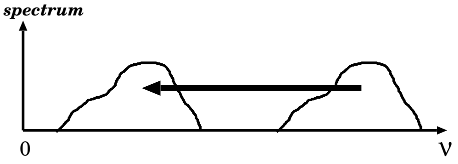

Figure 107: Frequency shift of the band limited signal.

Frequency conversion is needed in the radio telescope receiving system because

1. the received signal is much less attenuated in transmission cables and is much easily filtered, detected by a square–law detector, digitized, and so on, in the low frequency (lower than 1 GHz, say) than in the high frequency, and
2. it is necessary that the input and output signals are in different frequency bands before and after the enormous amplification of several tens to hundreds dB for avoiding possible leakage of a small amount of output power back to the input which could terribly oscillate the system.

5.2.1 Technical Terms in the Frequency Conversion

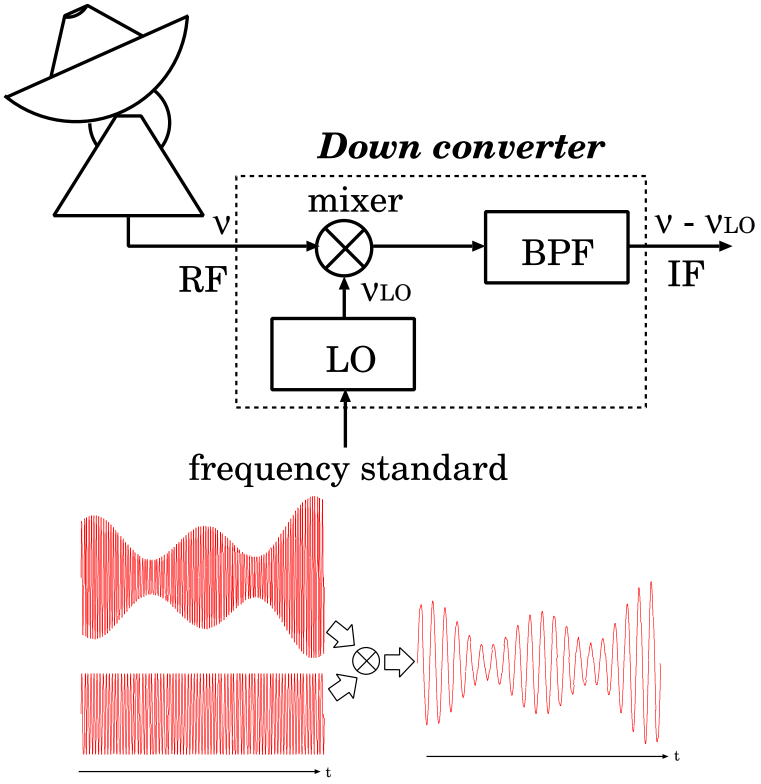

Figure 108: Elements and technical terms used in the frequency conversion.

A little peculiar technical terms are used in descriptions of the frequency conversion. They are

- **radio frequency (RF)**: the high frequency involved in the band which is directly received by an antenna, sometimes called also as "sky frequency",

- **intermediate frequency (IF)**: the low frequency obtained by the frequency conversion,

- **local oscillator (LO)**: an oscillator which provides a sinusoidal reference signal with a specified frequency,

- **mixer**: a nonlinear device which multiplies the reference signal to the received signal,

- **bandpass filter (BPF)**: a filter which passes only necessary band of the intermediate frequency and cuts off all other frequency components in the output from the mixer,

- **down converter**: a unit composed of the LO, mixer and BPF which converts RF ν to IF $\nu - \nu_{LO}$, where ν_{LO} is the frequency of the reference signal provided by the LO which is often called "LO frequency",

- **superheterodyne receiver**: a receiver based on the frequency conversion technique.

Figure 108 shows elements of the frequency conversion. For example, in a typical Mark III–type geodetic VLBI observation at 8 GHz, we can choose 8180 MHz $\sim$ 8600 MHz as the RF band and 8080 MHz as the LO frequency ν_{LO} to get 100 MHz $\sim$ 520 MHz as the IF band.

5.2.2 What Is the Mixer?

The main part of the mixer is a device (for example, a mixer diode) which has a nonlinear current (I) — voltage (V) relation:

$$I = a_0 + a_1 V + \boldsymbol{a_2 V^2} + a_3 V^3 + \cdots, \tag{234}$$

where a_i's are constant coefficients.

The received signal and the reference signal from LO are first summed up before entering to the nonlinear device. So, denoting the voltage of a frequency component with the angular frequency $\omega = 2\pi\nu$ in the RF band as $V_s \cos(\omega t + \phi)$ and the voltage of the reference signal with LO angular frequency ω_{LO} as $V_{LO} \cos(\omega_{LO} t + \phi_{LO})$, where ϕ and ϕ_{LO} are initial phases, we have the summed input voltage V to the nonlinear device:

$$V = V_s \cos(\omega t + \phi) + V_{LO} \cos(\omega_{LO} t + \phi_{LO}). \tag{235}$$

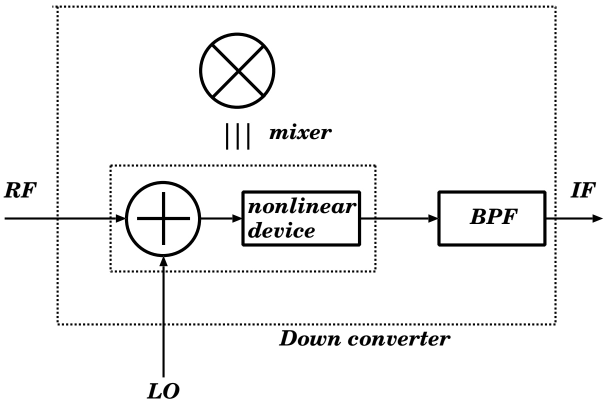

Figure 109: General concept of the mixer.

Therefore, we obtain a term proportional to $V_s V_{LO}$ in the output current from the nonlinear device due to the second order term $a_2 V^2$ of the I–V relation in equation (234), which is

$$\begin{aligned} & a_2 V_s V_{LO} \cos(\omega t + \phi) \cos(\omega_{LO} t + \phi_{LO}) \\ = & \frac{1}{2} a_2 V_s V_{LO} \cos[(\omega + \omega_{LO})t + \phi + \phi_{LO}] \\ + & \frac{1}{2} a_2 V_s V_{LO} \cos[(\omega - \omega_{LO})t + \phi - \phi_{LO}]. \end{aligned} \tag{236}$$

The first and second terms in the RHS of equation (236) correspond to up–converted and down–converted frequencies, respectively. So, we can realize the desired frequency conversion by picking up only the down–converted frequency with a suitably designed BPF which passes the down–converted frequency and cuts off the up–converted as well as all other frequencies produced by the I–V relation in equation (234). Note that the linearity of the received signal is preserved in this procedure though we used the nonlinear device.

5.2.3 Upper Sideband (USB) and Lower Sideband (LSB)

If the LO frequency is chosen within the received RF band, two frequencies ω_U and ω_L satisfying relations

$$\omega_U - \omega_{LO} = \omega_{IF} \tag{237}$$

and

$$\omega_{LO} - \omega_L = \omega_{IF}, \tag{238}$$

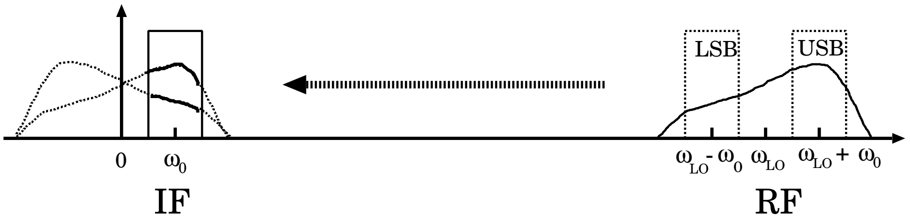

Figure 110: Upper and lower sidebands are converted to the same IF band.

both pass through the BPF and have the same IF ω_{IF}. In fact, they both have the same $\cos(\omega_{IF}t + \cdots)$ form in the mixer output as the above discusion on the mixer principle shows. The frequency higher than the LO frequency forms “upper sideband (USB)” and the lower one forms “lower sideband (LSB)”. When the both sidebands contribute to the IF band, the IF spectrum turns out to be a superposition of the down–converted spectra of the USB and the frequency–inverted LSB as illustrated in Figure 110. Frequencies in different sidebands corresponding to the same IF frequency are called “mirror frequencies” or “image frequencies”.

5.2.4 Sideband Rejection

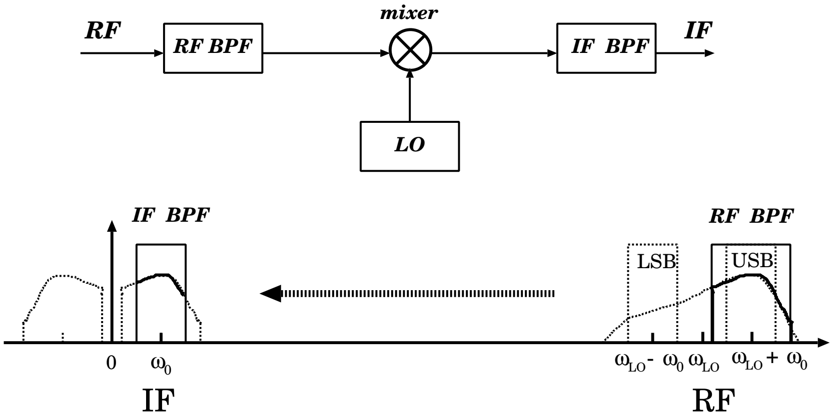

Figure 111: Sideband rejection in terms of the BPF in the RF band.

A superheterodyne receiving system which accepts both USB and LSB contributions to the IF band is called “double sideband (DSB)” receiver, while a system which receives only one of the two sidebands is called “single sideband (SSB)” receiver.

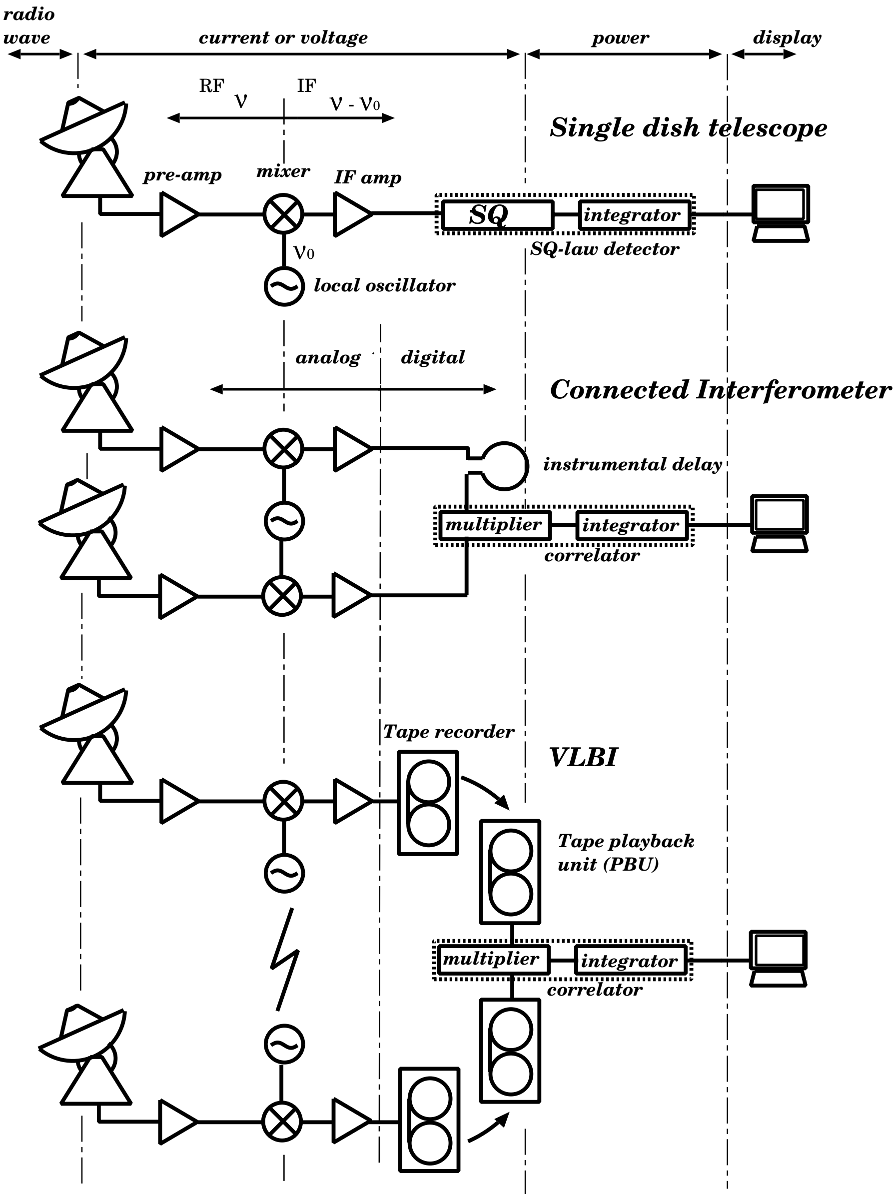

Figure 112: Superheterodyne receiving systems in single dish telescope (Top), connected interferometer (Middle) and VLBI (Bottom).

For observations of continuum sources, the DSB receivers offer better sensitivity, while for observations of spectralline sources, SSB receivers are preferred. In VLBI observations, SSB receivers are mostly used even for continuum sources for avoiding complication of the data processing.

The process to remove unnecessary sideband for a SSB observation is called “sideband rejection” or “image rejection”. The rejection is most simply realized by a suitable BPF in the RF range which limits the RF band of the mixer input in such a way that the LO frequency falls outside of the input band (Figure 111).

The frequency–conversion or superheterodyne technology is generally used in all kinds of radio telescopes including single dish telescopes, connected element interferometers and VLBIs (Figure 112).

5.3 Signal–to–Noise Ratio of a Single–Dish Radio Telescope

How can we estimate sensitivity (or signal–to–noise ratio) of a single–dish radio telescope?

In order to answer to this question, we have to address following three problems beforehand:

1. how can we separate a source signal and a system noise in our single–dish observation when both of them are Gaussian random noises?
2. how can we detect a weak source signal out of an overwhelmingly strong system noise?
3. how do we define the signal–to–noise ratio for a single–dish radio telescope?

We will consider these problems one by one.

1. *How can we separate a signal and a noise?*

In order to detect a signal of a radio source, of course we have to separate the signal from all kinds of noises coming from the receiver system and the environment (the system noise). However, the radio source signal itself is a Gaussian random noise, which is much the same with the system noise. In other words, we cannot separate the radio–source signal and the system noise by their temporal behaviors. If the observed source is a spectralline source, we could in principle distinguish the source signal by its spectral shape. But in case of a continuum source, spectral shapes of the signal and the system noise are much the same again. So there is no way for signal detection for a continuum source other than just watching an increase and a decrease of the level of the receiver output occuring when we direct our telescope towards the source and then off the source, as illustrated in Figure 113.

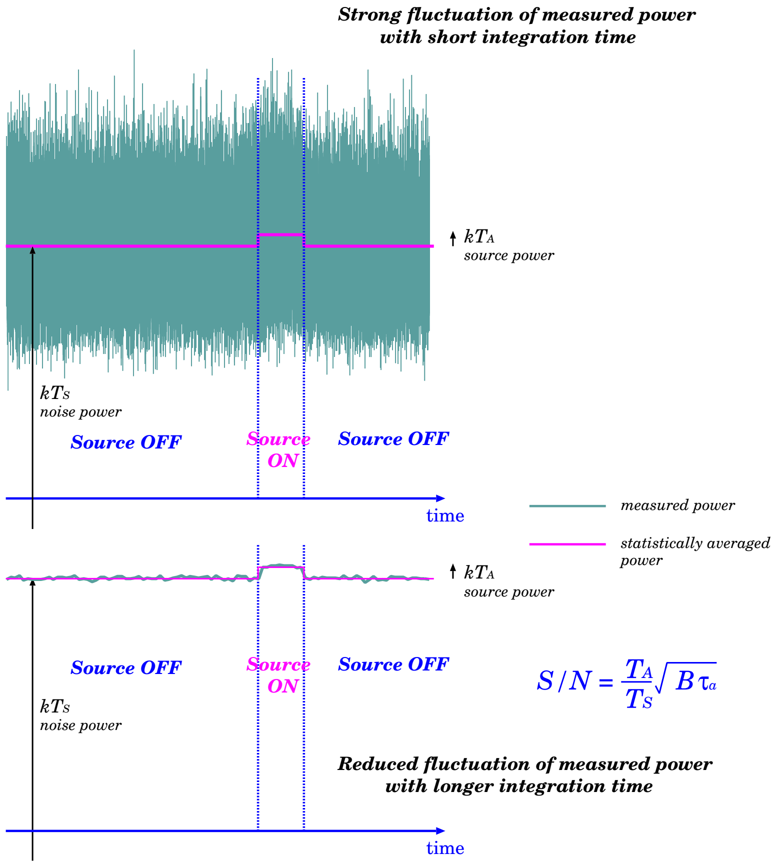

Figure 113: Source on—off observation and suppression of fluctuation in the measured power by integration (averaging). Number of averaged data points in the lower panel is 1000 times as large as that in the upper panel.

Then, how can we define and measure levels of the source signal and the system noise which are both Gaussian random noises?

If we time–average a noise, we usually get zero, as far as the noise randomly fluctuates around the zero state. However, if the noise is squared, i.e. converted to the power, then the power, though still fluctuates, always has some non–zero average value, which we can define as the noise level.

As we discussed before, average power of the system noise per unit bandwidth is kT_S, where k is the Boltzmann constant and T_S is the system noise temperature, while average power of the noise signal from the source per unit bandwidth is kT_A, where T_A is the antenna temperature. Therefore, we can expect an increase in the power of the receiver output due to T_A over the noise power due to T_S, when our telescope catches a source. Thus we can, in principle, separate the signal from the noise in this way.

2. *How can we detect a weak signal out of a much stronger noise?*

However, the signal T_A is usually much (several thousand times, say) smaller than the very high "noise floor" T_S for most of astronomical radio sources. Moreover, the squared random noise, i.e. the instantaneous noise power, itself randomly fluctuates in time around its average value, as we said before. If the fluctuation is larger than the average signal power, it is quite hard to detect the small increase of the output power due to the signal.

Fortunately, however, we can suppress the fluctuaion if we time–average the output power during some period of time (or "**integrate**" it). While the integration is not sufficiently long, it is still difficult to detect a weak source signal as illustrated in the upper panel of Figure 113. But if the integration time is long enough, the fluctuation is well suppressed and we can firmly detect the source as shown in the lower panel of Figure 113.

Actually, what we measure by our radio telescope is an integrated received power. In fact, as we saw in Figure 112, the radio signal from an astronomical source received by a radio telescope antenna is transmitted, together with the system noise, through the receiving system as a voltage (or a current). After several steps of amplification and down–conversion, a unit like a square–law detector squares the voltage to make the power, which is then time–averaged for some integration time by an integrator, and eventually displayed to observers by a power meter or other devices.

Note that the integration (time–averaging) is not a specific feature of the source on–off observation of a continuum source only, but is common to all kinds of radio astronomical observations. For example, source spectra which we obtain for spectralline sources are actually time–averaged power spectra of received voltages. If the integration is insufficient, we get jaggy and time–fluctuating spectrum due mainly to the noise, from which we cannot derive any reliable source spectrum.

Thus, we can detect a weak signal out of a much stronger noise if we integrate the received power for a sufficiently long time.

3. *How do we define the signal–to–noise ratio?*

Now it is natural to define the signal–to–noise ratio in the single–dish radio astronomy as a quantity showing how well we can detect the source through the integration (time–averaging) of the received power.

Specifically, we define it as a ratio between the average signal power and the **level of fluctuation** (standard deviation) of the time–averaged noise power.

Do not mix up this with the original ratio of the average signal power and the average noise power T_A/T_S, which is hopelessly small for most of astronomical radio sources.

This is our answer to the third problem.

A statistical theory of the dispersion of the time–averaged squared random data, which we will discuss in Chapter 3 in detail, shows that the signal–to–noise ratio S/N of the integrated received power is expressed in terms of the antenna temperature T_A, system noise temperature T_S, bandwidth B and integration (or averaging) time τ_a by a formula:

$$S/N = \frac{T_A}{T_S}\sqrt{B\tau_a}. \tag{239}$$

Or, if we express T_A, following equation (216), through Boltzmann constant $k = 1.381 \times 10^{-23}$, effective aperture A_e, effective flux density $\mathcal{S}_\nu$, diameter D and aperture efficiency η_A of a circular aperture antenna, we have

$$S/N = \frac{A_e \mathcal{S}_\nu}{2kT_S}\sqrt{B\tau_a} = \frac{\pi \eta_A D^2 \mathcal{S}_\nu}{8kT_S}\sqrt{B\tau_a}. \tag{240}$$

Thus, we can estimate the signal–to–noise ratio in a single–dish observation on the basis of this equation.

As we mentioned earlier, even if we observe a relatively strong radio source with the effective flux density of 1 Jy ($= 10^{-26}$ W m^{-2} Hz^{-1}) using an 20 m diameter antenna with the aperture efficiency of 60 %, the antenna temperature is only about

$$T_A = \frac{1}{2k} A_e \mathcal{S}_\nu = \frac{1}{8k} \eta_A \pi D^2 \mathcal{S}_\nu \simeq 0.068 \text{ K}.$$

Therefore, if the system noise temperature is 100 K (which is not a bad figure, by the way), the original ratio of the average signal power and the average system noise power is only

$$\frac{T_A}{T_S} = 6.8 \times 10^{-4} \ !$$

Nevertheless, if we observe the source with a fairly wide frequency bandwidth $B = 100$ MHz and integrate the output power for 1 second, then the signal–to–noise ratio is

$$S/N = \frac{T_A}{T_S}\sqrt{B\tau_a} = 6.8,$$

and therefore well detectable! This is the way how radio astronomers receive the radio source signals.

5.4 Gain Variation of Receivers and Switching Observations

The high signal–to–noise ratio does not necessarily guarantee the detection of a radio source since there might be disturbing effects other than the thermal noise. One of such effects is the gain variation of the receiving system. At frequencies higher than $\simeq$ 15 GHz, the time variation of the atmospheric thermal radiation is another serious problem.

In order to understand why the gain variation may prevent the detection of the signal from the astronomical source, we consider again the output power of the receiving system:

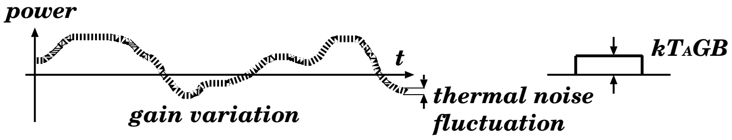

Figure 114: The gain variation prevents the detection of the astronomical radio source even when the S/R is sufficiently high.

$$W = k(T_A + T_S)GB, \tag{241}$$

where k is the Boltzmann constant, T_A is the antenna temperature due to the astronomical source, T_S is the system noise temperature, G is the total gain and B is the receiving bandwidth. Suppose that G shows some short–term (a few minutes, say) time variation ΔG. Then received power would vary as much as

$$\Delta W_G = k(T_A + T_S)\Delta G\, B. \tag{242}$$

Since the system noise temperature T_S is usually much larger than the antenna temperature T_A, the variation $\Delta W_G \simeq kT_S\,\Delta G\, B$ could easily exceed kT_AGB itself, making the detection of the source almost impossible (Figure 114).

The simple observation measuring the received power as described so far is called “total power mode observation” or “total power radiometry”.

The above discussion shows that a condition

$$\frac{T_A}{T_S} > \frac{\Delta G}{G}, \tag{243}$$

must hold, in order for a source to be detected against the gain variation in the total power mode observation. For a source with $T_A \simeq 10^{-4}T_S$, this implies that we must suppress the gain variation of the receiving system $\Delta G/G$ within a level as small as

$$\frac{\Delta G}{G} < 10^{-4}, \tag{244}$$

which is practically quite difficult.

Therefore, radio astronomers apply switching techniques to the single dish telescope observations in order to avoid the gain variation effect and firmly detect the weak astronomical radio sources.

5.4.1 Dicke Mode Switching Observation

A switching method was proposed by R.H. Dicke in 1946 and has been widely used. In this method, two input signals (voltages), one from the antenna feed horn and another from a noise source (for example, a cooled resistor) of a constant temperature T_R are quickly switched in front of the receiving system and, at the same time, the sign of the output power from the square–law detector is reversed with the same switching timing which are then summed up (i.e., the powers from the two inputs are subtracted) and averaged as shown in Figure 115.

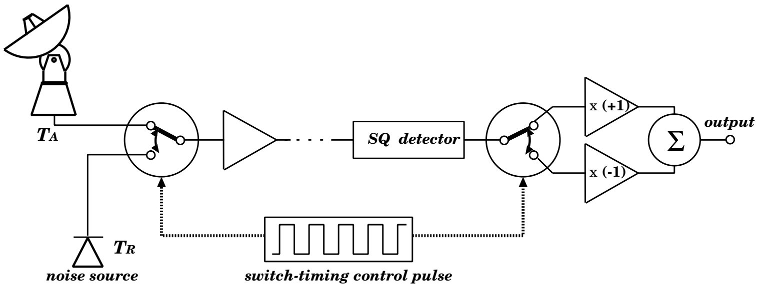

Figure 115: A general scheme of the Dicke mode receiver.

The square–law detector yields a power

$$W_A = k(T_A + T_S)GB, \tag{245}$$

in the upper switch position in Figure 115, while in the lower switch position,

$$W_R = k(T_R + T_{RX})GB, \tag{246}$$

where T_{RX} is the receiver noise temperature. At relatively low observing frequency ≤ 15 GHz, the atmospheric contribution to the system noise temperature is much smaller than T_{RX}, and the ground pickup effects are small as far as the elevation is not very low. Consequently, $T_S \cong T_{RX}$ in equation (233) for the low frequency and moderately high elevation observations. Therefore, the difference output from the Dicke mode receiver gives us

$$W_A - W_R \cong k(T_A - T_R)GB, \tag{247}$$

provided that the switching interval is short enough compared with the time scale of the gain variation. Therefore, the effect of the gain variation to this difference output is

$$\Delta(W_A - W_R) \cong k(T_A - T_R)\,\Delta G\,B \tag{248}$$

and hence the condition for the source detection is now

$$\frac{T_A}{T_A - T_R} > \frac{\Delta G}{G} \tag{249}$$

instead of equation (243). This new condition is easily satisfied if we suitably choose the temperature of the noise source T_R low enough to be $T_R \sim T_A$.

Instead of the noise source, we could use a small antenna like a horn antenna looking at the sky for the switching observation (Figure 116).

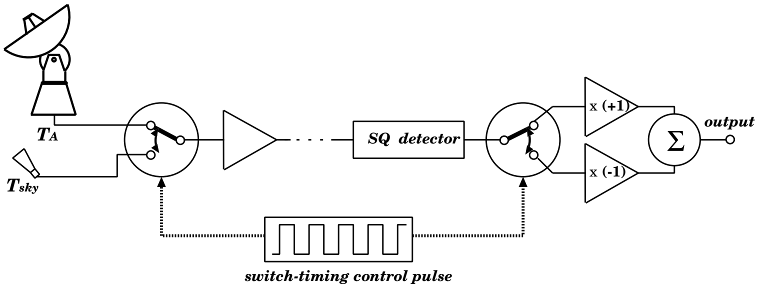

Figure 116: A switching mode observation using a small antenna.

For spectralline sources, quick "frequency switching" between inside and outside of the spectral lines can be used for detecting the sources against the gain variation of the receiving system.

5.4.2 Beam Switch

At frequencies higher than $\simeq$ 15 GHz, the radio signal from an astronomical radio source is badly masked by the time variation of the thermal radiation of the atmosphere along with the gain variation of the receiving sysytem. Also, it is not desirable at the high frequencies to install the switching mechanism in the RF signal transmision system since the switches themselves could become additional noise sources.

In this circumstance, another technique called "beam switching" is effective. The beam switching is a quick switching of the antenna beam between the on–source and the off–source directions and measuring the difference of the received powers at the two directions (Figure 117).

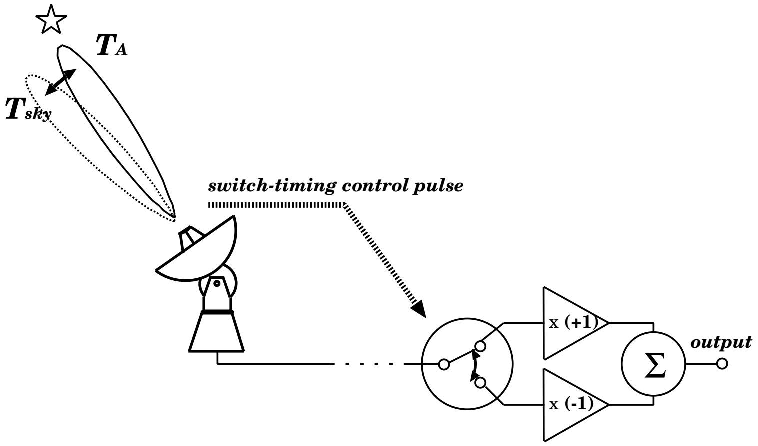

Figure 117: Beam switching between the on–source and the off–source directions.

Since the on–source output power is

$$W_{source} = k(T_A + T_S)GB, \tag{250}$$

while the off–source output power is

$$W_{sky} = kT_S GB, \tag{251}$$

the power difference yields

$$W_{source} - W_{sky} = kT_A GB. \tag{252}$$

If gain varies by ΔG, we have $\Delta(W_{source} - W_{sky}) = kT_A \Delta G\, B$. Therefore, we can easily detect $kT_A GB$ as far as $\Delta G \ll G$.

Also, we can obtain the antenna temperature T_A by a simple formula

$$T_A = \frac{W_{source} - W_{sky}}{W_{sky}} T_S, \tag{253}$$

if we know the system noise temperature T_S.

The atmospheric thermal radiation effects are well cancelled out in the above procedure, as far as the two beam directions are not too much separated on the sky.

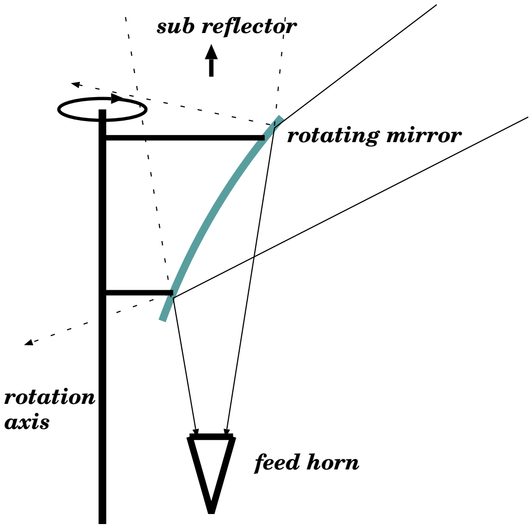

Figure 118: Beam switching using the vaned–wheel like rotating mirror.

Since it is mostly impossible to shake a big antenna with a frequency of several to tens Hz, which is usually required, a vaned–wheel like mirror is rotated in front of the feed horn for effectively altering the beam direction. The rotating mirror, which itself is a small antenna of the offset–paraboloidal shape, periodically intersects, and hence cuts off, the beam from the subreflector and instead guides the reflected radio wave from another direction of the sky to the feed horn (Figure 118). Although the beam pattern for the mirror–reflected radio wave must be wide, distorted and thus quite different from that of the main beam, the pattern must be good enough to collect the widespread thermal radiation of the atmosphere (see equations (219) and (222)). The timing of the sign reversal of the output power is synchronized to the mechanical rotation of the mirror. The off–source beam is usually designed to be shifted in the azimuthal direction from the on–source beam for avoiding effects of the elevation dependence of the atmospheric thermal radiation.

5.4.3 Additional Remarks on Switching Mode Observations

Since we observe the astronomical source only for about a half of the total observing time τ_a in the above switching mode observations, the signal–to–noise ratio is now

$$S/N \simeq \frac{T_A}{T_S}\sqrt{\frac{B\tau_a}{2}}, \tag{254}$$

which is by a factor of about $\sqrt{2}$ smaller than that of the total power mode observation (equation (239)). But the $1 - 1/\sqrt{2} \cong 29$ % loss is certainly better than nothing.

The above switching techniques are inevitable for measurements of the received power (radiometry) from astronomical radio sources by the single dish radio telescopes. On the other hand, for VLBI observations, and for interferometry observations in general, the switching techniques are usually not used in a direct sense. This is because the receiver noises in the voltages from different telescopes are not correlated with each other, and therefore the system noise temperature term T_S does not figure in the interferometer analog of equation (241) obtained in a correlator output. Thus the gain variation of the receiver hardly disturbs the source detection in VLBI. Nevertheless, the techniques are still important for VLBI in checking and adjusting the pointing performance of VLBI telescopes and in measuring single–dish flux densities of the sources which are necessary for interpreting the VLBI results.

6 Measurements of Antenna Performance

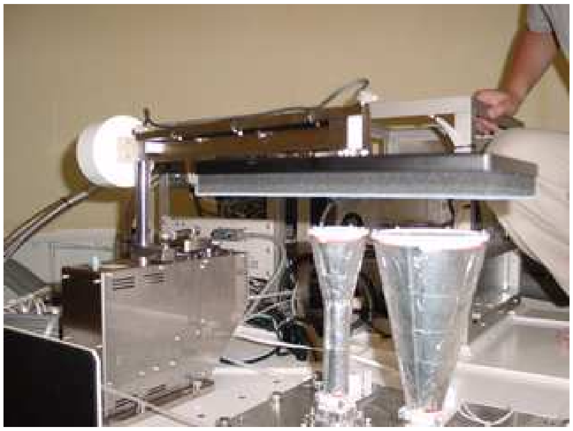

Figure 119: Room–Sky measurement device in a upper cabin of a VERA antenna.

For proper interpretaion of results of VLBI observations, accurate knowledge of basic performance parameters of component telescopes is necessary. Since actual parameters may differ from designed ones, they must be well measured before starting scientific observations. Moreover, the measurements must be regularly repeated, since the parameters are more or less time variable, depending on environmental conditions, system improvement works, and ages of the telescopes.

The regular measurements are also important for quickly finding and repairing possible mulfunctions in the antenna system.

6.1 System Equivalent Flux Debsity (SEFD)

The most important parameters to be regularly measured are the system noise temperature T_S and the aperture efficiency η_A which figure in a quantity called "system equivalent flux density" often denoted as SEFD. The SEFD is defined as

$$SEFD = \frac{2kT_S}{A_e} = \frac{2kT_S}{\eta_A A_g} = \frac{8kT_S}{\eta_A \pi D^2}, \tag{255}$$

where the last term is for a circular aperture antenna of diameter D, so that

$$\frac{T_A}{T_S} = \frac{\mathcal{S}_\nu}{SEFD}, \tag{256}$$

where again k is the Boltzmann constant, A_e is the effective aperture, A_g is the geometrical aperture, T_A is the antenna temperature and $\mathcal{S}_\nu$ is the effective flux density of an astronomical radio source. Therefore, if we know both $\mathcal{S}_\nu$ of a source and SEFD of a telescope, we can easily calculate an expected signal–to–noise ratio to be obtained when we observe the source by the telescope on the basis of a suitable equation like equation (239). The SEFD values are widely listed in system documents of VLBI networks as indicators of the sensitivities of component telescopes. For example, SEFD of an antenna with diameter 20 m, aperture efficiency 0.6 and system noise temperature 100 K is 1465 Jy. Of course, the smaller the SEFD, the better the system performance is.

Other important quantities are the receiver noise temperature T_{RX} and the pointing accuracy σ_θ of the telescope, which must be carefully monitored for checking the system status. Also, the optical depth of the atmosphere τ_{atm} is regularly measured as an parameter showing the observational condition of the telescope site.

We will see how to measure these parameters one by one.

6.2 Measurement of the Receiver Noise Temperature T_{RX}

The receiver noise temperature T_{RX} is measured usually in a scheme shown in Figure 120 known as “hot–cold method”.

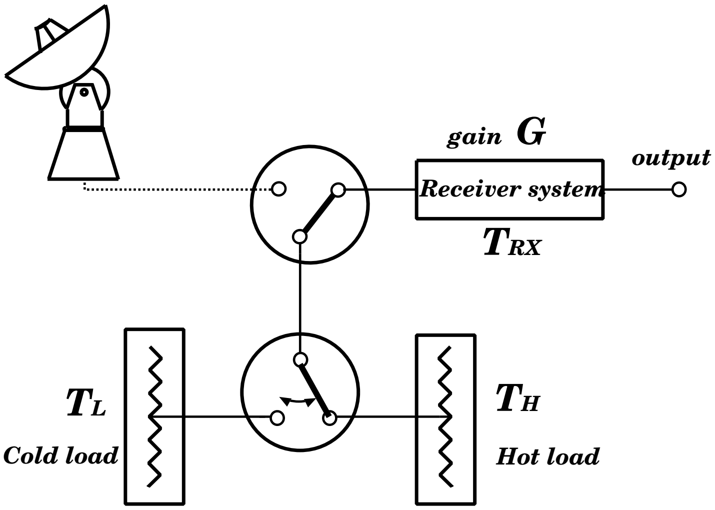

Figure 120: Measurement of the receiver noise temperature using hot and cold loads with known temperature values.

When the hot and cold loads with known temperatures T_H and T_L (for example, two resistors one in the room temperature and another cooled by the liquid nitrogen) are switched, the output power values W_L and W_H are

$$\begin{aligned} W_L &= k(T_L + T_{RX})GB, \\ W_H &= k(T_H + T_{RX})GB, \end{aligned} \tag{257}$$

where G and B are the total gain of the receiving system and the observed bandwidth, respectively. Therefore, introducing a factor

$$y \equiv \frac{W_H}{W_L} = \frac{T_H + T_{RX}}{T_L + T_{RX}},$$

we obtain the T_{RX} and GB by equations

$$\begin{aligned} T_{RX} &= \frac{T_H - yT_L}{y - 1}, \\ GB &= \frac{W_H - W_L}{k(T_H - T_L)}. \end{aligned} \tag{258}$$

This is an example of measuring something by using calibrators (Figure 121).

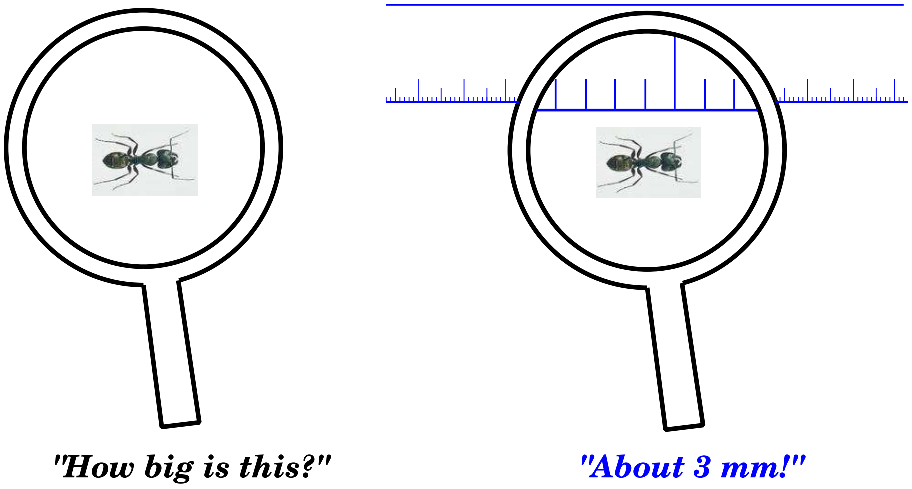

Figure 121: Measuring something by using a calibrator.

In geodetic VLBI antennas observing at 2 GHz and 8 GHz, switching schemes such as shown in Figure 120 are often builtin in the receiving system for regular monitoring of the receiver noise temperature. In high frequency antennas, two absorbers one in the room temperature and another immersed in the liquid nitrogen are often used to cover a feed horn one by one, instead of the switching mechanism shown above.

6.3 Measurement of the System Noise Temperature

In many VLBI antennas, noise diodes with known noise temperatures are used for measurements of the system noise temperature. The noise power of temperature T_{ND} from a diode is intermittently added through a wave guide coupler to the input signal of the antenna looking at the blank sky, as shown in Figure 122.

The output powers of the receiving system when the noise power is added and when it is off are

$$\begin{aligned} W_{ND} &= k(T_{ND} + T_S)GB, \\ W_{sky} &= kT_S GB, \end{aligned} \tag{259}$$

and hence

$$\frac{W_{ND} - W_{sky}}{W_{sky}} = \frac{T_{ND}}{T_S}, \tag{260}$$

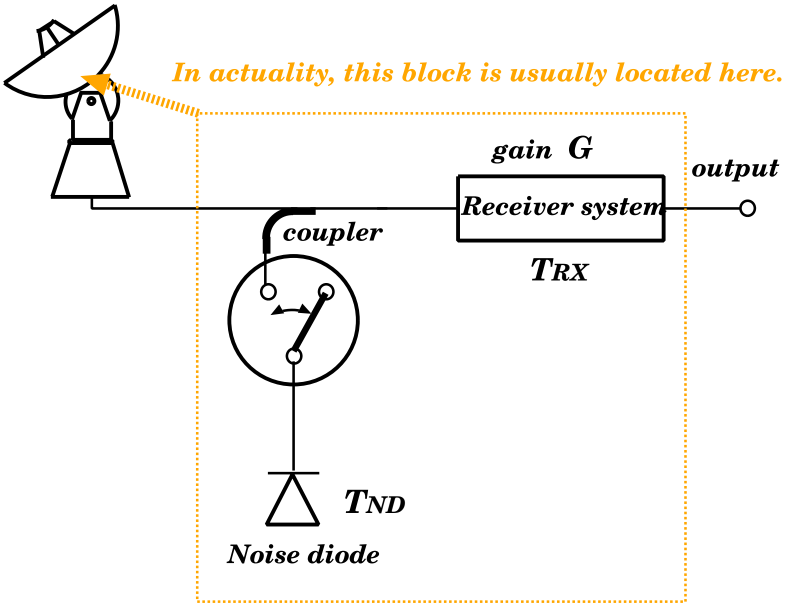

Figure 122: Measurement of the system noise temperature using a noise diode of the known noise temperature.

where the system noise temperature T_S includes contributions from the receiver noise, the ground pickup and the atmospheric thermal radiation as shown in equation (233). Now, if we introduce a factor y defined here as

$$y \equiv \frac{W_{ND}}{W_{sky}},$$

equation (260) yields a simple formula for the system noise temperature:

$$T_S = \frac{T_{ND}}{y-1}. \tag{261}$$

This is another example of measuring something using a calibrator.

Indeed, the system noise temperature as given in the input–equivalent form of equation (230) can be measured very easily. In VLBI observations, the measurements of the system noise temperature are usually highly automated and conducted in real time for every scan of radio sources.

6.4 System Noise Temperature and Antenna Temperature Referred to the Outside of the Atmosphere $T_S^\star$ and $T_A^\star$

The system noise temperature given in equation (233) and measured using the noise diode as described above is "referred to the antenna on the ground", that means the input point for both T_A and T_S is chosen at the front side of the antenna. In VLBI observations at frequency higher than $\simeq$ 15 GHz, however, the signal from a radio source received by an antenna could be heavily attenuated by a factor of $e^{-\tau_{atm}}$ due to the atmosphere with an optical depth τ_{atm} which often reaches 0.3 ($e^{-\tau_{atm}} \simeq 74\%$) or worse. It is much nicer for many astronomers to know the antenna temperature "referred to the outside of the atmosphere" (Figure 123), which means not attenuated by the atmosphere, in order to study the intrinsic properties of the radio source. But if we shift the input point for the antenna temperature to the outside of the atmosphere, we have to refer also the system noise temperature to the outside of the atmosphere, too. They are usually denoted as $T_S^\star$ and $T_A^\star$ and related to the ordinary T_S and T_A as

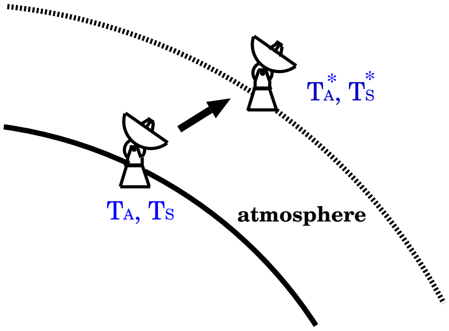

Figure 123: Input points within and outside the atmosphere.

$$\begin{aligned} T_S &= T_S^\star e^{-\tau_{atm}}, \\ T_A &= T_A^\star e^{-\tau_{atm}}, \end{aligned} \tag{262}$$

or, in view of equation (233),

$$\begin{aligned} T_S^\star &= T_S e^{\tau_{atm}} = (T_{RX} + T_{ant}) e^{\tau_{atm}} + T_{atm}(e^{\tau_{atm}} - 1), \\ T_A^\star &= T_A e^{\tau_{atm}}. \end{aligned} \tag{263}$$

We can derive equation (263) also from equation (231) regarding the atmosphere as the "first stage device" with "gain factor" $G_1 = e^{-\tau_{atm}}$ and system noise tempeature $T_{S1} = T_{atm}(e^{\tau_{atm}} - 1)$, and the receiving system as the "second stage device" with system noise temperature $T_{S2} = T_{RX} + T_{ant}$.

Note that we can describe $T_A^\star$ in terms of the brightness temperature $T_B^\star$ of the source outside of the atmosphere, introduced in subsection 5.1.5, as

$$T_A^\star = \frac{\oint P_n(\theta, \phi)\, T_B^\star(\theta, \phi)\, d\Omega}{\oint P_n(\theta, \phi) d\Omega},$$

where $P_n(\theta, \phi)$ is the normalized power pattern in the antenna–fixed coordinate system with angular variables θ and ϕ.

6.5 Measurement of the $T_S\star$

There is a clever method to directly measure the system noise temperature $T_S^\star$ referred to the outside of the atmosphere. In fact, the $T_S^\star$ can be measured by the so–called "R–Sky" or "Room–Sky" method where the feed horn of the antenna is covered and uncovered by an absorber at the room temperature T_{room} as shown in Figures 119 and 124.

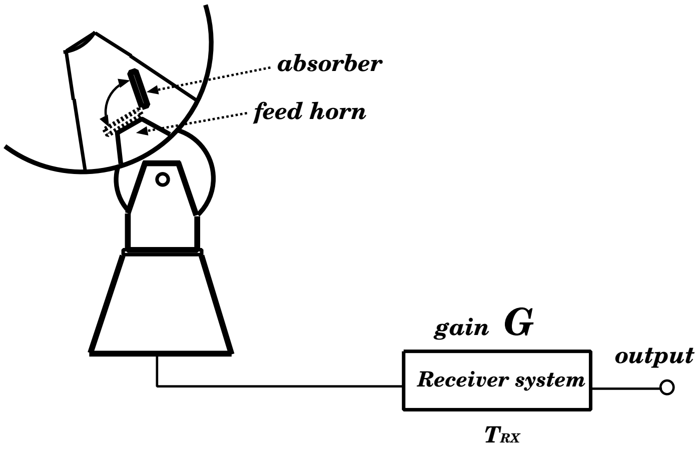

Figure 124: Measurement of the system noise temperature referred to the outside of the atmosphere by the R–Sky method.

Here we will ignore, for simplicity, the antenna noise temperature T_{ant} in equation (233), since the ground pickup effect which contributes to the T_{ant} the most is kept small even at moderately low elevations in well designed radio telescope antennas with sufficiently suppressed sidelobe levels.

Then, when the absorber is taken off from the feed horn, the antenna looks at the blank sky and produces an output power

$$W_{sky} = kT_S GB = kT_S^\star e^{-\tau_{atm}} GB = k[T_{RX} + T_{atm}(1 - e^{-\tau_{atm}})]GB, \quad (264)$$

where T_{atm} is the physical temperature of the atmosphere (see equations (259) and (263)). On the other hand, when the feed horn is covered by the absorber of room temperature T_{room}, the output power is

$$W_{room} = k(T_{RX} + T_{room})GB. \quad (265)$$

If we adopt here a reasonable assumption that $T_{atm} = T_{room}$ (this must be correct with an accuracy usually better than a few percent, since both of them must be around 300 K), then we have

$$W_{room} - W_{sky} = kT_{room} e^{-\tau_{atm}} GB, \quad (266)$$

and therefore

$$\frac{W_{sky}}{W_{room} - W_{sky}} = \frac{T_S^\star}{T_{room}}. \quad (267)$$

If we introduce a factor y now defined as

$$y \equiv \frac{W_{room}}{W_{sky}}, \quad (268)$$

we obtain the system noise temperature referred to the outside of the atmosphere

$$T_S^\star = \frac{T_{room}}{y - 1}. \quad (269)$$

Needless to say, this is another beautiful example of measuring something using a calibrator.

Note that the R-Sky method gives correct $T_S^\star$ value even when the measurement is done under a radome or feed–cone cover, as far as temperature of the cover membrane T_{mem} is well approximated by the room temperature ($T_{mem} = T_{room}$). In fact, the discussion in subsection 5.1.5 tells us that all equations from (262) to (267), and therefore equation (269), too, hold also in this case, if only we replace τ_{atm} by $\tau_{atm} + \tau_{mem}$, where τ_{mem} is the optical depth of the cover membrane as before.

6.6 Measurement of the Aperture Efficiency η_A

If we quickly switch the telescope beam between directions of a source and the blank sky using the beam switch, we obtain output powers:

$$\begin{aligned} W_{source} &= k(T_A + T_S)GB = k(T_A^\star + T_S^\star)e^{-\tau_{atm}} GB \\ W_{sky} &= kT_S GB = kT_S^\star e^{-\tau_{atm}} GB. \end{aligned} \quad (270)$$

Then, we easily get the antenna temperature referred to the outside of the atmosphere $T_A^\star$ if we know the sytem noise temperature referred to the outside of the atmosphere $T_S^\star$ by an equation:

$$T_A^\star = \frac{W_{source} - W_{sky}}{W_{sky}} T_S^\star. \tag{271}$$

We can measure $T_A^\star$ in this way even when our receiving system is placed under the radome or feed–cone cover. The only thing we have to note then is that τ_{atm} in equation (270) should be replaced by $\tau_{atm} + \tau_{mem}$.

If the radio source observed is a standard source with known effective flux density $\mathcal{S}_\nu$ and is much more compact than the beamwidth, we can calculate the effective aperture A_e from equation (220) as

$$A_e = \eta_A A_g = \frac{2kT_A^\star}{\mathcal{S}_\nu}, \tag{272}$$

where A_g is the geometrical aperture, and therefore the aperture efficiency

$$\eta_A = \frac{2kT_A^\star}{A_g \mathcal{S}_\nu} = \frac{8kT_A^\star}{\pi D^2 \mathcal{S}_\nu}, \tag{273}$$

where the last expression is for a circular aperture antenna with diameter D.

If the source is so bright that any short term variation of the receiver gain or the atmospheric noise can be ignored, we can just drive the telescope to switch the directions when the beam switching mechanism is not available.

The best standard sources are bright planets like Jupiter or Venus if the telescope beam is not narrower than their sizes, since their brightness temperatures are reliably known. Strong extragalactic AGN's like 3C84, 3C273, ... could also be used if their flux densities of the date are available.

6.7 Chopper Wheel method for Precise Measurement of the Antenna Temperature $T_A^\star$

In order to accurately measure the antenna temperature $T_A^\star$ referred to the outside of the atmosphere and aperture efficiency η_A, it is desirable to simultaneously measure the system noise temperature $T_S^\star$, too. For this purpose, one can use a method known as "absorbing disk method" or "chopper wheel method". In this method, a rotating vaned–wheel like device is used in front of the feed horn, which is much alike with the one used in the beam switch, but an absorber of the room temperature T_{room} is attached to one of the vanes in addition to the mirror. Thus the feed horn can now look at the source direction, the mirror–reflected blank sky, and the absorber in turn within a

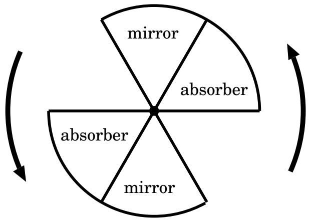

Figure 125: Absorbers and mirrors in the rotating vaned–wheel used in the chopper–wheel method.

short period of one revolution which is well less than 1 second (Figure 125). Since we now have three output powers nearly simultaneously, which are given by

$$\begin{aligned} W_{source} &= k[T_A^\star e^{-\tau_{atm}} + T_{RX} + T_{atm}(1 - e^{-\tau_{atm}})]GB, \\ W_{sky} &= k[T_{RX} + T_{atm}(1 - e^{-\tau_{atm}})]GB = kT_S^\star e^{-\tau_{atm}}GB, \\ W_{room} &= k(T_{room} + T_{RX})GB, \end{aligned} \tag{274}$$

if we again ignore the small ground pickup effect T_{ant}, we directly obtain the antenna temperature referred to the outside of the atmosphere

$$T_A^\star = \frac{W_{source} - W_{sky}}{W_{room} - W_{sky}} T_{room}, \tag{275}$$

as far as we are allowed to assume $T_{atm} = T_{room}$.

6.8 Measurement of the Optical Depth of the Atmosphere τ_{atm} — $\sec z$ Method

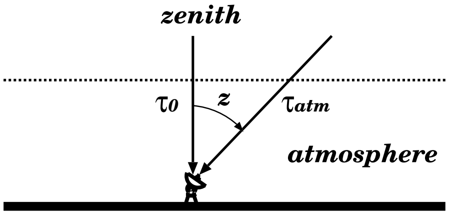

Figure 126: $\sec z$ dependence of the optical depth τ_{atm} in the plane–parallel model of the atmosphere.

Elevation dependence of the attenuation of the radio signal due to the atmosphere can be well modeled by a plane–parallel atmosphere ignoring the curvature of the Earth's surface (Figure 126). In such a model, the optical depth of the atmosphere τ_{atm}, which is approximately proportional to the path length within the atmosphere, depends on the zenith distance z (which is an angle of a direction from the zenith, i.e. $z = 90°-$ elevation) as

$$\tau_{atm} = \tau_0 \sec z. \tag{276}$$

Let us use the R–Sky method to measure the output powers when the feed horn is covered and uncovered by the absorber with the room temperature T_{room}. Then equations (264) and (265):

$$\begin{aligned} W_{sky} &= k[T_{RX} + T_{atm}(1 - e^{-\tau_{atm}})]GB, \\ W_{room} &= k(T_{RX} + T_{room})GB. \end{aligned}$$

give us, under the assumption of $T_{room} = T_{atm}$,

$$W_{room} - W_{sky} = kT_{room}e^{-\tau_{atm}}GB. \tag{277}$$

Therefore, taking the logarithm of equation (277), we obtain

$$-\ln(W_{room} - W_{sky}) = \tau_0 \sec z - \ln(kT_{room}GB), \tag{278}$$

where we used equation (276).

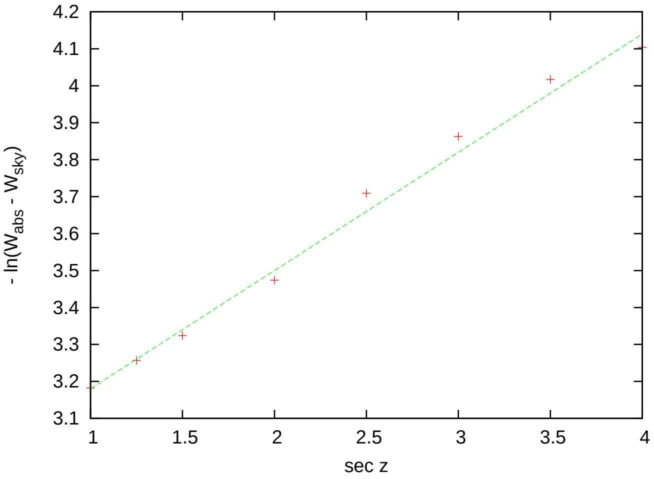

Figure 127: An example of the $[-\ln(W_{room} - W_{sky})]$ *vs.* $\sec z$ plot of measured data obtained in a $\sec z$ measurement.

Consequently, if we measure the $W_{room} - W_{sky}$ at several values of zenith distance z, and if $T_{room}GB$ is nearly constant during the measurement, then we can estimate the zenith optical depth τ_0 as the inclination of a straight line fitted to the measured data in the $[-\ln(W_{room} - W_{sky})]$ *vs.* $\sec z$ plane, as illustrated in Figure 127.

Knowing the zenith optical depth τ_0 and therefore $\tau_{atm} = \tau_0 \sec z$, as well as the $T_S^\star$ which is also available from the R–Sky method, we can estimate the receiver noise temperature T_{RX}. In fact, equation (263) shows that the system noise temperature $T_S^\star$ referred to the outside of the atmosphere must be equal to

$$T_S^\star = T_{RX} e^{\tau_{atm}} + T_{room}(e^{\tau_{atm}} - 1),$$

when the T_{ant} is ignored and $T_{atm} = T_{room}$ is assumed. Therefore, if we calculate a quantity T_{rcv} defined by

$$T_{rcv} \equiv T_S^\star e^{-\tau_{atm}} - T_{room}(1 - e^{-\tau_{atm}}), \tag{279}$$

using measured values of $T_S^\star$, τ_{atm}, and T_{room}, the T_{rcv} must give a good estimate of the receiver noise temperature T_{RX} as far as our assumptions are appropriate. Equation (279) is often used as a convenient way to easily estimate the T_{RX} and check the receiver performance.

Nevertheless, it is desirable to conduct the hot–cold measurement of the receiver noise temperature in parallel with the $\sec z$ measurement, in order to examine possible effect of gain variation during the $\sec z$ measurement, and also to confirm consistency of T_{RX} values estimated in the $\sec z$ and the hot–cold methods.

Note that the $\sec z$ method gives a correct estimate of the zenith optical depth τ_0 even when our antenna, or its feed horn, is covered by a radome or feed–cone cover, as far as the optical depth of the cover membrane τ_{mem} does not depend on the zenith distance z of the antenna beam. In fact, although equations (277) and (278) then should be replaced by

$$W_{room} - W_{sky} = k T_{room} e^{-(\tau_{atm} + \tau_{mem})} G B,$$

and

$$-\ln(W_{room} - W_{sky}) = \tau_0 \sec z - \ln(k T_{room} e^{-\tau_{mem}} G B),$$

as discussions in subsection 5.1.5 show, the straight–line fitting to the measured data in the $[-\ln(W_{room} - W_{sky})]$ *vs.* $\sec z$ plane still gives correct τ_0 as far as $e^{-\tau_{mem}}$ does not depend on z.

On the other hand, however, a straightforward application of equation (279) would not give a correct estimate of the actual receiver noise temperature T_{RX} when τ_{mem} is not negligiblly small. In fact, discussions in subsection

5.1.5 show that the system noise temperature $T_S^\star$ referred to the outside of the atmosphere is

$$T_S^\star = T_S \, e^{\tau_{atm}+\tau_{mem}} = T_{RX} \, e^{\tau_{atm}+\tau_{mem}} + T_{room} \, (e^{\tau_{atm}+\tau_{mem}} - 1),$$

in this case, as long as T_{ant} is ignored and $T_{atm} = T_{mem} = T_{room}$ is assumed. Therefore, equation (279) gives

$$T_{rcv} = T_{RX} \, e^{\tau_{mem}} + T_{room} \, (e^{\tau_{mem}} - 1),$$

and, hence, the T_{rcv} deviates from the receiver noise temperature T_{RX} by

$$T_{rcv} - T_{RX} = (T_{room} + T_{RX}) \, (e^{\tau_{mem}} - 1).$$

For example, if $T_{room} = 300$ K, $T_{RX} = 50$ K, and $e^{-\tau_{mem}} = 0.92$, then the deviation reaches as large as 30 K.

It is highly desirable to regularly measure the atmospheric optical depth, hopefully every day, for statistical study of the observational condition of the site. In particular, it will be useful to compare the measured relationship between the system noise temperature $T_S^\star$ and the optical depth $-\tau_{atm}$ (or the transparency $e^{-\tau_{atm}}$) with the theoretical prediction which is given by equation (263) and illustrated in Figure 128. For this purpose, regular $\sec z$ measurements during a year or so are needed. We will then be able to see if

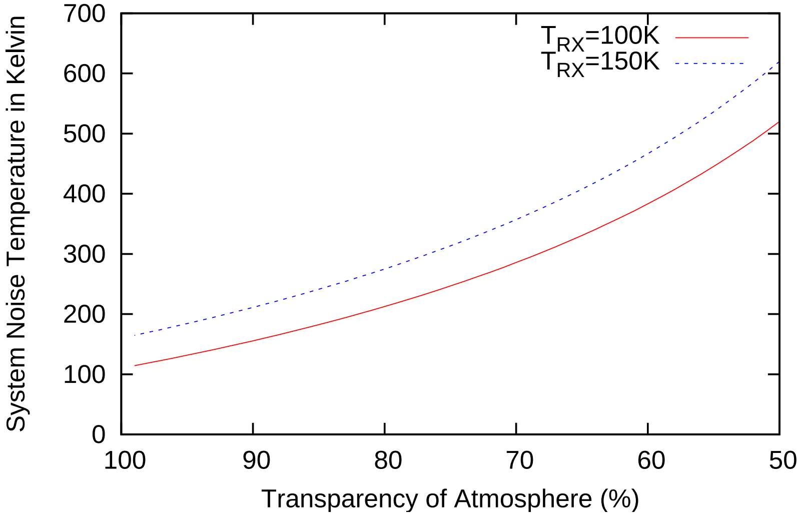

Figure 128: $T_S^\star$ – transparency $e^{-\tau_{atm}}$ relation expected from equation (263) for two cases of $T_{RX} = 100$ K and $T_{RX} = 150$ K.

the underlying assumptions of the equation well hold and T_{RX} is sufficiently stable for a year or so.

For efficient $\sec z$ measurements, we need a good operation software, which would point the radio telescope to desired sky directions with different elevation angles, drive the "R–Sky" measuring instrument, read power–meter outputs at "room" and "sky" states, plot figures such as Figure 127, calculate τ_{atm}, $T_S^\star$ and T_{rcv}, and store the results to an appropriate database.

6.9 Pointing Calibration and Pointing Accuracy σ_θ

Even in a well manufactured antenna, the azimuth axis may not be exactly parallel to the vertical line at the site. Likewise, the elevation axis may not be strictly perpendicular to the azimuth axis. In the antenna specifications, tolerance values for the axis–alignments are usually set to be at $0.^\circ 01$ level, but such a "large" axis–offset could easily cause pointing errors (offsets) exceeding the accuracy requirement of $\sim 0.1\lambda/D$ given in equation (213). Also, the gravitational yielding of the antennas causes noticeable pointing errors mainly in the elevation direction. These pointing errors are "systematic" in the sense, that we obtain the same error values repeatedly in the same direction of the sky. But this means that they are predictable as functions of azimuth and elevation of the beam direction of the telescope.

Therefore, these systematic errors must be estimated and calibrated before starting regular scientific observations. The pointing accuracy σ_θ, which characterizes more or less random errors of the telescope pointing due to mechanical inaccuracy of gears, bearings, as well as unpredictable deformations caused by the gravity and the wind, must be determined after removing the systematic deviations. Actually, the pointing accuracy is calculated from the residuals of the least–squares fitting of a number of parameters, characterizing systematic errors, to the measured values of the pointing errors. Hereafter, we call these parameters as "offset parameters".

Since the offset parameters may vary in time due to the mechanical change in the antenna structure, the measurements must be repeated periodically once a year or more, for keeping the best system performance.

6.9.1 Pointing Model

Let us consider a model which describes a functional dependence of the systematic pointing error on the offset parameters, assuming that we observe a radio source located in azimuth Az and elevation El with an Alt–Azimuth mount antenna. Here we adopt a convention that the azimuth is measured eastward from the North, i.e., $Az = 0°$ at the North, and $Az = 90°$ at the East.

Following 8 quantities are usually regarded as most important offset parameters for Alt–Azimuth mount antennas:

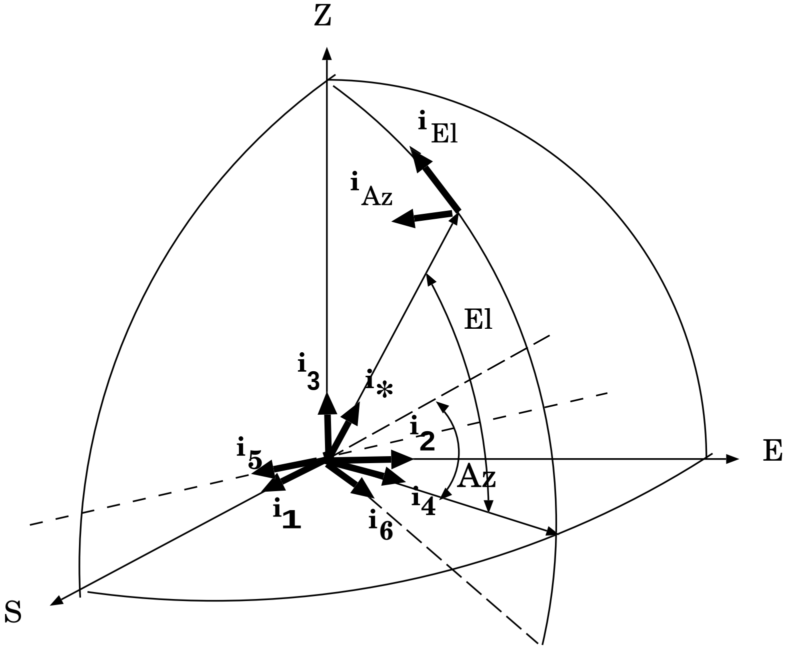

Figure 129: Unit vectors $\boldsymbol{i}_1, \cdots, \boldsymbol{i}_6$ for describing axis–offsets of an antenna.

1. a: tilt angle of the azimuth axis in the EW direction around $\boldsymbol{i}_1$,
2. b: tilt angle of the azimuth axis in the NS direction around $\boldsymbol{i}_2$,
3. c: offset of the origin of the azimuth encoder (angle detector), plus tilt angle of the elevation axis in the azimuthal direction, around $\boldsymbol{i}_3$,
4. d: tilt angle of the elevation axis in the elevational direction around $\boldsymbol{i}_4$,
5. e: offset of the origin of the elevation encoder, plus tilt angle of the beam axis in the elevational direction, around $\boldsymbol{i}_5$,
6. f: tilt angle of the beam axis in the azimuthal direction around $\boldsymbol{i}_6$,
7. g: cosine coefficient of the gravitational yielding in elevation,
8. h: sine coefficient of the gravitational yielding in elevation.

Parameters $a - f$ represent axis offset effects, i.e., effects of misalignments of telescope axes, while parameters g and h represent elastic deformation effects. In the present level of antenna manufacturing technology, these offset parameters are quantities of the order of a few minutes of arc, or smaller. Therefore, it is sufficient to consider the pointing model in a linear approximation with respect to the small offset parameters.

The axis–offset angles a, b, c, d, e and f correspond to small rotation angles around directions shown by the unit vectors $\boldsymbol{i_1}$, $\boldsymbol{i_2}$, $\boldsymbol{i_3}$, $\boldsymbol{i_4}$, $\boldsymbol{i_5}$ and $\boldsymbol{i_6}$ in Figure 129. Here we adopt the "right–handed screw rule" for the direction of the rotation, i.e., the positive rotation angle corresponds to the clock–wise rotation, viewed towards the direction of the unit vector.

In Figure 129, $\boldsymbol{i_1}$, $\boldsymbol{i_2}$, and $\boldsymbol{i_3}$ are basis vectors of the horizontal coordinate system at the antenna site. $\boldsymbol{i_3}$ is directed towards the zenith, while $\boldsymbol{i_1}$ and $\boldsymbol{i_2}$ are directed towards the South and the East, respectively, in the horizontal plane. The $\boldsymbol{i_3}$ is the vertical axis, towards which the azimuth axis of the antenna must be directed in an ideal case when there is no systematic axis offset.

$\boldsymbol{i_4}$ is directed towards azimuth Az in the horizontal plane, which is the azimuth of the radio source at the time of the observation.

$\boldsymbol{i_5}$ is chosen towards azimuth $Az + 90°$ in the horizontal plane. The $\boldsymbol{i_5}$ is the direction, along which the elevation axis of the antenna must be aligned in the ideal case when there is no systematic axis offset.

$\boldsymbol{i_6}$ is chosen in a direction with azimuth Az and elevation $El - 90°$, where El is the elevation of the radio source at the time of the observation.

$\boldsymbol{i_5}$, $\boldsymbol{i_6}$, and a unit vector $\boldsymbol{i_\star}$, which is directed towards the radio source with azimuth Az and elevation El, form a right–handed orthogonal triad. The $\boldsymbol{i_\star}$ is the direction, towards which the beam axis of the antenna must be oriented in the ideal case when there is no systematic axis offset.

Unit vectors $\boldsymbol{i_{Az}}$ and $\boldsymbol{i_{El}}$, which are directed towards azimuthal and elevational directions in a plane tangent to the celestial sphere at the radio source position, are related to $\boldsymbol{i_5}$ and $\boldsymbol{i_6}$, as

$$\boldsymbol{i}_5 = \boldsymbol{i}_{Az}, \tag{280}$$

$$\boldsymbol{i}_6 = -\boldsymbol{i}_{El}, \tag{281}$$

as evident from Figure 129.

In the linear approximation, the pointing error $\Delta\boldsymbol{i}_\star$ is expressed in terms of the offset of the unit vector $\boldsymbol{i}'_\star$, which represents the direction of the actual telescope beam axis, from the one in the desired direction $\boldsymbol{i}_\star$:

$$\Delta\boldsymbol{i}_\star = \boldsymbol{i}'_\star - \boldsymbol{i}_\star. \tag{282}$$

The azimuthal and elevational components of the pointing error can be expressed, in the linear approximation, as:

$$\begin{aligned} \cos El\,\Delta Az &= \Delta \boldsymbol{i}_{\star} \cdot \boldsymbol{i}_{Az}, \\ \Delta El &= \Delta \boldsymbol{i}_{\star} \cdot \boldsymbol{i}_{El}. \end{aligned} \tag{283}$$

These are the quantities which we can measure in "pointing measurements", as we will see later.

Now let us derive the functional dependence of these azimuthal and elevational components of the pointing error on the offset parameters, which is nothing but the pointing model we are looking for.

In the linear approximation, we can separately consider the effects of the axis offsets and the elastic deformation, and then sum up the results to obtain the total effect. Therefore, we first consider the axis offset effects, assuming that the radio telescope antenna is a rigid body.

From the theory of the rotational dynamics of the rigid body, we know that, if a rigid body rotates around an axis $\boldsymbol{i}$, where $\boldsymbol{i}$ is a unit vector, by a small angle $\Delta\theta$, any vector $\boldsymbol{x}$ fixed to the rigid body is displaced by:

$$\Delta \boldsymbol{x} = \Delta\theta\, \boldsymbol{i} \times \boldsymbol{x}, \tag{284}$$

in a linear approximation with respect to $\Delta\theta$. We can introduce here a vector of small angle rotation $\Delta\boldsymbol{\Theta}$ as:

$$\Delta\boldsymbol{\Theta} = \Delta\theta\, \boldsymbol{i}. \tag{285}$$

Then, equation (284) can be expressed as

$$\Delta \boldsymbol{x} = \Delta\boldsymbol{\Theta} \times \boldsymbol{x}. \tag{286}$$

It is known that the vectors of small angle rotations can be summed up as ordinary vectors in the linear approximation with respect to the small angles. Since, in our present problem, a rotational displacement of the radio telescope antenna is composed of rotations by small angles a, b, $\cdots$, f around the six unit vectors $\boldsymbol{i}_1$, $\boldsymbol{i}_2$, $\cdots$, $\boldsymbol{i}_6$, the total rotation angle vector of the antenna $\Delta\boldsymbol{\Theta}$ is expressed by:

$$\Delta\boldsymbol{\Theta} = a\boldsymbol{i}_1 + b\boldsymbol{i}_2 + c\boldsymbol{i}_3 + d\boldsymbol{i}_4 + e\boldsymbol{i}_5 + f\boldsymbol{i}_6. \tag{287}$$

The angular offset of the telescope beam axis $\Delta\boldsymbol{i}_{\star}^{a}$ from the desired direction $\boldsymbol{i}_{\star}$, due to the superposed axis offset effects, is then expressed as:

$$\Delta\boldsymbol{i}_{\star}^{a} = \Delta\boldsymbol{\Theta} \times \boldsymbol{i}_{\star}. \tag{288}$$

Now, it is evident from Figure 129 and equations (280), (281) that

$$\boldsymbol{i}_3 = \sin El\,\boldsymbol{i}_\star + \cos El\,\boldsymbol{i}_{El}, \tag{289}$$

$$\boldsymbol{i}_4 = \cos El\,\boldsymbol{i}_\star - \sin El\,\boldsymbol{i}_{El}, \tag{290}$$

and

$$\begin{aligned}
\boldsymbol{i}_1 &= \cos(180^\circ - Az)\,\boldsymbol{i}_4 + \sin(180^\circ - Az)\,\boldsymbol{i}_5 \\
&= -\cos Az\,\boldsymbol{i}_4 + \sin Az\,\boldsymbol{i}_5 \\
&= -\cos Az\,\cos El\,\boldsymbol{i}_\star + \cos Az\,\sin El\,\boldsymbol{i}_{El} + \sin Az\,\boldsymbol{i}_{Az}, && (291) \\
\boldsymbol{i}_2 &= \sin(180^\circ - Az)\,\boldsymbol{i}_4 - \cos(180^\circ - Az)\,\boldsymbol{i}_5 \\
&= \sin Az\,\boldsymbol{i}_4 + \cos Az\,\boldsymbol{i}_5 \\
&= \sin Az\,\cos El\,\boldsymbol{i}_\star - \sin Az\,\sin El\,\boldsymbol{i}_{El} + \cos Az\,\boldsymbol{i}_{Az}. && (292)
\end{aligned}$$

Taking into account that

$$\begin{aligned}
\boldsymbol{i}_\star \times \boldsymbol{i}_\star &= 0, \\
\boldsymbol{i}_{Az} \times \boldsymbol{i}_\star &= \boldsymbol{i}_{El}, \\
\boldsymbol{i}_{El} \times \boldsymbol{i}_\star &= -\boldsymbol{i}_{Az},
\end{aligned} \tag{293}$$

we obtain, from equations (280), (281), (289), (290), (291), and (292),

$$\boldsymbol{i}_1 \times \boldsymbol{i}_\star = -\cos Az\,\sin El\,\boldsymbol{i}_{Az} + \sin Az\,\boldsymbol{i}_{El}, \tag{294}$$

$$\boldsymbol{i}_2 \times \boldsymbol{i}_\star = \sin Az\,\sin El\,\boldsymbol{i}_{Az} + \cos Az\,\boldsymbol{i}_{El}, \tag{295}$$

$$\boldsymbol{i}_3 \times \boldsymbol{i}_\star = -\cos El\,\boldsymbol{i}_{Az}, \tag{296}$$

$$\boldsymbol{i}_4 \times \boldsymbol{i}_\star = \sin El\,\boldsymbol{i}_{Az}, \tag{297}$$

$$\boldsymbol{i}_5 \times \boldsymbol{i}_\star = \boldsymbol{i}_{El}, \tag{298}$$

$$\boldsymbol{i}_6 \times \boldsymbol{i}_\star = \boldsymbol{i}_{Az}. \tag{299}$$

Therefore, in view of equations (287) and (288), we have the following expression for the beam offset due to the axis offset effects:

$$\begin{aligned}
\Delta\boldsymbol{i}_\star^a &= \Delta\boldsymbol{\Theta} \times \boldsymbol{i}_\star \\
&= a\,(-\cos Az\,\sin El\,\boldsymbol{i}_{Az} + \sin Az\,\boldsymbol{i}_{El}) \\
&\quad + b\,(\sin Az\,\sin El\,\boldsymbol{i}_{Az} + \cos Az\,\boldsymbol{i}_{El}) \\
&\quad - c\,\cos El\,\boldsymbol{i}_{Az} + d\,\sin El\,\boldsymbol{i}_{Az} + e\,\boldsymbol{i}_{El} + f\,\boldsymbol{i}_{Az}.
\end{aligned} \tag{300}$$

Consequently, we obtain the azimuthal and elevational components of the beam offset due to the axis offset effects, using equation (283),

$$\begin{aligned}
\cos El\,\Delta Az^a &= \Delta\boldsymbol{i}_\star^a \cdot \boldsymbol{i}_{Az} \\
&= -a\,\cos Az \sin El + b\,\sin Az \sin El - c\,\cos El + d\,\sin El + f, \\
\Delta El^a &= \Delta\boldsymbol{i}_\star^a \cdot \boldsymbol{i}_{El} \\
&= a\,\sin Az \cos Az + b\,\cos Az + e.
\end{aligned} \tag{301}$$

The main terms of the elastic deformation effect, which are the cosine and sine of elevation terms due to the gravitational yielding of the radio telescope antenna, are just added to the elevational component of the above equations (301), and therefore, we obtain the total beam offset:

$$\begin{aligned} \cos El\,\Delta Az &= -a\,\cos Az\sin El + b\,\sin Az\sin El - c\,\cos El + d\,\sin El + f, \\ \Delta El &= a\,\sin Az\cos Az + b\,\cos Az + e + g\cos El + h\sin El. \end{aligned} \tag{302}$$

Note that signs of the terms in the above equations may differ in different literature, depending on senses of the rotation angles.

6.9.2 Pointing Measurement

Now, if we measure the azimuthal and elevational offsets of the actual beam direction from the desired one at many directions, we can fit the equation (302) to the measured values to estimate the 8 parameters from a to g and, from the residuals, the pointing accuracy σ_θ, by the method of the least squares. An example of the sky coverage of the water maser sources observed in a pointing measurement at 22 GHz is shown in Figure 130.

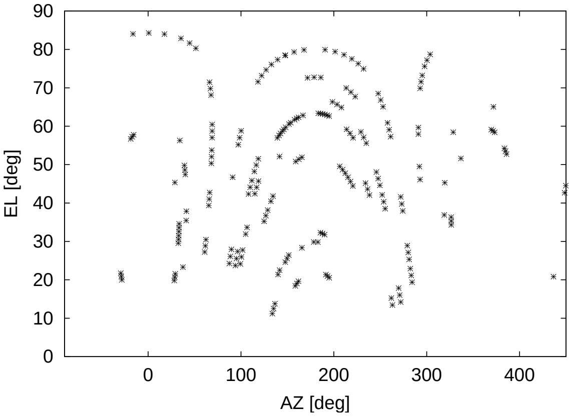

Figure 130: An example of the sky coverage of the sources in a pointing measurement.

Sometimes it is difficult to solve all 8 parameters due to the strong correlations among some of the parameters. In such a case, we have to assume reasonable values for some of the parameters and solve the least squares equations for rest of the parameters.

It is empirically known, for some of the wheel & track type antennas, that inclusion of additional terms with $\cos(2Az)$ and $\sin(2Az)$ dependences into the pointing model better fits the results of the pointing measurements.

In such a case, we have to increase the number of offset parameters to 12, or so.

The measurements are usually conducted by so–called “5 points scan” method. In this method, power from a radio source with well determined celestial position is measured at a telescope direction determined by a certain set of values of the azimuth– and elevation encoders (or angular scales) of the telescope, which are predicted by the source tracking software and instructed by the antenna control software, and at 4 more directions in North, South, East and West sides of the instructed one with the angular separation of roughly a half of the HPBW (Figure 131).

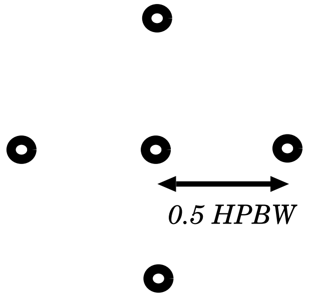

Figure 131: 5 points scan.

Given that the celestial positions and predicted Az and El values are accurate enough (at a level better than 1 arcsecond, say), the power must be strongest at the instructed direction and equally lower at four other directions, if the telescope does not have any systematic axis–offsets and gravitational yielding. If not, however, we will get an asymmetrical distribution of the measured powers at the 5 points. It is a usual practice to fit a two–dimensional Gaussian beam model to the measured power values to derive the offsets $\cos El\,\Delta Az$ and ΔEl between the actual and required beam directions which will be fitted by the model given in equation (302).

To achive the required accuracy of the prediction, the source tracking software must properly take into account major astrometric and geophysical effects including the abberation, the precession–nutation and the atmospheric refraction effects.

The radio sources used for the pointing measurements must be compact, strong enough, and must have well determined values of the position coordinates. Strong astronomical maser sources are often used for frquency bands, where such masers are available. For maser sources, we can easily obtain the antenna temperature value by comparing the “in–line” part and the “out–of–line” part of the frequency spectrum, as shown in Figure 132.

For other frequency bands, strong continuum sources such as quasars or supernova remnants are used with appropriate antenna temperature measuring instruments.

For efficient pointing measurements, we need a good scheduling software and a well automated antenna operation software, which would enable us to quickly observe "pointing sources" one by one at different sky directions, performing 5 points scans and automatically getting pointing offset values by the Gaussian fitting. In the case of the maser sources, we must correctly choose the "in–line" frequency range of the maser spectrum, where a desired line component is located. Since the range periodically shifts in frequency due to the Doppler effect assocaited with the orbital motion of the Earth, we need a software which calculates the "in–line" frequency range of date, from the local–standard–of–rest frequency value (or from the radial velocity v_{LSR},

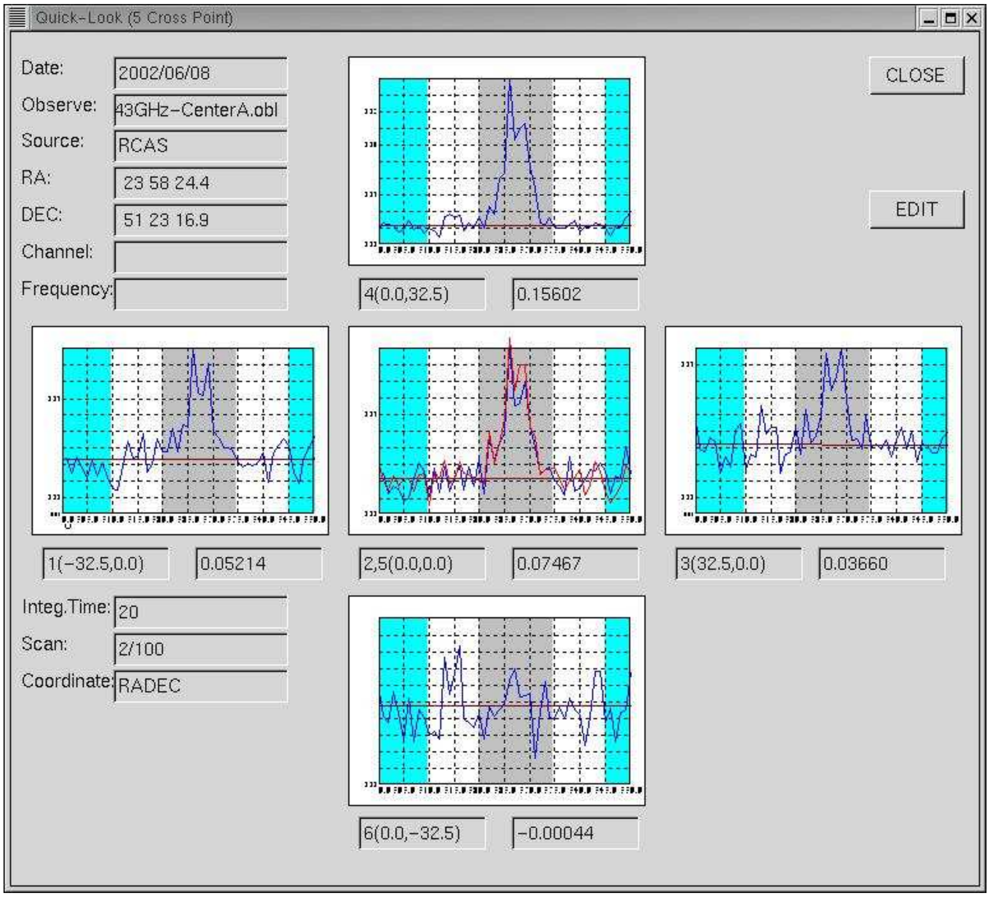

Date: 2002/06/08
Observe: 43GHz−CenterA.obl
Source: RCAS
RA: 23 58 24.4
DEC: 51 23 16.9
Channel:
Frequency:
4(0.0,32.5) 0.15602
1(−32.5,0.0) 0.05214
2,5(0.0,0.0) 0.07467
3(32.5,0.0) 0.03660
Integ.Time: 20
Scan: 2/100
Coordinate: RADEC
6(0.0,−32.5) −0.00044

Figure 132: 5 points scan result at 43 GHz for SiO maser source R Cas obtained at Iriki station of VERA which shows southward offset of the beam.

referred to the Local Standard of Rest).

In massive star forming regions, maser features are often spread over a wide area of the sky, exceeding tens of arcseconds in size. Therefore, we have to choose the “in–line” range, so that it covers a strong maser feature or features, which are concentrated within a compact region much smaller than the antenna beam.

6.10 Beam Pattern Measurement

Power pattern of an antenna beam can be derived by measuring received power (or antenna temperature) of a compact strong radio source, in terms of the “grid–mapping” method (Figure 134) or the “drift–scan” method (Figure 133).

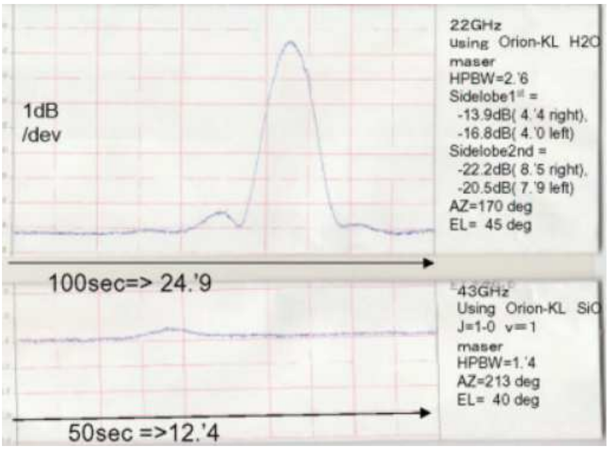

Figure 133: Beam patterns obtained with the drift–scan method at 22 GHz (Top) and at 43 GHz (Bottom) (courtesy of the VERA group, 2002).

In the grid–mapping method, the received power values are measured at centers of a number of grids in the sky, chosen around the source with equal spacing, typically corresponding to a half of the expected beam size, in right ascension and declination. The results are analyzed with standard single–dish imaging softwares, and two–dimensional beam patterns are obtained. An example is shown in the lower panel of Figure 134.

In the drift–scan method, the received power is measured while a source passes in front of the antenna beam due to the diurnal motion, or when the antenna is driven, so that the beam crosses the source in azimuth and elevation directions. In this case, one dimensional beam pattern, as shown in Figure 133, is obtained at each scan.

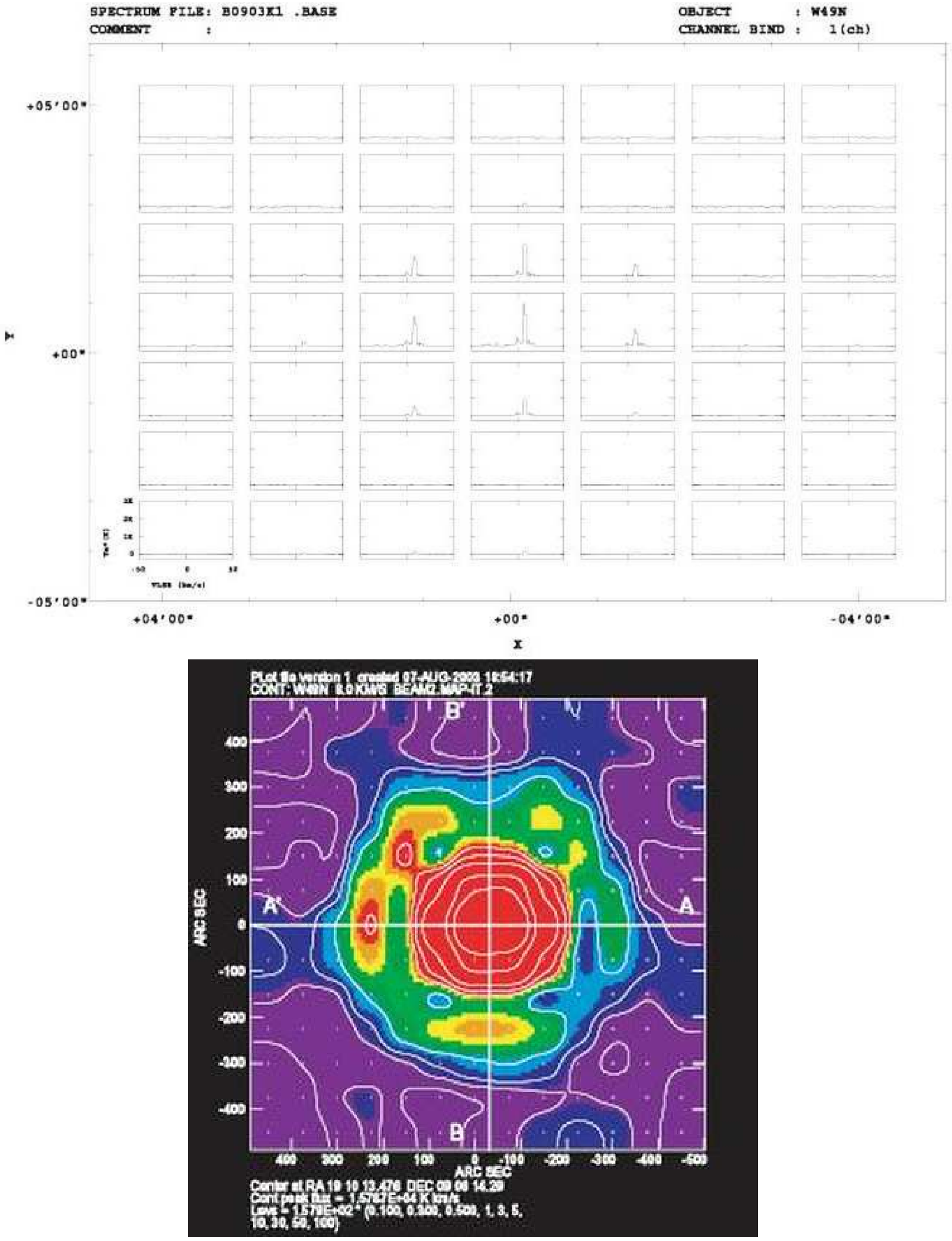

Figure 134: Grid–mapping method for beam pattern measurement (Top), and a resultant beam pattern (Bottom) (courtesy of the VERA group, 2004).

In the both methods, the antenna pointing must be well calibrated, and radio source positions must be precisely known. Also, the measurements must be done within a short time under the clear sky, in order to avoid atmospheric disturbances. It is highly desirable to have automated antenna–operation, data acquisition and analysis softwares for the beam pattern measurements.

References

Adachi, S., 1985, Electromagnetic Wave Engineering, *Koronasha*, (in Japanese).

Kraus, J.D., 1984, Electromgnetics, 3rd Edition, *McGraw–Hill* (Singapore).

Kraus, J.D., 1986, Radio Asronomy, 2nd Edition, *Cygnus–Quasar Books*.

Nyquist, H., 1928, Thermal Agitation of Electric Charge in Conductors, *Phys. Rev.*, **32**, 110–113.

Panofsky, W.K.H., and Phillips, M., 1962, Classical Electricity and Magnetism, 2nd Edition, *Dover Publications, Inc.* (New York).

Rohlfs, K., 1986, Tools of Radio Astronomy, *Springer–Verlag* (Berlin).

Rohlfs, K., and Wilson, T. L., 2000, Tools of Radio Astronomy, 3rd Edition, *Springer–Verlag* (Berlin).